UNIVERSITÀ
DEGLI STUDI
DI PADOVA

Sede Amministrativa: Università degli Studi di Padova
Dipartimento di Geoscienze

SCUOLA DI DOTTORATO DI RICERCA IN SCIENZE DELLA TERRA
VIA G. GRADENIGO, 6, 35131 PADOVA
CICLO XXVII

FRICTIONAL BEHAVIOR AND MICROSTRUCTURES OF CALCITE-BEARING FAULT GOUGES

Direttore della Scuola : Ch.mo Prof. Massimiliano Zattin

Supervisore: Ch.mo Prof. Giulio Di Toro

Dottoranda: Marieke Rempe

Abstract

The frictional behavior of a fault and the physical and mechanical properties of the fault rocks have important implications for earthquake nucleation, propagation and arrest. To further understand the mechanical behavior of carbonate-bearing faults, low- to high-velocity experiments on calcite gouge have been conducted using three rotary-shear apparatus: ROSA, located at the Department of Geosciences of the University of Padua, Italy; SHIVA, at the Istituto Nazionale die Geofisica e Vulcanologia (INGV) in Rome, Italy, and the *Phv*-apparatus of the Physical Property Research Group of the Kochi Institute for Core Sample Research, Kochi, Japan. Three main topics were addressed with the experimental approach: 1) The formation of clast-cortex aggregates in natural and experimental calcite-bearing fault zones (Chapter I); 2) Localization of strain in gouge layers (Chapter II); and 3) The effect of fluids on the frictional behavior of calcite gouge (Chapter III).

Clast-cortex aggregates (CCAs) are composite grains found in the slipping zones of faults hosted in calcite- and clay-rich rocks that were previously suggested to be textural evidence of seismic slip on a fault. Experimental investigation of the dependence of CCA formation in calcite gouge layers on the applied slip rate, normal stress, total displacement and ambient humidity showed that CCAs formed at all investigated slip rates (100 μm/s to 1 m/s) but only at relatively low normal stresses (≤5 MPa). The aggregates were better developed with increasing displacement (up to 5 m) and did not form in experiments with water-dampened gouges. In the experiments, aggregates formed in low-strain regions within the gouge layers, adjacent to the highest-strain slip zones. We propose that CCAs in calcite-bearing slip zones form in the shallow portions of faults during shearing in relatively dry conditions, but our experiments suggest that they cannot be used as indicators of seismic slip. Formation involves clast rotation due to granular flow accompanied by accretion of fine matrix material possibly facilitated by electrostatic forces.

To further understand strain localization during seismic slip, which is a fundamental mechanical process that has implications for frictional heating and the

earthquake energy budget, we performed intermediate- to high-velocity rotary-shear experiments on calcite gouge containing strain markers made of dolomite gouge. Sheared markers should provide microstructural information of the strain distribution in the gouge layer and its dependence on the applied total strain, normal stress, slip rate, and ambient conditions. Microstructural analysis revealed that in both dry and water-dampened gouges strain localization at 1 m/s occurs progressively and rapidly. The strain accommodated in the bulk of the gouge layer does not change significantly with increasing total displacement, suggesting that, once formed, the high-strain slipping zone and principal slip surface accommodate most of the ongoing displacement. This is supported by the presence of sintered and recrystallized grains and zones of calcite decarbonation adjacent to the principal slip surface, indicating localized frictional heating. Faster localization in water-dampened conditions, although suggested by the faster dynamic weakening, was not reflected in the investigated microstructures. Instead, weakening in water-dampened gouges may be enhanced by faster subcritical crack growth in the presence of fluids. When extrapolated to natural conditions, our results suggest that calcite-bearing gouge slip zones are more prone to slip in the presence of water than in relatively dry conditions.

The effect of fluids on the frictional behavior of calcite gouge was further investigated by conducting intermediate- to high-velocity experiments with controlled fluid pressure. Consistent with our results from experiments with strain-markers, slip appears to be localized on one or more slip surfaces adjacent to which zones of recrystallization are found. Grey or black material covering the slip surface of several samples was identified as disordered carbon by Raman spectroscopy indicating decarbonation of the calcite. In low-velocity (1 mm/s) experiments, a lower shear stress of water-saturated gouges as compared to room-dry conditions is attributed to intergranular lubrication and to the lower calcite fracture surface energy accelerating subcritical crack growth, consistent with a high degree of compaction. At the initiation of sliding at high velocity, weakening in saturated gouges occurs abruptly, while the room-dry gouges show a pronounced strengthening phase before the onset of weakening. For

a given effective normal stress, the peak stress is lower, and the strengthening phase is longer, for higher pore-fluid factors. The weakening in room-dry and water-saturated gouges sheared at high velocity likely occurs by flash heating, which is accelerated in the presence of fluids by subcritical crack growth. Consistent with flash heating, the presence of carbon on the slipping surface of our calcite samples indicated that decarbonation has occurred even though the bulk temperature of the gouge layer was lower than the decarbonation temperature. At high velocity, intense frictional heating leads to thermal pressurization and subsequent decrease of the shear stress in the experiments performed in undrained conditions. Zones of recrystallized grains adjacent to the principal slip surfaces are possibly featuring microstructures characteristic for grain boundary sliding aided by diffusion creep which suggests that strain was not only accommodated by frictional processes, but possibly by superplasticity. The experimental results suggest that the presence of water in carbonate-bearing faults facilitates earthquake nucleation and even more so if the fluids present are pressurized. This might explain the long-lasting earthquake sequences e.g. of Umbria-Marche and L'Aquila hosted on carbonate-bearing faults. Additionally, some of the slip distribution complexity during earthquakes occurring in carbonate sequences might be due to a difference in the degree of fluid saturation in different fault patches.

Abstract

Le proprietà frizionali delle faglie e le proprietà fisiche e meccaniche delle rocce di faglia influenzano in modo importante la nucleazione, la propagazione e l'arresto dei terremoti. Per capire più approfonditamente il comportamento meccanico delle faglie in rocce carbonatiche, sono stati fatti esperimenti a diverse velocità usando *gouge* (rocce granulari) di calcite, con tre diverse macchine *rotary shear*: ROSA, installata presso il Dipartimento di Geoscienze dell'Università di Padova, Italia; SHIVA, presso l'Istituto Nazionale di Geofisica e Vulcanologia (INGV), Roma, Italia, e il Phv-apparatus del Physical Property Research Group del Kochi Institute of Core Sample Research, Kochi, Giappone. Tre sono gli obiettivi principali indagati con il metodo sperimentale: 1) La formazione di *clast-cortex aggregates* (aggregati aventi al nucleo un clasto e una corteccia composta da detrito granulare ultrafine) nelle zone di faglia ricche in calcite sia naturali che sperimentali (Capitolo I); 2) Localizzazione della deformazione nei livelli di *gouge* (Capitolo II); e 3) L'effetto dei fluidi (acqua) nel comportamento frizionale del *gouge* di calcite (Capitolo III).

I *Clast-cortex aggregates* (CCAs) sono clasti compositi che si trovano nelle zone di slip delle faglie ricche in calcite e minerali argillosi, precedentemente candidati sulla base di evidenze tessiturali ad essere indicatori di scivolamento cosismico. Esperimenti mirati sono stati fatti per trovare la correlazione tra la formazione di CCA in *gouge* di calcite e velocità, sforzo normale, rigetto totale e condizioni ambientali (umidità atmosferica e saturazione in acqua). I risultati sperimentali mostrano che i CCA si formano a tutte le velocità di scivolamento (da 100 μm/s a 1 m/s) ma solo a sforzi normali relativamente bassi (<5 MPa). Gli aggregati sono più abbondanti e meglio sviluppati per grandi rigetti (massimo rigetto imposti pari a 5 m) e non si formano negli esperimenti con *gouge* saturo d'acqua. Negli esperimenti, gli aggregati si sono formati in regioni poco deformate del livello di *gouge*, ma adiacenti alle zone con elevata

104 localizzazione della deformazione. Da queste osservazioni sperimentali concludiamo che
105 i CCA si formino nelle parti più superficiali delle faglie durante lo la deformazione per
106 taglio in condizioni relativamente asciutte, ma non necessariamente durante lo
107 scivolamento cosismico. Di conseguenza i CCA non possono essere usati come indicatori
108 di slip cosismico. Il meccanismo di formazione dei CCA è per rotazione dei clasti dovuta
109 al flusso granulare accompagnato ad accrescimento per cattura di particelle più piccole
110 della matrice, probabilmente a causa di forze di natura elettrostatica.

111 Per meglio comprendere i meccanismi di localizzazione della deformazione
112 durante lo scivolamento cosismico, che controlla, p.e., lo sviluppo di calore per attrito su
113 faglia e il bilancio energetico di un terremoto, abbiamo condotto esperimenti
114 imponendo velocità di scivolamento da intermedie ad elevate con macchine tipo *rotary*
115 *shear* su *gouge* di calcite. All'interno dello spessore del *gouge* abbiamo posizionato dei
116 *marker* (indicatori) di deformazione per taglio composti da *gouge* di dolomite. I marker,
117 deformandosi unitamente alla matrice di calcite, consentono di misurare la distribuzione
118 della deformazione per taglio nel livello di *gouge* negli esperimenti. Le analisi
119 microstrutturali hanno dimostrato che sia in condizioni asciutte che in presenza d'acqua
120 la deformazione a velocità di scivolamento di 1 m/s, è molto rapida e si localizza in una
121 zona principale di scivolamento (ZPS) dallo spessore di poche decine di micrometri e
122 sulla adiacente superficie principale di scivolamento (SPS). La deformazione per taglio
123 accomodata nella parte rimanente del livello di *gouge* non cambia significativamente
124 all'aumentare del rigetto, suggerendo che, una volta localizzata, la ZPS e la SPS
125 accomodano la maggior parte del rigetto. Questa conclusione è supportata dalla
126 presenza di granuli sinterizzati e ricristallizzati e zone di decarbonatazione della calcite
127 adiacenti alla SPS, che indicano lo sviluppo, estremamente localizzato, di calore per
128 attrito. I dati meccanici indicano che i *gouge* saturi in acqua si indeboliscono (l'attrito
129 diminuisce più rapidamente con il rigetto) di quelli asciutti, ma le microstrutture sono
130 sostanzialmente simili per quanto riguarda la velocità di localizzazione della

131 deformazione. L'indebolimento frizionale nei *gouge* saturi d'acqua può essere innescato
132 dal meccanismo di crescita sub-critica delle microfratture, più efficiente in presenza
133 d'acqua. L'estrapolazione di questi risultati alle condizioni naturali, suggerisce che i
134 *gouge* ricchi in calcite sono più favorevoli allo scivolamento se saturi in acqua, piuttosto
135 che in condizioni relativamente più asciutte.

136 L'effetto dei fluidi sul comportamento frizionale di *gouge* di calcite è stato
137 ulteriormente studiato attraverso esperimenti in controllo di pressione di fluidi a
138 velocità da intermedie ad elevate. Coerentemente con i nostri esperimenti con gli
139 indicatori di deformazione, il rigetto appare localizzato su una o più superfici di
140 scivolamento che sono spesso contornate da zone di ricristallizzazione. La
141 microspettroscopia Raman ha evidenziato la presenza di carbonio amorfo sulla
142 superficie di scivolamento, indicatore di processi di decarbonatazione nella calcite. In
143 esperimenti condotti a basse velocità di scivolamento (1 mm/s), la minore resistenza al
144 taglio dei *gouge* saturi d'acqua rispetto ai *gouge* deformati in presenza di sola umidità
145 atmosferica, è attribuita a lubrificazione intergranulare operata dalla acqua e alla bassa
146 energia di superficie della calcite. Quest'ultima consente l'accelerazione dei processi di
147 crescita sub-critica delle microfratture cui corrisponde un alto grado di compattazione.
148 Nelle prime fasi di scivolamento ad alte velocità, l'indebolimento nei *gouge* saturi
149 avviene improvvisamente, mentre i *gouge* in presenza di umidità atmosferica mostrano
150 una fase di aumento di resistenza al taglio prima della fase di indebolimento. Per un
151 dato sforzo normale efficace, per rapporti più elevati di pressione di poro su sforzo
152 normale, lo sforzo di taglio di picco è minore e la fase di aumento di resistenza che
153 precede l'indebolimento più lunga. La riduzione della resistenza per attrito ad alte
154 velocità di scivolamento (cosismiche, ca. 1 m/s), sia in condizioni di umidità atmosferica
155 che sature d'acqua, occorre verosimilmente per meccanismo di "riscaldamento
156 istantaneo" (*flash heating*) alla scala delle asperità (decine di micrometri).
157 L'indebolimento per "*flash heating*" è accelerato in presenza di fluidi per il meccanismo

158 di crescita subcritica delle microfratture. Coerentemente con il verificarsi di *flash*
159 *heating*, la presenza di carbonio sulla superficie di scivolamento dei nostri campioni di
160 calcite indica che la decarbonatazione è avvenuta nonostante le temperature medie
161 nell'intera zona di scivolamento, misurate con termocoppia, fossero più basse di quella
162 di decarbonatazione. Ad alte velocità di scivolamento, in esperimenti in condizioni
163 sature non drenate, la presenza di un intenso riscaldamento frizionale comporta la
164 pressurizzazione termica del livello di *gouge*, con conseguente diminuzione dello sforzo
165 di taglio. Nella zona di scivolamento, la formazione di nanoparticelle, grani ricristallizati
166 di calcite e microcavità adiacenti alla superficie di scivolamento principale può essere
167 associata a processi di *grain boundary sliding* sostenuti da processi diffusivi dipendenti
168 dalla granulometria. Di conseguenza, la deformazione cosismica non è accomodata da
169 soli processi prettamente frizionali, ma anche di tipo superplastico. I risultati degli
170 esperimenti indicano che la presenza d'acqua in faglie all'interno di litologie
171 carbonatiche facilita l'enucleazione di terremoti, ancor più se i fluidi presenti sono in
172 pressione. Questa potrebbe essere una possibile spiegazione delle lunghe sequenze
173 sismiche all'interno di successioni carbonatiche, ad esempio Umbria-Marche e L'Aquila.
174 In aggiunta, la complessa distribuzione dei rigetti durante un singolo terremoto
175 potrebbe essere causata da differenze nel grado di saturazione in fluidi in diverse zone
176 della faglia.

Contents

General Introduction....15

Chapter I

Clast-cortex aggregates in experimental and natural calcite-bearing fault zones

Abstract....24
1. Introduction....25
2. Methods....28
2.1. *Experimental Set-Up*....28
2.1.1. Experiments with ROSA....29
2.1.2. Experiments with SHIVA....31
2.2. Sample Preparation and Analysis Techniques....32
3. Results....34
3.1. Mechanical Behavior of Calcite Gouges....34
3.2. Strain localization and textural zones in room-dry experiments....35
3.3. Strain distribution in room-dry experiments....36
3.4. Formation Conditions of Experimental Clast-Cortex Aggregates....40
3.4.1. Room-dry Conditions....40
3.4.2. Wet Conditions....42
3.4.3. Vacuum Conditions....42
3.5. Size and Shape Analysis of Clast-Cortex Aggregates....42
4. Discussion....47
4.1. Development of the textural zones....47
4.2. Comparison of natural and experimental CCAs....47
4.3. Deformation conditions necessary to form experimental CCAs....49
4.3.1. The role of displacement and strain....49
4.3.2. The role of slip velocity....50
4.3.3. The role of normal stress....51
4.3.4. Ambient Conditions....52
5. Conclusions....53
6. Acknowledgements....54
7. Figure Captions....55
8. Tables....59

Chapter II

Strain localization in experimentally-sheared calcite gouge layers

Abstract 66
1. Introduction 69
2. Methods 73
2.1. Experimental Set-Up 73
2.2. Sample Preparation 74
2.3. Analysis Techniques 75
3. Results 80
3.1. Mechanical behavior 80
3.2. Microstructures 85
3.2.1. Textural zones 85
3.2.2. Strain markers 91
4. Discussion 102
4.1. Effect of the rotary-shear configuration on strain localization 102
4.1.1. Effect of boundary conditions 102
4.1.2. Effect of the radial position 105
4.2. Strain localization and mechanical behavior 106
4.2.1. Strengthening phase 106
4.2.2. Dynamic weakening: Room-dry vs. water-dampened conditions 108
4.2.3. Post-dynamic-weakening behavior/ Progressive localization 110
4.3. Thickness of the localized zone 111
4.4. Dynamic weakening mechanisms 112
4.5 Implications for natural faults 114
5. Conclusion 115
6. Acknowledgements 116
7. Figure Captions 116
8. Tables 122

Chapter III

Frictional behavior of fluid-pressurized calcite gouge sheared at seismic velocity

Abstract 128
1. Introduction 131
2. Material and Methods 133

2.1. Experimental Set-Up 133
2.2. Experimental Procedures 135
2.2.1. Velocity-step experiments 135
2.2.2. Permeability measurements 136
2.3. Sample Preparation 137
2.4. Microanalytical Techniques 138
2.5. Thermodynamic calculations 139
3. Results 140
3.1. Mechanical data 140
3.1.1. Room-dry conditions 140
3.1.2. Fluid-saturated conditions 143
3.2. Permeability Measurements 159
3.3. Microanalysis 159
3.3.1. Scanning electron microscopy 159
3.3.2. Raman spectroscopy 169
3.3.3. X-ray diffraction analysis 173
3.4. Thermodynamic calculations 174
3.4.1. Thermal pressurization 174
3.4.2. Decarbonation temperatures 175
4. Discussion 178
4.1. Teflon contamination 178
4.2. Temperature evolution 183
4.3. Evidence of pressurization? Interplay of friction, temperature and axial displacement in the fluid-pressurized experiments 184
4.3.1. First low-velocity step: mechanical pressurization 185
4.3.2. High-velocity step 186
4.3.3. Larger displacements/Second low-velocity step 190
4.4. Dynamic weakening mechanisms 193
4.4.1. Role of thermal pressurization and alternative weakening mechanisms 193
4.4.2. Effect of the pore-fluid factor 199
4.5. Comparison to cohesive Carrara marble 199
4.6. Implications for natural faults 200
5. Conclusion 200
6. Acknowledgements 202
7. Figure Captions 203

8. Tables 209
Concluding Remarks.....213
References.....215
Appendix A 231
Appendix B 248
1. Additional figures 248
2. SEM images 248
Appendix C 261

General Introduction

Fault zones dominantly influence the mechanical behavior of the Earth's crust (Scholz, 2002; Handy et al., 2007; Faulkner et al., 2010). The frictional behavior of a fault and the physical and mechanical properties of the fault rocks have important implications for earthquake nucleation, propagation and arrest (Scholz, 2002; Rice and Cocco, 2007). Upon tectonic loading of a fault, the fault may remain locked, undergo stable creep or unstable stick-slip behavior, or experience seismic slip (Brace and Byerlee, 1966; Scholz et al., 1969). The frictional response of a fault is usually well described by the rate-and-state friction laws (Dieterich, 1979; Ruina, 1983; Marone, 1998), that were developed empirically from numerous experimental studies performed at low slip velocities (<0.1 m/s) and for small displacements (of few centimeters) and are thus associated with the earthquake initiation stage. However, the rate-and-state friction laws do not adequately describe the significant dynamic weakening of rocks deforming at seismic slip rates (> 0.1 m/s). The different frictional behavior of faults sliding at seismic conditions is attributed to the relatively large mechanical work rate triggering various weakening mechanisms (Di Toro et al., 2011). The technical possibility to study the seismic behavior of faults and the associated weakening mechanisms, that up to data could only be inferred from field and seismological studies, in the laboratory was achieved through the development of a new generation of high-velocity rotary-shear machines (Shimamoto and Tsutsumi, 1994; Di Toro et al., 2010). The high-velocity rotary-shear experiments that were subsequently performed showed that rocks weaken dramatically at seismic slip rate, mostly independent of the lithology (Di Toro et al., 2011). Several thermally- and mechanically-activated weakening mechanisms were proposed including thermal pressurization, frictional melting, dehydration or decarbonation reactions, or lubrication by (nano)powders, silica gel, and graphite that formed from carbonaceous material (Di Toro et al., 2004, 2011; Rice, 2006; Han et al., 2010, 1011; Reches and Lockner , 2010; Goldsby and Tullis, 2011; Kuo et al., 2014), most of which remain poorly understood. Out of these, frictional melt lubrication leaves the up to date only unambiguous field evidence of seismic slip on a fault through pseudotachylytes, i.e., solidified friction melts (Sibson, 1975; Di Toro et al., 2005). Even though the presence of silica gel and graphite in natural fault zones has been confirmed (Oohashi et al., 2012;

Kirkpatrick et al., 2013; Kuo et al., 2014), their nature and role in fault weakening remains to be completely understood. It remains a key goal to identify field evidence for seismic slip on a fault, necessary e.g. for field geologists to understand the regional tectonic history and seismic hazard in areas where no long-term record of seismicity exists.

Investigation of the microstructures developing in high-velocity experiments on rocks and fault gouges may help to recognize new textural evidence of seismic slip. In addition to pseudotachylytes, such evidence may be provided by injections of granular material (Lin, 1996; Smith et al., 2008; Rowe et al., 2012), pulverized fault zone rocks (Brune, 2001; Dor et al., 2006; Rempe et al., 2013), localized zones of recrystallization (Kim et al., 2010; Brantut et al., 2011; Bestmann et al., 2012; Smith et al., 2013), thermal maturation of organic molecules (Polissar et al., 2011; Rabinowitz et al., 2013; Savage et al., 2014), mirror-like slip surfaces (Boneh et al., 2013; Chen et al., 2013; Fondriest et al., 2013; Siman-Tov et al., 2013), and graphitization of carbonaceous materials (Oohashi et al., 2013; Kuo et al., 2014).

Additionally, high-velocity experiments on gouges identified so-called clast-cortex aggregates (CCAs) that were initially thought to form during slip at high velocity (Boutareaud et al., 2008, 2010; Ferri et al., 2011), but later found to form also at velocities as low as 0.0005 m/s in quartz and quartz-bentonite gouges (Han and Hirose, 2012). The main characteristic of CCAs is a central clast enclosed by an outer cortex of fine-grained material that defines a composite rounded structure. CCAs have also been found in the slipping zones of landslides (Boyer and Hossack, 1992; Beutner and Craven, 1996; Anders et al., 2000, 2010; Beutner and Gerbi, 2005) and faults with various lithologies (Warr and Cox, 2001; Boullier et al., 2009; Smith et al., 2011; see Han and Hirose, 2012 and Rempe et al., 2014 (Appendix A) for a summary). For instance, the CCA-bearing slipping zone of the Tre Monti fault (Central Apennines, Italy) was entirely comprised of carbonates (Smith et al., 2011).

We further investigated the processes contributing to the formation of natural and experimental CCAs in calcite-bearing slip zones like the Tre Monti normal fault by performing low- to high-velocity rotary-shear experiments on calcite gouge, the results of which are discussed in Chapter I of this thesis (as published in Rempe et al., 2014; Appendix A). The

chapter describes our systematic study of the dependence of the CCA formation on slip velocity, total displacement, normal stress, and ambient humidity. Our results contribute to a better understanding of the significance of CCAs in tectonic fault zones, and provide constraints on the deformation processes active within shallow, granular slipping zones in carbonates.

Mirror-like slip surfaces in dolostones have been shown to be a seismic indicator (Fondriest et al., 2012, 2013; Siman-Tov et al., 2013), even though in other lithologies they might form at lower slip rates (Verberne et al., 2013, 2014). Additionally, mirror-like slip surfaces provide an excellent example of intensive strain localization during seismic slip on a fault. Strain localization is an abundant feature in many natural fault zones (Chester et al., 1993; Lee et al., 2001; Sibson, 2003; Wibberley and Shimamoto, 2003). Additionally, many seismological studies reveal a high degree of localization of seismicity along large faults (e.g., Li et al., 1998; Schaff et al., 2002; Thurber et al., 2006), suggesting that slip localization occurs in major fault zones throughout the crustal seismogenic zone (Rockwell and Ben-Zion, 2007) and beneath (Shelly, 2010). The degree of strain localization and the thickness of the principal slip zone can have a great effect on the mechanical behavior of faults (Ben-Zion and Sammis, 2003; Heermance et al., 2003; Rockwell and Ben-Zion, 2007) because they influence the production of frictional heat, the critical slip distance and the earthquake energy budget (e.g. fracture energy vs. radiated energy) (Cocco et al., 2009; Marone et al., 2009). Thus, strain localization in gouges and the correlation with the frictional behavior has been the subject of many dedicated experimental (Marone et al., 1992; Beeler et al., 1996; Scruggs and Tullis, 1998; Rathbun and Marone, 2010) and numerical studies (Rice, 2006; Segall and Rice, 2006; Mair and Abe, 2008; Platt et al., 2014; Rice et al., 2014). For instance, Platt et al. (2014) modeled the effect of localization on the shear strength evolution considering thermally-driven weakening mechanisms and found that while during early stages of deformation the shear-strength evolution is similar to that modeled for uniform shearing (Rempel and Rice, 2006), the onset of strain-rate localization is accompanied by an acceleration in dynamic weakening. Similarly, results from high-velocity rotary-shear experiments on room-dry calcite gouges indicate that localization of shear is a necessary precursor to dynamic weakening (Smith et al., 2015).

To further understand the localization of strain and its effect on friction was the aim of a second part of my Ph.D. studies. The study of Smith et al. (2015) was extended by conducting rotary-shear experiments on calcite gouges using strain markers and by including wet calcite gouges and a wider range of slip velocities and total displacements. The results and implications from these strain-marker experiments are discussed in Chapter II of this thesis.

As stated above, thermal pressurization of pore-fluids has been invoked to be involved in dynamic fault weakening. The concept of thermal pressurization is based on the relationship between shear stress, effective stress and pore-fluid pressure described by the Terzaghi law, $\tau = \mu(\sigma_n - p_f) = \mu\sigma_{eff}$ (Terzaghi, 1923; Nur and Byerlee, 1971), which states that an increase in the pore pressure p_f will lead to a decrease in the effective normal stress σ_{eff} which results in a decrease of the shear stress τ. Thus, as it has been long recognized, fluids trapped in fault zones will play a fundamental role in controlling the fault's strength and earthquake nucleation, propagation and arrest (Hubbert and Rubey, 1959; Sibson, 1973; Lachenbruch, 1980; Rice, 1992; Hickman et al., 1995). For instance, high pore-fluid pressures might explain the apparent weakness of large fault zones (Rice, 1992; Faulkner and Rutter, 2001; Chester et al., 1993) and may allow for slip on unfavorably-orientated faults (Sibson, 1990).

High pore-fluid pressures might be generated by frictional heating during seismic slip (Sibson, 1973). This thermal pressurization will decrease the effective stress and ultimately lead to fault weakening (Rempel and Rice, 2006; Rice, 2006; Segall and Rice, 2006; Rudnicki and Rice, 2006). Moreover, dehydration and decarbonation of minerals may result in further thermo-chemical pressurization (Famin et al., 2008; Sulem and Famin, 2009; Brantut et al., 2008, 2010; Ferri et al., 2010; Proctor et al., 2014). For instance, thermal and thermochemical pressurization has likely caused the catastrophic displacement of the Vaiont (Voight and Faust, 1982; Veveakis et al., 2007; Ferri et al., 2011) and Heart Mountain (Beutner and Craven, 1996; Beutner and Gerbi, 2005; Anders et al., 2010; Mitchell et al., 2015) landslides. Experimental evidence of thermal and thermochemical pressurization in high-velocity experiments has long been missing due to technical restrictions to confine pore fluids and measure the pore pressure in-situ (Violay et al., 2013). To our knowledge, first evidence of pressurization due to

frictional heating was measured by Violay et al. (2013, 2014) in high-velocity experiments on carbonate rocks using a purposely-designed sample holder. In Chapter III of this thesis, we now provide further evidence of thermal pressurization in calcite gouges sheared at seismic velocity. Chapter III describes the investigation of the effect of (pressurized) pore fluids on the mechanical behavior of calcite rocks and discusses processes that may have been active such as thermal pressurization and physico-chemical fluid effects. Physico-chemical mechanisms – e.g., pressure solution (Rutter, 1976; Robin, 1978; Wheeler, 1992), subcritical crack growth (Rice, 1978; Atkinson, 1984), or reaction weakening (Wintsch et al., 1995; Collettini et al., 2004; Wibberley, 2005) – may also act to weaken a fault, even though they depend greatly on the chemistry and mineralogy of the involved fluids and rocks, respectively.

Additionally, fluids may accelerate mechanisms controlled by diffusive processes, e.g., grain boundary sliding aided by diffusion creep ("superplastic behavior", Poirier, 1985). Although these processes are thought to occur at high temperature and low strain-rates ($< 10^{-5}$ s^{-1}) in geological materials (Boullier and Gueguen, 1975; Schmid et al., 1977; Poirier, 1985), several orders of magnitude lower than the strain rates typically applied in high-velocity experiments ($> 10^{2}$ s^{-1}), recent experimental results suggests the activation superplastic behavior in high-velocity experiments on carbonate-bearing gouges (Green et al., 2010; Holdsworth et al., 2013; De Paola et al., 2014). However, the experiments of Green et al. (2010), Holdsworth et al. (2013) and De Paola et al. (2014) were conducted in nominally dry conditions and the activation of superplastic behavior was contributed to the presence of nanoparticles causing enhanced diffusion rates (Würschum et al., 2003; Tjong and Chen, 2004) rather than to the presence of fluids. In agreement with the experimental results of Green et al. (2010), Holdsworth et al. (2013) and De Paola et al. (2014), our experimental results may be consistent with strain accommodation by crystal-plastic processes at seismic slip rates.

All experiments of this thesis were conducted on calcite-bearing gouges. This was mainly inspired by the abundance of faults in carbonates settings in Europe [e.g. in Italy (e.g., Collettini & Holdsworth, 2004; De Paola et al., 2008; Smith et al., 2011) and in Greece (e.g, Moretti et al., 2003; Bastesen et al., 2009)], and worldwide (e.g., Longmenshan fault zone; Zhang and He, 2013). Laboratory experiments on carbonate-bearing rocks can thus contribute

to our understanding of earthquake mechanics in these settings. Additionally, the occurrence of mirror-like slip surfaces in limestones and dolostones showed the importance of strain localization (Fondriest et al., 2012, 2013; Siman-Tov et al., 2013) in carbonate-bearing faults. Furthermore, experiments on calcite gouges allowed us to compare experimentally-formed CCAs with the natural examples of the Tre Monti fault (Smith et al., 2011).

The mechanical properties of gouges will be important during seismic slip of faults, as most faults contain a "core zone" consisting of highly comminuted gouge material (e.g., Chester and Logan, 1986, 1987; Sibson, 2003; Chester et al., 2004). Experimental studies have shown that gouges have a stabilizing effect during the earthquake nucleation phase (Marone and Scholz, 1988; Verberne et al., 2013) and that at seismic slip rates dynamic weakening in gouges is delayed compared to slip on initially bare rock surfaces (Smith et al., 2015) which is likely related to need to localize slip in the gouge layer prior to weakening. As argued by Smith et al. (2015), even if previously-formed gouge material in a fault core was recrystallized or cemented during the interseismic period (e.g. Gratier and Gueydan, 2007; Tenthorey and Cox, 2006), the mechanical properties of gouge will play a significant role because fresh gouge material is continuously formed during earthquake rupture (Power et al., 1988; Reches and Dewers, 2005).

The rotary-shear experiments described in this thesis were conducted with three different apparatus: ROSA, located at the Department of Geosciences of the University of Padua, Italy; SHIVA, at the Istituto Nazionale die Geofisica e Vulcanologia (INGV) in Rome, Italy, and the *Phv*-apparatus of the Physical Property Research Group of the Kochi Institute for Core Sample Research, Kochi, Japan. The machines differ in the range of slip rates and normal stresses they can apply (Ma et al., 2014), with ROSA being able to apply the largest span of velocities (10^{-6}–1 m/s), while SHIVA has the most powerful engine (280 kW) and can apply slip rates of up to 6.5 m/s. SHIVA is equipped with a Pfeiffer Hi cube vacuum pump that can create a minimum pressure of 10^{-4} mbar in a chamber surrounding the samples (described in Violay et al., 2013). The *Phv*-apparatus is equipped with a pore-fluid pressure system that can apply pore pressures of up to 50 MPa (Tadai et al., 2009). Thus, using the different machines, experiments could be carried out in room-dry, vacuum, water-dampened, and water-saturated

conditions. In experiments with water-dampened (and, to a small extend, room-dry) gouges, the pore pressure is not controlled or measured during the experiment and thus the exact effective stress is unknown and a calculated coefficient of friction $\mu = \frac{\tau}{\sigma_{eff}}$ would only be an apparent one. To avoid this, we chose to report the shear stress measured in our experiments rather than an apparent coefficient of friction.

Chapter I

Clast-cortex aggregates in experimental and natural calcite-bearing fault zones

(This study was performed in collaboration with Steven Smith, Fabio Ferri, Thomas Mitchell, and Giulio Di Toro (see Appendix A). I performed all the work described in this chapter. I was assisted (but not continuously) in the laboratory by Steven Smith and Fabio Ferri. XRD analysis was performed by Federico Zorzi. The material presented here was discussed with Steven Smith, Fabio Ferri, Thomas Mitchell and Giulio Di Toro.)

Abstract

We investigated the formation mechanisms of rounded clast-cortex aggregates, a composite grain found in the slipping zones of faults hosted in calcite- and clay-rich rocks. The natural aggregates contain a central clast commonly made of host-rock fragments or reworked cataclasite from the slipping zone. The central clasts are surrounded by an outer cortex of calcite or clay grains a few μm or less in size. In laboratory experiments on calcite gouges using two rotary-shear apparatus we investigated the dependence of clast-cortex aggregate formation on the applied slip rate, normal stress, total displacement and ambient humidity. Clast-cortex aggregates formed at all investigated slip rates (100 μm/s to 1 m/s) but only at relatively low normal stresses (≤5 MPa). The aggregates were better developed with increasing displacement (up to 5 m) and did not form in experiments with water-dampened gouges. In the experiments, aggregates formed in low-strain regions within the gouge layers, adjacent to the highest-strain slip zones. We propose that clast-cortex aggregates in calcite-bearing slip zones form in the shallow portions of faults during shearing in relatively dry conditions, but our experiments suggest that they cannot be used as indicators of seismic slip. Formation involves clast rotation due to granular flow accompanied by accretion of fine matrix material possibly facilitated by electrostatic forces.

1. Introduction

A wide variety of micro- and meso-structural features are produced in fault zones from the interaction of deformation processes operating (often synchronously) across a range of time and length scales (e.g. Snoke et al., 1998). Recognizing (micro)structures that are characteristic of particular deformation conditions (e.g. of strain rate, total strain, fluid content) is a critical step towards interpreting fault mechanical behavior. For example, identifying seismic slip in the rock record (Cowan, 1999) relies on the identification of tectonic pseudotachylytes formed by frictional melting (Sibson, 1975; Di Toro et al., 2009), although many other fault-related structures and geochemical signatures are currently being investigated as potential seismic indicators, including, but not restricted to, injections of granular material (Lin, 1996; Smith et al., 2008; Rowe et al., 2012), pulverized fault zone rocks (Brune, 2001; Dor et al., 2006; Rempe et al., 2013), mirror-like slip surfaces (Boneh et al., 2013; Chen et al., 2013; Fondriest et al., 2013; Siman-Tov et al., 2013), localized zones of recrystallization (Kim et al., 2010; Brantut et al., 2011; Bestmann et al., 2012; Smith et al., 2013), graphitization of carbonaceous materials (Oohashi et al., 2013; Kuo et al., 2014) and thermal maturation of organic molecules (Polissar et al., 2011; Rabinowitz et al., 2013; Savage et al., 2014).

In this contribution, we focus on the conditions that determine the formation of rounded clast-cortex aggregates (CCAs; an abbreviation also used for *clay*-clast aggregates, (Boutareaud et al., 2008)), a distinctive type of composite grain recognized in several different lithologies and geological settings (Table 1). CCAs have been found in the localized slipping zones of tectonic faults (e.g. Warr and Cox, 2001; Boullier et al., 2009; Smith et al., 2011) (Figure 1) and in the basal detachment zones of large landslides (e.g. Beutner and Craven, 1996; Beutner and Gerbi, 2005; Anders et al., 2010). The main characteristic of CCAs is a central clast enclosed by an outer cortex of fine-grained material that defines the composite rounded structure (Figure 1).

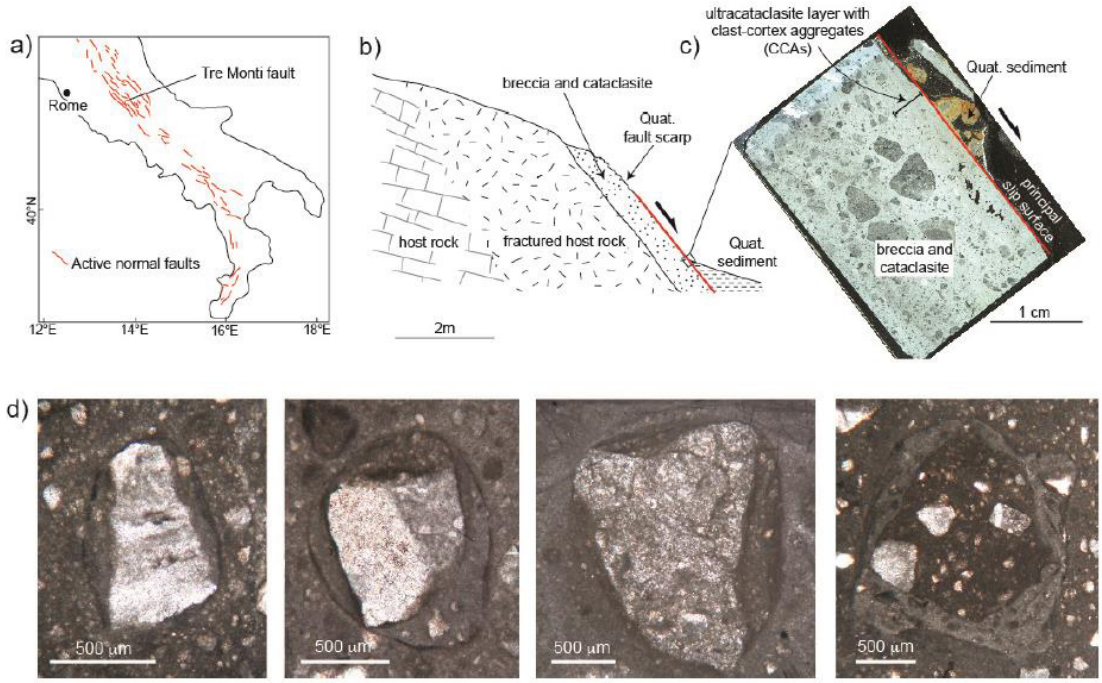

Figure 1. Summary of the occurrence of clast-cortex aggregates (CCAs) in the Tre Monti normal fault, central Italy, (a) Map of southern Italy with red lines showing the locations of the Tre Monti fault and other active normal faults that cut Holocene deposits (modified from Roberts and Michetti (2004), (b) Schematic cross-section through a segment of the Tre Monti fault showing the transition from intact host rock to breccias and cataclasites (modified from Smith et al. (2011)). The active Quaternary fault scarp, corresponding to the principal slip surface in this fault, is marked in red. The hanging wall at the surface is composed of well-cemented Quaternary sediments, (c) scanned thin section image showing the principal slip surface and cataclastic to ultracataclastic principal slipping zone. The ultracataclasite layer closest to the principal slip surface contains well-developed CCAs. (d) Optical photomicrographs in plane-polarized light showing examples of CCAs from the ultracataclastic slipping zone of the Tre Monti fault. From left to right the CCAs increase in size and complexity. The central clasts can be composed of limestone host rock fragments (first three images) or reworked cataclastic material from the slipping zone (fourth image). In some cases, the cortex contains multiple laminations (third and fourth images and other examples in Smith et al. (2011)).

Clast-cortex aggregates composed of calcite have been found in the principal slipping zone of the Tre Monti fault, an active normal fault hosted mainly in limestones in the Central Apennines of Italy (Figure 1a, b) (Smith et al., 2011). Geological constraints indicate that exposures of the principal slip zone of the Tre Monti fault were exhumed from depths of <2 km (Smith et al., 2011). The cataclastic principal slip zone (Figure 1c) consists almost entirely of calcite (from Energy Dispersive X-Ray Spectroscopy in the Scanning Electron microscope (SEM) and X-ray powder diffraction (XRD) measurements) and is up to several centimeters thick. The principal slip zone contains a texturally distinct ultracataclasite layer <10 mm thick containing CCAs between 50 μm – 3 mm diameter (Figures 1c, d). The central clasts are composed of either host-rock (fossiliferous and micritic limestone) fragments or reworked cataclasitic material (Figure 1d). The outer cortexes are up to 1 mm thick and composed of calcite with a grain size (<5 – 20 μm) similar to the surrounding matrix. The cortexes are distinguished in the petrographic microscope by a dark brown rim visible in plane-polarized light. The cortexes also contain internal color variations that often define roughly concentric laminations (Figure 1d).

Laboratory experiments can contribute to our understanding of the deformation processes resulting in the formation of CCAs. In high-velocity rotary-shear experiments on clay-bearing gouges, Boutareaud et al. (2008) and (2010) produced rounded “clay-clast aggregates” similar to those found in the most-recently active slipping zone of the Chelengpu thrust fault (1999 Mw 7.6 Chi-Chi earthquake; Boullier et al. (2009)). In the experiments of Boutareaud et al. (2008) and (2010), clay-clast aggregates were formed in both dry and water-dampened conditions, at high slip velocities (≥0.09 m/s), low normal stresses (≤1.2 MPa) and up to several tens of meters displacement. Boutareaud et al. (2008); (2010) proposed that the clay-clast aggregates were formed by dehydration of clays and subsequent thermal pressurization of pore fluids due to frictional heating, causing rotation of clasts in a liquid water/vapor medium. It was proposed that finer-grained clay materials accreted to the clasts due to electrostatic and capillary forces.

Since the initial findings of Boutareaud et al. (2008), rounded aggregates have been produced in several experimental studies (Table 1 in Han and Hirose (2012)) using clay-bearing gouges. In particular, Han and Hirose (2012) performed an experimental study on quartz and quartz-bentonite gouges. By conducting low- to high-velocity rotary-shear experiments, Han and Hirose (2012) found that clay-clast aggregates developed in their experiments at both sub-seismic and seismic sliding velocities (500 μm/s – 1.3 m/s) and only under room-dry conditions. The results of Han and Hirose (2012) suggest that rounded aggregate grains may not be a reliable indicator of fast slip in clay-bearing gouges, and that the mechanisms leading to the formation of aggregate grains warrant further study.

In this study, rotary-shear experiments were conducted on layers of synthetic calcite gouge to investigate the processes contributing to the formation of natural and experimental CCAs in calcite-bearing slip zones like the Tre Monti normal fault (Smith et al., 2011). We systematically studied not only the dependence on slip velocity, on which Boutareaud et al. (2008) and Han and Hirose (2012) concentrated, but also the effect of total displacement, normal stress, and ambient humidity (i.e. room-dry, water-dampened and vacuum). Our results contribute to a better understanding of the significance of CCAs in tectonic fault zones, and provide constraints on the deformation processes active within shallow, granular slipping zones in carbonates.

2. Methods

2.1. *Experimental Set-Up*

A total of thirty-six rotary-shear experiments were conducted using two rotary-shear apparatus at normal stresses ranging from 1 to 17 MPa, slip rates over four orders of magnitude (0.0001 to 1 m/s) and total displacements from 0.27 to 5.58 m under both room-dry and water-dampened conditions (Table 2). Twenty-two experiments were performed at low normal stresses (1 to 3 MPa) with ROSA (**Ro**tary-**S**hear **A**pparatus) installed at the

Department of Geosciences of Padua University (Padua, Italy). Fourteen experiments were performed at higher normal stresses (2.8 – 17.3 MPa) with SHIVA (**S**low- to **HI**gh-**V**elocity **A**pparatus) installed at the Istituto Nazionale di Geofisica e Vulcanologia (INGV) in Rome, Italy. SHIVA was also used to perform three additional experiments under vacuum (10^{-4} mbar) conditions.

Due to the circular sample geometry used in the rotary-shear configuration, slip velocity and total displacement depend on the position along the radius of the sample. Thus, we follow Hirose and Shimamoto (2005) and calculate an "equivalent velocity" $v_e = \frac{4\pi R(r_i^2+r_i r_o+r_o^2)}{3(r_i+r_o)}$, with r_i and r_o being the inner and outer radius of the sample, respectively, and R the number of revolutions per minute. The total displacement consequently corresponds to the equivalent displacement $d_e = v_e t$.

2.1.1. Experiments with ROSA

The basic set-up of ROSA, built by MARUI & CO., LTD (model MIS-233-1-77) as designed by T. Shimamoto, is illustrated in Figure 2a. It has a 11 kW servomotor with revolving speeds from 1.5 rpm to 1500 rpm, which can be reduced by a factor of up to 10^{-6} by a gear system. The revolution speed is measured via a rotary encoder (Figure 2a, R1; 3600 pulses/revolution). The torque is measured by averaging the output from two compression load cells (Figure 2a, T1 and T2) with a resolution of 0.5 N. To obtain information about shortening and dilation of the samples, the axial displacement is measured with a high-sensitivity displacement gauge (Figure 2a, D) with a resolution of 1 µm. A normal load of up to 10 kN can be applied on the stationary column via a pneumatic system; for higher normal stresses of up to 50 kN a hydraulic cylinder can be installed. The applied load is monitored by a compression load cell (Figure 2a, L) with a resolution of 5 or 25 N for the pneumatic and hydraulic cylinders, respectively. Mechanical data are collected at a rate of up to 1 kHz.

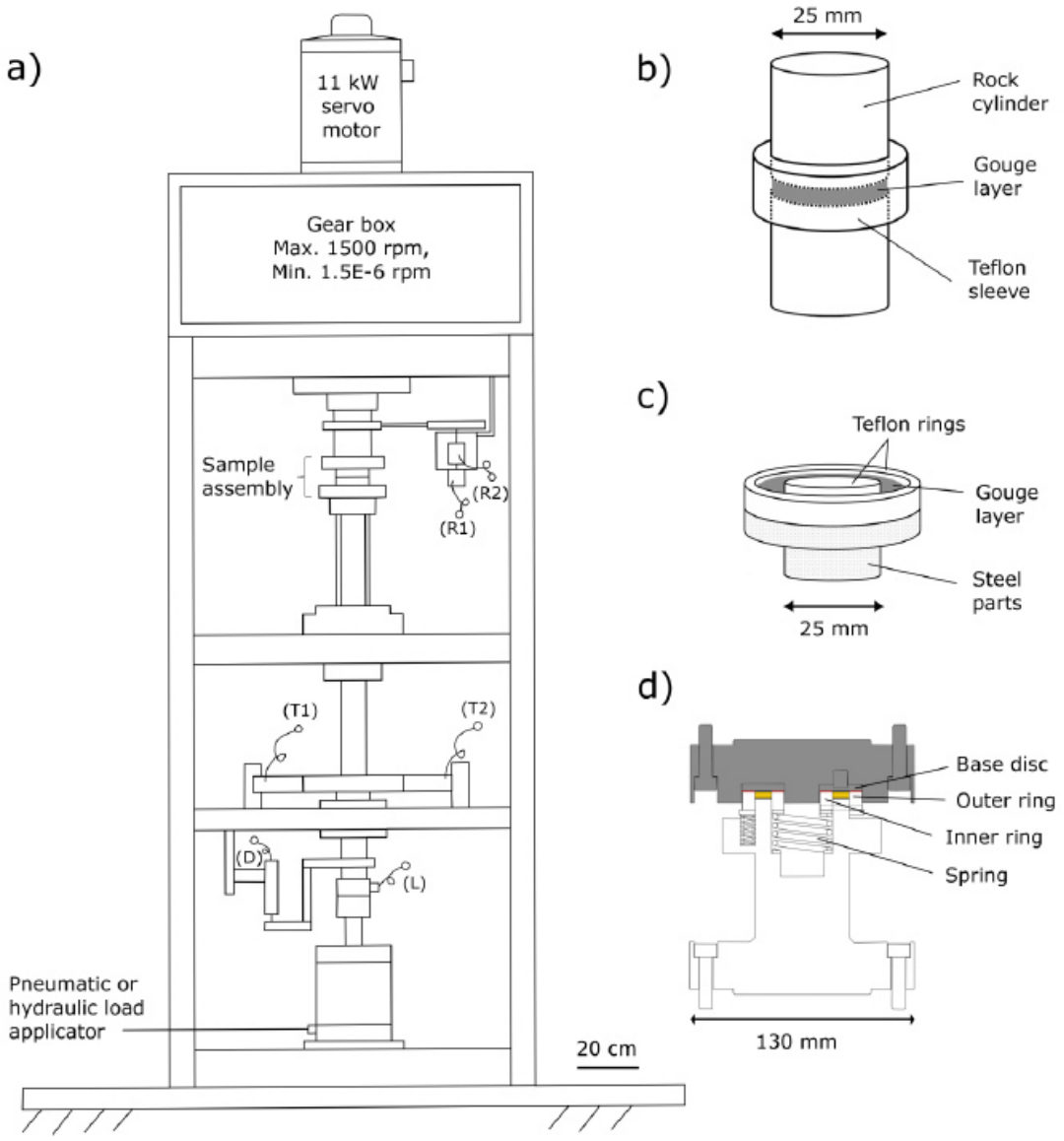

Figure 2. Experimental set-up and gouge sample holders, (a) Schematic of the ROSA rotary-shear apparatus at Padua University. (R1) and (R2): rotary encoder and potentiometer measuring revolution speed (rpm) and rotation angle, respectively. (T1) and (T2): Two compression load cells measuring the torque; output values are averaged. (D): Strain-gauge type displacement gauge measuring vertical displacement of the axial column and the experimental sample. (L): Compression load cell measuring the axial load applied to the sample via the pneumatic or hydraulic cylinders. (b) Gouge sample assembly using two solid rock cylinders and an outer Teflon ring to contain the gouge layer. The jubilee clip fastened around the Teflon sleeve is not shown in this figure. (c) Annular steel sample holder with inner and outer Teflon rings. (d) Metal sample holder used with SHIVA (modified from Smith et al., 2013). White regions: stationary parts, grey regions: rotary parts. Yellow areas show position of gouge layer contained by inner and outer metal sliding rings. Red lines demonstrate where metal parts are in sliding contact during the experiments.

120 Of the twenty-two gouge experiments conducted with ROSA (Table 2), fourteen were
121 performed by sandwiching a layer of gouge up to a few millimeters thick between two solid
122 rock cylinders 25 mm in diameter (typically tonalite or gabbro). The surfaces of the solid rock
123 cylinders were roughened with 150 grit to promote deformation within the gouge layer. The
124 gouges were contained along the outside by a Teflon sleeve fastened with a jubilee clip (Figure
125 2b). Several tests run to measure the friction of the Teflon sleeve showed that it contributes
126 approximately 10-15% (corresponding to $0.05<\mu<0.1$) to the measured friction values (where
127 the friction coefficient, μ, is calculated as shear stress/normal stress). This is consistent with
128 the findings of Sawai et al. (2012) who reviewed the influence of Teflon friction in ten high-
129 velocity experimental studies that employed a similar sample geometry. We have chosen not
130 to correct the mechanical data for the effects of Teflon friction. The sample assembly is fixed in
131 the apparatus with hydraulic-mechanical locks. Rotation of the upper column shears the gouge
132 layer. After the experiment, the entire sample assembly (solid rock cylinders + gouge layer +
133 Teflon ring + jubilee clip) can be impregnated with epoxy resin thus minimizing gouge loss and
134 potential disruption of microstructures. Eight experiments were conducted using an annular
135 steel sample holder (Figure 2c). In this setup, the ring-shaped gouge layer (with int./ext.
136 diameters of 25/40 mm) is contained by inner and outer Teflon rings.

137 ### 2.1.2. Experiments with SHIVA

138 A detailed report of the design and capabilities of SHIVA is provided in Di Toro et al.
139 (2010). With SHIVA, an annular steel gouge sample holder was used (description and
140 calibration tests in Smith et al. (2013)). Inner and outer rings contain the gouge layer (int./ext.
141 diameters of 35 and 55 mm) and slide over a base disc (Figure 2d). Using an all-steel gouge
142 holder prevents contamination of the gouge sample by decomposition of Teflon. Mechanical
143 data are collected at a rate of up to 25 kHz. SHIVA is equipped with a Pfeiffer Hi cube vacuum
144 pump that is able to create a minimum pressure of 10^{-4} mbar in a chamber surrounding the
145 samples (described in Violay et al. (2013)). During an experiment in near-vacuum conditions,

this pre-imposed pressure might increase due to the release of volatiles from the gouge sample, in our case due to thermal decomposition of calcite.

2.2. Sample Preparation and Analysis Techniques

The gouge experiments were conducted on powder derived from Carrara marble (Figure 3a). The marble was first ground to a powder in a pestle and mortar for several minutes and then sieved to different particle size fractions. For the starting materials, the fractions <150 µm and <180 µm were used in, respectively, Padua and Rome. The single fractions were weighted to obtain the particle-size distribution of the starting material (Figure 3b). Three batches of starting material (CMG1, 2 and 3) were prepared consecutively, two of which were analyzed using semi-quantitative X-ray powder diffraction at the Geoscience Department, University of Padua (Figure 3c). The software package High Score Plus (PANalytical) was used for phase identification and quantitative phase analysis by the Rietveld method (Rietveld, 1967). Batch CMG2 is composed of c. 72.3% magnesium calcite, 21.7% dolomite, and 6% white mica (muscovite/illite). Batch CMG3 is composed of >98% calcite and <2% white mica. SEM analysis indicates that the composition of CGM1 is similar to that of CMG3, containing only minor amounts (<2%) of dolomite and white mica.

For experiments with ROSA, 1.5 g of starting material was used to produce a pre-experiment gouge layer thickness of c. 1.5 mm. For SHIVA, 5 g of starting material were used to produce a gouge layer thickness of c. 3 mm. When water-dampened gouge was used, 20 wt% deionized H_2O was evenly added to the gouge layer using a syringe.

After each experiment the deformed gouge sample was saved in epoxy, and polished petrographic sections were prepared for microstructural analysis. The sections were cut approximately parallel to the slip direction and perpendicular to gouge layer boundaries. Samples were analyzed using a JEOL JSM-6500F Field-Emission Scanning Electron Microscope (SEM) in backscattered mode (acceleration voltage 20 kV; working distance 8 - 20 mm) at the Istituto Nazionale di Geofisica e Vulcanologia (INGV) in Rome. SEM images of selected samples

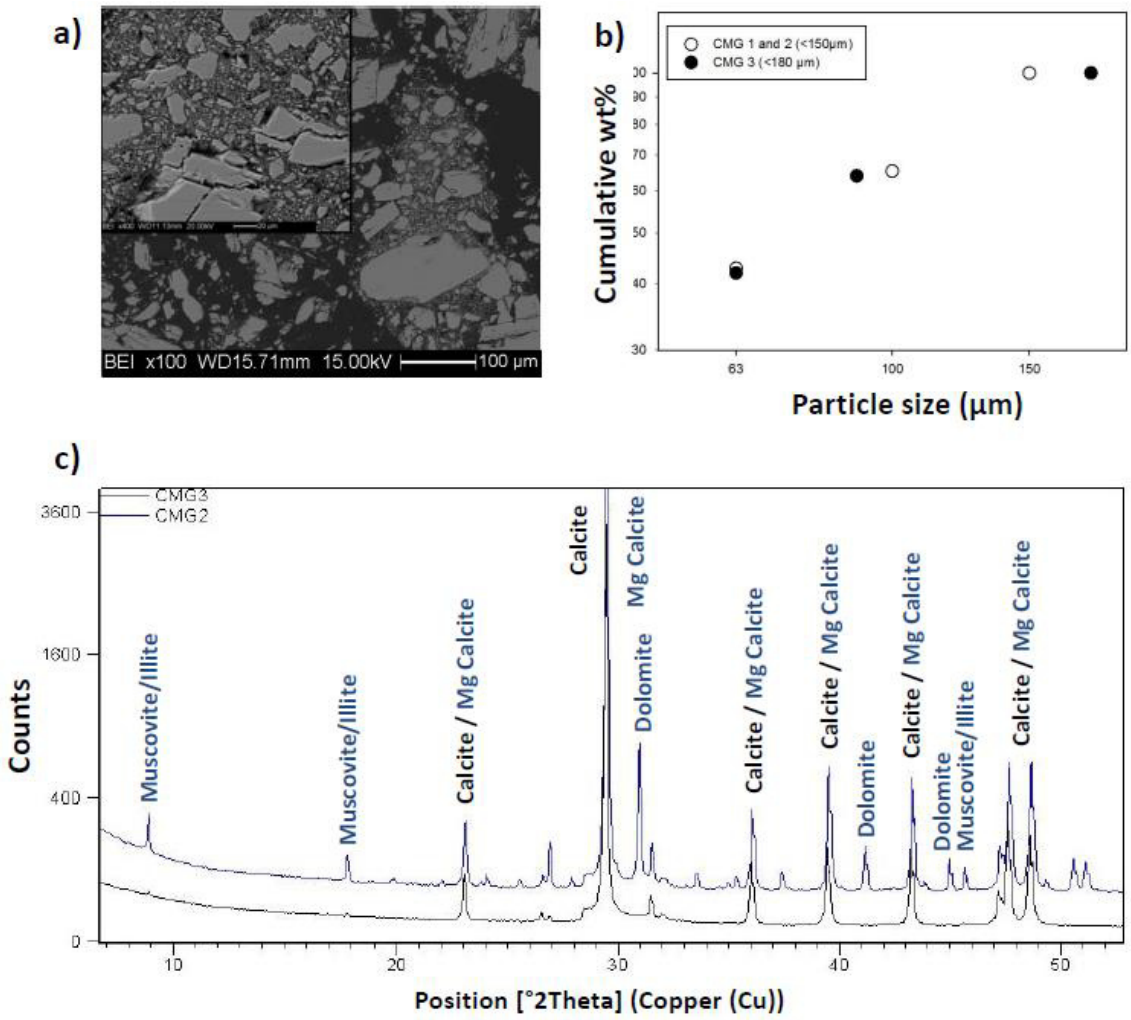

Figure 3. Characterization of starting materials used in gouge experiments**,** (a) SEM images of the starting gouge material derived by crushing Carrara Marble (batch CMG 1, scale bar in inlet is 20 µm), (b) Particle size distribution of starting material derived from sieving and weighting, (c) X-ray powder diffraction spectrum for batches CMG2 (blue curve and labels) and CMG3 (black curve and labels).

172

were used to investigate grain size and shape characteristics using the image analysis software Fiji (Schindelin et al., 2012).

3. Results

3.1. Mechanical Behavior of Calcite Gouges

The friction coefficient (μ; shear stress/normal stress) in both room-dry (Figure 4a) and water-dampened (Figure 4b) experiments ranges from 0.5 to 0.8. In experiments at high-velocity (>1 m/s) and high normal stress (>10 MPa), initial peak friction of c. 0.8 was observed after 0.1-0.2 m of slip (e.g. s272 in Figure 4a). In such cases, peak friction was followed by dynamic weakening that reduced the friction coefficient to a "steady-state" value between 0.3-0.6.

All experiments conducted with room-dry and water-dampened gouges showed initial gouge compaction of 100 – 300 μm (Figures 4a, b). In some room-dry experiments, a transient phase of dilation occurred following initial compaction (e.g. s272, Figure 4a). When observed, this transient dilation was between 10 – 30 μm and was followed by renewed compaction (e.g. 272, Figure 4a). In some experiments, a second phase of dilation was recorded after displacements >0.5 m (e.g. s776 in Figure 4a). In those cases, secondary dilation was between 5 – 180 μm, but may include a component that reflects minor gouge loss (in the experiments performed with ROSA). Figure 5 summarizes measurements of transient dilation and total dilation (i.e. transient + secondary dilation). In room-dry experiments, the amount of secondary dilation tends to increase with displacement. No significant amount of gouge layer dilation was recorded at any stage during experiments with water-dampened gouges (Figure 5).

3.2. Strain localization and textural zones in room-dry experiments

Up to three distinct microstructural zones are present within the deformed room-dry samples (Figure 6a):

1. Zone I consists of relatively coarse-grained gouge similar to the starting material. In zone I, grains are angular to sub-angular and up to c. 150 µm in size.
2. Zone II is up to 800 µm thick and has a compacted and highly comminuted matrix with grain sizes on the order of a few microns (Figures 6a, b). The matrix contains larger grains up to 100 µm in size composed of a central clast surrounded by a fine-grained outer cortex defining an overall rounded shape, i.e. calcite CCAs (Figure 6b-d). In all of the experimental samples that were analyzed with the SEM, Zone II is the only zone in which CCAs were developed. The central clasts often contain angular embayments along their outer margins that are in-filled by finer cortex material (Figure 6c). Calcite grains comprising the cortex are <1 µm in size and appear to be loosely aggregated (Figure 6d). Individual rounded grains on the order of 100 nm in size are recognizable.
3. Zone III is up to 300 µm thick and comprises highly comminuted and banded gouge material (Figures 6a, e). The banding is wavy and defined by variations in grain size and porosity (Figure 6e). Internally, single bands up to 100 µm wide contain grain size grading, with finer-grained material towards the stationary side. The stationary side of each band is typically marked by a discrete fracture surface that may have originated as a shear surface in the experiments.

The distribution of the three zones depends on experimental conditions, and not all three zones are always present. In experiments with relatively high displacements or high slip velocities (e.g. r88 in Figure 6a), zones II and III are well developed at the expense of zone I. Zones II and III are typically best developed at a distance of a few millimeters from the outer edge of the cylindrical samples (Figure 6a), before they thin again towards the outer edge where slip velocity and total displacement were highest (Figure 6a). Within zone II, CCAs

formed preferentially in areas with relatively high porosity (e.g. Figure 6b). In some samples, a thin sliver (<100 μm) of comminuted material belonging to zone II is variably developed adjacent to the stationary side of the gouge holder (Figure 6a), although this sliver does not contain CCAs.

3.3. Strain distribution in room-dry experiments

Figure 7 shows the microstructure of an experiment (s886) containing a c. 2 mm-wide strain marker made from dolomite gouge (particle size <250 μm). The vertical marker was constructed perpendicular to gouge layer boundaries and the imposed shear direction, allowing the angular strain (γ) within the deformed gouge layer to be calculated as $\gamma = \tan\phi$, where ϕ is the angle between the original and deformed marker (Figure 7a). In this experiment, the margins of the marker were not sheared to the same degree (Figure 7b), which may be due to the thickness of the marker and the annular geometry of the sample. For the evaluation of shear strain an average of the angles as shown in Figure 7b was taken. Towards the rotary side of the gouge layer, the marker is only slightly distorted, defining a zone of low strain (mean $\gamma \leq 1.6$). Further towards the stationary side of the gouge layer, the marker is sheared progressively towards parallelism with the gouge layer boundaries, defining an intermediate-strain domain (mean $\gamma \geq 3.1$). In a layer c. 220 μm thick adjacent to the stationary-side, the marker is heavily disrupted, but some individual dolomite grains are dispersed throughout this layer. Assuming that almost all of the total displacement was accommodated in this layer (only a negligible amount of displacement is accommodated in the low- and intermediate-strain domains where the dolomite marker remains intact), the bulk strain can be approximated by dividing its thickness (220 μm) by the total experimental displacement of 2.5 m, resulting in a finite shear strain of c. 1850.

Several R1-Riedel shears (terminology after e.g. Logan et al., 1979), defined by bands of grain-size reduction and fractures (the latter assumed to have formed by normal stress unloading), cut through the low- and intermediate-strain domains at angles of c. 15-20° to the

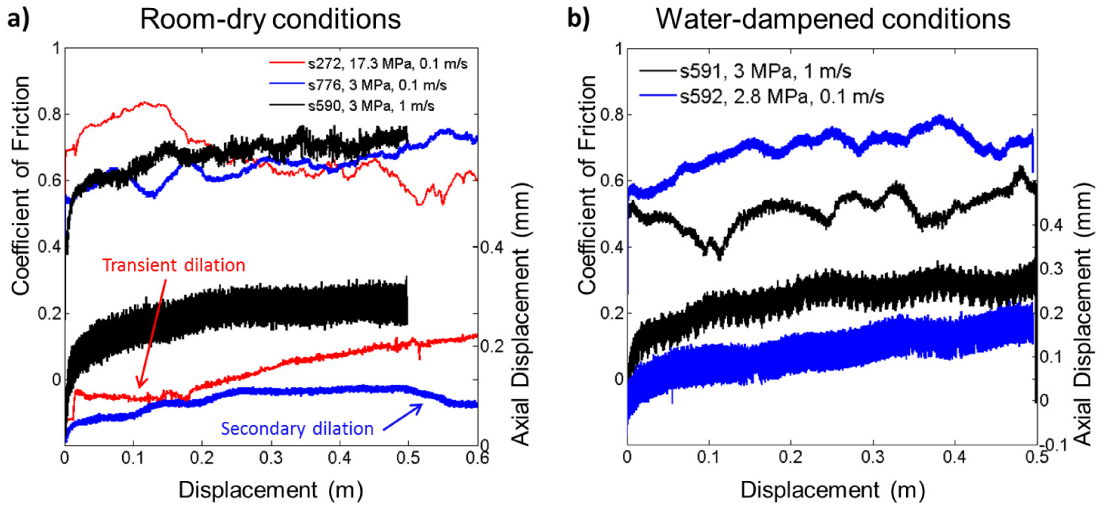

Figure 4. Mechanical data from calcite gouge experiments, (a) Friction coefficient (upper three data curves) and axial displacement (lower three curves) for experiments conducted with room-dry calcite gouge. Positive changes in axial displacement indicate shortening, negative changes indicate dilation. Experiments s590 (black lines) and s776 (blue lines) performed at a normal stress of 3 MPa and slip rates of 1 and 0.1 m/s, respectively, show no weakening or transient dilation. Experiment s272 (red lines) performed at higher normal stress (17.3 MPa) at a slip rate of 0.1 m/s exhibits some weakening following peak stress after approximately 0.15 m displacement. In s272, initial gouge layer compaction is followed by transient dilation of c. 20 µm, and then renewed compaction. (b) Coefficient of friction (upper two data curves) and axial displacement (lower two data curves) for water-dampened experiments s591 (black lines; 3 MPa, 1 m/s) and s592 (blue lines; 2.8 MPa, 0.1 m/s). Neither of these experiments exhibits transient dilation or weakening.

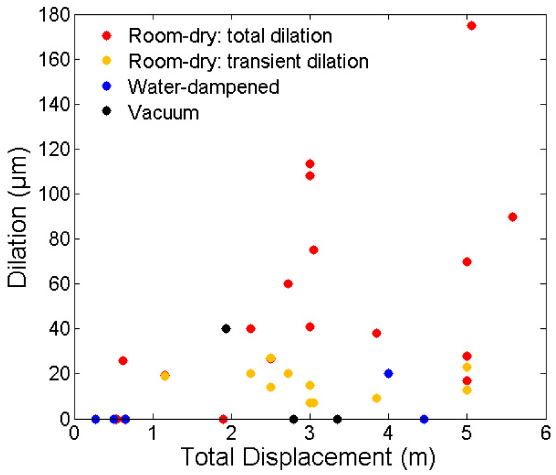

Figure 5. Dilation vs. total displacement for experiments conducted under room-dry, wet and vacuum conditions. Transient and total (i.e. transient + secondary) dilation are plotted separately for the room-dry experiments.

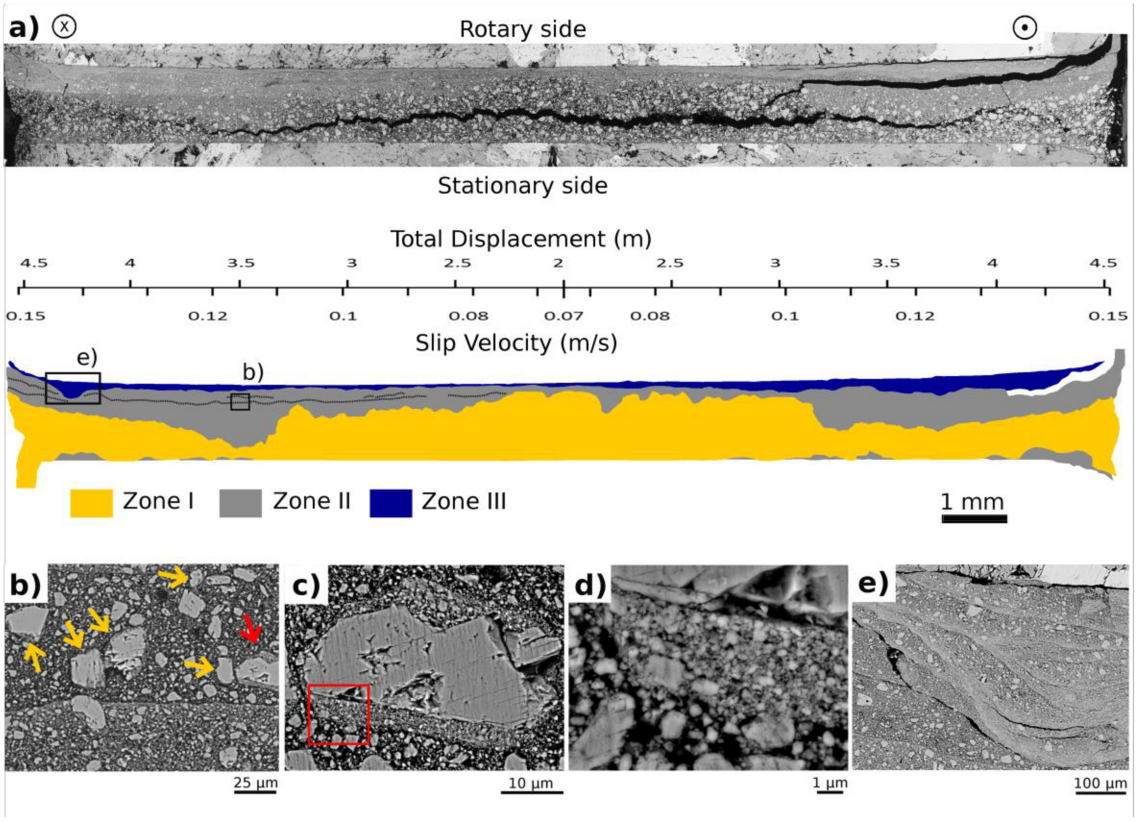

Figure 6. Microstructural zones in sheared calcite gouges, (a) SEM mosaic and line drawing of room-dry experiment r88 (equivalent velocity 0.1 m/s; 1 MPa normal stress; 3 m displacement). Thin section was cut approximately halfway between edge and center of the cylindrical sample to analyze the distribution of microstructural zones at different radial positions in the sample. Three distinct microstructural zones (Zones I-III) are recognized on the basis of grain size variations and the presence of CCAs and banding. Black boxes show the positions of b) and e). (b-e) SEM images of microstructural zones, (b) CCAs (yellow arrows) developed in Zone II. Note that the CCAs developed in a layer with relatively high porosity, (c) Close-up of CCA marked by red arrow in part b). In this example, the outer cortex is up to 10 µm wide and fine-grained materials in the cortex in-fill embayments in the central clast. Red box denotes location of d). (d) Zoom of fine-grained cortex material <1 um in size. The cortex material appears loosely aggregated, individual rounded grains down to c. 100 nm in size are recognized. (e) Anastomosing shear bands and extensive grain comminution within Zone III.

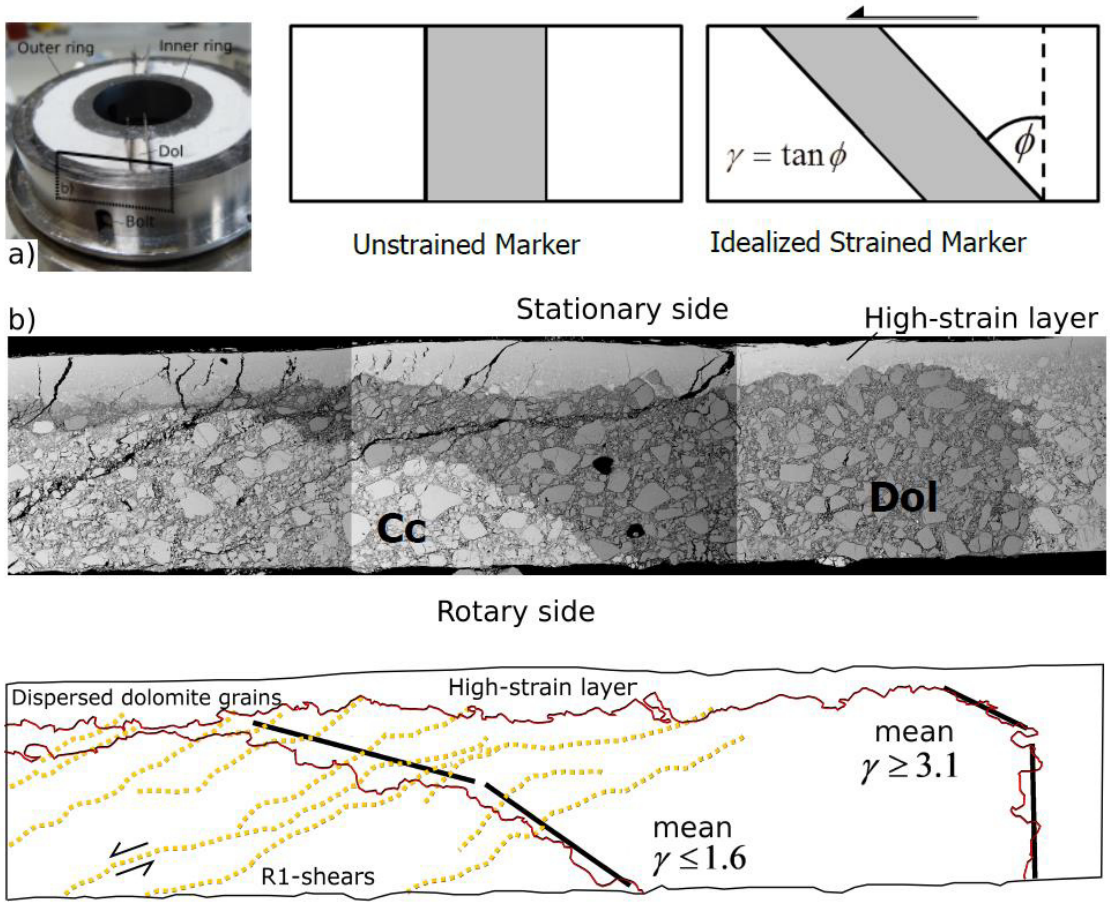

Figure 7. Strain distribution in sheared calcite gouge layers. (a) Rotary side of the steel sample holder used with SHIVA, filled with calcite gouge and prepared with two thin vertical markers of dolomite with the aid of razor blades. The starting particle size of both the calcite and the dolomite gouges in this experiment was <250 µm. Black box illustrates how post-experiment sample was cut. Sketches (modified after Scruggs and Tullis, 1998) show section though sample with unstrained and idealized strained marker assuming homogeneous strain distribution. (b) SEM mosaic and interpreted line drawing of sample s886 (3 MPa normal stress, equivalent slip velocity of 1 m/s, 2.5 m of total displacement, room-dry). The dolomite marker is distinguished by its darker grey color. The geometry of the dolomite marker broadly defines low-, intermediate- and high-strain domains. The left margin of the dolomite marker is cut by a series of R1-Riedel shears with offsets between c. 10–180 µm.

gouge layer boundaries (yellow dashed lines in Figure 7b). Where the R1-shears cut the dolomite marker, discrete offsets of c. 10-180 μm are observed along the margins of the marker, with the sense of offset systematically the same as the bulk shear sense (i.e. synthetic R1-shears). The fine-grained high-strain layer is also cut by fractures that link downwards into the R1-shears. These fractures are characteristically observed in the highest-strain layers at the end of experiments and are thought to have formed by normal stress unloading at the end of the experiments.

3.4. Formation Conditions of Experimental Clast-Cortex Aggregates

As noted above, CCAs formed exclusively within Zone II in the deformed gouges. In addition, they were formed only under certain experimental conditions. In Figure 8, experiments performed over a wide range of normal stresses, slip velocities and displacements are classified as having mainly well-developed (W), poorly-developed (P) or no (N) CCAs. Red letters indicate room-dry experiments and blue letters indicate water-dampened experiments. Well-developed CCAs are those with a cortex that completely surrounds the central clast, defining an overall rounded structure (e.g. Figure 8d). Poorly-developed CCAs are those where the cortex does not completely surround the central clast (e.g. Figure 8e).

3.4.1. Room-dry Conditions

Figure 8a shows the dependence of CCA formation on slip velocity and displacement at 1 and 3 MPa normal stress under room-dry conditions (red letters). At 1 MPa normal stress CCAs are generally well developed (e.g. example in Figure 8d), except in experiments that have low velocity (<0.1 m/s) combined with low total displacement (0.5 m). At higher displacements (>3 m), aggregates form at all investigated slip velocities. At a higher normal stress of 3 MPa, longer displacements are needed to form aggregates: At 3 MPa, no CCAs developed in experiments with 0.5 m displacement and well-developed CCAs only formed in experiments with displacements of more than c. 4 m.

a)

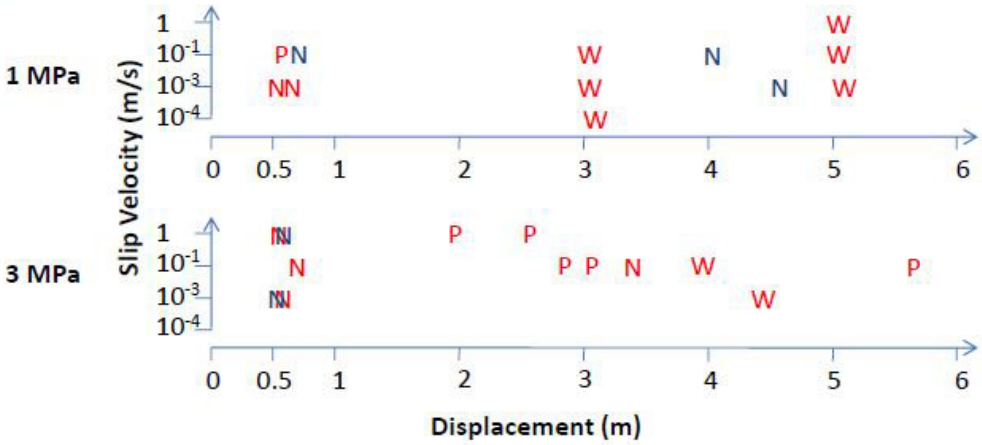

b)

σ_n (MPa)	Gouge layer (mm)	Aggregates
1	1.5	W
3	1.5	P
5	3	W
10	3	P
17	3	N

c)

σ_n (MPa)	Gouge layer (mm)	Aggregates
3	3	N
5	3	P
10	3	N

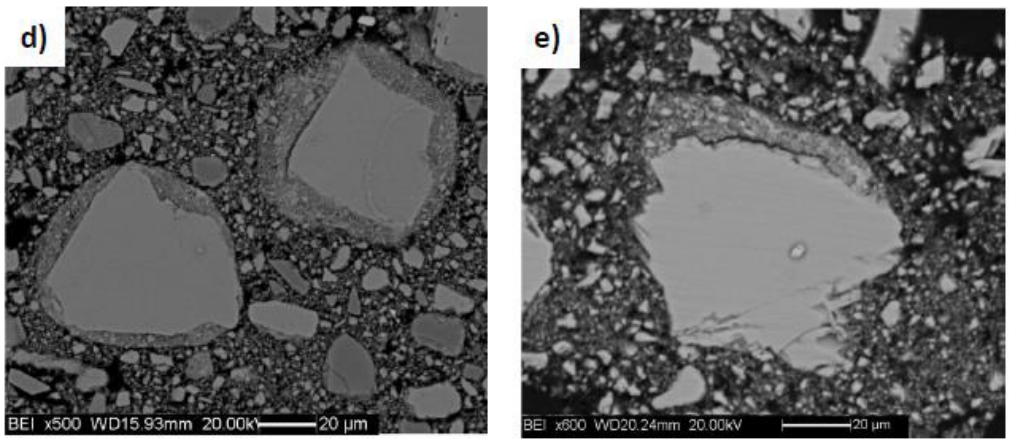

Figure 8. Summary of experiments performed under different conditions of slip velocity, normal stress, and ambient humidity. In the tables, **N** denotes no CCAs, **P**: poorly-developed CCAs, **W**: well-developed CCAs (see text for definitions). Red letters denote experiments in room-dry conditions, blue letters denote water-dampened experiments. (a) Results for experiments conducted at normal stresses of 1 MPa (upper graph) and 3 MPa (lower graph), for velocities ranging from 10^{-4} - 1 m/s (log scale) and displacements ranging from 0.35 to 5.58 m. (b) Results for experiments conducted with varying normal stress and gouge layer thickness but the same target slip rate (0.1 m/s) and total displacement (3.0 m), all in room-dry conditions. (c) Results for experiments conducted in vacuum conditions with slip rates of 0.1 m/s, 3 m displacement, and variable normal stress. (d) SEM image of experimental CCAs with well-developed cortexes (experiment r89). Aggregates are abundant in this sample; most clasts with a diameter >10 µm are fully surrounded by cortexes. (e) SEM image of poorly-developed CCAs in experiment r68. In this experiment, only a few aggregates with rudimentary cortexes formed.

272 The effect of normal stress on the formation of CCAs was further tested by carrying out
273 a separate series of five experiments over a wider range of normal stresses than shown in
274 Figure 8a, at a constant slip velocity of 0.1 m/s and a total displacement of 3 m (Figure 8b).
275 These experiments show that for a given layer thickness, CCAs are better developed at lower
276 normal stresses. With a 3 mm thick starting gouge layer, CCAs were not developed at a normal
277 stress of 17 MPa, poorly developed at 10 MPa, and well developed at 5 MPa. With a 1.5 mm
278 thick gouge layer, CCAs were

279 poorly developed at 3 MPa and well developed at 1 MPa. These data indicate that in room-dry
280 calcite gouges CCAs are preferentially formed at relatively low normal stress.

281 #### 3.4.2. Wet Conditions

282 No CCAs developed under wet conditions (Figure 8a, blue letters), regardless of the slip
283 velocity or total displacement. The microstructure of the wet samples (Figure 9) is
284 characterized by a relatively thick zone adjacent to the rotary side which contains large
285 rounded to sub-rounded grains embedded in a uniformly fine-grained matrix (grain size <20
286 μm).

287 #### 3.4.3. Vacuum Conditions

288 Three experiments with SHIVA were conducted under vacuum conditions (i.e., at 10^{-4}
289 mbar) at 0.1 m/s, 3 m total displacement and normal stresses of 3, 5 and 10 MPa (Figure 8c). In
290 the samples from the 3 and 10 MPa experiments the three characteristic microstructural zones
291 were not observed and no CCAs were found, but this may be due to poor sample preservation.
292 Poorly-developed CCAs formed at 5 MPa normal stress.

293 ### *3.5. Size and Shape Analysis of Clast-Cortex Aggregates*

294 Two-dimensional image analysis (Fiji software, Schindelin et al., 2012) was used to
295 calculate two shape factors for the central clasts and outer cortexes of the CCAs; the circularity
296 and the solidity (Heilbronner and Barrett, 2013). The circularity is defined as $C = 4\pi \frac{A}{P^2}$ where

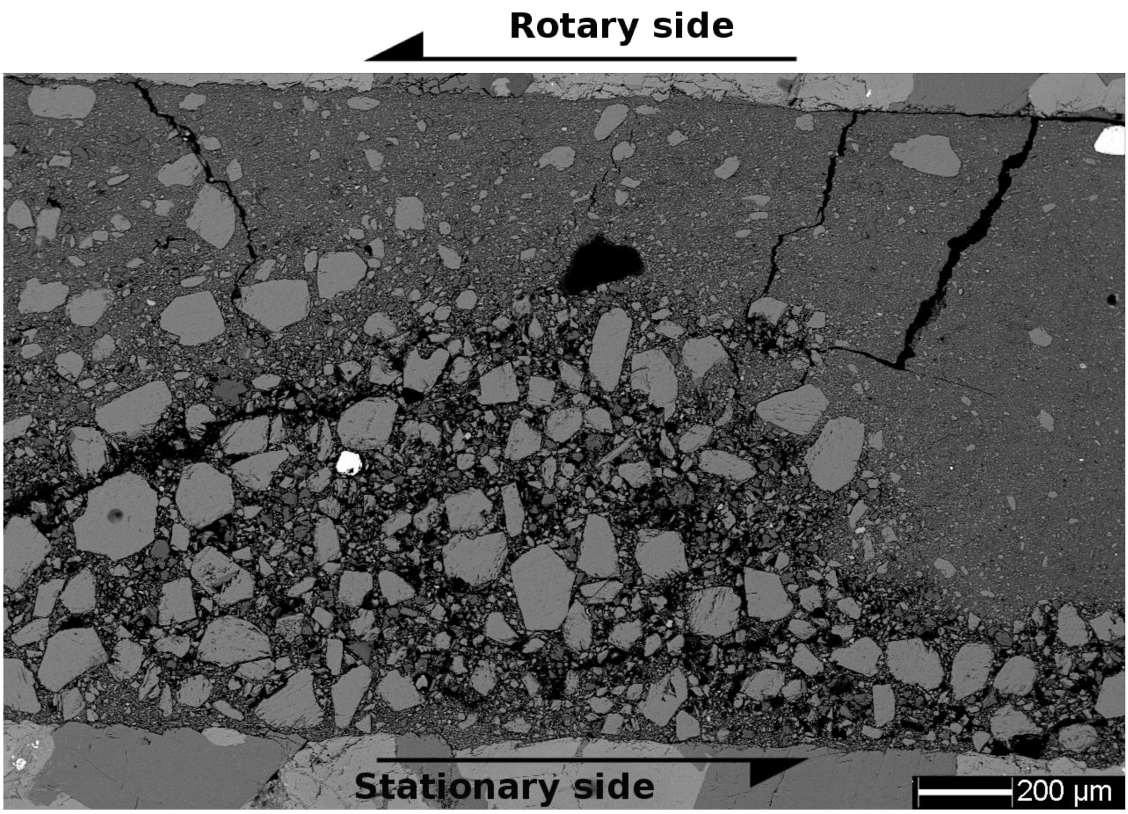

Figure 9. Gouge layer (experiment r91) deformed in water-saturated conditions. The microstructure of water-dampened layers is characterized by a relatively thick zone adjacent to the rotary side in which rounded to sub-rounded clasts are surrounded by a homogenously fine-grained matrix. CCAs were not identified in water-dampened experiments.

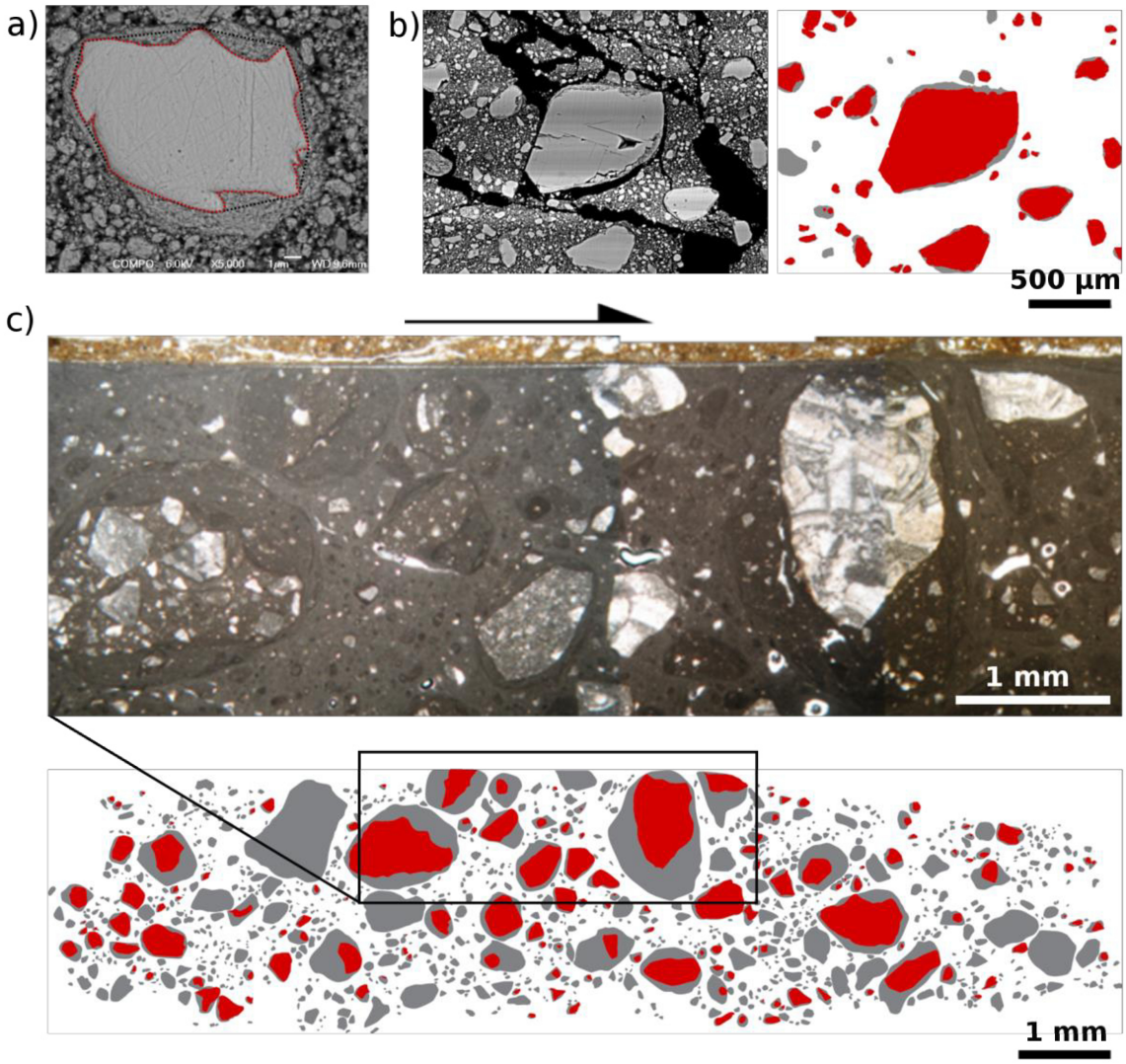

Figure 10. Grain size and shape analysis of natural and experimental CCAs, (a) The circularity of an object, in this case the central clast of a CCA, is calculated from its area and its perimeter (red dotted line) as described in the text. Solidity is calculated by dividing the area of the object (red dotted line) by the convex area having no embayments (black dotted line). (b) SEM image (left) and corresponding tracing (right) of experimental sample r80 containing well-developed CCAs (n = 45). In the tracing, red grains are central clasts, grey areas are outer cortexes. (c) Optical photomicrograph mosaic (upper image) and corresponding tracing (lower image) of natural CCAs (n = 137) from the principal slip zone of the Tre Monti fault. The box shows the area of the photomicrograph mosaic. In the tracing, red grains are central clasts, grey areas are outer cortexes.

297 *A* is the area and *p* the perimeter of the central clast or outer cortex (Figure 10a). A circularity
298 of $C = 1$ describes a perfect circle. The solidity is the ratio between the area of the object and
299 the convex area $S = \frac{A}{A_{convex}}$ (Figure 10a), so that a structure with no embayments yields $S = 1$.

300 SEM backscatter images (for the experimental samples; Figure 10b) or optical
301 photomicrographs (for the natural samples; Figure 10c) were used to trace the outlines of
302 central clasts and outer cortexes. For the experimental example, a representative SEM image
303 from sample r80 was evaluated (Figure 10b). The area covered by the image was 190 µm x 240
304 µm and contained 45 CCAs (Figure 10b). For the natural example, the optical
305 photomicrographs used to trace the CCAs covered an area
306 of approximately 24 mm x 5.4 mm and contained 137 CCAs (Figure 10c). Circularity and solidity
307 were calculated separately for 1) experimental central clasts, 2) experimental cortexes (i.e. the
308 outer margins of the CCAs), 3) natural central clasts, and 4) natural cortexes. The frequency of
309 a certain circularity or solidity value was then plotted using bin sizes of 0.1 and 0.025,
310 respectively (Figure 11).

311 The results in Figure 11a show that the cortexes are more circular than the central clasts in
312 both natural and experimental cases. The experimental cortexes have a notably higher mean
313 circularity ($C_{mean} = 0.761$) than the experimental central clasts ($C_{mean} = 0.696$). The natural
314 cortexes have a mean circularity of 0.81 whereas the natural central clasts have a mean
315 circularity of 0.764. Additionally, the data indicate that natural cortexes and central clasts are
316 more rounded on average than their experimental counterparts.

317 The solidity values (Figure 11b) show the same overall results. In both natural and
318 experimental samples, the cortexes have a higher mean solidity than the central clasts,
319 suggesting that the fine-grained material comprising the cortexes fills embayments within the
320 central clasts, consistent with microstructural observations. This effect is most pronounced in
321 the experimental samples, where the solidity values for the outer cortexes are notably higher
322 (S_{mean} = 0.943) than for the central clasts (S_{mean} = 0.905).

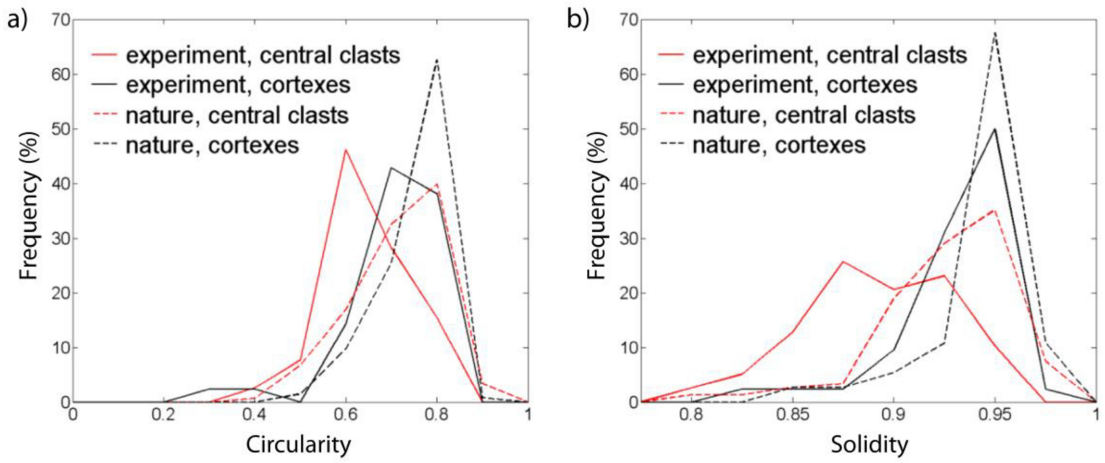

Figure 11. Results of quantitative analysis of circularity (a) and solidity (b) of samples shown in Figure 10. Bin sizes were chosen to reveal differences in the data and are 0.1 for circularity and 0.025 for solidity.

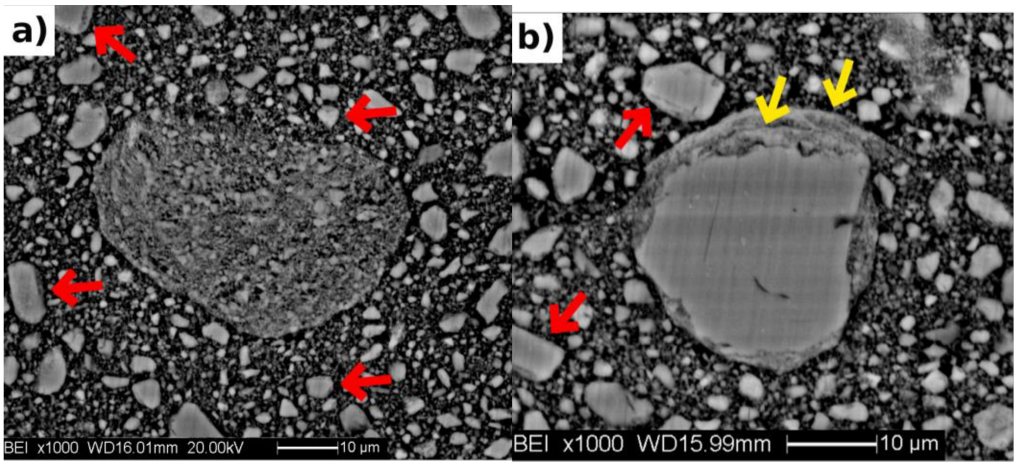

Figure 12. Examples of experimental CCAs from sample r80, (a) Rounded grain composed of reworked matrix material and lacking a central clast, (b) CCA consisting of two laminations (yellow arrows) surrounding a central clast. Note that in both of the images some of the smaller grains are also CCAs (red arrows).

4. Discussion

4.1. Development of the textural zones

The development of distinct textural zones is a common feature in rotary-shear gouge experiments (e.g. Beeler et al., 1996; Kitajima et al., 2010). In this study, the distribution of textural zones I, II and III depends both on experimental conditions and the radial position within the gouge layer. Zones II and III generally become thicker towards the margins of the cylindrical samples where slip velocity and displacement are higher, but then become thinner again close to the outer margins (Figure 6a). This effect has previously been described by Beeler et al. (1996) who attributed it to the friction of the moving gouge material against the outer containment ring (Teflon in the their case)
reducing the degree of deformation close to the border. We observed a similar effect in our gouge experiments where the deforming gouge was in contact with the outer steel ring (in SHIVA) or Teflon ring (in ROSA) (Figure 2d).

The strain-marker experiment indicates that the highly-comminuted material in zone III represents the principal slip layer where most of the strain was localized. The banded appearance of the gouge in this layer, and the grain size grading within individual bands, is comparable to that reported by other authors, e.g. Kitajima et al. (2010) and Yao et al. (2013). Yao et al. (2013) observed that the finest material (<1 μm) within these bands was welded or sintered, a process likely caused by the localization of slip and subsequent frictional heating in the localized zone (Lachenbruch, 1980; Rempel and Rice, 2006; Platt et al., 2014). As suggested by Shimamoto and Togo (2012), the welding of grains may act to strengthen the slip zone and cause deformation within it to “migrate” to an adjacent area, resulting in multiple bands within a localized zone of high strain.

4.2. Comparison of natural and experimental CCAs

The CCAs found in the experimental and natural samples are similar in structure and shape. This is confirmed by quantitative analysis of two shape factors (circularity and solidity). In both experiment and nature, the central clasts are generally more angular than the outer

cortexes (see Figure 1 and 8). Natural CCAs have higher circularities and solidities than their experimental counterparts. This may be due to the natural central clasts and outer cortexes having experienced multiple slip episodes (and hence more comminution and abrasion), as opposed to the single slip episodes represented by the experiments. The size of the experimental CCAs is limited by the maximum particle size used in the experiments (180 μm) and, possibly, by the layer thickness (1.5 or 3 mm). The natural CCAs are up to 3 mm in size, and confined to an ultracataclastic slipping zone up to c. 2 cm thick.

In both experiment and nature, the aggregates sometimes consist of clustered matrix material rather than single host rock grains with a cortex. In the natural examples, the clustered material is typically reworked cataclasite that can contain relatively large angular grains within a finer matrix (Figure 1d). In the case of the experiments, the material clusters are likely to be fragments of fine-grained material from the high-strain zones (Figure 12a).

The cortex of fine-grained calcite in the natural examples ranges in thickness from ≤10 μm to c. 500 μm. In some samples from the natural slipping zones, outer cortexes surround almost all host rock fragments larger than c. 100 μm. In many cases, the natural cortexes are laminated (Figure 1b) and, infrequently, grain size grading within the cortex material is observed, with slightly larger grains towards the inside of individual cortex laminations (Smith et al., 2011). In the experimental samples, the maximum thickness of the outer cortex is on the order of 15 μm, and multiple laminations are observed in some samples (Figure 12b).

It was proposed by Boutareaud et al. (2008) and (2010), in the case of clay-bearing aggregates, that the central clasts accreted fine-grained material from the surrounding matrix. They further suggested that the aggregation process was controlled by electrostatic charges (due to the electrical double layer at the surface of the clay particles and a triboelectric effect) and that thermal pressurization of the gouge layers played a significant role. The triboelectric effect is responsible for electrostatic charging of particles due to frictional contact (Matsusaka et al. (2010), and references therein). Thermal pressurization creates dilation that is thought to

provide additional space for grain rolling and accretion of fine material (Boutareaud et al., 2010).

There is no microstructural evidence for crystal-plastic processes (e.g. sutured or sintered grains, lobate grain boundaries) in any of the experimental CCAs we studied. High-resolution SEM images of our experimental CCAs show that the grains in the cortexes (<500 nm) appear loosely aggregated (Figure 6d). Most of the grains are angular or sub-angular, with only the smallest grains (<500 nm) having a rounded shape.

CCAs only formed in our room-dry and vacuum experiments, in which total dilation was up to 180 μm. Additionally, *well*-developed CCAs were favored at large displacements, in experiments that had relatively large amounts of secondary dilation. In wet experiments, CCAs did not form and dilation was not measured at any stage. Following Han and Hirose (2012) and Boutareaud et al (2008, 2010), we suggest that the CCAs in our experiments formed by rolling of the central clasts facilitated by shear dilatancy, and that this provided the frictional contacts resulting in electrostatic charging of the smaller matrix particles. If thermal pressurization contributed to (secondary) layer dilation at larger displacements, it may be an important process in the formation of well-developed CCAs.

4.3.Deformation conditions necessary to form experimental CCAs

4.3.1. The role of displacement and strain

CCAs were better developed in our experiments at displacements exceeding 0.5 m. Significantly, they only formed in the intermediate-strain zone (Zone II) in the samples, suggesting that there is an upper and lower strain limit for their formation. This is consistent with previous experimental studies that typically show CCAs developing outside the zone of highest strain (e.g. Boutareaud et al., 2008; Kitajima et al., 2010; Han and Hirose, 2012). The strain-marker experiment reported here, combined with ongoing work on additional strain-marker experiments (Di Toro et al., 2013), suggests that CCAs developed in the experimental calcite gouges at relatively low strains on the order of $2 \leq \gamma \leq 14$.

The upper bound for strain (γ = 14) in the CCA-bearing Zone II results from strain localizing in Zone III. After localization has been achieved, a bulk of the displacement is hosted in the high-strain layer (Zone III), limiting strain accumulation in the CCA-bearing Zone II. Under the normal stress conditions investigated in these experiments, strain localization in 1.5 – 3 mm thick calcite gouge layers typically occurs in the first few tens of centimeters of displacement (Smith et al., 2012). However, CCAs were well developed in these experiments for displacements >0.5 m. This suggests that CCAs form and continue to evolve after localization has occurred, indicating that there must be ongoing shearing in Zone II (and possibly Zone I) of the samples throughout the experiments. This also explains the occurrence in Zone II of reworked fragments of fine-grained Zone III material.

4.3.2. The role of slip velocity

In the experiments, CCAs formed independently of the applied slip velocity, which covered four orders of magnitude (from 100 µm/s to 1 m/s). These results suggest that CCAs found in the slipping zones of calcite-bearing faults in nature are not unequivocal evidence for seismic slip. This is in agreement with the results of Han and Hirose (2012) for quartz and quartz-bentonite gouges, who found that clay-clast aggregates formed in low-velocity (0.0005 m/s) rotary-shear experiments.

When interpreting the experimental microstructures, it is important to consider the strong velocity gradient across the thickness of the gouge layer. Like strain, the strain *rate* in Zone III will be much higher, while the bulk of the gouge (Zones I and II) experiences much lower strain rates. Assuming that the different strain domains started to develop at the onset of the experiments and were sheared at a constant rate, we can roughly calculate the strain rate in each zone as maximum slip velocity / zone thickness. For the strain-marker experiment s886 we find that the strain rates in Zones I, II and III were approximately 0.64 s^{-1}, 1.2 s^{-1} and 740 s^{-1}, respectively, indicating that the strain rate in Zone III was more than two orders of

magnitude higher than in the other zones. The values for Zones II and III likely represent lower limits because those zones probably started to develop later than Zone I.

The natural calcite CCAs from the Tre Monti fault are sharply truncated in some cases by discrete principal slip surfaces (Figure 12 in Smith et al., 2011). Similar truncated clasts associated with discrete "mirror-like" slip surfaces in dolomite gouges were produced in experiments at seismic slip velocities (Fondriest et al., 2013). If the conclusions of Fondriest et al. (2013) are also applicable to calcite gouges, the occurrence of truncated CCAs in the Tre Monti fault suggests that it experienced seismic slip, even if the CCAs themselves may have formed at lower slip velocities.

4.3.3. The role of normal stress

Normal stress plays a crucial role in the formation of experimental CCAs. Well-developed CCAs were only found in experiments at normal stresses ≤5 MPa, although the normal stress at which CCAs form also depends on the gouge layer thickness (Figure 8b). Possible factors preventing formation of CCAs at higher normal stresses are 1) faster strain localization (Smith et al., 2012) and 2) increased compaction at higher normal stresses. In the first instance, faster localization of strain to a narrow high-strain zone may result in the bulk of the gouge layer experiencing strain of $\gamma<2$, below the lower bound necessary to form CCAs under the investigated conditions. In the second instance, greater compaction and hence reduction of porosity in the gouge matrix might restrict rolling of clasts to such a degree that the outer cortexes do not form.

Although gouge zone thickness along natural faults is highly variable, compilations of geological and geophysical data pertaining to the thickness of the coseismic slip zone in the brittle crust suggest typical layer thicknesses on the order of several millimeters to a few centimeters (Sibson, 2003), comparable to the layer thicknesses used in our experiments. Our results suggest that in nature the formation of CCAs may be restricted to relatively shallow crustal levels. This is broadly compatible with existing case studies reporting CCAs in natural

slipping zones, which all come from fault zones exhumed from relatively shallow crustal depths (<4 km; Table 1). For example, in the Tre Monti fault (Smith et al., 2011), the CCA-bearing cataclastic slip zone directly underlying the principal slip surface is 2 to 10 mm thick and exhumed from a depth of <2 km. In cores from borehole A drilled through the Chelungpu thrust fault, clay-clast aggregates were found in the 2-3 cm thick principal slip zone of the 1999 Chi-Chi earthquake located at depths of c. 1.11-1.14 km (Boullier et al., 2009). Interestingly, in borehole B, where the principal slip zone is much thinner (c. 0.3 cm) CCAs were only found in gouge material flanking the principal slip zone (Boullier et al., 2009). Based on our experiments, this may be because the strain in the thin principal slip zone itself was higher than that required for CCA formation.

4.3.4. Ambient Conditions

No CCAs developed in the experiments with water-dampened calcite gouges. In studies on the charging characteristics of various materials it was shown (Greason, 2000; Nomura et al., 2003) that the net charge due to triboelectrification (in the order of 10^{-8} Coulomb) generally decreased with increasing humidity. If this is applicable to charging induced by friction of calcite grains against each other, or against the steel and Teflon walls of the gouge holders, the reduced triboelectric force due to the high (~20 wt%) water content of the gouge could be too low to attract the fine material to the larger clasts. Due to the higher permittivity in a water-saturated gouge as compared to room-humid gouge (Hector and Schultz, 1936; Chistyakov, 2007), the electrostatic Coulomb force acting between the particles will also be reduced.

In addition, the presence of water causes faster slip localization, reducing the strain accommodated in the bulk gouge layer outside the principal slip zone (Faulkner et al., 2010; Ferri et al., 2010). Dilation of the gouge layers was almost never observed in wet experiments. Faster slip localization combined with rapid compaction of the gouge layer are likely to restrict grain rolling, and thus the formation of CCAs, in the water-dampened gouges.

Our results showing that CCAs did not form in water-dampened gouges are consistent with the experiments on clay-bearing gouges by Han and Hirose (2012) and Ferri et al. (2011), but contrast the results of Boutareaud et al. (2008), (2010). The latter authors found that clay-clast aggregates developed in clay-bearing gouge samples that were initially saturated with water. However, as noted by Han and Hirose (2012), the total displacements in the experiments by Boutareaud et al. (2008), (2010) were up to 64 m. Due to frictional heating at such large displacements, the temperatures in the experiments of Boutareaud et al. (2008), (2010) increased to c. 200°C in the center and c. 400°C at the periphery of the samples. This may have resulted in evaporation of the water, resulting in effectively dry conditions after displacements of a few meters.

According to the experiments performed in this study, the formation of CCAs is favored by relatively dry conditions. Smith et al. (2011) found evidence of layer fluidization and syn-tectonic vein formation in the CCA-bearing principal slip zone of the Tre Monti fault, suggesting fluid involvement in faulting. The same is true for the slipping zones of the Chi-Chi earthquake (Boullier et al., 2009), where there is evidence of gouge layer fluidization. This raises two possibilities that warrant further investigation; the first is that fluidization processes (that cannot be effectively investigated in the present gouge experiments) play a role in the formation of CCAs in nature. The second is that fluid availability in natural slipping zones is highly variable in time (e.g. during the seismic cycle) and space (e.g. due to fault geometry), with the natural CCAs forming during restricted time intervals in relatively dry parts of the slipping zones.

5. Conclusions

We investigated the conditions necessary to form clast-cortex aggregates (CCAs) in granular calcite gouges by performing low- to high-velocity experiments in a rotary-shear configuration. The experimental results show that in calcite gouges CCAs are well developed at

displacements >0.5 m, normal stresses ≤5 MPa, and in room-dry or vacuum conditions. Significantly, CCAs developed at all investigated slip rates (0.001 m/s to 1 m/s), spanning the subseismic to seismic range. No CCAs formed in water-dampened gouges.

Experimental CCAs were formed in relatively low-strain domains outside the principal slipping zones, where the bulk shear strain was between 2 and 14. Analysis of the circularity and solidity of the experimental CCAs as well as of natural examples from the calcite-dominated principal slip zone of the Tre Monti normal fault in Italy, indicates that experimental and natural examples have similar microstructural characteristics and grain shapes. We suggest that CCAs in calcite gouges form by grain rolling associated with shear dilatancy, accompanied by progressive accretion of fine-grained matrix material. The interface-scale mechanisms leading to accretion of fine-grained matrix material in the cortexes require further investigation by higher-resolution methods.

Overall, our results suggest that CCAs in calcite-bearing slipping zones likely form in shallow and (at least locally) fluid-poor fault environments, in granular layers flanking the highest-strain ultracataclasites. In experiments, CCAs form in calcite gouges over a range of subseismic to seismic slip rates, suggesting that in natural slipping zones they cannot be used as a reliable indicator of seismic slip.

6. Acknowledgements

The authors would like to thank Michele Fondriest, Silvia Mittempergher, Stefan Nielsen, Nicola Praticelli and Marie Violay for technical assistance, Leonardo Tauro for help with the sample preparation, Luca Perruzo, Andrea Cavallo and Rolf Neuser for support with the SEM and Federico Zorzi for XRD analyses. Anne-Marie Boullier and Raehee Han are thanked for constructive comments. MR acknowledges funding by Ca.Ri.Pa.Ro., SAFS acknowledges funding from a 2014 University of Otago Research Grant. GDT acknowledges the European Research Council Starting Grant USEMS (no. 205175).

7. Figure Captions

Figure 1. Summary of the occurrence of clast-cortex aggregates (CCAs) in the Tre Monti normal fault, central Italy, (a) Map of southern Italy with red lines showing the locations of the Tre Monti fault and other active normal faults that cut Holocene deposits (modified from Roberts and Michetti (2004), (b) Schematic cross-section through a segment of the Tre Monti fault showing the transition from intact host rock to breccias and cataclasites (modified from Smith et al. (2011)). The active Quaternary fault scarp, corresponding to the principal slip surface in this fault, is marked in red. The hanging wall at the surface is composed of well-cemented Quaternary sediments, (c) scanned thin section image showing the principal slip surface and cataclastic to ultracataclastic principal slipping zone. The ultracataclasite layer closest to the principal slip surface contains well-developed CCAs. (d) Optical photomicrographs in plane-polarized light showing examples of CCAs from the ultracataclastic slipping zone of the Tre Monti fault. From left to right the CCAs increase in size and complexity. The central clasts can be composed of limestone host rock fragments (first three images) or reworked cataclastic material from the slipping zone (fourth image). In some cases, the cortex contains multiple laminations (third and fourth images and other examples in Smith et al. (2011)).

Figure 2. Experimental set-up and gouge sample holders, (a) Schematic of the ROSA rotary-shear apparatus at Padua University. (R1) and (R2): rotary encoder and potentiometer measuring revolution speed (rpm) and rotation angle, respectively. (T1) and (T2): Two compression load cells measuring the torque; output values are averaged. (D): Strain-gauge type displacement gauge measuring vertical displacement of the axial column and the experimental sample. (L): Compression load cell measuring the axial load applied to the sample via the pneumatic or hydraulic cylinders. (b) Gouge sample assembly using two solid rock cylinders and an outer Teflon ring to contain the gouge layer. The jubilee clip fastened around the Teflon sleeve is not shown in this figure. (c) Annular steel sample holder with inner and outer Teflon rings. (d) Metal sample holder used with SHIVA (modified from Smith et al., 2013).

White regions: stationary parts, grey regions: rotary parts. Yellow areas show position of gouge layer contained by inner and outer metal sliding rings. Red lines demonstrate where metal parts are in sliding contact during the experiments.

Figure 3. Characterization of starting materials used in gouge experiments**,** (a) SEM images of the starting gouge material derived by crushing Carrara Marble (batch CMG 1, scale bar in inlet is 20 μm), (b) Particle size distribution of starting material derived from sieving and weighting, (c) X-ray powder diffraction spectrum for batches CMG2 (blue curve and labels) and CMG3 (black curve and labels).

Figure 4. Mechanical data from calcite gouge experiments, (a) Friction coefficient (upper three data curves) and axial displacement (lower three curves) for experiments conducted with room-dry calcite gouge. Positive changes in axial displacement indicate shortening, negative changes indicate dilation. Experiments s590 (black lines) and s776 (blue lines) performed at a normal stress of 3 MPa and slip rates of 1 and 0.1 m/s, respectively, show no weakening or transient dilation. Experiment s272 (red lines) performed at higher normal stress (17.3 MPa) at a slip rate of 0.1 m/s exhibits some weakening following peak stress after approximately 0.15 m displacement. In s272, initial gouge layer compaction is followed by transient dilation of c. 20 μm, and then renewed compaction. (b) Coefficient of friction (upper two data curves) and axial displacement (lower two data curves) for water-dampened experiments s591 (black lines; 3 MPa, 1 m/s) and s592 (blue lines; 2.8 MPa, 0.1 m/s). Neither of these experiments exhibits transient dilation or weakening.

Figure 5. Dilation vs. total displacement for experiments conducted under room-dry, wet and vacuum conditions. Transient and total (i.e. transient + secondary) dilation are plotted separately for the room-dry experiments.

Figure 6. Microstructural zones in sheared calcite gouges, (a) SEM mosaic and line drawing of room-dry experiment r88 (equivalent velocity 0.1 m/s; 1 MPa normal stress; 3 m

displacement). Thin section was cut approximately halfway between edge and center of the cylindrical sample to analyze the distribution of microstructural zones at different radial positions in the sample. Three distinct microstructural zones (Zones I-III) are recognized on the basis of grain size variations and the presence of CCAs and banding. Black boxes show the positions of b) and e). (b-e) SEM images of microstructural zones, (b) CCAs (yellow arrows) developed in Zone II. Note that the CCAs developed in a layer with relatively high porosity, (c) Close-up of CCA marked by red arrow in part b). In this example, the outer cortex is up to 10 µm wide and fine-grained materials in the cortex in-fill embayments in the central clast. Red box denotes location of d). (d) Zoom of fine-grained cortex material <1 um in size. The cortex material appears loosely aggregated, individual rounded grains down to c. 100 nm in size are recognized. (e) Anastomosing shear bands and extensive grain comminution within Zone III.

Figure 7. Strain distribution in sheared calcite gouge layers. (a) Rotary side of the steel sample holder used with SHIVA, filled with calcite gouge and prepared with two thin vertical markers of dolomite with the aid of razor blades. The starting particle size of both the calcite and the dolomite gouges in this experiment was <250 µm. Black box illustrates how post-experiment sample was cut. Sketches (modified after Scruggs and Tullis, 1998) show section though sample with unstrained and idealized strained marker assuming homogeneous strain distribution. (b) SEM mosaic and interpreted line drawing of sample s886 (3 MPa normal stress, equivalent slip velocity of 1 m/s, 2.5 m of total displacement, room-dry). The dolomite marker is distinguished by its darker grey color. The geometry of the dolomite marker broadly defines low-, intermediate- and high-strain domains. The left margin of the dolomite marker is cut by a series of R1-Riedel shears with offsets between c. 10–180 µm.

Figure 8. Summary of experiments performed under different conditions of slip velocity, normal stress, and ambient humidity. In the tables, **N** denotes no CCAs, **P**: poorly-developed CCAs, **W**: well-developed CCAs (see text for definitions). Red letters denote experiments in room-dry conditions, blue letters denote water-dampened experiments. (a) Results for

606 experiments conducted at normal stresses of 1 MPa (upper graph) and 3 MPa (lower graph),
607 for velocities ranging from 10^{-4} - 1 m/s (log scale) and displacements ranging from 0.35 to 5.58
608 m. (b) Results for experiments conducted with varying normal stress and gouge layer thickness
609 but the same target slip rate (0.1 m/s) and total displacement (3.0 m), all in room-dry
610 conditions. (c) Results for experiments conducted in vacuum conditions with slip rates of 0.1
611 m/s, 3 m displacement, and variable normal stress. (d) SEM image of experimental CCAs with
612 well-developed cortexes (experiment r89). Aggregates are abundant in this sample; most clasts
613 with a diameter >10 μm are fully surrounded by cortexes. (e) SEM image of poorly-developed
614 CCAs in experiment r68. In this experiment, only a few aggregates with rudimentary cortexes
615 formed.

616 **Figure 9.** Gouge layer (experiment r91) deformed in water-saturated conditions. The
617 microstructure of water-dampened layers is characterized by a relatively thick zone adjacent
618 to the rotary side in which rounded to sub-rounded clasts are surrounded by a homogenously
619 fine-grained matrix. CCAs were not identified in water-dampened experiments.

620 **Figure 10.** Grain size and shape analysis of natural and experimental CCAs, (a) The circularity of
621 an object, in this case the central clast of a CCA, is calculated from its area and its perimeter
622 (red dotted line) as described in the text. Solidity is calculated by dividing the area of the
623 object (red dotted line) by the convex area having no embayments (black dotted line). (b) SEM
624 image (left) and corresponding tracing (right) of experimental sample r80 containing well-
625 developed CCAs (n = 45). In the tracing, red grains are central clasts, grey areas are outer
626 cortexes. (c) Optical photomicrograph mosaic (upper image) and corresponding tracing (lower
627 image) of natural CCAs (n = 137) from the principal slip zone of the Tre Monti fault. The box
628 shows the area of the photomicrograph mosaic. In the tracing, red grains are central clasts,
629 grey areas are outer cortexes.

630 **Figure 11**. Results of quantitative analysis of circularity (a) and solidity (b) of samples shown in
631 Figure 10. Bin sizes were chosen to reveal differences in the data and are 0.1 for circularity and
632 0.025 for solidity.

633 **Figure 12.** Examples of experimental CCAs from sample r80, (a) Rounded grain composed of
634 reworked matrix material and lacking a central clast, (b) CCA consisting of two laminations
635 (yellow arrows) surrounding a central clast. Note that in both of the images some of the
636 smaller grains are also CCAs (red arrows).

637 # 8. Tables

638 **Table 1.** Summary of naturally-occurring CCAs in tectonic fault zones and landslides. Modified
639 after Han and Hirose (2012).

640 **Table 2.** Summary of experimental conditions, dilation measurements, and classification of
641 CCAs.

Table 1: Summary of naturally-occurring CCAs in tectonic fault zones and landslides. Modified after Han and Hirose (2012).

Location	Setting	CCA host rock composition	Formation /Exhumation Depth	Evidence of fluids	Reference
Tre Monti fault, Italy	Normal fault	Fossiliferous and micritic limestone	<2 km	Evidence of layer fluidization and syn-tectonic vein formation	Smith et al. (2011)
Alpine fault, New Zealand	Strike-slip fault	Mylonite-derived clay-gouge	2-4 km (attributed to the depth of growth of swelling clays)	Hydrous chloritization, dissolution, fluid-induced sub-critical cracking	Warr and Cox (2001)
Chelungpu fault, Taiwan	Thrust fault	Clay-rich gouge	1.11-1.14 km	Evidence for gouge layer fluidization	Boullier et al. (2009)
Palisades slide block, USA	Landslide	Basal layer where lithologies of upper plate (limestones) and lower plate (sandstone-conglomerate-like rock with clayey matrix) mix	<250 m	No evidence for or against involvement of fluids	Anders et al. (2000), Boyer and Hossack (1992)
Heart Mountain, WY, MT, USA	Landslide	Dolomite	2-4 km	Evidence for fluidization either with or without water	Beutner and Craven (1996), Beutner and Gerbi (2005), Anders et al. (2010)

Table 1

Table 2: Summary of experimental conditions, dilation measurements, and classification of CCAs.

	Name	wt% H_2O	σ_n (MPa)	v_e (m/s)[a]	d_e (m)[b]	Sample holder	Starting material batch	Gouge layer thickness (mm)	Net axial displacement (µm)[c]	Transient dilation (µm)	Total dilation	Aggregates
Room-Humidity conditions	r103	0	1	0.0001	3.05	Gabbro	CMG2	1.5	250	7	75	**W**
	r69	0	1	0.001	0.62	Steel	CMG1	1.5	20	0	26	N
	r78	0	1	0.001	0.64	Steel	CMG1	4.3	730	0	0	N
	r93	0	1	0.001	3	Gabbro	CMG2	1.8	30	7	108	**W**
	r89	0	1	0.001	5.05	Rock	CMG2	2.1	-80	120	175	**W**
	r68	0	1	0.1	0.53	Steel	CMG1	1.5	290	0	0	P
	r73	0	1	0.1	0.53	Steel	CMG1	0.36	70	0	0	P
	r88	0	1	0.1	3	Rock	CMG1	1.5	300	7	15	**W**
	r80	0	1	0.1	5	Tonalite	CMG1	1.5	250	23	28	**W**
	r82	0	1	1	5	Tonalite	CMG1	1.5	380	13	17	**W**
	r71	0	3	0.001	0.65	Steel	CMG1	1.5	270	0	0	N
	r105	0	3	0.001	5	Gabbro	CMG2	1.5	120	0	70	**W**
	r70	0	3	0.1	0.54	Steel	CMG1	0.9	105	0	0	N
	s787	0	3	0.1	2.72	SHiVA	CMG2		100	20	60	P
	r85	0	3	0.1	3	Tonalite	CMG1	1.5	1140	15	41	P
	s776	0	3	0.1	3.35	Shiva	CMG2	3	100	140	140	N
	r90	0	3	0.1	3.85	Gabbro	CMG2	1.7	120	9	38	**W**
	s775	0	3	0.1	5.58	SHiVA	CMG2	1.8	230	90	90	P
	s590	0	3	1	0.5	SHiVA	CMG1	3	280	0	0	N
	r86	0	3	1	1.9	Tonalite	CMG1	1.7	220	0	0	P
	s777	0	3	1	2.5	SHiVA	CMG2	1.8	60	14	14	P
	s886	0	3	1	2.5	SHiVA	<250 µm	3	125	27	26.614	N

	s778	0	5	0.1	3	SHiVA	CMG2	3	90	60	113.4	**W**
	s811	0	10	0.1	2.25	SHiVA	CMG2	3	100	20	40	P
	s272	0	17.3	0.1	1.15	SHiVA	CMG3	3	280	19	19.42	N
Water-dampened	r92	22	1	0.001	4.45	Gabbro	CMG2	1.8	400	0	0	N
	r74	20	1	0.1	0.65	Steel	CMG1	0.4	360	0	0	N
	r91	25	1	0.1	4	Rock	CMG2	1.6	200	0	20	N
	r83	20	1.6	0.0005	0.27	Tonalite	CMG1	1.8	170	0	0	N
	s592	~15	2.8	0.1	0.5	SHiVA	CMG1	3	185	0	0	N
	r84	20	3	0.001	0.5	Tonalite	CMG1	1.5	640	0	0	N
	r72	40	3	0.1	>0.5	Steel	CMG1	1.5	-	0	0	N
	s591	20	3	1	0.5	SHiVA	CMG1	3	320	0	0	N
											0	
Vacuum	s812	0	3	0.1	1.93	SHiVA	CMG3	3	160	10	50	N
	s813	0	5	0.1	3.35	SHiVA	CMG3	3	220	0	0	P
	s814	0	10	0.1	2.79	SHiVA	CMG3	3	360	0	0	N

[a]equivalent velocity, [b]equivalent displacement, see text for definitions. [c]positive value: net compaction, negative value: net dilation

Table 2

642

Chapter II

Strain localization in experimentally-sheared calcite gouge layers

(This study was performed in collaboration with Steven Smith, Thomas Mitchell, and Giulio Di Toro. I performed all the work described in this chapter. I was assisted (but not continuously) in the laboratory by Elena Spagnuolo. The material presented here was discussed with Steven Smith, Thomas Mitchell and Giulio Di Toro.)

Abstract

Strain localization during coseismic slip in natural faults is a fundamental mechanical process that has implications for understanding frictional heating and the earthquake energy budget (e.g. fracture energy vs. radiated energy). To assess the nature of strain localization during shearing of calcite fault gouges, and to understand how the localization process varies depending on imposed conditions, intermediate- to high-velocity rotary-shear experiments were conducted on synthetic calcite gouges containing narrow strain markers made of dolomite gouge. Within an annular steel sample holder (with outer and inner radii of 55 and 35 mm, respectively), a c. 3 mm thick calcite gouge layer (starting grain size < 250 μm) was prepared with a c. 2 mm wide dolomite gouge strain marker cutting vertically through the calcite layer. The marker was orientated perpendicular to the imposed shear direction. The strain marker experiments were conducted at varying slip rates (10^{-3}–1 m/s), total displacements (0.01–2.5 m), normal stresses (3 to 21 MPa) and ambient conditions (room-dry and water-dampened) to test the dependence of the strain distribution on these various experimental conditions. Mechanical data (shear stress, shortening and dilation, etc.) were recorded during the experiments. Afterwards, the preserved samples were cut vertically through the dolomite strain markers (approximately parallel to the slip direction) and microstructural analysis was conducted with the scanning electron microscope.

At low velocity (≤1 cm/s), dynamic weakening did not occur in either room-dry or water-dampened calcite gouges, consistent with previous experimental results. Room-dry and water-dampened gouges sheared at 1 m/s both dynamically weaken, but the evolution of strength at the onset of slip is different: room-dry gouges show a prolonged strengthening prior to dynamic weakening, whilst the water-dampened gouges near-instantaneously weaken to a steady-state stress that is slightly higher than in room-dry conditions. Microstructural analysis revealed that in both dry and water-dampened gouges strain localization at 1 m/s occurs progressively and rapidly. A thin (< 600 μm) high-strain layer and through-going principal slip surface developed after several cm of slip at most. The strain accommodated in the bulk of the gouge layer does not change significantly with increasing total displacement, suggesting that, once formed, the high-strain slipping zone and principal slip surface

accommodate most of the ongoing displacement. This is supported by the observation of sintered and recrystallized grains, as well as zones of calcite decarbonation, adjacent to the principal slip surface, indicating localized frictional heating. Faster localization in water-dampened conditions was not reflected in the investigated microstructures, which resemble those under room-dry conditions. Thus, faster weakening in water-dampened conditions, and the lower steady-state shear stress in the room-dry gouges, are likely not due to different degrees of localization. Instead, weakening in water-dampened gouges may be enhanced by faster subcritical crack growth in the presence of fluids. Localization to a principal slip surface likely occurs during and after weakening. When extrapolated to natural conditions, our results suggest that calcite-bearing gouge slip zones are more prone to slip in the presence of water than in relatively dry conditions, which might explain some of the slip distribution complexity during earthquakes occurring in carbonate sequences.

1. Introduction

Field observations from many mature crustal faults, e.g. the San Andreas fault system, California (e.g. Chester et al., 1993), the Chelungpu fault, Taiwan (Lee et al., 2001), and the Median Tectonic Line, Japan (Wibberley and Shimamoto, 2003), show that while the surface trace of a fault may have a complex geometry and the damage zone may be broad (Rockwell and Ben-Zion, 2007), trench exposures and outcrops of exhumed fault zones show that at depths greater than a few tens of meters accumulated co-seismic slip can be localized within subcentimeter-thick principal slip zones (PSZ). There is evidence that during individual coseismic slip events further localization down to the mm-scale can occur (Sibson, 2003; Rockwell and Ben-Zion, 2007; Fondriest et al., 2012, 2013; Siman-Tov et al., 2013), although distributed coseismic deformation must also occur at fault irregularities (Sibson, 1986; Pavlis et al., 1993). Evidence of localized slip is given by the occurrence of narrow layers of highly comminuted gouge or ultracataclasite material that built up the PSZ within host rocks where grain size reduction was minimal (Chester et al., 2004). In addition, gouge lithology is often different from that of the surrounding rocks, indicating that – if no fluid-rock interaction took place (e.g. Wintsch et al., 1995) – more slip is accumulated in the gouge (e.g. Chester and Logan, 1986; Flinn, 1977). Even though some counterexamples exist, where deformation was evenly distributed in the fault core or where multiple fault cores had developed (e.g., in the Carboneras fault, Rutter et al., 1986; Faulkner et al., 2003), many field observations and seismological studies reveal a high degree of localization of seismicity along large faults (e.g., Li et al., 1998; Schaff et al., 2002; Thurber et al., 2006), suggesting that slip localization occurs in major fault zones throughout the crustal seismogenic zone (Rockwell and Ben-Zion, 2007) and beneath (Shelly, 2010).

The gouge or ultracataclasite layers in the fault core are often bounded by the fault "damage zone" in which the degree of fracturing due to secondary faults, macro- and microfractures and grain size reduction typically increases towards the fault core (e.g. Chester and Logan, 1986, 1987; Vermilye and Scholz, 1998; Mitchell and Faulkner, 2009). Fault core and damage zones often form a symmetrical damage structure (Fig. 1, Chester et al., 1993), however, slip may also localize close to a damage zone boundary, resulting in an asymmetric

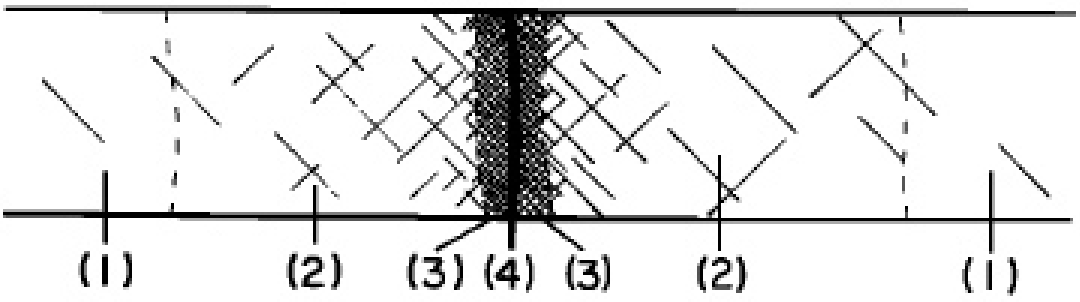

Figure 1. Strain localization in nature. The internal structure of the north branch of the San Gabriel fault from Chester et al. (1993). This symmetric damage structure with a wide damage zone surrounding a relatively thin fault core zone, where most of the slip is localized, is a characteristic of many fault zones.

damage structure (Sibson, 2003; Ben-Zion & Sammis, 2003; Dor et al., 2006; Mitchell et al., 2011). The thickness of both the fault core and the damage zone seems to scale with the total displacement on the fault (Robertson, 1983; Scholz, 1987; Evans, 1990; Billi, 2005; Faulkner et al., 2011), although faults can display significant variations in damage zone thickness along strike due to geometrical constraints (Chester et al., 1993). The degree of strain localization and the thickness of the PSZ can have a great effect on the mechanical behavior of faults (Ben-Zion and Sammis, 2003; Heermance et al., 2003; Rockwell and Ben-Zion, 2007) because they influence the production of frictional heat and thus effective pressure conditions and fault-rock mineralogy. Thus, the correlation of the frictional behavior of gouges and the degree of shear localization has been the subject of many dedicated experimental and numerical studies.

Numerical studies of the degree of localization and the shear stress of granular materials sheared at high velocity were conducted by e.g. Mair and Abe (2008), Platt et al. (2014) and Rice et al. (2014), and specifically the effect of shear heating was considered by e.g., Lachenbruch, (1980), Rice (2006) and Segall and Rice (2006). In a recent model by Platt et al., (2014) using a 1D-model of a fluid-saturated gouge layer sheared at seismic slip rates (1 m/s) between two poroelastic half-spaces, the localized zone thickness at peak strain-rate localization was found to depend only on the physical properties of the gouge (Tables 1 in Platt et al. (2014) and Rice et al. (2014), respectively) (not the initial width of the gouge layer) and the slip rate. Platt et al. (2014) found that the localized zone thickness is set by a balance between thermal pressurization, hydraulic and thermal diffusion, and either frictional rate-strengthening or dilatancy, depending on the model approach, and ranges from c. 50 to c. 340 µm at shallow depths (18 MPa effective normal stress and an ambient temperature of 30°C), and from c. 2 to 45 µm at greater depths of 7 km (due to different thermal and hydraulic properties). For localization limited by dilatant strengthening, a transient strain-rate localization is followed by a switch to homogeneous straining. Platt et al. (2014) also modeled the effect of localization on the shear strength evolution considering thermally-driven weakening mechanisms. They found that while during early stages of deformation the shear strength evolution is similar to that modeled for uniform shearing (Rempel and Rice, 2006), the onset of strain-rate localization is accompanied by an acceleration in dynamic weakening,

because localization focuses the frictional heating to a thinner zone, rendering thermal pressurization more effective (Lachenbruch, 1980).

The shear-stress evolution of gouge material and its relation to the degree of localization was also investigated in numerous experimental studies using both dry and wet samples. In low-velocity (mostly 1–100 μm/s) gouge experiments (direct-shear and rotary-shear configurations), relevant to an understanding of the earthquake nucleation phase, a transition from velocity-strengthening to velocity-weakening behavior has been observed and associated to a change from distributed to localized shear (Marone et al., 1992; Beeler et al., 1996; Scruggs and Tullis, 1998; Rathbun and Marone, 2010). The transition was observed to be displacement-dependent, but the critical displacement (up to the transition) was only affected by the gouge particle size and the roughness of the bounding surfaces, not by the gouge layer thickness (Dieterich, 1981), indicating that strain localizes before the peak frictional strength is reached. During the velocity-strengthening phase, that is possibly due to shear dilation of the granular material that requires work to be done, aseismic slip and creep behavior are expected to occur (e.g., Marone et al., 1990).

In high-velocity experiments, weakening of cohesive (silicate and serpentinite) rocks was triggered by flash heating following strain localization in a thin (≤ 30 μm) layer of wear material" (Goldsby and Tullis, 2011; Kohli et al., 2011). In intermediate- to high-velocity experiments on cohesive and powdered serpentinite, Proctor et al. (2014) found that cohesive rocks weaken at lower displacements and velocities and show a lower steady-state friction than gouges. The delayed weakening in the gouges was attributed to the need to localize the in gouges initially distributed slip before flash heating could be efficient. In many high-velocity experimental studies, shear was found to localize in a thin (< 300 μm) highly-comminuted and compacted gouge layer cut by one or several discrete slip surfaces (Kitajima et al., 2010; Fondriest et al., 2013). Microstructural evidence of localized frictional heating due to intense strain localization was provided by sintered or recrystallized grains adjacent to the principal slip surface (e.g. Smith et al., 2013; Yao et al., 2013). Results from high-velocity experiments on room-dry calcite gouges (Smith et al., 2015) show that shear was localized in a high-strain shear band prior to dynamic weakening, although localization to a through-going principal slip

surface continued during the weakening phase. Smith et al. (2015) concluded that localization of shear in dry gouges is a necessary precursor to dynamic weakening.

The aim of this study was to build on the results of Smith et al. (2015) by conducting rotary-shear experiments on calcite gouges with the systematic use of strain markers, and to extend the study of Smith et al. (2015) to include wet calcite gouges and a wider range of slip velocities and total displacements. In rotary-shear experiments with cohesive Carrara marble (Violay et al., 2013; 2014), the fluid-saturated marble weakens much quicker than the dry rocks showing that the frictional behavior of cohesive rocks may be significantly different in room-dry and wet conditions. However, cohesive rocks and gouges of the same mineralogy may behave very differently (e.g., serpentinite, Proctor et al., 2014; calcite, Smith et al., 2015), which may be due to different mechanisms of friction (Hatano, 2009). However, previous experimental studies on gouges of various lithologies (including calcite) performed at low velocity (< 1 mm/s) showed a smaller shear stress of wet compared to dry gouges (e.g., Morrow et al., 2000; Verberne et al., 2013). The same effect was observed in high-velocity friction experiments with clay-bearing gouges (e.g., Ujiie and Tsutsumi, 2010; Kitajima et al., 2011, Han and Hirose, 2012), but no experimental data on the high-velocity frictional behavior of wet calcite gouges are available to date. In the following, we will describe the mechanical data obtained from calcite gouge experiments conducted in room-dry and water-dampened conditions and evaluate the distribution and localization of strain in the gouge layer that were investigated with the use of strain markers.

2. Methods

2.1.Experimental Set-Up

To study the distribution of strain in the gouge layers, a total of 25 rotary-shear experiments were performed using strain markers. The gouge experiments were performed with applied normal stresses ranging from 3–20 MPa, slip velocities from 0.001–1.2 m/s, an acceleration of 6 m/s^2, total displacements from 0.011–2.5 m, and different ambient (i.e. in room-dry and water-dampened) conditions (Table 1). The experiments were performed using the **S**low- to **Hi**gh-**V**elocity **A**pparatus SHIVA located at the Istituto Nazionale di Geofisica e

157 Vulcanologia (INGV) in Rome, Italy. The design and capability of SHIVA is described in detail in
158 Di Toro et al., 2010. The annular gouge holder used with SHIVA (description and calibration
159 tests in Smith et al., 2013) is built completely out of steel avoiding contamination of the
160 sample due to Teflon decomposition. (Teflon is used as the confining medium in most
161 experimental studies with gouges; see Chapter III of this thesis and Sawai et al., 2012.) The
162 gouge layer is confined by an inner and an outer steel ring with diameters of 35 and 55 mm,
163 respectively, that slide over the base disc (Fig. 2a). To minimize the contribution of these rings
164 to the measured torque, the contact area of the rings with the base disc is lubricated with
165 high-temperature grease prior to an experiment. Additionally, springs located underneath the
166 confining rings ensure that the normal load is mainly supported by the gouge layer (see Smith
167 et al., 2013).

168 ## 2.2.Sample Preparation

169 The calcite and dolomite gouge used in the experiments was derived by crushing,
170 respectively, Carrara marble and cohesive dolostones from the Foiana Tectonic Line (Fondriest
171 el al., 2013). The powder was sieved to particle sizes < 250 µm (Fig. 2b). 5 g of calcite gouge
172 were distributed inside the gouge holder yielding an initial gouge layer thickness of c. 3 mm.
173 Afterwards a c. 2 mm wide, vertical dolomite strain marker was constructed perpendicular to
174 the imposed shear direction and the gouge layer boundaries (Fig. 2c). For experiments with
175 water-dampened gouge, 20 wt.% (1 ml) distilled H_2O was added evenly to the top surface of
176 the gouge layer using a pipette. The gouge layer was pre-compressed at c. 0.1 MPa using a
177 pneumatic press. This was necessary because the upper and lower parts of the holder had to
178 be hold together tightly with screws as the holder is turned by 90° to be fixed to the horizontal
179 column of SHIVA. After the experiment, a sample of the gouge layer containing the sheared
180 strain marker was preserved in epoxy resin (EpoFix, Struers GmbH) and then cut (using a
181 water-cooled saw) subparallel to the shear direction to obtain a cross-section through the
182 sheared marker (Fig. 2d, e). Due to the annular sample geometry, maximum slip velocity and
183 total displacement vary inside the gouge layer depending on the radial position. (In Table 1 we
184 thus list the “equivalent” velocity and displacement, respectively, following Hirose and
185 Shimamoto, 2005; see definition in Chapter I of this thesis.). When preparing the sample, it is

thus important to cut the strain marker at the same radial position and, if possible, with the same angle to its boundaries in order to produce comparable results. This was difficult to achieve because of the fragility of the sample. Particularly in samples from short-displacement experiments with room-dry gouges, the material was still relatively incohesive and the sample often broke along the marker. Thus, small variations in the strain calculated from the distortion of the marker can be due to the imprecise sample preparation that has to be taken into account when interpreting the results.

2.3.Analysis Techniques

The cut samples were polished in the presence of water using 3000 and 5000 grit Si paper followed by 1 and 0.3 µm de-agglomerated alpha alumina powder (Buehler Micropolish II). The samples were then coated with carbon or chrome for the investigation with the Scanning Electron Microscope (SEM). SEM analysis was performed using the JEOL JSM-6500F Field-Emission Scanning Electron Microscope at the Istituto Nazionale di Geofisica e Vulcanologia (INGV) in Rome, Italy, the CamScan MX3000 SEM at the University of Padua, and the LEO (Zeiss) 1530 Gemini High resolution thermally-aided Field Emission SEM at the Institute of Geology, Mineralogy and Geophysics of the Ruhr-Universität Bochum, Germany. Images were obtained in backscattered electron mode using an acceleration voltage of 8–20 kV and a working distance of 7.3–20 mm. In backscattered mode, the dolomite marker can easily be distinguished from the surrounding calcite due to its darker grey color (Fig. 2e). The marker is sheared in the direction of slip (Fig. 2e, f) and the finite strain γ in the gouge layer can be calculated from the angle of distortion φ: $\gamma = tan\varphi = \frac{dx}{x}$, where x is the thickness of the layer and dx the amount of horizontal displacement (Fig. 2f). The strain in the calcite gouge experiments, however, is not evenly distributed throughout the gouge layer like it is in the sketch in Fig. 2f. Instead, we distinguish between low-, intermediate-, and high-strain domains and estimate an average strain for each of these domains (Fig. 2e).

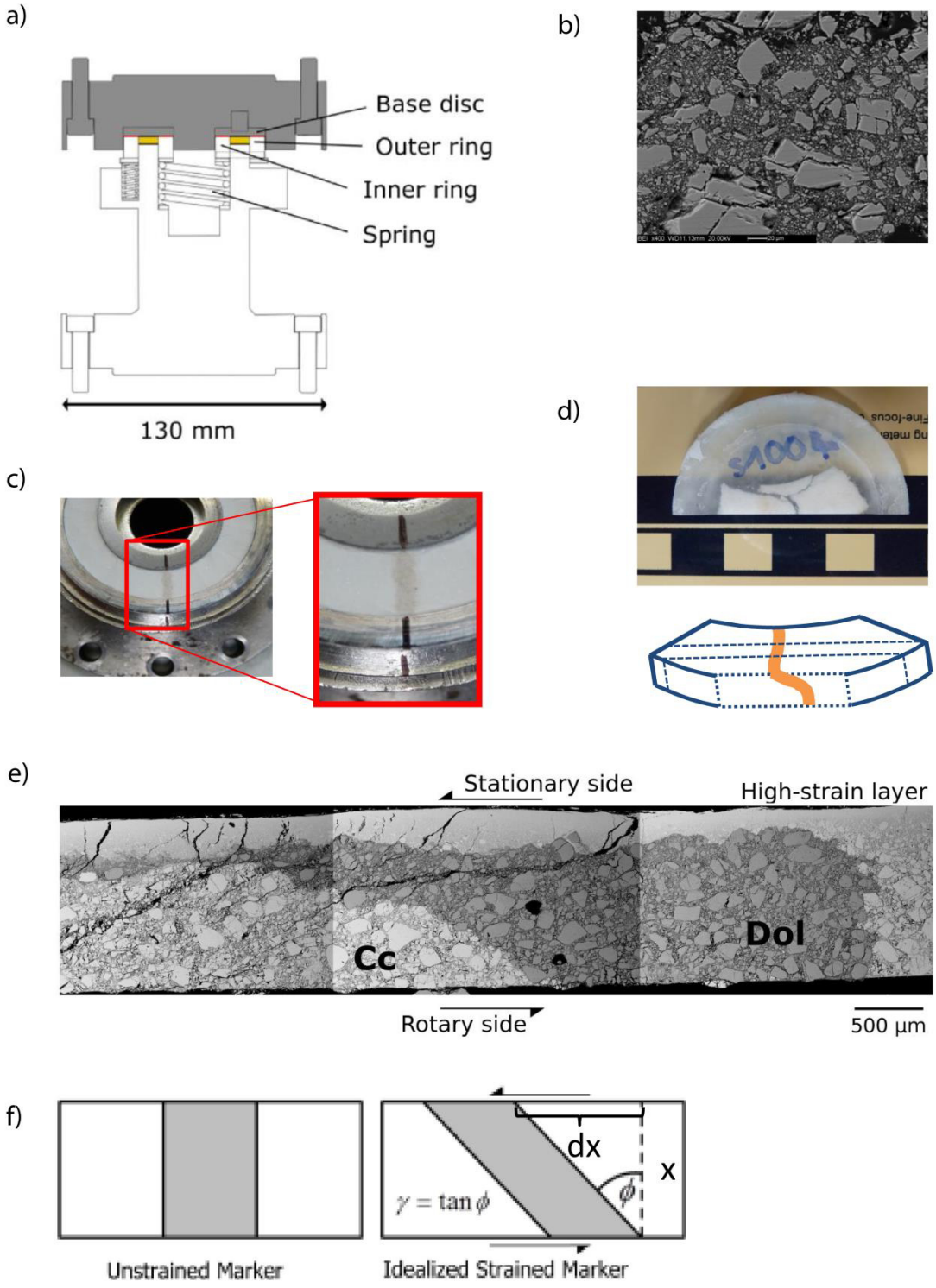

Figure 2. See next page for caption.

Figure 2 (previous page). Gouge sample set-up used with SHIVA. a) All-steel annular gouge holder, modified from Smith et al., 2013. Yellow areas show position of gouge layer contained by inner and outer metal sliding rings. White and grey parts slide move against each other during the experiments (both parts can be used as the rotary or stationary part), red lines demonstrate where metal parts are in sliding contact. **b)** Backscattered Electron image of the starting material: calcite gouge derived from Carrara marble with particle sizes <250 µm. **c)** Gouge holder (white part in a)) filled with light-colored calcite gouge and with a darker-colored dolomite marker. Inset shows magnification of the marker constructed perpendicular to the layer boundaries and the imposed shear direction. **d)** Epoxied calcite gouge sample (s1004), cut perpendicular to the strain marker as shown in the sketch, where the orange line schematically depicts the trace of the sheared marker. **e)** Sample s886 sheared at 3 MPa normal stress, equivalent slip velocity of 1 m/s, 2.5 m of total equivalent displacement and room-dry conditions (mosaic of backscattered electron images). The dolomite marker is distinguished by its darker grey color. The geometry of the dolomite marker broadly defines low-, intermediate- and high-strain domains. **f)** Sketches (modified after Scruggs and Tullis, 1998) show section through sample with unstrained and idealized strained marker assuming homogeneous strain distribution. The strain experienced by the marker can be calculated from its angle of distortion Φ.

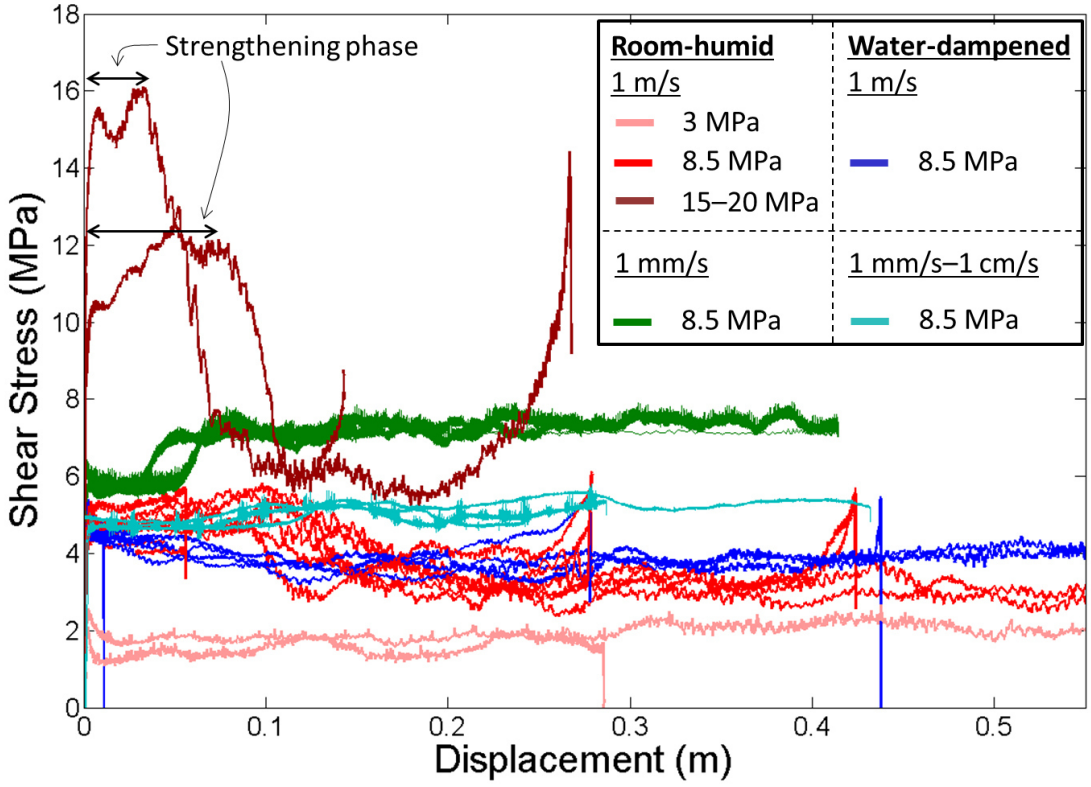

Figure 3. Shear stress evolution with displacement for room-dry and water-dampened strain-marker experiments. The shear-stress data are well-reproducible in experiments conducted at the sample normal stress, slip velocity and ambient conditions. Reddish curves correspond to room-dry experiments performed at 1 m/s, with lighter red colors for lower normal stress: dark red, 15–20 MPa normal stress; bright red, 8.5 MPa; light pink, 3 MPa. Green curves are for room-dry experiments at 1 mm/s and 8.5 MPa. Water-dampened experiments are plotted in blue (1 m/s, 8.5 MPa) and turquoise (1 mm/s and 1 cm/s at 8.5 MPa).

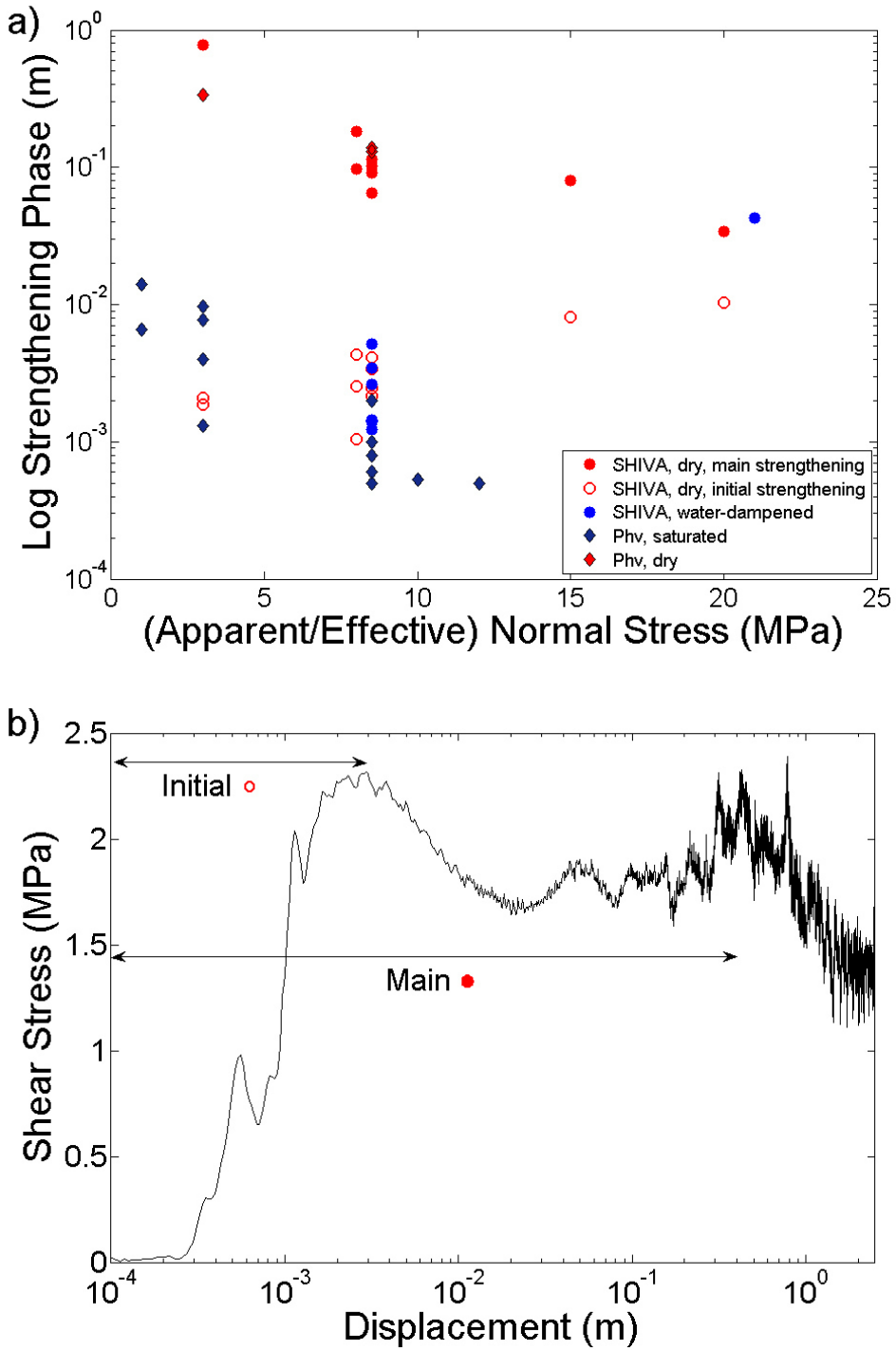

Figure 4. Strengthening phase in room-dry, water-dampened and water-saturated gouges. **a)** Length of the strengthening phase (i.e. the slip distance to the onset of dynamic weakening) on a logarithmic scale vs. the effective normal stress for experiments performed at a slip velocity of 1 m/s. **b)** Initial and main strengthening illustrated for sample s886 (3 MPa, room-dry, 1 m/s).

3. Results

3.1.Mechanical behavior

The evolution of shear stress τ with displacement is reproducible for experiments conducted under the same experimental conditions (i.e., the same, target slip velocity, acceleration, normal stress, and ambient conditions; Fig. 3). At high slip velocity of 1 m/s, peak stress ranges from c. 2.5 to c. 16 MPa at normal stresses σ_n ranging from 3 to 20 MPa (corresponding to an apparent friction coefficient $\mu = \tau/\sigma_n$ of c. 0.6–0.7, respectively), with higher values reached at higher normal stresses. (The normal-stress dependence of the shear stress is commonly expressed by reporting the coefficient of friction $\mu = \frac{\tau}{\sigma'}$, but this is not adequate when the pore pressure and thus the effective normal stress is not known as it is the case in our water-dampened experiments. Thus we chose to report the shear stress instead of an apparent coefficient of friction. A plot of the evolution of the apparent coefficient of friction for selected experiments can be found in the Appendix B, Fig. B1a.) Peak stress is reached after a strengthening phase (i.e. the slip distance prior to the onset of dynamic weakening) that is annotated schematically in Figure 3–5.

The length of the strengthening phase is significantly different for room-dry and water-dampened gouges. The length of the strengthening phase and its dependence on the applied normal stress is shown in Fig. 4. Here, the data from room-dry calcite gouge experiments are plotted in red, blue symbols show the data from the water-dampened experiments. In addition to data from experiments performed with SHIVA (plotted as circles), Fig. 4 shows the data from experiments on calcite gouges performed with the *Phv* rotary-shear apparatus installed at the Kochi Institute for Core Sample Research in Kochi, Japan (plotted as diamond symbols; the results from those experiments are discussed in detail in Chapter III of this thesis). These *Phv*-experiments were performed with controlled fluid pressure, not with water-dampened gouge, and thus the effective normal stress is known contrary to the experiments with SHIVA. The gouge thickness was c. 3 mm both in experiments performed with both machines. The acceleration to the target velocity of c. 1 m/s was greater with SHIVA (6 m/s^2) than with the *Phv*-apparatus (0.5 m/s^2). The results from Fig. 4 are summarized as follows:

- For a given apparent (experiments with SHIVA) or effective (*Phv*-apparatus) normal stress, the length of the strengthening phase in room-dry gouges is up to two orders of magnitude longer than in wet gouges. However, one experiment performed with SHIVA at 21 MPa show an unusually long strengthening phase inconsistent with the data from the other water-dampened and water-saturated experiments.
- The strengthening phase in both room-dry and wet calcite gouges generally decreases with increasing normal stress. For effective normal stresses of 3–21 MPa, the length of the strengthening phase ranges from 3.5–75 cm of displacement in the room-dry gouges and from 1–40 mm of displacement in the water-dampened and water-saturated gouges.
- The strengthening phase in experiments performed under fluid-pressure controlled conditions (*Phv*-apparatus) appears to be slightly shorter than in water-dampened conditions (SHIVA apparatus).

Following peak shear stress, the gouges sheared at 1 m/s weaken to a steady-state shear stress τ_{ss} (Fig. 3). The amount of weakening scales with the normal stress, such that the τ_{ss} is c. 77% of the peak stress in the room-dry experiment performed at 3 MPa, c. 58% at 8.5 MPa, but only c. 35% at 20 MPa. τ_{ss} in water-dampened conditions is 75% of the peak shear stress and thus higher than in the room-dry experiments at the same normal stress of 8.5 MPa (Fig. 3).

During the first millimeters of slip in the experiments performed with SHIVA at target slip rates of 1 m/s, the evolution of the shear stress is very similar in the room-dry and water-dampened gouge experiments (Fig. 5a): in both cases the gouge strengthens during a phase of c. 1–10 mm of displacement. However, while the water-dampened gouges gradually weakens, the room-dry gouges weaken only very slightly before they continue to strengthen during a main strengthening phase of several cm to tens of cm as described above. This initial strengthening phase in the room-dry gouges is plotted vs. the normal stress in Fig. 4 as open red circles (see Fig. 4b for an annotation of initial and main strengthening phases). To the contrary of the effective strengthening phase in the room-dry gouges or the strengthening

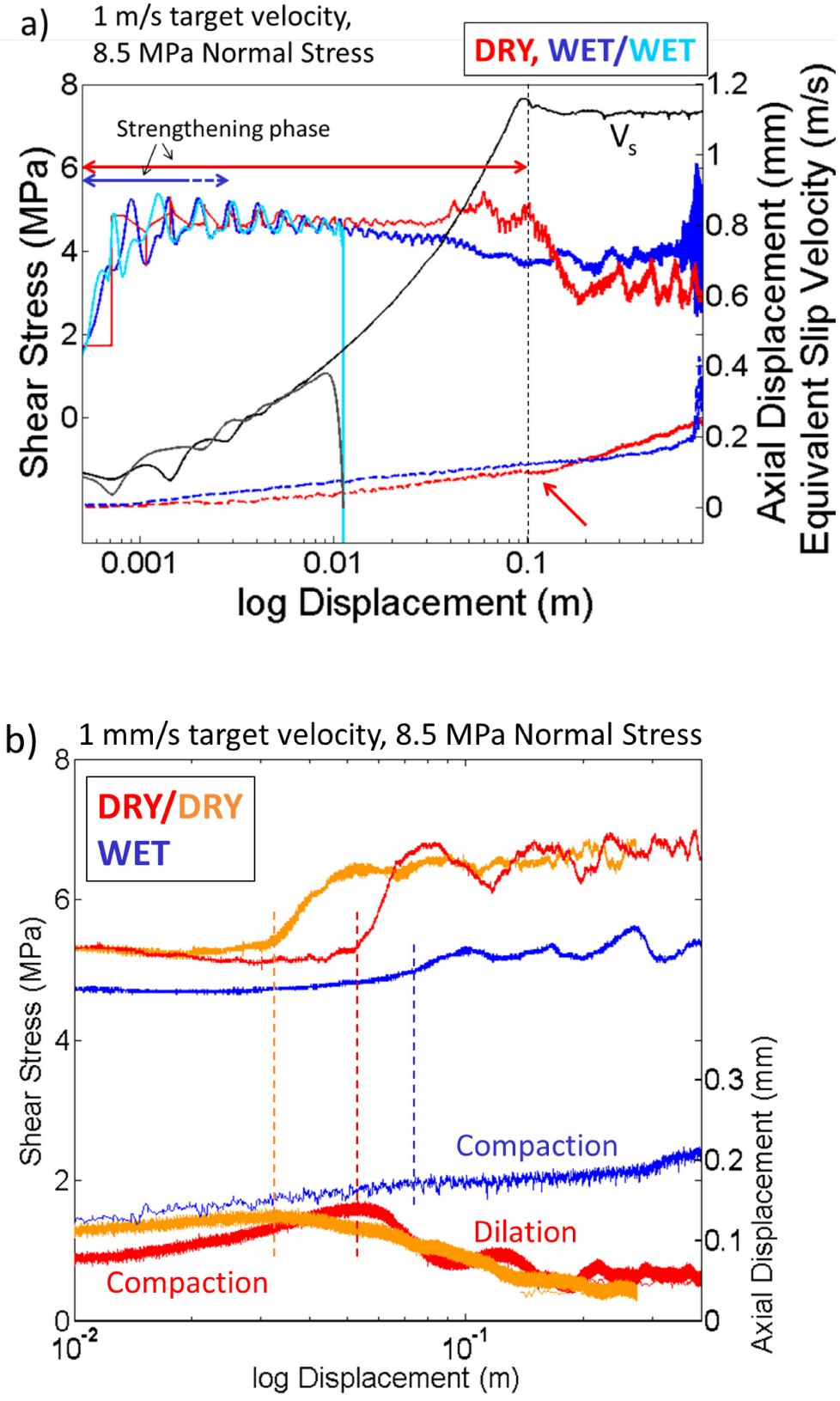

Figure 5. See next page for caption.

Figure 5 (previous page). Evolution of shear stress and axial displacement in comparison for room-dry and water-saturated gouges. a) Exemplary data from high-velocity experiments (1 m/s) for a room-dry (s896, red curves) and two water-dampened (s962, s959, blue and cyan curves, respectively) experiments, all performed at 8.5 MPa normal stress and with the same acceleration and target velocity (black and grey curves, secondary y-axis). In experiment s959, the target velocity was not reached ($v_{s,max}$=0.38 m/s). The shear stress (primary y-axis) evolution in the first 10^{-2} m of displacement is very similar in the room-dry and water-dampened conditions. After the strengthening phase, the room-dry gouges weaken more abruptly and to lower shear stress values than the water-dampened experiments. The axial displacement for s896 and s962 is plotted on the secondary y-axis, a positive axial displacement denotes compaction. At the initiation of sliding, the water-dampened gouge compacts at a slightly faster rate than the room-dry gouge. The net compaction is similar in both room-dry and water-dampened experiments, as the room-dry gouge compacts faster after the onset of dynamic weakening. In the room-dry experiment, a small amount of transient dilation (red arrow, c. 10 µm) can typically be observed at a displacement of c. 9 cm (dashed vertical line), coinciding with the onset of dynamic weakening. **b)** Shear stress (primary y-axis) and axial displacement (secondary y-axis) from low-velocity experiments (1 mm/s) for two room-dry (s882, red curves; s874, orange curves) and a water-dampened (s1007, blue curves) experiment, all performed at 8.5 MPa normal stress and with the same acceleration and target velocity. Note that in the room-dry gouges (red and orange curves) the compaction denoted by a positive axial displacement is followed by dilation (negative axial displacement) that occurs simultaneously with an increase in shear stress (orange and red dashed vertical lines). No dilation is observed in the water-dampened experiment (blue curves), but the onset of strengthening (blue dashed line) is accompanied by a decrease in the compaction rate.

phase in the water-dampened and saturated gouges, however, this initial strengthening phase slightly increases in length with increasing normal stress. A similar initial strengthening phase was observed by Steven Smith in high-velocity experiments on room-dry calcite gouge using SHIVA (S. Smith, personal communication, 2015) and in the room-dry calcite gouge experiments with the Phv-apparatus (see also Chapter III, Fig. 5b of this thesis).

In the room-dry and water-dampened experiments performed at low velocity (< 1 cm/s; Fig. 3), no weakening occurs and thus no clear strengthening phase can be determined. Instead, both room-dry (green curves) and water-dampened (turquoise curves) gouges exhibit a slip-strengthening behavior initiating at displacements >8 cm. The shear stress at low velocity is higher compared to equivalent experiments at higher velocity. At displacements larger than c. 18 cm, the shear stress has reached a steady state (Fig. 3). In the experiments performed at 8.5 MPa normal stress and with a low slip velocity (< 1 cm/s), where no dynamic weakening occurs (Fig. 3, green and turquoise curves), the steady-state shear stress is generally higher in room-dry than in water-dampened gouges. To the contrary, at high velocities (1 m/s), the shear stress in the room-dry gouges is slightly lower than in the water-dampened gouges.

The axial displacement of the gouge layer depends on the ambient conditions and the slip velocity (Fig. 5). At the initiation of sliding at a velocity of 1 m/s (Fig. 5a), the water-dampened gouge compacts at a slightly faster rate than the room-dry gouge. In the room-dry gouges, a small amount of dilation (c. 10 µm) can be observed that roughly coincides with the onset of dynamic weakening. Following this transient dilation, the room-dry gouge compacts at a faster rate than the water-dampened experiments, yielding a similar net compaction in both room-dry and water-dampened experiments (c. 250 µm after a displacement of 80 cm; corresponding to <10% of the starting layer thickness). (The apparent large increase in compaction at the end of the water-dampened experiment is in fact an oscillation likely caused by a misalignment of the axial column; the oscillation can also be observed in the shear stress.)

In experiments conducted at 1 mm/s, the room-dry gouge initially compacts by about 150 µm, before it starts to dilate (Fig. 5b). The onset of dilation is accompanied by the relatively abrupt slip-strengthening. After c. 9–11 cm of displacement, there is no further

significant amount of axial displacement. The water-dampened gouges do not exhibit dilation; however, the compaction is interrupted by a short phase where no axial displacement takes place (Fig. 5b).

3.2.Microstructures

3.2.1. Textural zones

In the calcite gouge experiments with dolomite strain markers, a wide range of slip velocities (10^{-3}–1 m/s), apparent normal stresses (3–21 MPa) and total displacements (0.011–2.5 m) was applied. Additionally, different ambient conditions, i.e. room-dry and with the presence of pore fluids, were simulated. This causes differences in the textures of the post-experimental samples, e.g. in the degree of comminution of the material and the localization of strain as investigated with the use of the strain markers. Despite the different experimental conditions, some microstructural features are common to all samples. The microstructures are made up of up to three more or less distinct textural zones (I to III) that are characterized by differences in the grain size and porosity (Fig. 6):

- In Zone I, the gouge material resembles the starting material (Fig. 6a, b; compare Fig. 2b). The particles are angular to sub-angular, often showing fractures along cleavage planes. The particle size is relatively unaltered and the porosity in this zone is relatively high. Zone I has a thickness of c. 1–1.4 mm (Fig. 7a, Table 2), c. 30-50% of the starting gouge-layer thickness. In some cases Zone I is thinner (e.g. s953 and s895) which is likely due to some incohesive material being lost during sample recovery.
- In Zone II (Fig. 6a, c), larger particles which are still relatively angular and range from several tens of µm up to c. 200 µm in size are embedded in a fine-grained matrix with particle sizes on the order of a few tens of µm or less. The thickness of this zone ranges from 140–800 µm in room-dry samples (Fig. 7a). In water-dampened conditions, it has a thickness of up to 230 µm (Fig 7b); however, Zone II did not develop in all water-dampened experiments (e.g., s895, Appendix B2).
- Zone III forms towards one side of the sample holder, more specifically towards its "lid" (grey-colored part in Fig. 2a), as a thin layer (c. 125–600 µm; Fig. 7c) of highly-

comminuted and -compacted gouge (Fig. 6a, c). Generally, larger particles in this layer are c. 10 µm in size, while the matrix particle size may be <1 µm. This Zone III is generally cut by one or more sharp slip surfaces sub-parallel to the gouge layer boundary (Y-shears; terminology after Logan et al., 1979).

The extent and thickness of the different zones depends on the experimental conditions. In experiment s959 that had a very short total equivalent displacement of only 1.1 cm, the starting material remained almost un-comminuted (Fig. 6d). At larger displacements (≥ 43 cm), the material in Zone I is further comminuted and compacted, thus leading to an increase in the thickness of Zone II (denoted by black arrow in Fig. 7a) (Note that likely some of the incohesive Zone I-material was lost in experiment s959 leading to small Zone I- and bulk layer thicknesses). Some Zone II-material may develop towards the "bottom" of the sample holder (in touch with the base plate, white parts in Fig. 2a). The transition from Zone I to Zone II is relatively gradual while the boundary between Zone II and Zone III is sharper. Both Zone II and Zone III taper towards the vertical boundaries of the gouge layer, where the gouge is confined by the steel rings (Fig. 2a).

The thickness of Zone I is similar (1–1.4 mm) in both room-dry and water-dampened samples in experiments performed at 1 m/s and 8.5 MPa normal stress, (Fig. 7a, b; red symbols). Zone II is slightly thicker on average in room-dry conditions (c. 500 µm) than in water-dampened conditions (c. 300 µm) (Fig. 7a, b; magenta and black symbols, respectively). In room-dry experiments, the thickness of Zone III ranges between c. 100 and 600 µm (Fig. 7a, c), but the thickness is >400 µm only in experiments performed at high normal stress (>8.5 MPa) or at low velocity (1 mm/s) (Fig. 7c). At comparable conditions (8.5 MPa, 1 m/s), the thickness of Zone III ranges from 125–390 µm in room-dry conditions and from 205–330 µm in water-dampened conditions, and is thus not significantly different in different ambient conditions.

In the up to 600 µm-thick Zone III of the low-velocity (1 mm/s), room-dry experiments, shear strain seems to have been distributed over a wider zone than in the high-velocity experiments, the grain size is very small (≤ 1 µm), and several bands of shear are often

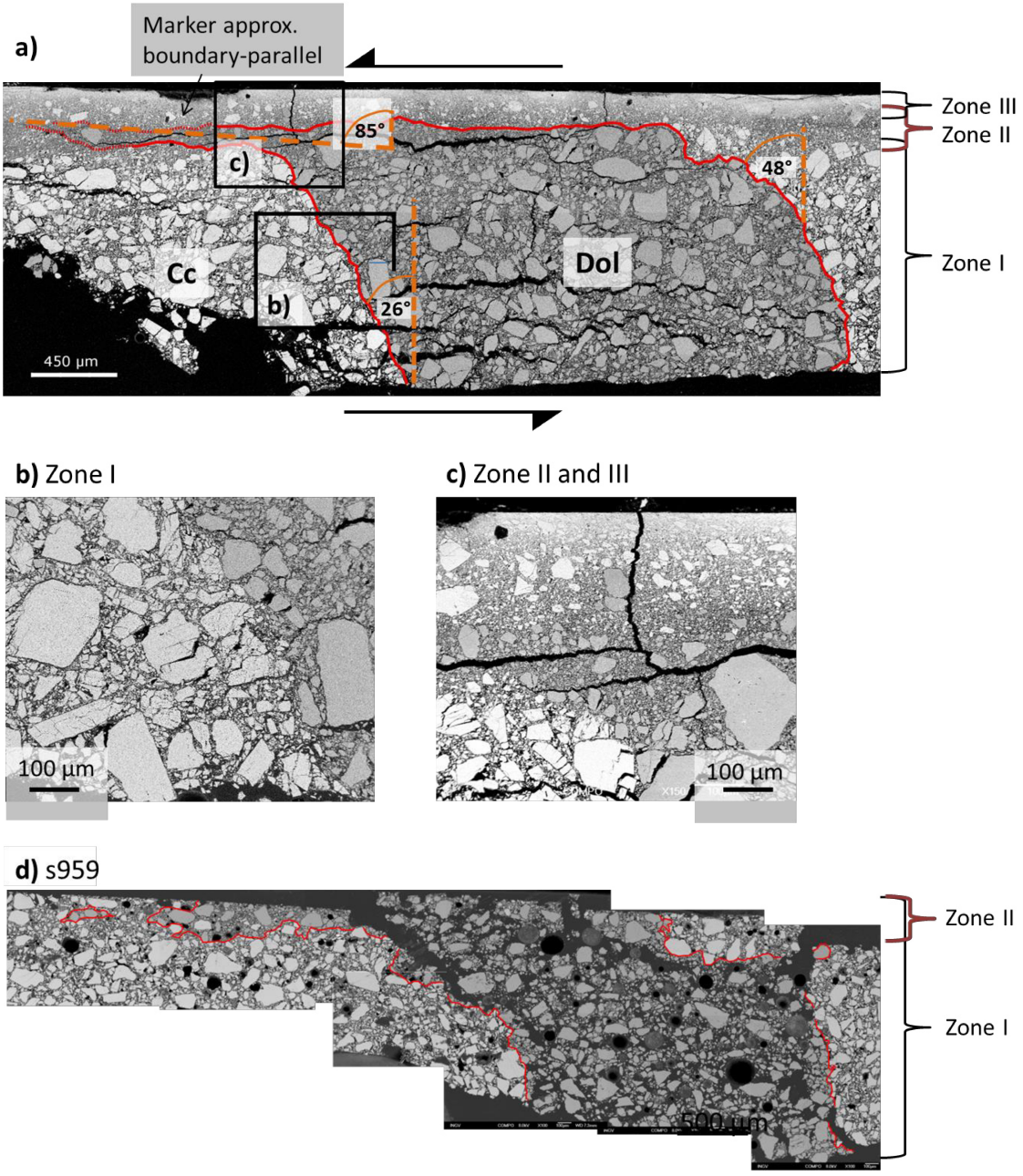

Figure 6. See next page for caption.

Figure 6 (previous page). Distribution of textural zones and strain in the gouge layer. a) Calcite (Cc) sample s943 with dolomite (Dol) strain marker (room-dry, 1 m/s, 8.5 MPa, 1.3 m total displacement). Textural zones are marked on the right of the sample picture. In Zone I, the marker boundary is sheared only slightly. Towards Zone II, the marker is progressively sheared, , with an angle of distortion of up to c. 48°, yielding a strain of <1.3. In Zone II, the marker is almost parallel to the boundary and the direction of slip, yielding a strain of c. 12. The marker cannot be traced in Zone III. **b)** Zoom of Zone I marked in a) consisting of relatively uncomminuted, angular particles. **c)** Zoom of Zone II and III marked in a). Particles are progressively comminuted with decreasing distance from the discrete principal slip surface that may be lined by recrystallized grains or a zone of decarbonation. **d)** Sample from experiment s959, stopped after an equivalent displacement of 1.1 cm (experimental conditions: 1 m/s target velocity, 8.5 MPa normal stress, water-dampened). Almost no comminution has taken place and no Zone III has developed.

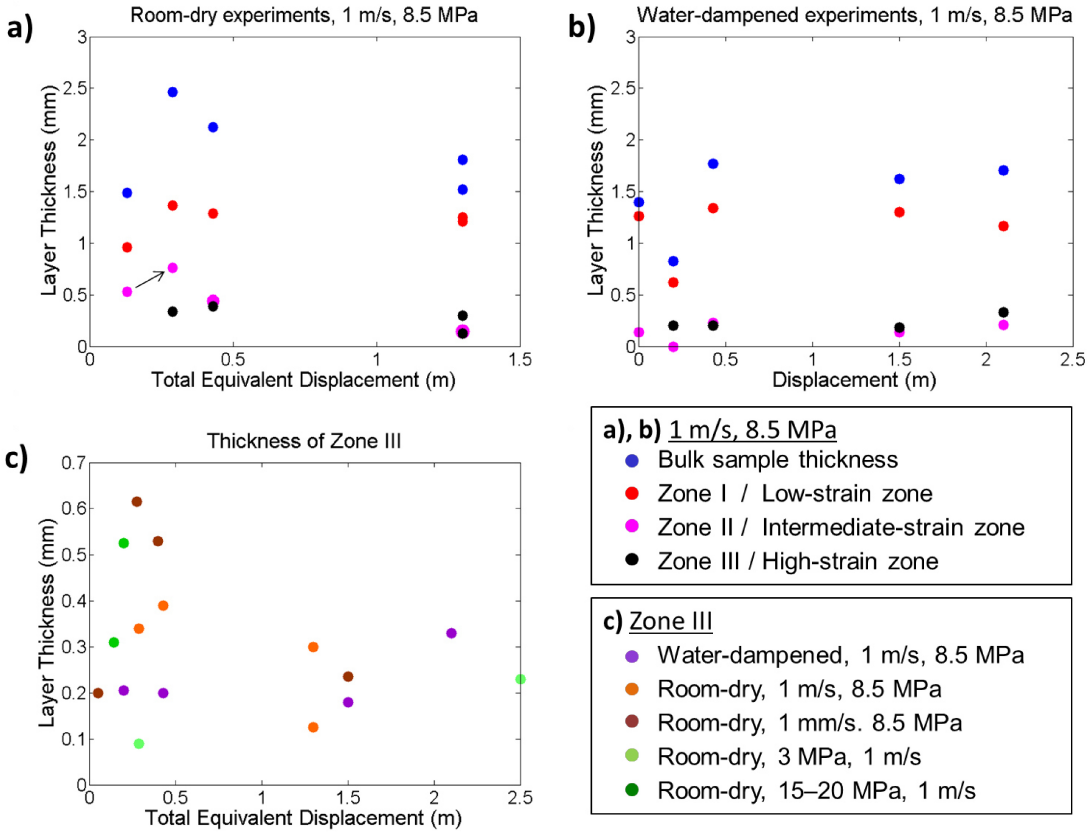

Figure 7. Thickness of textural layers. Thickness in a) room-dry samples and b) water-dampened samples from experiments performed at a slip velocity of 1 m/s and a normal stress of 8.5 MPa. Blue symbols, bulk sample thickness; red symbols, textural Zone I or low-strain zone; magenta symbols, textural Zone II or intermediate-strain zone; black symbols, textural Zone III or high-strain zone. Black arrow in Fig. 7a illustrates thickening of Zone II with increasing displacement. (Note that small bulk- and Zone I-thickness at low displacement is likely due to loss of incohesive material, while it is unlikely that compacted material from Zone II was lost during sample preservation.)

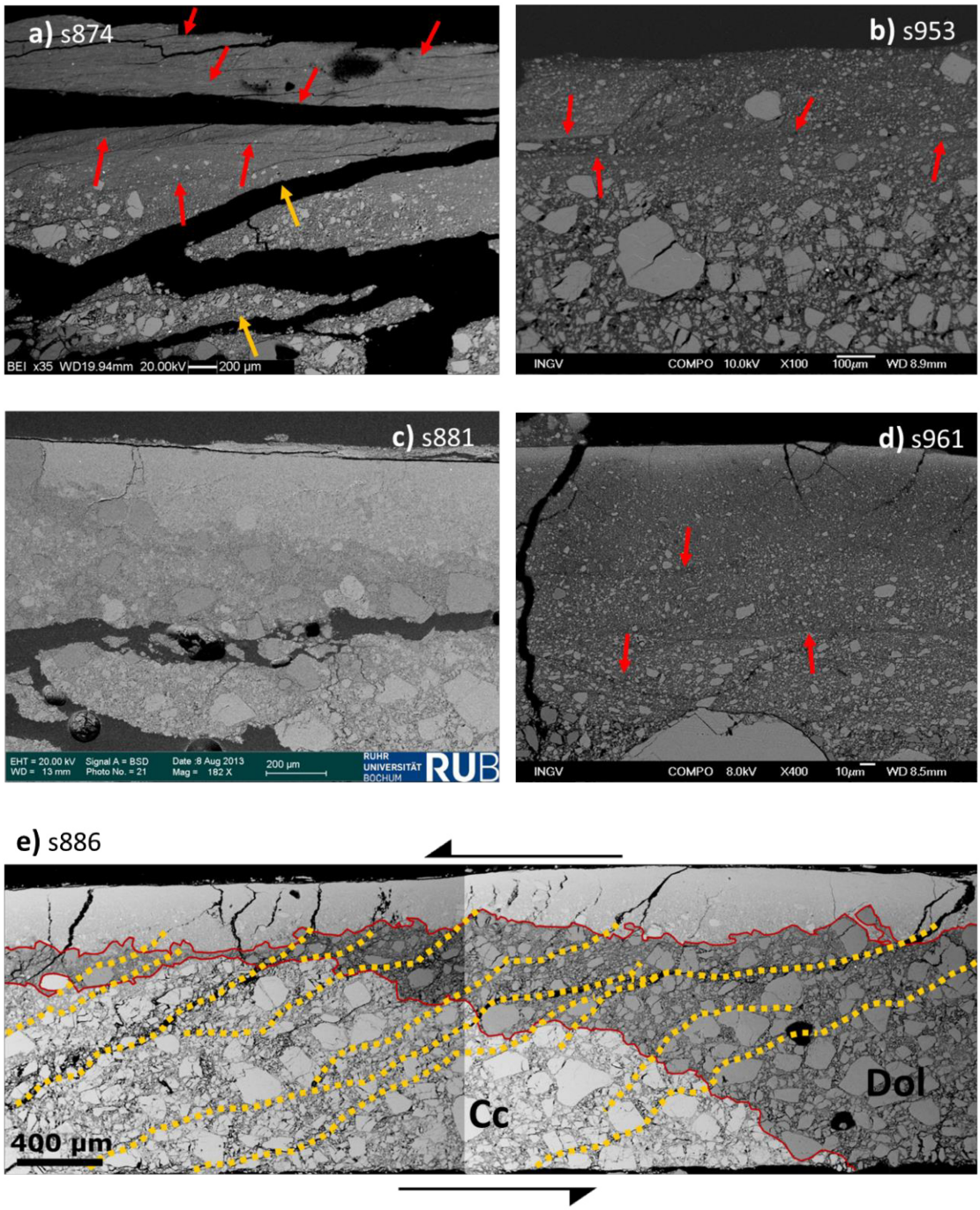

Figure 8. Progressive development of textural zones. SEM backscattered images from **a)** sample s874 (1 mm/s, 27.5 cm total equivalent displacement, 8.5 MPa, room-dry conditions), **b)** s953 (1 m/s, 13 cm displacement, 8.5 MPa, room-dry conditions), **c)** s881 (1 m/s, 43 cm displacement, 8.5 MPa, room-dry conditions), and **d)** s961 (water-dampened, 1 m/s, 43 cm displacement, 8.5 MPa). Room-dry samples show progressive deformation with increasing displacements (b-c). Red arrows point at shear bands and secondary, abandoned slip surfaces. Yellow arrows show open Riedel fractures cutting through bulk of sample.

352

developed (red arrows in Fig. 8a), that mostly resemble R1-shears (terminology after Logan et al., 1979) and along which fractures and hair fissures have opened that extend through the less-deformed material (yellow arrows). In the room-dry experiments performed at a higher target slip velocity of 1 m/s, the high-strain layer evolves from a broad zone of comminuted material (grain sizes of up to 50 μm) that is only slightly compacted and contains several poorly-developed shear bands (e.g., red arrows in Fig. 8b, 13 cm of total equivalent displacement) to a zone of highly-comminuted (particle size < 20 μm) and -compacted gouge cut by a discrete principal slip surface (Fig. 8c, 43 cm displacement). Progressive deformation is also evident in the water-dampened experiments: after 43 cm of total equivalent displacement, similar to the room-dry sample (Fig. 8c), a discrete principal slip surface has developed adjacent to which the material is heavily comminuted and compacted (Fig. 8d) and cut by several secondary shear bands (red arrows in Fig. 8d), while no Zone III material had yet developed (or was preserved) in experiment s959, that was stopped after 1.1 cm of slip (Fig. 6d). In the high-velocity experiments, systems of shear fractures, namely P- and R1-shears, that may have opened during sample unloading, are also commonly observed. R1-shears, which have the same sense of shear as the imposed bulk shear sense, are the most common (Fig. 8e). They dip with angles of 15–20° in the textural Zones I and II, but tend to be more vertical in textural Zone III, where they are thus thought to form during sample unloading. The R1-shears accommodate some strain as is evidenced by an offset of the dolomite marker margin by 10–180 μm (Fig. 8e).

In some room-dry experiments performed at high velocity (1 m/s) and with a large total displacement (≥0.43 m), particles are sintered in a zone c. 50 μm in thickness adjacent to the principal slip surface (Fig. 9a, b). In water-dampened conditions and at displacements ≥1.3 m, zones of decarbonation may be present (Fig. 9c-e), shown by the lighter colors in backscattered electron images (Fig. 9c) and higher Ca content as determined by EDS analysis (Fig. 9d) suggesting the presence of CaO (lime) in a 70–200 μm thick layer adjacent to the principal slip surface. On the other hand, in some cases (e.g. Fig. 9e) the bright-colored zones also consist of recrystallized grains and their low porosity might be another possible explanation of the bright coloring. Recrystallized grains are another common feature in high-

velocity, high-displacement experiments independently of the ambient conditions. Zones of recrystallized grains 10–40 μm thick, adjacent to the principal slip surface (Fig. 9f-h). The recrystallized grains are c. 500 nm in size, and have a shape preferred orientation with the long axis sub-parallel to the principal slip surface consistent with the imposed sense of shear (sinistral in both Fig. 9f and g), resembling mylonitic shear zones (e.g., Snoke et al., 1998). In a zone a few micrometers away from the principal slip surface, the recrystallized grains are slightly bigger in size (c. 1 μm) and show a less clear shape-preferred orientation (area in red box in Fig. 9h). In both water-dampened and room-dry conditions, zones of recrystallization were found in experiments that experienced ≥ 43 cm of slip (Fig. 9f, g). At low velocity (1 mm/s) no recrystallization or decarbonation was observed (Fig. 8a).

3.2.2. Strain markers

3.2.2.1. General characteristics

Out of 23 strain-marker experiments, 19 samples containing a more or less intact strain marker were studied. The dark grey dolomite strain markers are easily distinguished from the lighter grey calcite "matrix" in backscattered electron images (Fig. 6a, 6e). Despite several differences in the appearance of the marker, there are also several common characteristics independent of the experimental conditions (with the exception of s959 where a very small finite strain was imposed, Fig. 6d):

- Within textural Zone I, the boundaries of the marker are sheared slightly in the direction of slip, but are still relatively straight and can easily be traced (Fig. 6a, 6e). The angle of distortion (i.e., the angle between the original and the sheared marker, Fig. 2f) ranges from c. 0°–60°, resulting in relatively low strains, γ, of 0–2. This zone is thus termed the low-strain zone.
- In the textural Zone II or the intermediate-strain zone, further towards the principal slip surface, the marker is sheared towards parallelism with the gouge layer boundaries (Fig. 6a). Like the textural transition from Zone I to Zone II that is gradual, there is not necessarily a sharp change in the distortion angle of the marker boundary. The angle of distortion can be up to 90° which yields maximum strains of c. γ=57. The

dolomite marker material still forms a through-going layer that, however, tapers off at larger distances from the original marker position (red dotted line in Fig. 6a), where single dolomite particles can be found dispersed in the calcite matrix.

- In the high-strain textural Zone III, the marker cannot be traced anymore (Fig. 6a), only single dolomite grains may be found embedded in the highly-comminuted matrix (Fig. 6c). The finite strain in this zone can thus be calculated from the finite strain measured in Zones I and

II subtracted from the bulk strain (the ratio of the total displacement and the thickness of the gouge layer).

3.2.2.2. Effect of the experimental conditions

Quantitative results of the strain distribution in the gouge layer are difficult to obtain for three main reasons: Firstly, because the strain is not evenly distributed within the same textural zone; secondly, because the margins of the marker (i.e. the left and the right marker boundaries) are sheared to a different degree (Fig. 10a) in most samples; and thirdly because of the different shape/geometry of the strain marker in different samples. For instance, in a few samples the marker is sheared towards parallelism with the gouge layer boundary close to the "bottom" of the sample, opposite from the PSS where the strain usually localizes (Fig. 10b). This could either be due to a second zone of localization or the formation of a Riedel or boundary shear that offsets the marker. Finally, the sample is highly fractured in many cases (especially in low-velocity and in high-normal stress experiments (e.g., s 874, s882; Appendix B2). The following rules were thus applied to achieve comparable results: The strain was estimated separately for Zone I and Zone II. In cases where it was impossible to define a single angle of distortion for both sides of the marker, an average angle was determined. The results of the strain estimation can be found in summary in Table 2 and more detailed in Table A1. The SEM images of each sample are collected in the Appendix B2, together with sketches showing how the strain was estimated in each case.

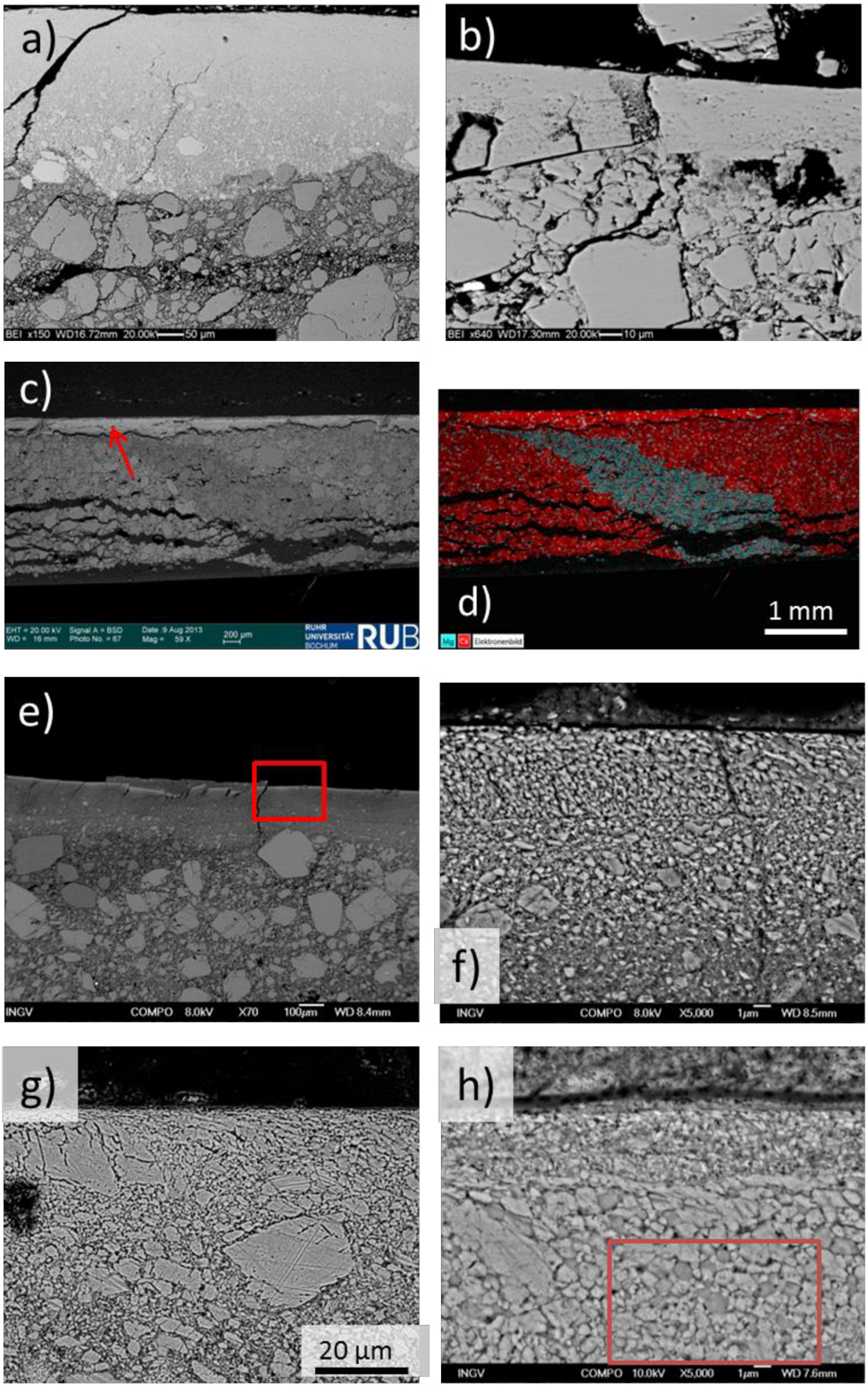

Figure 9. See next page for caption.

Figure 9 (previous page). Microstructural features in high-velocity, high-displacement experiments. a) Sintered grains in c. 50 µm wide zone in the calcite gouge adjacent to the principal slip surface in sample from experiment s886 performed at 3 MPa normal stress, an equivalent slip rate of 1 m/s, with a total displacement of 2.5 m, and in room-dry conditions. In the lower region of the image, the dark-colored dolomite strain marker can be seen. **b)** Zoom of sintered zone in a). **c-e)** Evidence of decarbonation in the high-strain layer (red arrow in c)) as suggested by the light color in backscattered electron image (c) or high relative abundance of Ca as determined by EDS analysis (d). Images shown are from sample s898 (8.5 MPa, 1 m/s, 1.5 m total displacement, water-dampened conditions). e) Zone of decarbonation and/or recrystallization in sample s961 (see f) for zoom of possibly decarbonated recrystallized grains in the area of the slipping zone marked in e). **f-h)** Zones of likely dynamically (f, g) and possibly in parts statically (h) recrystallized grains in water-dampened (f, h) and room-dry (g) experiments. Recrystallized grains are orientated in the orientation of shear (sinistral). Note in f) the secondary shear surface a few microns from and parallel to the principal slip surface cutting through the recrystallized zone, supporting the conclusion that grains were recrystallized dynamically. Images are from samples f) s961 (water-dampened, 8.5 MPa, 1 m/s, 0.43 m displacement), g) s943 (room-dry, 8.5 MPa, 1 m/s, 1.3 m displacement) and h) s962 (water-dampened, 8.5 MPa, 1 m/s, 2.1 m displacement).

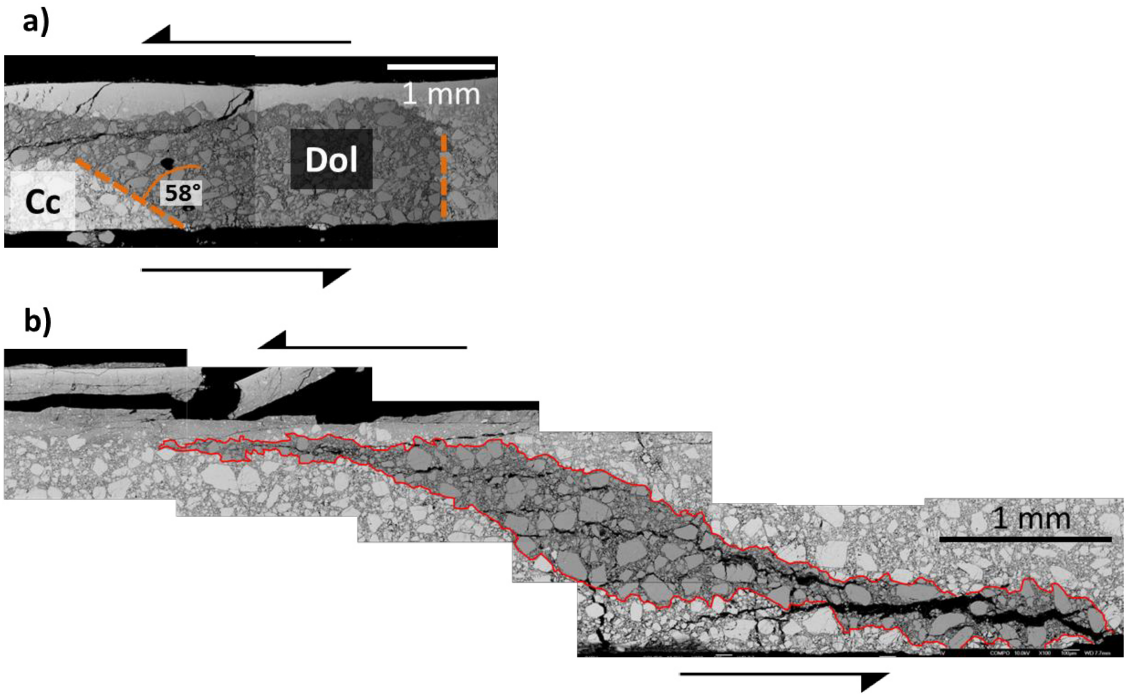

Figure 10. Strain-marker characteristics. a) The two margins of the strain marker are not sheared to the same degree. Example from experiment s886 (room-dry, 1 m/s, 3 MPa, 2.5 m). **b)** The marker is also sheared towards boundary-parallelism on the side of the gouge layer, where strain does not usually localize in some cases (s962, s874 and s882).

436 For better comparability we first describe the results from experiments performed at
437 the same velocity (1 m/s) and apparent normal stress (8.5 MPa) to evaluate the dependence of
438 the strain distribution in the gouge layers on the total displacement. The geometry of the
439 markers in room-dry and water-dampened samples is relatively similar. The total displacement
440 in the room-dry experiments ranged from 0.13 to 1.3 m. The finite strain in these samples
441 ranges from c. 0.6 to 1.2 in the low-strain zone (Fig. 11a, Table 2a, not considering samples
442 where the relatively low thickness suggests poor sample preservation as not to bias the strain
443 estimate) and from 2.9 to 12.7 in the intermediate-strain zone (Fig. 11b). In the two room-dry
444 samples with the same total displacement (1.3 m, s896 and s943), the values of strain of 1.24
445 and 0.83 in the low-strain zone and of 12.71 and 11.43 in the intermediate-strain zone are
446 similar (standard deviations of 0.2 and 0.6, respectively). In the water-dampened experiments
447 performed under otherwise identical experimental conditions, with total displacements of
448 0.011–2.1 m, the strain ranges from c. 0.3–2.0 in the low-strain zone and from c. 4.3–28.6 in
449 the intermediate-strain zones, yielding similar values to the room-dry samples (Fig. 11a, b;
450 Table 2b). In both room-dry and water-dampened experiments, the strain hosted in the low-
451 strain zone increases slightly at higher displacements (Fig. 11a).

452 In the intermediate-strain zone, no dependence of the amount of strain on the total
453 displacement can be observed (Fig. 11b). However, because the tangent of an angle close to
454 90° is taken (and the tangent approaches infinity as the angle approaches 90°), small variations
455 in the angle have a large effect on the strain, increasing the error in the strain estimations in
456 this zone. The total strain hosted in the low- and intermediate-strain zones (which constitute
457 the bulk of the sample) seems to be slightly higher in the room-dry samples compared to the
458 water-dampened experiments (Fig. 11c), with the exception of one water-dampened
459 experiment (s961) that hosted unusually large strains in the low- and intermediate-strain
460 layers.

461 The strain hosted in the high-strain zone (i.e., the total displacement minus the
462 displacement hosted in the low- and intermediate strain zones divided by the post-
463 experimental thickness of the sample) ranges from c. 81–853 in the room-dry samples, and
464 from 0.01–1232 in the water-dampened samples, and correlates with the total displacement

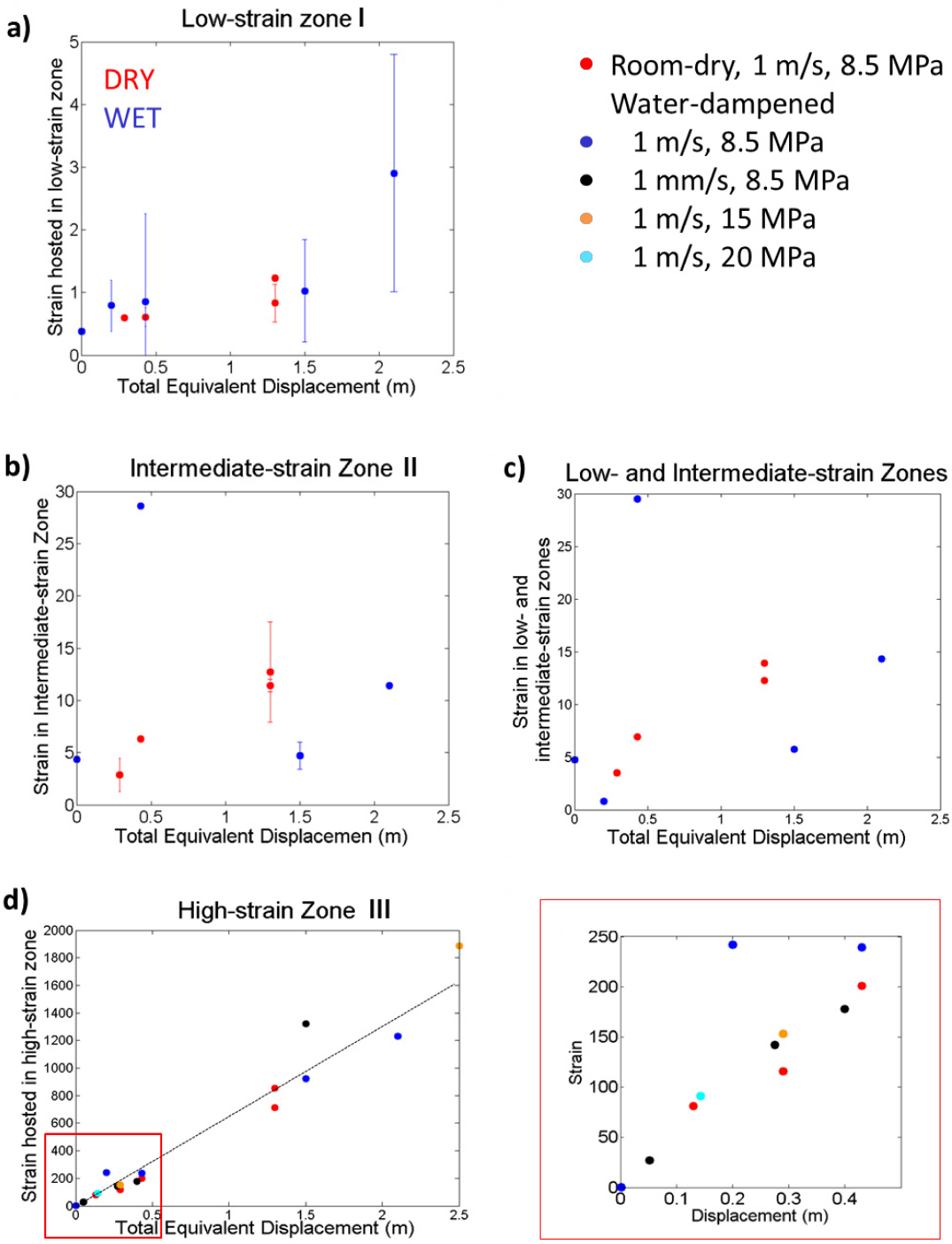

Figure 11. See next page for caption.

Figure 11 (previous page). Strain distribution in the gouge layer. Strain vs. Total Displacement for the **a)** low-, **b)** intermediate-, and **c)** low- and intermediate-strain zones in samples from experiments performed at 8.5 MPa normal stress, a slip rate of 1 m/s and room-dry (red symbols) and water-dampened (blue symbols) conditions, respectively. Samples where the relatively low thickness suggests poor sample preservation were not considered as not to bias the strain estimate. **d)** Strain vs. Total Displacement for the high-strain zone. Red box shows area of zoom to the right. Color-coding as in legend on the far right (red and blue symbols: room-dry water-dampened experiments, respectively, performed at 1 m/s and 8.5 MPa like in a), b), and c); black symbols: room-dry experiments performed at 1 mm/s and 8.5 MPa; orange and cyan symbols: 1 m/s and 15 and 20 MPa, respectively). In the low- and high-strain zones, there is a slight and a significant, respectively, dependence of the strain on the total displacement. No significant dependence is present in the intermediate-strain zone.

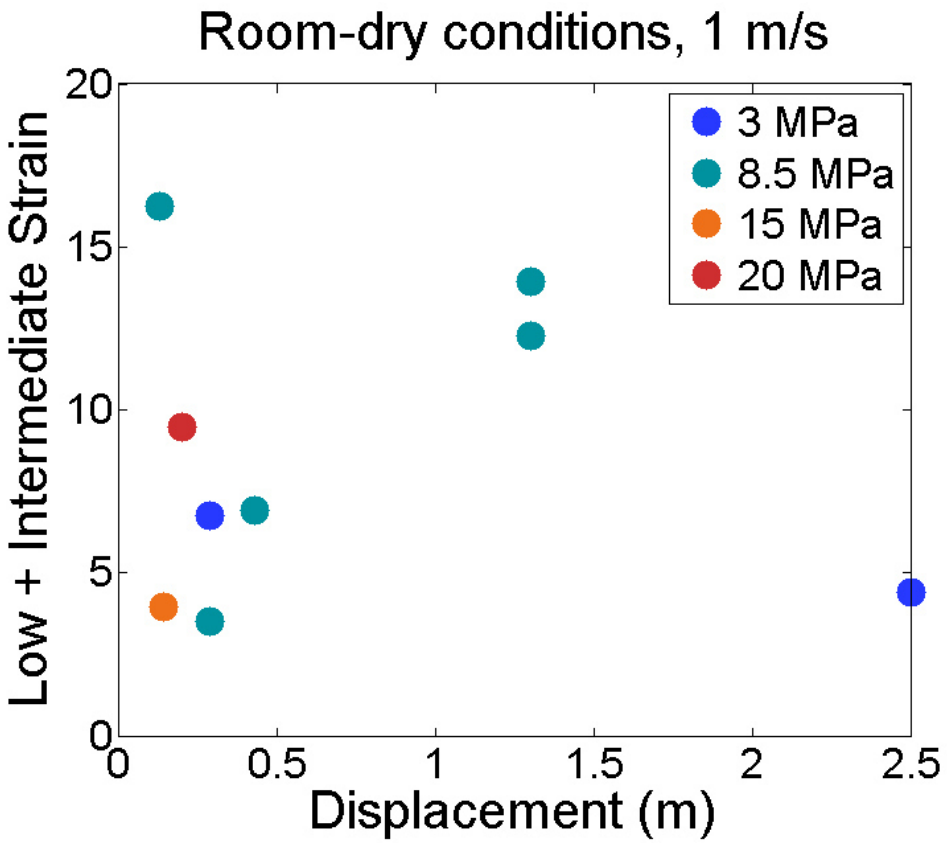

Figure 12. Normal-stress dependence of strain localization. The sum of the strains hosted in the low- and the intermediate-strain zones against the total equivalent displacement for experiments performed at 3 MPa (blue symbols), 8.5 MPa (teal symbols), 15 MPa (orange symbol), and 20 MPa (red symbol) normal stress. For a given displacement, there is no systematic variation of the strain with the normal stress.

(Fig. 11d), increasing approximately linearly with increasing total displacement. At short total displacements (≤0.43 m), the strain hosted in the high-strain zone is larger in the water-dampened than in the room-dry samples.

Experiments at low slip velocities of 1–10 mm/s were performed at a normal stress of 8.5 MPa, with total displacements ranging from 0.052 to 1.5 m, and in room-dry and water-dampened conditions. Samples from the water-dampened experiments are poorly preserved; the intermediate- and high-strain material was typically lost. The room-dry samples are better preserved, and the strain was determined from 4 samples (Table 2c). These samples are highly fractured, however, and thus it is difficult to obtain data on the strain distribution that are comparable with those above. The spread in the strain data for the low- and intermediate-strain zones is very large (Fig. A2), thus, only the values for the high-strain layer are plotted in Fig. 11d. As in the experiments performed at higher velocity, the strain in the high-strain layer increases approximately linearly with increasing total displacement.

Figure 12 shows the strain hosted in the low- and intermediate strain zones of several experiments performed at the same target velocity (1 m/s) and with similar total displacements but at different normal stresses of 3, 8.5, 15 and 20 MPa (Table 2d). There is no systematic variation of the strain depending on the applied normal stress as far as can be deduced from these few data points. The spread in data obtained at the same normal stress and similar (or the same) total displacements is as large as the spread in the data obtained at different normal stresses. Experiments with a higher range of normal stresses might give further insights into the normal-stress dependence of strain distribution and localization.

3.2.2.3. Effect of the rotary-shear sample configuration

To test the dependence of the strain distribution on the radial position within the annular gouge layer, samples from two experiments, s961 and s886, were cut at different distances from the sample edge. The SEM images obtained from these sections are shown in Fig. 13 (s961) and Fig. 14 (s886).

In sample s961 (water-dampened, 8.5 MPa apparent normal stress, 1 m/s slip rate and 43 cm equivalent displacement) the marker position was approximately in the center of each

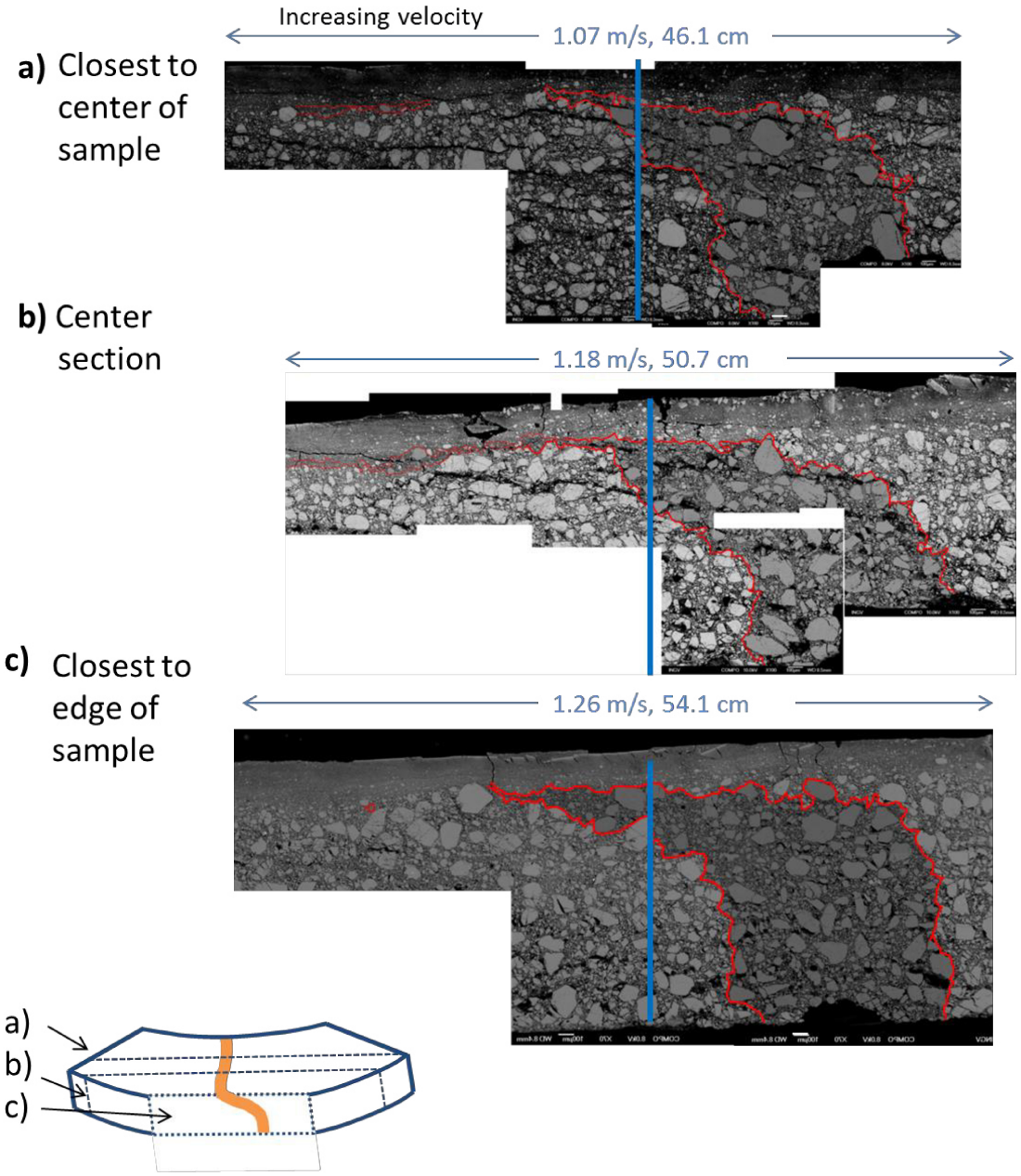

Figure 13. Dependence of the strain distribution on the radial position I. SEM backscattered images of three sections cut as shown in the sketch from the water-dampened sample s961 that had experienced 43 cm of total equivalent displacement, a slip velocity of 1 m/s, and a normal stress of 8.5 MPa. Due to the annular geometry of the sample, the sections from different radial positions [a) closest to the center of the sample, b) further to the outer radius, and c) closest to the edge of the sample] experienced different maximum velocities and displacements.

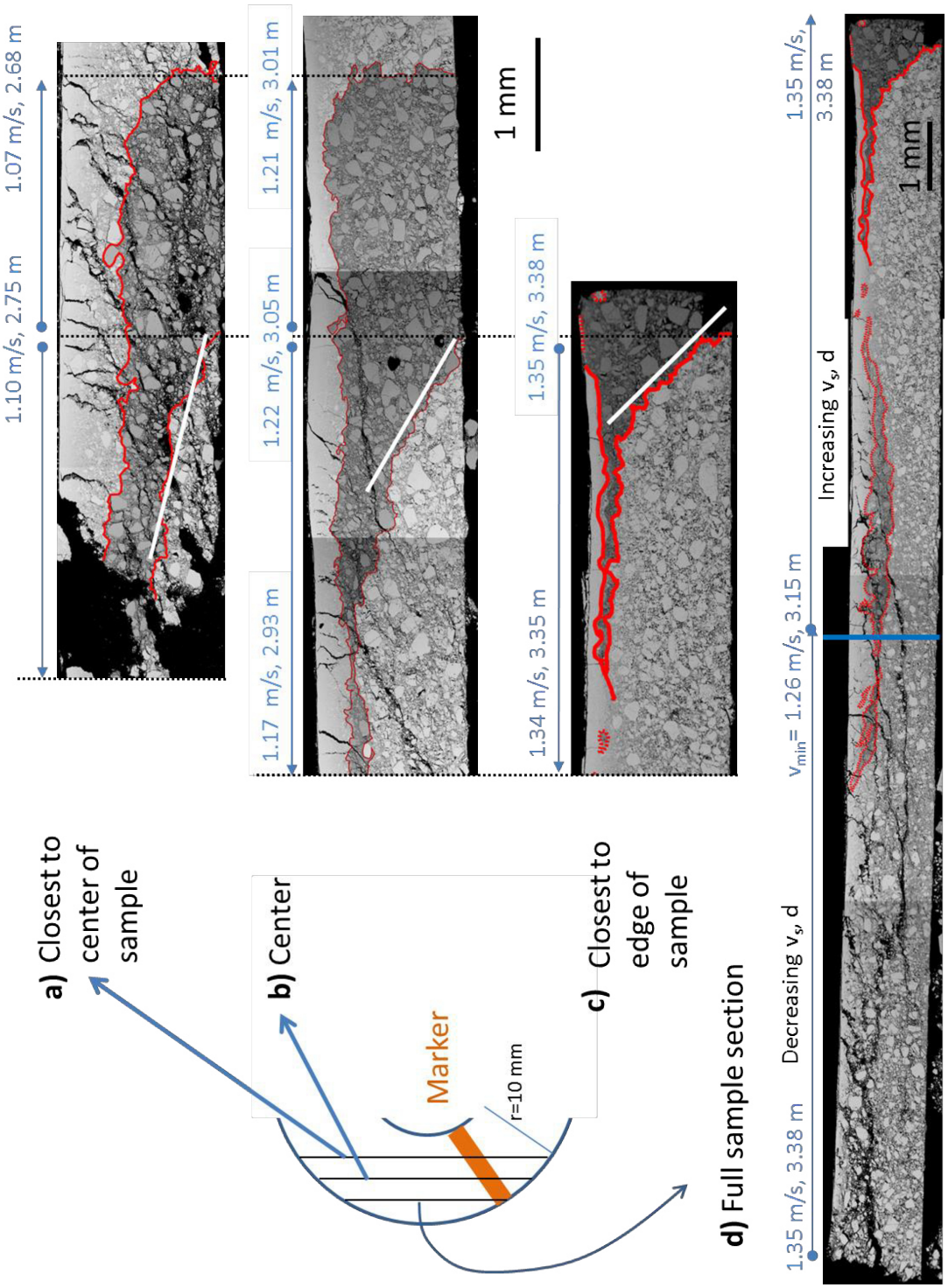

Figure 14. Dependence of the strain distribution on the radial position II. SEM backscattered images of three sections cut as shown in the sketch from the room-dry sample s886 that had experienced 2.5 m of total equivalent displacement at a slip velocity of 1 m/s and a normal stress of 3 MPa. Due to the annular geometry of the sample, the sections from different radial positions [a) closest to the center of the sample, b) further to the outer radius, and c) and d) closest to the edge of the sample] experienced different maximum velocities and displacements. d) shows the full length of the section in c) including the part of the sample where it was in contact with the outer confining steel ring.

493 of the sections (Fig. 13). The minimum velocity (marked by the blue vertical lines) is 1.07 m/s in
494 the section that was cut closest to the center of the sample (Fig. 13a), 1.18 m/s in the middle
495 section (Fig. 13b), and 1.26 m/s in the outermost section (Fig. 13c), yielding a velocity
496 difference of up to 0.19 m/s between the sections. The minimum total displacement for of
497 each section is 46.1, 50.7 and 54.1 cm, so the displacement difference from the inner- to the
498 outermost section is 8 cm. Also within a given section, the velocity and total displacement
499 experienced by the gouge increases from a minimum value at approximately the center of the
500 image to a higher value at the outer edges: the area covered by one image experienced a
501 maximum velocity difference of c. 0.04 m/s for the innermost (Fig. 13a), c. 0.02 m/s for the
502 middle (Fig. 13b), and 0.006 m/s for the outermost section (Fig. 13c), corresponding to a
503 maximum difference in the total displacement of 16, 8.6, and 2.6 mm, respectively. Overall,
504 the texture and the geometry of the strain marker do not change significantly from section to
505 section: the thickness of the marker in the low-strain zone is similar (1.35, 1.28 and 1.26 mm
506 for the innermost, central and outermost sections, respectively), as are the angles of distortion
507 of the marker margins. Grain sizes and shapes and the distribution and thicknesses of the
508 textural zones I, II and III are similar in all sections. However, a network of P-shears becomes
509 more apparent in the sections closer to the center where fractures are more open.

510 In sample s886 (room-dry conditions, 8.5 MPa normal stress, 1 m/s equivalent velocity
511 and 2.5 m equivalent displacement) the marker position was close to (Figs. 12a, b) or adjacent
512 (Fig. 14c) to the external metal confining ring. The minimum velocity of each section
513 corresponds to 1.10, 1.22 and 1.35 m/s (Fig. 14a, b, c), yielding a velocity difference from
514 inner- to outermost section of 0.25 m/s. The minimum total displacements are 2.75, 3.05, 3.35
515 m; thus the displacement difference is 0.6 m. Within a given section, the velocity increases
516 from the minimum to a higher value at the outer edges. In case of the innermost section (Fig.
517 14a), Δv_s=0.03 m/s and Δd=70 mm; $\Delta v_{s.max}$=0.05 m/s and Δd_{max}=120 mm for the center section
518 (Fig. 14b) and Δv_s=0.09 m/s and Δd=230 mm for the outermost section (Fig. 14d). The
519 outermost of the sections of sample s886 (Fig. 14c, d) shows the outer edge of the sample,
520 where the gouge material, in this case the dolomite marker, was in contact with the confining
521 steel ring. The texture and the geometry of the marker are significantly different in these

sections. Where the marker is located in the outermost section, the dolomite material covers all of the thickness of the gouge layer. It is only slightly sheared in the low-strain layer (angle of distortion of 45°; i.e. γ=1), and the high-strain layer above the portion of the marker that is sheared towards parallelism with the layer boundary is relatively thin (c. 130 μm). In the middle section, the left marker margin has a slightly larger angle of distortion (c. 60°; γ=1.7) and the high-strain layer is up to 350 μm thick. In the third section, closest to the center of the sample, the marker is sheared to an even higher degree (the angle of distortion in the low-strain domain being c. 75°; γ=3.7) and sits beneath an even thicker (c. 530 μm) overlying zone that, however, is not completely made up of highly-comminuted material. The thickness of the true high-strain zone is c. 175 μm. As in the water-dampened sample (s961), the degree of fracturing seems to decrease towards the outer edge of the radial sample, although in this case the fracture network consists of R1 Riedel-shears rather than P-shears. In the outermost section, some R1-shears are present in the center of the section (Fig. 14d), where the velocity was smaller (1.26 m/s) and the high-strain layer is the thickest. The shears (that in in some cases turn into Y-shears) can be traced in the direction of shear until the edge of the sample, where it is highly fractured and incohesive. In all sections and in many of the other experimental samples (e.g., Fig. 8e) the high-strain layer is cut by sub-vertical fractures that link downwards into the R1-shears.

4. Discussion

4.1. Effect of the rotary-shear configuration on strain localization

4.1.1. Effect of boundary conditions

In gouge experiments performed with the annular sample holder in SHIVA, the high-strain principal slip layer and discrete slip surface always form on the same side of the sample holder. This is consistent with results from experiments performed with different sample holders and rotary-shear machines and with reported results from previous studies (e.g. Beeler et al., 1996), where the principal slip zone always formed in the same position within the gouge layer. For instance, in the sample configuration used for gouge experiments by Beeler et al. (1996), the gouge layer is sandwiched between two rock cylinders and confined by a Teflon

jacket that is split in two halves (Fig. 15a). The upper ring is stationary, while the lower rotates, causing a slip discontinuity along the jacket split. According to Beeler et al. (1996), this boundary condition resembles a mode III crack affecting the stress field in the gouge layer and causing the strain to localize adjacent to the jacket split, in their case approximately in the center layer of the gouge layer.

This explanation is in agreement with the sample assembly used with SHIVA. The sample holder used with SHIVA can be described as having a "bucket-and-lid" configuration: All parts belonging to the "bucket" (Fig. 15b, white parts) are e.g. stationary, while the "lid" (grey parts) is rotating, causing a slip discontinuity (marked in red) at the surfaces in contact that slide against each other (S. Nielsen, personal comment). Like in the case of Beeler et al. (1996), the slip discontinuity causes strain localization within the gouge layer to nucleate at this discontinuity.

A similar configuration to that of Beeler et al. (1996) is used with the rotary-shear apparatus ROSA installed at the University of Padua (Fig. 15c). The sample assembly consists of full rock cylinders and an outer confining Teflon ring that, however, is not split in half. Thus, the lower stationary piston and the stationary confining Teflon ring form a "bucket". The rotating upper piston acts as the "lid". The slip discontinuity in the gouge layer is thus located at the boundary with the upper piston. If the Teflon ring rotates because it sits more tightly on the upper cylinder, the slip discontinuity will be around the lower piston and the principal slip layer will form on the stationary side of the gouge layer. The same basic configuration is used in the *Phv*-apparatus in Kochi, Japan, except that the holder there is annular.

In summary, the location of the principal slip surface is dependent on the boundary conditions in a specific experimental configuration. The stress concentration due to the boundary conditions might also speed up the localization process. According to Beeler et al. (1996), gouge sheared in a simple- or direct-shear configuration might be less prone to localized.

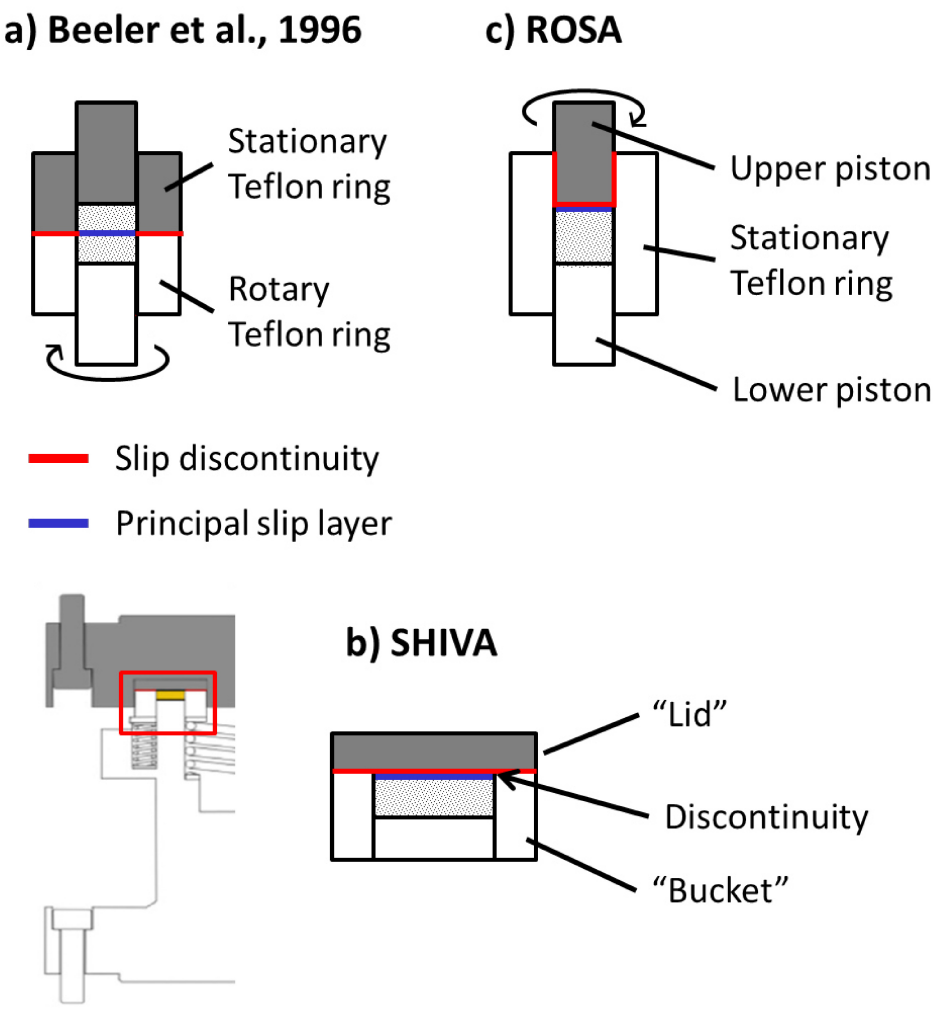

Figure 15. Location of slip localization in different experimental assemblies. a) The experimental configuration used in gouge experiments by Beeler et al. (1996) uses a confining Teflon ring that is split in two half. The upper ring is stationary, while the lower rotates, causing a slip discontinuity along the jacket split and the gouge to localize adjacent to the jacket split. b) The all-steel annular gouge holder used with SHIVA has a true "bucket-and-lid" configuration: All parts belonging to the "bucket" (white parts) are e.g. stationary, while the "lid" (grey parts) is rotating, causing a slip discontinuity at the surfaces in contact (marked in red). The localization of slip/strain within the gouge layer (dotted region) nucleates at this discontinuity. Thus, the location of the principal slip surface (marked in blue) is dependent on the boundary conditions. c) The sample assembly used with Rosa consists of full rock cylinders and an outer Teflon ring that confines the gouge. With Rosa, the upper column is used to apply the rotation. If the Teflon ring remains stationary, they form a "bucket". The rotation upper piston acts as the "lid". The slip discontinuity and the accordingly forming principal slip layer are again marked in red and blue, respectively. The Teflon ring may rotate, if it sits more tightly on the upper cylinder. In that case, the slip discontinuity will be around the lower piston and the principal slip layer will form on the stationary side of the gouge layer. The same basic configuration is used in the Phv-apparatus in Kochi, Japan, except that the holder there is annular.

4.1.2. Effect of the radial position

Another possible effect on the distribution of strain could be due to the velocity and displacement gradient in the gouge sample because of the circular geometry in the rotary-shear configuration. To test this, two samples (s961 and s886, Fig. 13 and 12, respectively) were cut at three radial positions, so the strain marker could be investigated at different effective velocities and total displacements. For the three sections obtained from sample s961 (0.43 m of equivalent slip, Fig. 13a), the maximum difference in slip velocity and total displacement experienced by the material at the different radial positions that were investigated was 0.19 m/s and 8 cm, respectively. The displacement difference corresponds to a strain difference of c. 40 (for a sample thickness of 2 mm), which appears to have an insignificant effect on the strain distribution based on the geometry of the dolomite marker. The only marked difference in the microstructures of the three sections is the higher abundance of open P-shear fractures in the sections closer to the center of the sample which might be due to the shear planes dipping slightly towards the inner edge of the sample. Because differences in the three sections are minor, we can deduce that small irregularities in the cutting of the samples that resulted in samples from different radial positions have a small effect on the results of the strain evaluation if the total equivalent displacement is relatively small. This is at least true for the water-dampened samples, but because of the geometric similarity of the water-dampened and room-dry markers in experiments at 8.5 MPa normal stress and a slip velocity of 1 m/s we can likely extend our conclusion to the room-dry conditions.

The total equivalent displacement of 2.5 m in sample s886 is significantly larger than that of the previously discussed sample s961. This results in the larger velocity and displacement difference between the inner- and the outermost section of 0.25 m/s and 60 cm, respectively, which explains the significantly different marker geometries in the three sections. The larger velocities and displacements in the outer sections likely lead to a faster localization of slip. This limits the amount of strain hosted in the lower-strain domains, because most of the slip is hosted in the high-strain layer after localization is achieved. Thus, the degree of

604 distortion of the marker will decrease with increasing sample radius, which is consistent with
605 our microstructural observations (Fig. 14a-c).

606 Additionally, in the outermost section of sample s886 the marker was cut very close to
607 the outer confining ring, where it is influenced by a boundary effect that is caused by the
608 friction of the granular material against the confining ring as previously described by Beeler et
609 al. (1996). The boundary effect causes a reduction in the degree of deformation which in our
610 case inhibits the deformation of the marker: close to the border, the dolomite covers the
611 whole thickness of the sample which consists of un-comminuted Zone I-material; no high-
612 strain layer formed here (Fig. 14c). With distance from the border, the corner effect decreases
613 and the thickness of the high-strain layer (Zone III) increases (Fig. 14d). The dolomite marker
614 follows the boundary between intermediate (Zone II) and high-strain zone (Zone III), resulting
615 in the apparent dipping of the marker. The geometry of the marker in the three sections of
616 sample s886 is probably also influenced by the sections not being cut perpendicular to the
617 marker but at an angle to it (sketch in Fig. 14). This might also be the reason why the angle of
618 distortion of the left and the right margins of the marker are different.

619 ## 4.2.Strain localization and mechanical behavior

620 ### 4.2.1. Strengthening phase

621 In high-velocity experiments (1 m/s), the length of the main strengthening phase in
622 both room-dry and water-dampened calcite gouges generally decreases with increasing
623 normal stress (Fig. 4). This different behavior could be due to higher temperatures achieved in
624 the slipping zone at higher normal stresses (see Fig. 7a in Chapter III of this thesis). Our results
625 are consistent with those obtained in room-dry conditions by Smith et al. (2015) who conclude
626 that triggering of dynamic weakening in calcite-bearing fault zones is dependent on the normal
627 stress, and large coseismic slip may be impeded at shallow crustal depths due to a particularly
628 long strengthening phase (in addition to the stabilizing effect of gouges present in a fault zone
629 during the earthquake nucleation phase (Marone and Scholz, 1988)). However, our complete
630 dataset shows that dynamic weakening occurs much more abruptly in water-dampened
631 gouges (Fig. 3, Fig. 5a), which is also true for cohesive carbonate rocks in the presence of fluids

(Violay et al., 2013). The unusually long strengthening phase in one water-dampened experiments performed with SHIVA may be due to loss of water during sample loading and compaction, or – quite to the contrary – due to a thermal or mechanical pressurization of the pore fluids effectively decreasing the normal stress. A decrease of the effective normal stress due to pressurization of the pore fluid in the water-dampened experiments might also be responsible for the slightly longer strengthening phase than observed in experiments performed under fluid-pressure controlled conditions (with the *Phv*-apparatus in Kochi; Chapter III of this thesis) (Fig. 4). Alternatively, the longer strengthening phase in the water-dampened experiments performed with SHIVA may also be due to the fact that the experiments performed in Kochi had already accumulated 30 cm of displacement at low velocity (1 mm/s) before the high-velocity step (1 m/s) was initiated, so that strain was already well localized and temperatures were slightly higher prior to the high-velocity step.

For a fluid-saturated 1 mm-thick gouge layer sheared at a rate of 1 m/s and at a depth of 7 km, Platt et al. (2014) predict the peak strain-rate localization to be reached at displacements of 3.2 mm and 0.13 mm for frictional rate-strengthening and dilatant-strengthening approaches, respectively (Platt et al.'s Fig. 2 and 12). The former displacement is roughly consistent with the length of the strengthening phase in our water-dampened and water-saturated experiments (Fig. 4) which is c. 5 mm at normal stresses of 10–12 MPa and will likely decrease further for higher normal stresses. Our microstructural investigation does not reflect this rapid localization at displacement of a few mm, however, in order to be reflected in the microstructures, strain-rate localization must last for some time and – as shown by the model of Platt et al (2014), the peak strain rate will decrease again at larger displacements indicating a thickening of the localized zone.

The initial shear-stress evolution is remarkably similar for room-dry and water-dampened gouges sheared at the same experimental conditions (Fig. 5): independently of the ambient conditions, the gouge strengthens during the first few millimeters of displacement. However, while the strengthening phase in the water-dampened experiments decreases slightly in length with increasing normal stress, the opposite trend is observed for the **initial** strengthening (Fig. 4, open circles) in the room-dry experiments. This initial strengthening

phase in the room-dry gouges could be associated with a first slip localization after few millimeters of displacement leading to a transient weakening stage, which is followed by renewed, "main" strengthening due to a broadening of the shear band (which may be associated with layer dilation). However, verification of this hypothesis will require further analysis of the microstructures associated with few millimeters of displacement.

4.2.2. Dynamic weakening: Room-dry vs. water-dampened conditions

The mechanical data of the calcite gouge experiments show an almost instantaneous weakening in the water-dampened gouges when sheared at 1 m/s, while the room-dry gouge strengthens during a phase that is c. two orders of magnitude longer than in the water-dampened conditions before dynamic weakening initiates (Fig. 5a). If the strengthening phase is attributed to progressive localization of strain to a high-strain shear band that has to evolve to a critical state prior to weakening (as it was done in several previous studies, e.g. by Marone et al., 1992; Beeler et al., 1996; Rathbun & Marone, 2010; Smith et al., 2015), the almost absent strengthening phase in the water-bearing gouges suggests that strain localizes faster in water-dampened and water-saturated conditions as compared to room-dry conditions.

Evidence for this could be provided by the axial displacement data recorded during the experiments. In previous high-velocity rotary-shear experiments with **room-dry** calcite gouges performed with the same apparatus and sample configuration as used in our study, Smith et al. (2015) observed that progressive slip localization during the strengthening phase is accompanied by a phase of transient gouge layer dilation. The transient dilation is thought to be due to shear dilatancy during rolling and comminution of particles (e.g. Mandl et al., 1977). The strengthening phase must be associated with some distributed deformation rather than fully localized shear (Marone et al., 1990; Rathbun and Marone, 2010), because localized sliding on a smooth slip surface would not cause dilation. But while the length of the strengthening phase in our room-dry experiments (3.5–75 cm for normal stresses of 21–3 MPa) is comparable with that of Smith et al. (2015) (5–29 cm for normal stresses of c. 25–5 MPa), the transient dilation data are not as similar. In our room-dry experiments, transient dilation occurs at the onset of dynamic weakening (e.g., Fig. 5a), but is not always observed and is not as pronounced as in the experiments by Smith et al. (2015). This may be due to a

690 different starting particle-size distribution influencing the comminution rate, a different
691 humidity of the gouge layer, or a different state of pre-compaction (e.g. Feda, 1982; Sammis
692 and Biegel, 1989). Nevertheless, the rate of compaction is larger in our water-dampened
693 gouges than in the room-dry material prior to weakening (Fig. 5a), which possibly suggests that
694 the finite strain is in fact more localized in water-dampened than in room-dry conditions.

695 For the samples sheared at 1 m/s and at 8.5 MPa, as shown in Fig. 11c, the strain
696 hosted in the low- and intermediate-strain zones (Zones I and II) may be slightly larger in the
697 room-dry compared to the water-dampened experiments. This could mean that either
698 localization occurred earlier in water-dampened conditions thus limiting the amount of strain
699 hosted in the bulk of the gouge layer, or that the localization is more effective such that the
700 amount of strain hosted in the lower-strain domains after localization is achieved is smaller
701 than in room-dry conditions. However, the error of these data is large (Fig. 11a, b) and it is
702 thus unclear if the trend is real.

703 If localization occurs faster in water-dampened conditions, this should be reflected in
704 the microstructures and the degree of shearing of the markers in our post-experimental
705 samples. Zones of decarbonation were only found in water-dampened samples. This may be
706 due to 1) decarbonation being present in the room-dry samples but not being detected, or 2)
707 decarbonation occurring at lower temperatures in the presence of fluids, or 3) localized
708 frictional heating being more efficient in water-dampened conditions due to a higher degree of
709 strain localization.

710 To further understand if localization occurs more abruptly in water-dampened
711 conditions, experiment s959 was stopped prior to the onset of dynamic weakening (cyan curve
712 in Fig. 5a), after a total equivalent displacement of only 1.1 cm. Unfortunately, this sample was
713 badly preserved and if a high-strain shear band had developed it was lost (Fig. 6d). The thin
714 post-experiment sample thickness of only c. 1.5 mm suggests that some of the low- and/or
715 high-strain material was lost during sample preservation. However, the strain estimated for
716 the preserved sample is c. 4.7 which is similar to the bulk strain indicating that no high-strain
717 material was lost. Whatever the case, parts of the marker are sheared towards parallelism

718 with the gouge layer boundaries (Fig. 6d) showing that the process of localization has started
719 during the first 1.1 cm of slip.

720 We were not able to preserve a room-dry strain-marker sample with a total
721 displacement as low as in sample s959 (1.1 cm). However, Smith et al. (2015) performed a
722 room-dry experiment with a total displacement of 1 cm at otherwise identical conditions (c. 1
723 m/s target velocity, acceleration of 6 m/s^2, 8.5 MPa normal stress, a starting gouge layer
724 thickness of c. 3 mm, starting particle size of <250 μm) and found that a well-defined, <20 μm
725 wide shear band had developed, consisting of angular particles <10 μm in size embedded
726 within an even finer-grained matrix (Fig. 6 in Smith et al., 2015). However, it is not known if
727 strain localization occurred faster in this room-dry sample, or if it is just better preserved. To
728 summarize, our mechanical data suggest faster strain localization in calcite gouges in the
729 presence of water, consistent with previous high-velocity experimental results (e.g. Violay et
730 al, 2013, 2014; Faulkner et al, 2010). However, the microstructural evidence for this remains
731 ambiguous and additional strain-marker experiments should be performed to determine
732 whether the strain-localization mechanisms are different in room-dry and water-bearing gouge
733 layers.

734 **4.2.3. Post-dynamic-weakening behavior/ Progressive localization**

735 According to Smith et al. (2015), the high-strain shear band that developed in their
736 room-dry calcite gouges during the strengthening phase continued to evolve during dynamic
737 weakening to form a discrete principal slip surface which subsequently hosted most of the slip
738 displacement. This form of progressive localization of deformation was also observed in this
739 study both in room-dry and water-dampened conditions (Fig. 8): in the room-dry conditions,
740 the high-strain layer evolves from a broad zone of comminuted and slightly compacted
741 material containing several poorly-developed shear bands (s953, total equivalent displacement
742 of 13 cm, Fig. 8b) to a zone of highly-comminuted and compacted gouge cut by a discrete
743 principal slip surface (s881, displacement of 43 cm, Fig. 8c). After the same equivalent
744 displacement, of 43 cm, a similar microstructure developed in the water-dampened
745 conditions (s961, Fig. 8d). As observed in Smith et al. (2015), the discrete principal slip surface
746 is often lined with recrystallized calcite grains (Fig. 9f-h) and in the underlying highly-

comminuted layer, abandoned shear bands can be observed (e.g. Fig. 8d). In addition to recrystallization, sintered grains and decarbonation were observed in several of the high-displacement, high-velocity experiments (Fig. 9a-e) occurring adjacent to the principal slip surface in a zone several tens of micrometers thin. These textures are evidence of high local temperatures due to highly-localized frictional sliding (Han et al., 2007a; Kim et al., 2010; Shimamoto and Togo, 2012; Smith et al., 2013). The textures found in our post-experimental samples thus suggest that most of the slip is hosted adjacent to and on the principal slip surface once localization is achieved.

This conclusion is also supported by the clear positive dependence of the strain hosted in the high-strain layer on the total displacement of a sample; this is valid for all experimental and ambient conditions (Fig. 11d). However, the data also show that after localization is achieved, a small amount of slip probably still occurs in the bulk of the gouge material adjacent to the principal slip surface. This is suggested by the slightly increasing amount of strain in the low-strain zone with increasing total displacement (Fig. 11a). It is also consistent with the microstructural observations of Smith et al. (2015) who found that the grain size in the bulk of the gouge layer continued to decrease even after localization was achieved, suggesting at least some distributed deformation. (This implication is important for the formation of clast-cortex aggregates (CCAs, see Chapter I of this thesis or Rempe et al. (2014) for more details), that most likely only form at relatively low strains of c. 2–14. Additionally, CCAs are better developed for larger displacements, suggesting that the "necessary" amount of strain is only reached in the low-strain layer when strain is already localized.) Part of the strain in the bulk of the gouge layer is also accommodated on R1- and P-shears (Fig. 8e) that are observed in many samples, independently of the total displacement, and thus these shears are likely form continuously throughout the experiment (Beeler et al., 1996).

4.3. Thickness of the localized zone

In samples from experiments performed at 1 m/s, the thickness of the high-strain zone (textural Zone III) ranges from c. 130–240 µm in room-dry conditions (Fig. 7a). In water-dampened conditions it ranges from 205–330 µm (Fig. 7c). After localization is achieved, however, the actively deforming gouge layer is likely much thinner. Zones of sintered or

recrystallized grains c. 10–45 µm in thickness adjacent to the a principal slip surface show that frictional heating mainly occurred in this zone, and that the principal slip surface thus likely had a "thickness" of < 10 µm. This is roughly consistent with the width of the principal slip surface of 2–3 µm observed by Smith et al. (2015) and of highly-deformed slip zones of <20 µm consisting of welded or sintered grains reported in gouge experiments by Yao et al. (2013).

Localized zone widths modeled by Platt et al. (2014) are also roughly consistent with our experimental results, even though the boundary conditions introduced by our rotary-shear sample configuration are different from those used in the model by Platt et al. (2014). Additionally, friction was modeled using a law derived from experiments performed at much lower slip rates in the order of 1–10 µm/s. Nevertheless, our experimental high-strain zone thicknesses are similar to the upper bound of the localized zone width of c. 340 µm predicted by Platt et al. (2014) for fluid-saturated, damaged gouge material sheared at 1 m/s at a depth of 1 km, when rate-strengthening friction is taken as the stabilizing mechanism. The much thinner width of the experimental principal slip surface (<10 µm) is more consistent with the values predicted from dilatancy-strengthening (14 µm) (Platt et al., 2014). For localization limited only by dilatancy, Platt et al. (2014) predicted localization to be transient so that for large slips the gouge will be sheared mainly uniformly. In our experiments, slips are often large compared to gouge layer thickness, but strain localization is always observed in the post-experimental samples. This could mean that either a mechanism other than dilatancy is stabilizing the slip, or that the model is not valid for our experimental conditions.

4.4. Dynamic weakening mechanisms

The different shear-stress evolution of room-dry and water-dampened gouges could not be unambiguously attributed to a difference in the degree of localization. This suggests, that the weakening mechanisms active are either different for the different ambient conditions or more or less efficient, causing the faster weakening in water-dampened conditions and the lower steady-state shear stress in the room-dry gouges.

Almost instantaneous weakening in the presence of fluids was also observed by Violay et al. (2014) in high-velocity rotary-shear experiments on cohesive carbonate rock. They

suggest that abrupt weakening in fluid-saturated carbonate rock is due to subcritical crack-growth by stress corrosion (Atkinson and Meredith, 1987) leading to brittle failure of the asperities. Stress corrosion, which is thought to take place during sample loading, is much more efficient in fluid-saturated than in room-dry conditions. In calcite, the fracture surface energy is 2–3 times lower in the presence of water resulting in faster crack propagation (Røyne et al., 2011). At larger slips and independently of the ambient conditions, the weakening is thought to be further enhanced by frictional heating triggering e.g. decarbonation and formation of CaO nanograins (Han et al., 2010, Violay et al., 2014).

The mechanisms proposed for the case of the cohesive carbonate rocks are likely also applicable to the behavior of calcite gouges. Dynamic weakening in gouges sheared at high velocity (c. 1 m/s in our study) might be due to a form of flash weakening that requires a high degree of strain localization, as proposed by Smith et al. (2015), in both room-dry and water-dampened conditions, because the temperature rise due to frictional heating in water-dampened and water-saturated calcite gouge or rocks is not significantly lower than in room-dry or vacuum conditions. This was modeled by Violay et al. (2014) and shown by the temperature measurements in the calcite gouge experiments performed with the *Phv*-apparatus described in Chapter III of this thesis, which showed a higher temperature for higher normal stresses, but not for room-dry compared to fluid-saturated conditions. Weakening in the water-dampened gouges is possibly accelerated by subcritical crack growth. Localization to a principal slip surface in water-dampened conditions likely occurs during and after weakening.

The lower steady-state shear stress of the room-dry gouges cannot be explained with more efficient thermal weakening processes, either. Thermal pressurization of the pore fluid in the water-dampened gouges, for instance, would cause a *decrease* in the effective normal stress and thus in the shear stress of the water-dampened gouges. Possibly, steady-state shear stress is controlled by crystal-plastic deformation processes such as grain boundary sliding aided by (Coble-type) diffusion creep, as suggested by Holdsworth et al. (2013) for calcite deformed at conditions similar to ours, and similarly to the behavior described by Verberne et al. (2014) for calcite sheared at 1 µ/s. Due to the strain-rate dependence of diffusion creep in carbonate rocks (Passchier and Trouw, 1996; Schmid et al., 1977), a slightly thicker actively

deforming zones in room-dry conditions, which is the case in our experiments if Zone II is counted towards the effectively deforming zone (Fig. 7a, b), would yield a lower strain rate than in water-dampened gouges and might thus be responsible for the lower steady-state shear stress (since there was no microstructural prove suggesting different grain sizes in room-dry and water-dampened conditions and assuming similar diffusion rates). (See Chapter III of this thesis for a calculation of expected shear stresses.) Microstructural evidence for crystal-plastic deformation processes is provided by recrystallized grains that often showed a preferred orientation (Fig. 9f-h) which suggests that recrystallization occurred dynamically.

Since frictional heating at **low** velocity (1–10 mm/s in our case) or low normal stress (3 MPa) is insignificant (compare to Fig. 3b, Chapter III of this thesis), it is unlikely that flash heating takes place in room-dry experiments performed at ≤1 cm/s, leading to a relatively high steady-state shear stress (Fig. 3). The lower steady-state shear stress in water-dampened conditions again can be attributed to the lower fracture surface energy of calcite in the presence of fluids. Slip-strengthening in the room-dry gouges is caused by a switch from compaction to dilation towards a steady-state density (Fig. 5b), consistent with the previous studies e.g. by Feda (1982) and Marone et al. (1990). In water-dampened conditions no dilation occurs but the slip-strengthening is more moderate than in room-dry conditions. The much higher relative decrease in shear stress (65%) in the room-dry experiments performed at high normal stresses (20 MPa) than at 8.5 MPa (c. 40%) (Fig. 3) are likely caused by the presumably higher temperatures.

4.5 Implications for natural faults

Independently of the acting dynamic weakening mechanisms, the shorter strengthening phase in the water-dampened conditions implies that carbonate gouge-bearing natural faults at shallow depths will be more prone to slip if only a small amount of water (only 20 wt.% H_2O were used in our experiments), even if not pressurized, is present. This has important implications for coseismic rupture behavior of faults where the degree of saturation may vary along the fault. Namely, weakening will occur faster in relatively wet fault patches (Violay et al., 2013, Faulkner et al., 2010), which might explain some of the slip distribution complexity during earthquakes occurring in carbonate sequences (Cirella et al., 2009; Pino and

Di Luccio, 2009; Di Stefano et al., 2011). For instance, the heterogeneous slip distribution of the 2009 L'Aquila earthquake correlates well with the on-fault pattern of aftershocks that cluster around the high-slip patches (Cirella et al., 2009) and that were attributed to the presence of high-pressure fluids at depth (Miller et al., 2004).

Strain localization in gouges occurs in the first tens of cm of slip, independently of the presence of water. After localization is achieved, most of the strain is hosted in a thin principal slip layer, where the finite strain increases with cumulated slip. The thickness of the principal slip layer, however, does not systematically increase with displacement (Fig. 7). As noted previously (Power et al., 1988), this yields a discrepancy to natural fault systems, where the thickness of gouge or ultracataclasites often increases approximately linearly with increased accumulated displacement. This discrepancy must thus be a result of geometrical properties of the fault zone (e.g., fault surface roughness; Power et al., 1988; Sagy and Brodsky, 2009; Savage and Brodsky, 2011). This conclusion is further supported by the fact that in relatively straight fault segments fault core thickness are almost independent of the cumulated slip (e.g., Di Toro and Pennacchioni, 2005).

5. Conclusion

A series of intermediate- to high-velocity rotary-shear experiments was conducted on synthetic calcite gouges prepared with dolomite strain markers. The strain marker experiments were conducted at varying slip rates (10^{-3}–1 m/s), displacements (0.011–2.5 m), normal stresses (3 to 21 MPa) and ambient conditions (room-dry and water-dampened) to test the dependence of the strain distribution on these various experimental conditions.

The mechanical behavior of room-dry and water-dampened gouges sheared at 1 m/s is significantly different: while the room-dry gouges show a prolonged strengthening phase prior to dynamic weakening, the water-dampened gouges near-instantaneously weaken to a steady-state shear stress that is slightly higher than in room-dry conditions. Microstructural analysis of the sheared dolomite markers revealed progressive strain localization to a thin (125–600 µm) high-strain layer that developed after several cm of slip in both room-dry and water-saturated conditions. The strain hosted in the bulk of the gouge layer does not change significantly with

increasing total displacement, suggesting that, once formed, the high-strain slipping zone and slip surface accommodate most of the subsequent displacement. This is supported by sintered or recrystallized grains and zones of decarbonation adjacent to the principal slip surface, indicating localized frictional heating. No significant differences in the degree of localization was observed in room-dry and water-dampened gouges. Thus, faster weakening in water-dampened conditions and the lower steady-state shear stress in the room-dry gouges, are likely not due to faster localization. Instead, weakening may be enhanced in the presence of fluids by subcritical crack growth, as proposed for solid calcite marble by Violay et al (2014). The faster dynamic weakening in the presence of fluids might explain some of the observed slip distribution complexity in natural carbonate-bearing fault zones.

6. Acknowledgements

Andrea Cavallo, Rolf Neuser and Leonardo Tauro are thanked for assistance with SEM analysis. Elena Spagnuolo and Fabio Ferri are thanked for technical assistance. MR acknowledges funding from Ca.Ri.Pa.Ro. and SAFS from a 2014 University of Otago Research Grant. All authors were funded by the European Research Council Starting Grant USEMS (no. 205175) and European Research Council Consolidator Grant NOFEAR (no. 614705).

7. Figure Captions

Figure 1. Strain localization in nature. The internal structure of the north branch of the San Gabriel fault from Chester et al. (1993). This symmetric damage structure with a wide damage zone surrounding a relatively thin fault core zone, where most of the slip is localized, is a characteristic of many fault zones.

Figure 2. Gouge sample set-up used with SHIVA. a) All-steel annular gouge holder, modified from Smith et al., 2013. Yellow areas show position of gouge layer contained by inner and outer metal sliding rings. White and grey parts slide move against each other during the experiments (both parts can be used as the rotary or stationary part), red lines demonstrate where metal parts are in sliding contact. **b)** Backscattered Electron image of the starting material: calcite gouge derived from Carrara marble with particle sizes <250 μm. **c)** Gouge

holder (white part in a)) filled with light-colored calcite gouge and with a darker-colored dolomite marker. Inset shows magnification of the marker constructed perpendicular to the layer boundaries and the imposed shear direction. **d)** Epoxied calcite gouge sample (s1004), cut perpendicular to the strain marker as shown in the sketch, where the orange line schematically depicts the trace of the sheared marker. **e)** Sample s886 sheared at 3 MPa normal stress, equivalent slip velocity of 1 m/s, 2.5 m of total equivalent displacement and room-dry conditions (mosaic of backscattered electron images). The dolomite marker is distinguished by its darker grey color. The geometry of the dolomite marker broadly defines low-, intermediate- and high-strain domains. **f)** Sketches (modified after Scruggs and Tullis, 1998) show section through sample with unstrained and idealized strained marker assuming homogeneous strain distribution. The strain experienced by the marker can be calculated from its angle of distortion Φ.

Figure 3. Shear stress evolution with displacement for room-dry and water-dampened strain-marker experiments. The shear-stress data are well-reproducible in experiments conducted at the sample normal stress, slip velocity and ambient conditions. Reddish curves correspond to room-dry experiments performed at 1 m/s, with lighter red colors for lower normal stress: dark red, 15–20 MPa normal stress; bright red, 8.5 MPa; light pink, 3 MPa. Green curves are for room-dry experiments at 1 mm/s and 8.5 MPa. Water-dampened experiments are plotted in blue (1 m/s, 8.5 MPa) and turquoise (1 mm/s and 1 cm/s at 8.5 MPa).

Figure 4. Strengthening phase in room-dry, water-dampened and water-saturated gouges. **a)** Length of the strengthening phase (i.e. the slip distance to the onset of dynamic weakening) on a logarithmic scale vs. the effective normal stress for experiments performed at a slip velocity of 1 m/s. **b)** Initial and main strengthening illustrated for sample s886 (3 MPa, room-dry, 1 m/s).

Figure 5. Evolution of shear stress and axial displacement in comparison for room-dry and water-saturated gouges. a) Exemplary data from high-velocity experiments (1 m/s) for a room-dry (s896, red curves) and two water-dampened (s962, s959, blue and cyan curves, respectively) experiments, all performed at 8.5 MPa normal stress and with the same

945 acceleration and target velocity (black and grey curves, secondary y-axis). In experiment s959,
946 the target velocity was not reached ($v_{s,max}$=0.38 m/s). The shear stress (primary y-axis)
947 evolution in the first 10^{-2} m of displacement is very similar in the room-dry and water-
948 dampened conditions. After the strengthening phase, the room-dry gouges weaken more
949 abruptly and to lower shear stress values than the water-dampened experiments. The axial
950 displacement for s896 and s962 is plotted on the secondary y-axis, a positive axial
951 displacement denotes compaction. At the initiation of sliding, the water-dampened gouge
952 compacts at a slightly faster rate than the room-dry gouge. The net compaction is similar in
953 both room-dry and water-dampened experiments, as the room-dry gouge compacts faster
954 after the onset of dynamic weakening. In the room-dry experiment, a small amount of
955 transient dilation (red arrow, c. 10 μm) can typically be observed at a displacement of c. 9 cm
956 (dashed vertical line), coinciding with the onset of dynamic weakening. **b)** Shear stress
957 (primary y-axis) and axial displacement (secondary y-axis) from low-velocity experiments (1
958 mm/s) for two room-dry (s882, red curves; s874, orange curves) and a water-dampened
959 (s1007, blue curves) experiment, all performed at 8.5 MPa normal stress and with the same
960 acceleration and target velocity. Note that in the room-dry gouges (red and orange curves) the
961 compaction denoted by a positive axial displacement is followed by dilation (negative axial
962 displacement) that occurs simultaneously with an increase in shear stress (orange and red
963 dashed vertical lines). No dilation is observed in the water-dampened experiment (blue
964 curves), but the onset of strengthening (blue dashed line) is accompanied by a decrease in the
965 compaction rate.

966 **Figure 6. Distribution of textural zones and strain in the gouge layer. a)** Calcite (Cc) sample
967 s943 with dolomite (Dol) strain marker (room-dry, 1 m/s, 8.5 MPa, 1.3 m total displacement).
968 Textural zones are marked on the right of the sample picture. In Zone I, the marker boundary is
969 sheared only slightly. Towards Zone II, the marker is progressively sheared, , with an angle of
970 distortion of up to c. 48°, yielding a strain of <1.3. In Zone II, the marker is almost parallel to
971 the boundary and the direction of slip, yielding a strain of c. 12. The marker cannot be traced
972 in Zone III. **b)** Zoom of Zone I marked in a) consisting of relatively uncomminuted, angular
973 particles. **c)** Zoom of Zone II and III marked in a). Particles are progressively comminuted with

decreasing distance from the discrete principal slip surface that may be lined by recrystallized grains or a zone of decarbonation. **d)** Sample from experiment s959, stopped after an equivalent displacement of 1.1 cm (experimental conditions: 1 m/s target velocity, 8.5 MPa normal stress, water-dampened). Almost no comminution has taken place and no Zone III has developed.

Figure 7. Thickness of textural layers. Thickness in a) room-dry samples and b) water-dampened samples from experiments performed at a slip velocity of 1 m/s and a normal stress of 8.5 MPa. Blue symbols, bulk sample thickness; red symbols, textural Zone I or low-strain zone; magenta symbols, textural Zone II or intermediate-strain zone; black symbols, textural Zone III or high-strain zone. Black arrow in Fig. 7a illustrates thickening of Zone II with increasing displacement. (Note that small bulk- and Zone I-thickness at low displacement is likely due to loss of incohesive material, while it is unlikely that compacted material from Zone II was lost during sample preservation.)

Figure 8. Progressive development of textural zones. SEM backscattered images from **a)** sample s874 (1 mm/s, 27.5 cm total equivalent displacement, 8.5 MPa, room-dry conditions), **b)** s953 (1 m/s, 13 cm displacement, 8.5 MPa, room-dry conditions), **c)** s881 (1 m/s, 43 cm displacement, 8.5 MPa, room-dry conditions), and **d)** s961 (water-dampened, 1 m/s, 43 cm displacement, 8.5 MPa). Room-dry samples show progressive deformation with increasing displacements (b-c). Red arrows point at shear bands and secondary, abandoned slip surfaces. Yellow arrows show open Riedel fractures cutting through bulk of sample.

Figure 9. Microstructural features in high-velocity, high-displacement experiments. a) Sintered grains in c. 50 µm wide zone in the calcite gouge adjacent to the principal slip surface in sample from experiment s886 performed at 3 MPa normal stress, an equivalent slip rate of 1 m/s, with a total displacement of 2.5 m, and in room-dry conditions. In the lower region of the image, the dark-colored dolomite strain marker can be seen. **b)** Zoom of sintered zone in a). **c-e)** Evidence of decarbonation in the high-strain layer (red arrow in c)) as suggested by the light color in backscattered electron image (c) or high relative abundance of Ca as determined by EDS analysis (d). Images shown are from sample s898 (8.5 MPa, 1 m/s, 1.5 m total

displacement, water-dampened conditions). e) Zone of decarbonation and/or recrystallization in sample s961 (see f) for zoom of possibly decarbonated recrystallized grains in the area of the slipping zone marked in e). **f-h)** Zones of likely dynamically (f, g) and possibly in parts statically (h) recrystallized grains in water-dampened (f, h) and room-dry (g) experiments. Recrystallized grains are orientated in the orientation of shear (sinistral). Note in f) the secondary shear surface a few microns from and parallel to the principal slip surface cutting through the recrystallized zone, supporting the conclusion that grains were recrystallized dynamically. Images are from samples f) s961 (water-dampened, 8.5 MPa, 1 m/s, 0.43 m displacement), g) s943 (room-dry, 8.5 MPa, 1 m/s, 1.3 m displacement) and h) s962 (water-dampened, 8.5 MPa, 1 m/s, 2.1 m displacement).

Figure 10. Strain-marker characteristics. a) The two margins of the strain marker are not sheared to the same degree. Example from experiment s886 (room-dry, 1 m/s, 3 MPa, 2.5 m). **b)** The marker is also sheared towards boundary-parallelism on the side of the gouge layer, where strain does not usually localize in some cases (s962, s874 and s882).

Figure 11. Strain distribution in the gouge layer. Strain vs. Total Displacement for the **a)** low-, **b)** intermediate-, and **c)** low- and intermediate-strain zones in samples from experiments performed at 8.5 MPa normal stress, a slip rate of 1 m/s and room-dry (red symbols) and water-dampened (blue symbols) conditions, respectively. Samples where the relatively low thickness suggests poor sample preservation were not considered as not to bias the strain estimate. **d)** Strain vs. Total Displacement for the high-strain zone. Red box shows area of zoom to the right. Color-coding as in legend on the far right (red and blue symbols: room-dry water-dampened experiments, respectively, performed at 1 m/s and 8.5 MPa like in a), b), and c); black symbols: room-dry experiments performed at 1 mm/s and 8.5 MPa; orange and cyan symbols: 1 m/s and 15 and 20 MPa, respectively). In the low- and high-strain zones, there is a slight and a significant, respectively, dependence of the strain on the total displacement. No significant dependence is present in the intermediate-strain zone.

Figure 12. Normal-stress dependence of strain localization. The sum of the strains hosted in the low- and the intermediate-strain zones against the total equivalent displacement for

1030 experiments performed at 3 MPa (blue symbols), 8.5 MPa (teal symbols), 15 MPa (orange
1031 symbol), and 20 MPa (red symbol) normal stress. For a given displacement, there is no
1032 systematic variation of the strain with the normal stress.

1033 **Figure 13. Dependence of the strain distribution on the radial position I.** SEM backscattered
1034 images of three sections cut as shown in the sketch from the water-dampened sample s961
1035 that had experienced 43 cm of total equivalent displacement, a slip velocity of 1 m/s, and a
1036 normal stress of 8.5 MPa. Due to the annular geometry of the sample, the sections from
1037 different radial positions [a) closest to the center of the sample, b) further to the outer radius,
1038 and c) closest to the edge of the sample] experienced different maximum velocities and
1039 displacements.

1040 **Figure 14. Dependence of the strain distribution on the radial position II.** SEM backscattered
1041 images of three sections cut as shown in the sketch from the room-dry sample s886 that had
1042 experienced 2.5 m of total equivalent displacement at a slip velocity of 1 m/s and a normal
1043 stress of 3 MPa. Due to the annular geometry of the sample, the sections from different radial
1044 positions [a) closest to the center of the sample, b) further to the outer radius, and c) and d)
1045 closest to the edge of the sample] experienced different maximum velocities and
1046 displacements. d) shows the full length of the section in c) including the part of the sample
1047 where it was in contact with the outer confining steel ring.

1048 **Figure 15. Location of slip localization in different experimental assemblies. a)** The
1049 experimental configuration used in gouge experiments by Beeler et al. (1996) uses a confining
1050 Teflon ring that is split in two half. The upper ring is stationary, while the lower rotates,
1051 causing a slip discontinuity along the jacket split and the gouge to localize adjacent to the
1052 jacket split. **b)** The all-steel annular gouge holder used with SHIVA has a true “bucket-and-lid”
1053 configuration: All parts belonging to the “bucket” (white parts) are e.g. stationary, while the
1054 “lid” (grey parts) is rotating, causing a slip discontinuity at the surfaces in contact (marked in
1055 red). The localization of slip/strain within the gouge layer (dotted region) nucleates at this
1056 discontinuity. Thus, the location of the principal slip surface (marked in blue) is dependent on
1057 the boundary conditions. **c)** The sample assembly used with Rosa consists of full rock cylinders

and an outer Teflon ring that confines the gouge. With Rosa, the upper column is used to apply the rotation. If the Teflon ring remains stationary, they form a “bucket”. The rotation upper piston acts as the “lid”. The slip discontinuity and the accordingly forming principal slip layer are again marked in red and blue, respectively. The Teflon ring may rotate, if it sits more tightly on the upper cylinder. In that case, the slip discontinuity will be around the lower piston and the principal slip layer will form on the stationary side of the gouge layer. The same basic configuration is used in the Phv-apparatus in Kochi, Japan, except that the holder there is annular.

8. Tables

Table 1. Experimental conditions.

Table 2. Results. Thickness of textural layers and accumulated strain.

		Experiment	Normal stress (MPa)	Equivalent slip rate (m/s)	Total equivalent displacement (m)	Applied bulk strain [a]	Applied bulk strain rate (1/s)	SEM?
a)	**Room-dry**	s897	3	1	0.29	96.7	333.3	Y
		s886	3	1	2.5	833.3	333.3	Y
		s883	8.5	0.001	0.052	17.3	0.3	Y
		s884	8.5	0.001	0.15	50.0	0.3	Y
		s874	8.5	0.001	0.275	91.7	0.3	Y
		s882	8.5	0.001	0.4	133.3	0.3	Y
		s885	8.5	0.001	1.5	500.0	0.3	Y
		s873	8.5	1	0.08	26.7	333.3	N
		s953	8.5	1	0.13	43.3	333.3	Y
		s871	8.5	1	0.28	93.3	333.3	N
		s887	8.5	1	0.29	96.7	333.3	Y
		s881	8.5	1	0.43	143.3	333.3	Y
		s1013	8.5	1	0.43	143.3	333.3	N
		s952	8.5	1	0.5	166.7	333.3	N
		s896	8.5	1	1.3	433.3	333.3	Y
		s943	8.5	1	1.3	433.3	333.3	Y
		s875	15	1	0.14	46.7	333.3	Y
		s889	20	1	0.29	96.7	333.3	Y
b)	**Water-dampened [b]**	s1004	8.5	0.001	0.2	66.7	0.3	Y
		s1006	8.5	0.01	0.2	66.7	3.3	Y
		s1007	8.5	0.01	0.43	143.3	3.3	Y
		s959	8.5	1	0.011	3.7	333.3	Y
		s895	8.5	1	0.2	66.7	333.3	Y
		s961	8.5	1	0.43	143.3	333.3	Y
		s898	8.5	1	1.5	500.0	333.3	Y
		s962	8.5	1	2.1	700.0	333.3	Y

[a] for a sample thickness of 3 mm, [b] 20 wt.% distilled H_2O

Table 1. Experimental conditions.

Sample	Total Displacement (m)	Bulk strain	Thickness (mm) [a]				Strain			
			Zone I	Zone II	Zone III	Bulk sample	Zone I	Zone II	Zone I + II	Zone III [b]
a) Room-dry, normal stress: 8.5 MPa, slip velocity: 1 m/s										
s953	0.13	87	0.960	0.530	-	1.490	1.96	14.30	16.26	81
s887	0.29	118	1.365	0.760	0.340	2.465	-	2.90	3.51	116
s881	0.43	203	1.290	0.440	0.601	2.120	0.61	6.31	6.92	201
s896	1.3	718	1.210	0.300	0.300	1.810	1.23	12.71	13.94	715
s943	1.3	855	1.250	0.145	0.125	1.520	0.83	11.43	12.26	853
b) Water-dampened, normal stress: 8.5 MPa, slip velocity: 1 m/s										
s959	0.0011	1	1.26	0.14	-	1.40	0.38	4.33	4.72	0.01
s895	0.2	242	0.62	0.00	0.21	0.83	0.79	-	0.79	242
s961	0.43	243	1.34	0.23	0.20	1.77	0.85	28.64	29.49	239
s898	1.5	926	1.30	0.14	0.18	1.62	1.03	4.70	5.73	925
s962	2.1	1233	1.16	0.21	0.33	1.70	2.90	11.43	14.33	1232
c) Normal stress: 8.5 MPa, slip velocity: 0.001 m/s										
s883	0.052	28	1.44	0.22	0.20	1.86	0.87	2.36	3.23	27
s874	0.275	145	0.83	0.45	0.62	1.90	3.27	7.12	10.39	142
s882	0.4	181	1.09	0.60	0.53	2.22	2.75	5.40	8.14	178
s885	1.5	1322	0.69	0.21	0.24	1.14	0.40	2.75	3.21	1321
d) Normal stress: 3 MPa, slip velocity 1 m/s										
s897	0.29	155	1.49	0.29	0.09	1.87	1.34	5.40	6.74	153
s886	2.5	1887	0.88	0.22	0.23	1.33	1.60	2.79	4.39	1885
Normal stress: 15 MPa, slip velocity 1 m/s										
s875	0.143	93	0.72	0.52	0.31	1.54	0.80	3.17	3.97	91
Normal stress: 20 MPa, slip velocity 1 m/s										
s889	0.2	135	0.74	0.22	0.53	1.49	1.33	8.14	9.47	133

[a] approximate values, since thickness of zones varies across the length of the sample

[b] lower bound (displacement hosted in high-strain layer divided by bulk sample thickness)

Table 2. Results. Thickness of textural layers and accumulated strain.

Chapter III

Frictional behavior of fluid-pressurized calcite gouge sheared at seismic velocity

(This study was performed in collaboration with Giulio Di Toro, Thomas Mitchell, Takehiro Hirose, Steven Smith and Kentaro Hatakeda. I performed all the work described in this chapter. XRD analysis was performed by Federico Zorzi and Osamu Tadai. I was initially assisted in the laboratory by Kentaro Hatakeda. The material presented here was discussed with Giulio Di Toro, Thomas Mitchell, Takehiro Hirose, and Steven Smith.)

Abstract

Fault slip generally occurs in a thin principal slip zone commonly within highly-comminuted fault gouge; thus the gouge's properties play an important role in the mechanical behavior of faults. The presence of fluids in natural fault zones affects the faults' strength and the nucleation and propagation of earthquakes. It was shown previously that calcite-bearing cohesive rocks are more prone to slip in the presence of water (Violay et al., 2013). Now we present experimental results on the frictional behavior of fluid-pressurized calcite gouges.

A series of gouge experiments was conducted at the Kochi Institute for Core Sample Research in Kochi, Japan, using a rotary-shear apparatus equipped with a servo-controlled pore-fluid pressure system. For the experiments an annular metal and Teflon holder with an inner and outer radius of 30 and 60 mm, respectively, was used. Circa 3 mm thick layers of calcite gouge derived from Carrara marble with a grain size < 180 µm were sheared in water-saturated or room-dry conditions. For the wet experiments, distilled water was used as the pore fluid and the gouge was saturated before each experiment. The fluid pressure can be controlled either in pressure or in volume control mode. The applied effective stress σ_{eff} ranged from 1 to 12 MPa and the pore fluid factor $\lambda=p_f/\sigma_n$ from 0.15 to 0.7. The slip velocity was applied in steps (mostly 1 mm/s, 1 m/s and 1 mm/s) for total displacements of 5 to 22 m. During the experiments, the shear torque, the axial displacement of the gouge layer and the pore-fluid pressure/volume were measured. The temperature evolution was monitored via a thermocouple sitting close to where the principal slip surface usually develops within the gouge layer. After an experiment, the sample was air-dried and preserved in order to analyze the developed microstructures. Microanalytical techniques included scanning electron microscopy (SEM), energy-dispersive X-ray diffraction (EDS), Raman spectroscopy and X-ray diffraction (XRD).

Microstructures of room-dry and water-saturated post-experimental samples show intense grain-size reduction and comminution. Slip appears to be localized on one or more slip surfaces that are often lined by zones of recrystallization that appears to have occurred at least partly dynamically. Cavities and the geometric arrangement of recrystallized grains show possibly evidence of grain boundary migration aided by diffusion creep. Grey or black material

covering the slip surface of several samples was identified as disordered carbon by Raman spectroscopy indicating decarbonation of the calcite has taken place. Raman spectroscopy as well as SEM and XRD analysis detected the presence of PTFE (Teflon) or its decomposition products in several of the samples sheared for large displacements. Thus, only the mechanical data for experiments < 5.5 m are interpreted, because at larger displacement, there are likely influenced by the Teflon contamination.

The mechanical data of the room-dry gouges show a relatively high steady-state shear stress when sliding at low velocity (1 mm/s), while the shear stress in the water-saturated gouges is significantly lower for a given effective normal stress. The degree of compaction is relatively high in saturated experiments. Pressurization, as evidenced by the pore-pressure increase measured in undrained experiments and by the fluid-volume decrease in drained conditions, is inferred to be due to the compaction, as temperatures are still relatively low when sliding at 1 mm/s. The lower shear stress of water-saturated gouges as compared to room-dry conditions is attributed to intergranular lubrication and to the lower calcite fracture surface energy accelerating subcritical crack growth, consistent with the high degree of compaction.

At the initiation of sliding at high velocity weakening in saturated gouges occurs abruptly, while the room-dry gouges show a pronounced strengthening phase before the onset of weakening. Additionally, for a given effective normal stress, the peak stress is lower for higher pore-fluid factors $\lambda = \frac{p_f}{\sigma_n}$. The weakening in room-dry and water-saturated gouges sheared at high velocity likely occurs by flash heating, which is accelerated in the presence of fluids by subcritical crack growth. Consistent with flash heating, the presence of carbon on the slipping surface of our calcite samples indicated that decarbonation has occurred even though bulk temperatures were lower than the decarbonation temperature. At high velocity, intense frictional heating leads to thermal pressurization and subsequent decrease of the shear stress in the experiments performed in undrained conditions. Thermal pressurization is most likely caused by thermal expansion of the pore fluid (water), as the temperatures should be too low to induce extensive decarbonation.

Zones of recrystallized grains adjacent to the principal slip surfaces possibly featuring microstructures characteristic for grain boundary sliding aided by diffusion creep suggest that strain was not only accommodated by frictional processes, but possibly by superplasticity. At larger displacements, the similarly low steady-state shear stress of room-dry and water-saturated gouges, that is not significantly influenced by thermal pressurization, is roughly consistent with values calculated using the law for superplastic behavior given by Schmid et al. (1977).

The experimental results suggest that the presence of water in carbonate-bearing faults facilitates earthquake nucleation and even more so if the fluids present are pressurized. This might explain the long-lasting earthquake sequences e.g. of Umbria-Marche and L'Aquila hosted on carbonate-bearing faults.

1. Introduction

Fluids, mostly H_2O and CO_2, are abundant at depths due to their release from hydrous minerals at high temperature and pressure conditions and their slow ascent due to minimal hydraulic connectivity to the free surface (Miller, 2013). Indeed, field evidence for presence of fluids in fault zones is ubiquitous, including hydrothermal fracturing and mineral vein precipitation (Sibson, 1981). It has been widely recognized that fluids trapped in fault zones may play a fundamental role in controlling the fault's strength and earthquake nucleation, propagation and arrest (Hubbert and Rubey, 1959; Sibson, 1973; Lachenbruch, 1980; Rice, 1992; Hickman et al., 1995), due to the relationship between shear stress, effective stress and pore-fluid pressure described by the Terzaghi law (Terzaghi, 1923; Nur and Byerlee, 1971). Frictional heating – unless it triggers endothermic mineral reactions which will inhibit a further temperature rise (Sulem and Famin, 2009; Brantut et al., 2010, 2011) – will generate high pore pressures that will decrease the effective stress on the fault which may ultimately lead to fault weakening (Rempel and Rice, 2006; Rice, 2006; Segall and Rice, 2006; Rudnicki and Rice, 2006). If a high pore pressure is maintained in a fault zones greatly depends on its permeability (Mitchell and Faulkner, 2008; Faulkner et al., 2010), thus fault zones may act as a fluid barrier (Byerlee, 1990; Rice, 1992; Faulkner and Rutter, 2001). Permeability may also evolve during the seismic cycle, being high immediately after an earthquake due to newly formed fractures, and decreasing over time due to compaction, leading to renewed fluid overpressures (i.e., "fault-valve behavior"; Sibson, 1990, 1992).

A second class of fluid-related effects on deformation are physico-chemical mechanisms. Among these are pressure solution and other mechanisms controlled by diffusive processes (e.g., Rutter 1976, Robin 1978; Wheeler, 1992), subcritical cracking (Rice, 1978; Atkinson, 1984), or (syntectonic) reaction weakening (Wintsch et al., 1995; Collettini et al., 2004; Wibberley, 2005). These physico-chemical mechanisms may act to weaken a fault, even though they depend greatly on the chemistry and mineralogy of the involved fluids and rocks, respectively.

Particularly the effect of CO_2 and H_2O-rich fluids on the mechanical behavior of carbonate rocks has been of interest in recent years due to two long-lasting earthquake

sequences, the Umbria-Marche (1997-1998; Cocco et al., 2000; Chiaraluce, 2004; Collettini et al., 2009) and L'Aquila (2008-2009; Chiaraluce et al., 2011; Chiaraluce, 2012) sequences that hit Central Italy. In the case of the L'Aquila 2008-2009 sequence, most of the aftershocks and possibly the main shock (Speranza and Minelli, 2014) nucleated and propagated within carbonate rocks (Chiaraluce et al., 2012; Valoroso et al., 2014). In the two earthquake sequences, fluid (over)pressures likely played a major role as confirmed by borehole drilling (Chiodini and Cioni, 1989; Collettini and Barchi, 2002) and seismological modeling (Miller et al., 2004; Di Luccio et al., 2010; Terakawa et al., 2010) that provided evidence of high-pressure fluids at depth. Further evidence of fluid overpressures in the Umbria-Marche region might be provided by the long-term geochemical monitoring of gases that suggested syntectonic decarbonation to occur (Italiano et al., 2009), which would lead to further pressurization if permeabilities are sufficiently low.

The observed high pore-fluid pressure does not necessarily explain the notably complex nature and prolonged duration of the earthquake sequences of Umbria-Marche and L'Aquila. Laboratory experiments on carbonate-bearing rocks aimed to further understand the weakening process at seismic slip rates (c. 1 m/s) were performed by Violay et al. (2013, 2014). They found that in the presence of pressurized pore fluids, carbonate-bearing rocks are more prone to slip than in dry conditions, which they attributed to enhanced subcritical crack growth. Since, firstly, in most mature fault zones slip occurs within a thin layer of fault gouge, and secondly, previous studies have shown that cohesive rocks and gouges of the same lithology may show significantly different weakening behavior (Proctor et al., 2014; Smith et al., 2015), we aimed to extend the study of Violay et al. (2013) by conducting intermediate- to high-velocity rotary-shear experiments on calcite fault gouges. In the following, we specifically address the question whether fluid-overpressure by frictional heating can develop at slip velocities and over slip distances typical for major crustal earthquakes and whether this thermal pressurization influences the dynamic weakening of the fault gouges. Microanalysis of the sheared calcite gouges allowed us to propose alternative weakening mechanisms that would explain the behavior observed in nature.

2. Material and Methods

2.1.Experimental Set-Up

The experiments were conducted with the "*Phv*" rotary-shear friction apparatus installed at the Kochi Institute for Core Sample Research/JAMSTEC in Nankoku, Japan, which is equipped with a 30 kW servo-controlled electric motor and a gear system that can reduce the velocity by a factor of 100 (Tanikawa et al., 2012). Maximum rotation speed and torque are 660 rpm and 700 Nm, respectively. The rotation is applied from the lower part of the vertical column (Fig. 1a), so that the torque is measured at the upper part, where the axial load is applied. The servo-controlled axial loading system can apply a maximum load of 100 kN (Tadai et al., 2009; Tanikawa et al., 2012). The axial load and displacement (i.e., the shortening or dilation of the sample in axial direction) are monitored via a load cell and a displacement transducer, respectively (Fig. 1a). Data were recorded at an acquisition rate of 1 kHz.

The *Phv*-apparatus is equipped with a servo-controlled pore-fluid pressure system (Fig. 1b). Initial pore pressure is build up pneumatically (Fig. 1b, "*P*") and can be increased up to 50 MPa (Tadai et al., 2009). During an experiment, the fluid pressure is monitored with two pressure gauges, one upstream ("P_{up}") and one downstream ("P_{down}") of the sample, and is adjusted via a servo-controlled moving piston ("*M*"). For permeability measurements, the downstream fluid pressure can also be applied using gas pressure ("*G*") that, however, is not servo-controlled. If this is not in use, valve 3 (Fig. 1b) is kept closed. The pore fluid is introduced into the sample through tubes ending in the base plate of the stationary (upper) part of the sample holder ("upstream" of the sample) (Fig. 1c, yellow parts). The fluid outlet is located in the center of the ring, so the water should travel through the gouge material, before passing through the porous rotary base disc and spacers into the fluid-outlet tube in the center of the rotary part of the gouge holder (Fig. 1c, green parts) and further into the outlet tube in the stationary part of the holder. The system permeability (controlled by the porous base discs and spacers) is very high as was determined with an empty gouge holder with the steady-state flow method (see Section 2.2.2). The fluid inlet and outlet can be connected outside the sample holder by opening valve 2 (Fig. 1b). This "shortcut" ensures an equal fluid pressure upstream and downstream of the sample and helps to reach the target fluid-pressure faster

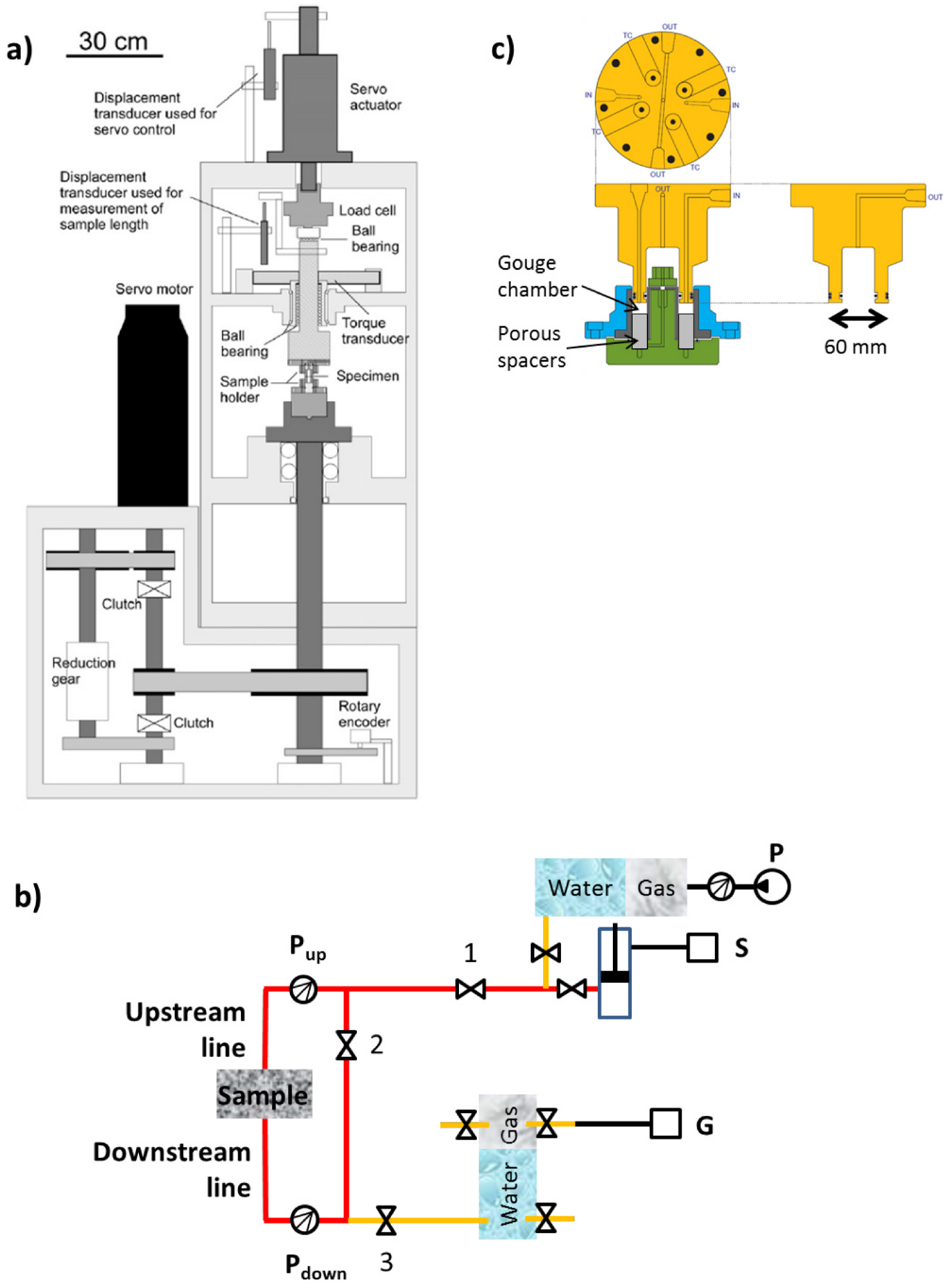

Figure 1. **Experimental Set-up. a)** Schematic diagram of the rotary-shear apparatus installed at the Kochi Institute for Core Sample Research (from Tanikawa et al., 2012). **b)** Schematic diagram of the pore-fluid pressure system. Red: main fluid path, yellow: fluid path used to build up initial pressure or to control downstream pressure individually. ***S***: Main fluid-pressure control using moving piston to control fluid volume and pressure; P_{up}/P_{down}: upstream/downstream pressure gauge; *P*: Pneumatic pump to apply initial pressure; *G*: Gas-pressure control of down-stream pressure. **c) Gouge holder assembly.** Yellow: stationary parts; blue, green and grey: rotary parts. Grey: Teflon. "*IN*" and "*OUT*": fluid inlet and outlet, respectively. "*TC*": thermocouples. With the set-up used during the experiments, the upper part of the holder is almost fully extracted and the size of the sample chamber is adjusted by using porous spacers.

within the gouge layer. The pore pressure within the gouge layer still cannot be controlled perfectly since the pressure gauges are located outside the sample chamber (Fig. 1b), but opening the shortcut at least minimizes the effect of the relatively impermeable principal slip layer that forms in the gouge layer close to the stationary side base disc, which acts as a fluid barrier and would otherwise hinder the pore-fluid pressures up- and downstream of the sample to equilibrate.

2.2.Experimental Procedures

2.2.1. Velocity-step experiments

Seventeen calcite gouge were performed at velocities of 1 mm/s–1 m/s, effective normal stresses of 3–12 MPa, with total displacements ranging from c. 5 to 20 m, and in different ambient conditions (i.e., room-dry and fluid-saturated). The details of the experimental conditions are listed in Table 1a.

Three experiments were performed with room-dry gouges and fourteen with fluid-saturated gouges. In the saturated-gouge experiments, the initial effective pressure $\sigma_{eff} = \sigma_n - p_f$ (where σ_n is the normal pressure acting on the gouge layer and p_f is the pore-fluid pressure; Terzaghi, 1923; Skempton, 1960; Nur and Byerlee, 1971) at the start of the experiments ranged from 1 to 12 MPa and the initial pore-fluid factor $\lambda = \frac{p_f}{\sigma_n}$ (Hubbert and Rubey, 1959) from 0.15 to 0.7. The pressure p in a rock unit at a given depth is given by $p = \rho g h$ where ρ is the density of the overlaying rock or the pore fluid, h the depth, and g the gravitational constant. For a density $\rho_r = 2.5$ g/cm^3 typical for limestones or marble and a pore-fluid density $\rho_f = 1$ g/cm^3, $\lambda = 0.4$ (hydrostatic pressure). The fluid pressure approaches lithostatic values as λ approaches 1. Of the twelve fluid-pressure controlled experiments, ten were performed in pressurized sub-hydrostatic conditions (pore-fluid factor $\lambda < 0.4$) and two in super-hydrostatic conditions (λ=0.6 and 0.7, experiments phv305 and 290, respectively). In fluid-volume controlled conditions the pore-fluid factor changed with the fluid pressure.

Most experiments were performed applying up to three velocity steps. The first step had a velocity of 1 mm/s and a displacement of c. 30 cm, the second a velocity of 1 m/s with an acceleration of 0.5 m/s^2 and varying displacements, and the third again of 1 mm/s. In some

experiments only the first and second velocity steps were applied and one experiment (phv313) was performed at 1 m/s only. Both the low and high velocity were imposed using the high-speed gear. The switch between the velocity steps could be performed without losing the torque.

2.2.1.1. Fluid-pressure controlled experiments

A total number of twelve experiments was performed under fluid-pressure controlled (drained) conditions (Table 1b). Before the experiment, the normal stress and fluid pressure were increased stepwise to reach the target normal stress and fluid pressure, which are then held constant throughout the experiment. This is done by adjusting the fluid volume in the system. E.g., when the fluid is pressurized due to compaction or increase in temperature, the piston (Fig. 1b, "*S*") moves out to reduce the fluid volume in the system and keep the pore pressure down. When the sample dilates again or when the temperature goes down reducing the volume of the fluid, the piston moves inward again to push the fluid back into the system. However, the fluid might not flow back into the sample easily, because after shearing the permeability of the gouge will be reduced. It was tried to minimize this effect by opening Valve 2 (Fig. 1b) in most of the experiments (Valve 2 was closed in only two experiments, phv291 and 292).

2.2.1.2. Fluid-volume controlled experiments

Two of the seventeen velocity-step experiments were performed under fluid-volume controlled (undrained) conditions. Before the experiment, the normal stress and fluid pressure were increased stepwise to reach the initial conditions of σ_n = 10 MPa and $p_{f,initial}$=1.5 MPa, leading to an initial effective stress of $\sigma_{eff,initial}$=8.5 MPa. Valves 2 and 3 (Fig. 1b) upstream and downstream of the sample were then closed to ensure a constant volume of fluid during the experiment. Due to compaction of the gouge or increase in temperature, the fluid pressure and thus the pore-fluid factor can increase during the experiment.

2.2.2. Permeability measurements

The permeability of the system and of the gouge layer was measured in three experiments using the steady-state flow method (Bernabe, 1987) (Table 1c). A constant

differential fluid pressure is applied across the sample causing a steady flow of the fluid. In our case, the higher pressure was applied upstream of the sample, so that – to account for the "loss" of the fluid that flowed through the sample and keep the upstream pressure constant – the piston moved inwards (Fig. 1b, "*S*") increasing the water volume. This fluid-volume increase per unit time was monitored and used to calculate the permeability *k*:

$$k = \frac{Q}{A} * \frac{\eta L}{(P_{up} - P_{down})} \quad (1)$$

where *Q* is the flow rate, *A* and *L* the cross-sectional area and the thickness of the sample, respectively, η the viscosity of the flowing fluid, and P_{up} and P_{down} the up- and downstream fluid pressures, respectively.

2.3. Sample Preparation

The starting material used in our experiments was derived from Carrara marble, that was crushed and sieved to particle sizes < 180 µm. Fifteen grams of this synthetic calcite gouge was filled into the gouge holder in each experiments yielding a gouge layer thickness of c. 3 mm. The exact gouge layer thickness was measured before each experiment with the displacement transducer (Fig. 1a). In the saturated experiments, after measuring the exact gouge layer thickness at an axial load of 1 kN by subtracting the value shown by the displacement transducer from the known axial displacement for an empty holder, the holder was opened again and some distilled water that was used as the pore fluid was added to the starting gouge and left for c. one hour to accelerate water saturation. The gouge layer was then put under load again and saturated. For this purpose, the downstream line was left open to the atmosphere until water flow was steady and without air bubbles.

After an experiment, the sample holder was taken out of the apparatus and the sample was preserved. It was left to dry in air at least for 24 hours before parts of it were impregnated with epoxy resin for microstructural analysis. For SEM analysis, samples were cut normal to the sliding surface, either parallel and perpendicular to the slip direction. The section was then either polished in the presence of water with 1200, 2400 and 4000 grit SiC paper, followed by 4, 1 and ¼ µm diamond paste (if prepared at the Department of Geosciences in Padua), or polished using 1000 and 3000 or 5000 grit SiC paper and 1 and 0.3

µm de-agglomerated alpha alumina powder (Buehler Micropolish II) (if prepared at INGV in Rome). The samples were coated with carbon or chrome. Parts of each sample were preserved without epoxy resin to use for XRD analysis and Raman spectroscopy.

2.4.Microanalytical Techniques

Microstructural and mineralogical analysis was performed with scanning electron microscopy (SEM), X-ray diffraction (XRD), as well as Raman microspectroscopy. An account of the analytical techniques used with each sample can be found in Table 2. SEM-analysis of samples from seven experiments was performed using a JEOL JSM-6500F Field-Emission SEM at the Istituto Nazionale di Geofisica e Vulcanologia (INGV) in Rome. Images were taken mainly in backscattered electron mode (BSE) with an acceleration voltage of 8–10 kV and a working distance of 7.5–10 mm. In addition to obtaining images, the chemistry of some of the eight samples was analyzed using energy-dispersive X-ray spectroscopy (EDS). The advantage of this technique is that chemistry of a distinct point on the sample can be examined and directly qualitatively linked to the texture. EDS peak identification was done with the NIST DTSA-II software.

Qualitative XRD analysis was performed on six samples at the Geoscience Department of the University of Padua. For the XRD analysis, c. 5 g of a sample was crushed to very fine particle sizes. The samples contained parts of the slip surface as well as of the bulk material, yielding a broader view of the composition of a sample than with the EDS and Raman point analyses. The software package High Score Plus (PANalytical) was used for phase identification.

Finally, Raman spectroscopy was performed at the Chemistry department of the University of Padua. In Raman spectroscopy, a laser is directed at the unprepared sample and the scattered light, which energy is shifted due to an interaction with the molecules in the sample, is detected (Long, 1977; Colthup et al., 1990). This Raman shift is expressed in units of the wavenumber, i.e. the number of waves per unit length, typically in cm^{-1}. The chemistry of several points on the principal slip surface of eleven samples, in addition to the starting material, was investigated. An un-oriented laser with a wavelength of 532 nm and a power of 2 to 5 mW was used. Pinhole size was 25 µm and exposure time 10 s. A fluorescence correction

was performed automatically. The RRUFF™ database was used for the identification of the measured Raman spectra.

2.5.Thermodynamic calculations

Thermodynamic calculations were performed to determine 1) the expansion of pore fluids and the associated increase in the pore-fluid pressure and 2) the decarbonation temperature of calcite in without and with the presence of water. The thermal expansion of pore fluids *dV* can be calculated for a specific temperature rise *dT* and initial fluid volume *Vf*. We assume that only the volume of fluid in the pore space of the gouge layer $V_{f,gouge}$ is affected by the frictional heating. The thermal expansion then is

$$dV = \alpha \, dT \, V_{f,gouge} \quad (2)$$

with α being the coefficient of thermal expansion of water (assuming to be constant at $2.07*10^{-4}$ 1/°C), *dT* the temperature increase, and $V_{f,gouge}$ the fluid volume in the pore space of the gouge material. Then, if we assume, following Violay et al (in prep.), that the volume expansion is accommodated by the total water volume in the fluid system $V_{f,total}$, the pressure increase *dP* is

$$dP = \frac{\kappa \, dV}{(V_{f,gouge}+V_{f,total})} = \frac{\kappa \, \alpha \, dT \, V_{f,gouge}}{(V_{f,gouge}+V_{f,total})} \quad (3)$$

Where κ is the water incompressibility of $2.1*10^{9}$ Pa and $V_{f,total}$ the total fluid volume in the system.

The calculations of the decarbonation temperature were performed with the Perple_X software by James Connolly, which uses the method described in Connolly (1990) for calculations (unconstrained minimization computational mode). Thermodynamic input data were taken from the database by Holland & Powell (1998) (revised by the authors in 2002), appropriate for calculations at depths < 440 km. For the calculations, H_2O and CO_2 were selected as saturated fluids and CaO as the thermodynamic component. The stability of calcite ($CaCO_3$) and lime (CaO), respectively, was calculated for a specific pressure condition and for different temperatures and fluid compositions (0.01–99.99% CO_2).

3. Results

3.1.Mechanical data

3.1.1. Room-dry conditions

Three experiments were conducted in room-dry conditions with room-dry (phv299, 311) and oven-dry (phv301) starting material (Table 1a). Phv299 and 301 were conducted with 8.5 MPa normal stress applied and slid in three velocity steps (1 mm/s, 1 m/s, 1 mm/s) to a total displacement of 15.6 and 17.6 m, respectively. Phv311 was performed at a normal stress of 3 MPa; only two velocity steps were imposed and the total displacement was 5.5 m.

The experiments with dry gouges were carried out in room-humidity conditions. The gouges thus likely still contain a small amount of water. Previous studies have shown that this residual water can have an effect on the frictional behavior. For instance, Morrow et al. (2000) measured a coefficient of friction for dry and wet calcite gouges of 0.85 and 0.72, respectively (when sheared at a velocity of 0.5 µm/s and 100 MPa normal stress). Shimamoto and Logan (1981) on the other hand measured a coefficient of friction for *dry* calcite of $\mu = 0.74$, similar to the value Morrow et al. (2000) measured for wet calcite. Morrow et al. (2000) attributed the lower value of the dry friction coefficient measured by Shimamoto and Logan (1981) to the fact that the calcite gouge was not vacuum-dried at high temperature before testing, even though the experiments by Shimamoto and Logan (1981) were also performed at higher (confining) normal stress (300 MPa) and slip rate (20 µm/s), which will likely have contributed to the lower coefficient of friction. The steady-state coefficient of friction in our room-dry gouges sheared at 1 mm/s and 3–8.5 MPa ranges from 0.8–0.85 and is thus similar to Morrow et al.'s (2000) thoroughly dried gouges.

Shear Stress Evolution

The mechanical data of the two experiments performed at 8.5 MPa (phv299 and phv301) show a very similar frictional behavior (Fig. 2a). During the first velocity step (1 mm/s) the gouge has a steady-state shear strength of c. 7 MPa. When the velocity is increased to 1 m/s, the gouge experiences a renewed strengthening to a peak strength of c. 8 MPa. Weakening initiates after 12 cm of displacement at high velocity (not taking into account the

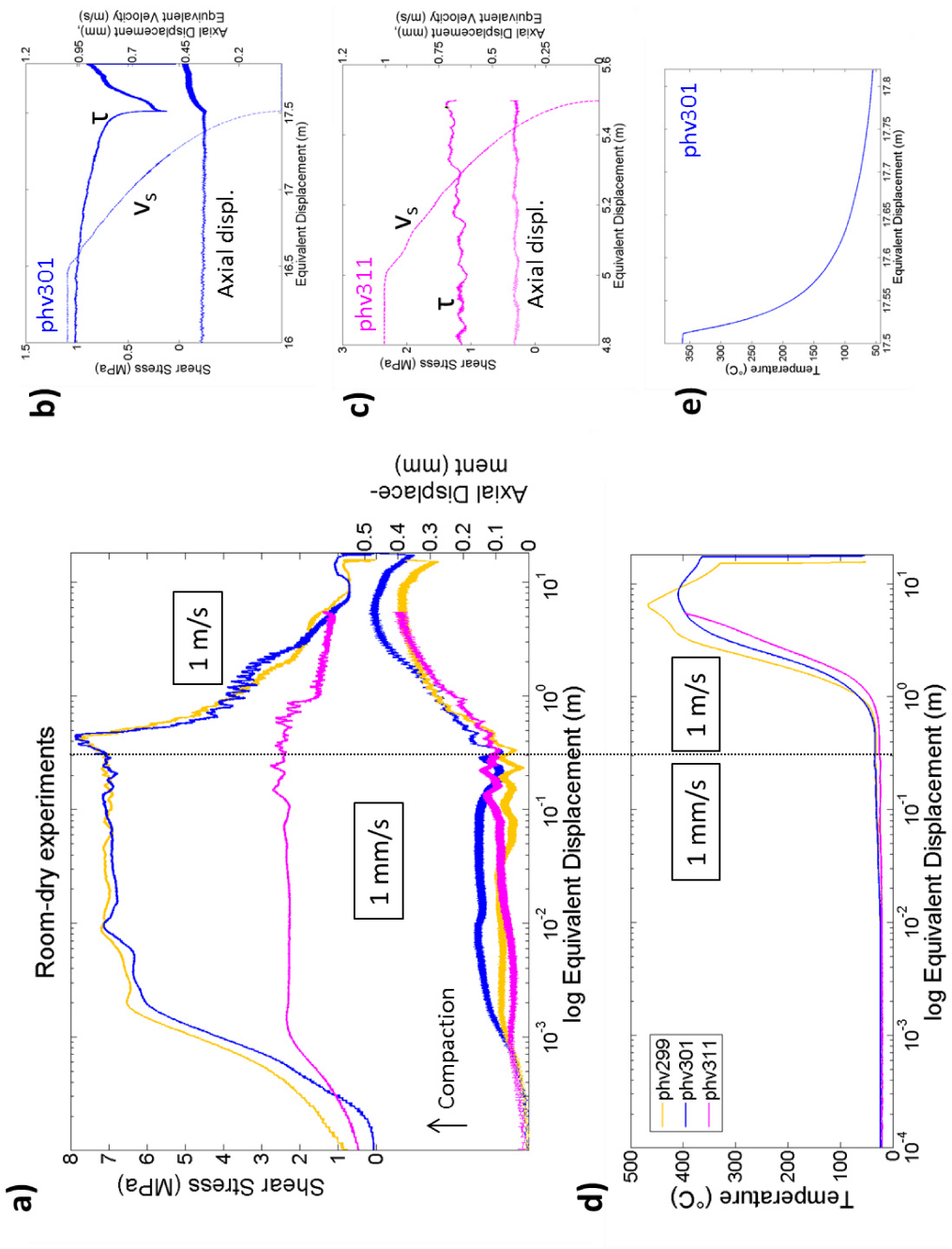

Figure 2. Mechanical data of room-dry experiments. a) Evolution of shear stress (primary y-axis) and axial displacement (secondary y-axis) with displacement (on logarithmic x-axis) of experiments performed in room-dry conditions, at a normal stress of 8.5 MPa (phv299, yellow curves; phv301, blue curves) and 3 MPa (phv311, magenta curves), respectively, and with slip velocities of 1 mm/s, 1 m/s, and – in the case of phv299 and 301 – 1 mm/s. The switch from velocity step 1 to step 2 is marked by the vertical dotted line. Positive changes in the axial displacement denote compaction, negative changes dilation of the gouge layer. **b-c)** Evolution with displacement (linear scale) of shear stress, axial displacement and equivalent velocity when the velocity is reduced at the end of the high-velocity step of **b)** experiment phv301 (blue curves, upper plot) and **c)** phv311 (magenta curves, lower plot). **d)** Evolution of temperature of the experiments shown in a). **e)** Temperature evolution with displacement (linear scale) during the third (low-) velocity step of experiment phv301.

displacement accumulated at low velocity sliding) and occurs in two stages: rapid weakening down to a shear stress of c. 4 MPa after 67 cm total displacement followed by more gradual weakening until the gouge reaches a steady-state shear strength of c. 1 MPa after c. 6 m. At the end of the high-velocity step, the velocity is gradually decreased down to a velocity of 1 mm/s (Fig. 2b, phv301) which – curiously – causes the shear stress to drop to c. 0.2 (corresponding to a coefficient of friction $\mu \approx 0.02$). During the 31 cm of displacement of this third velocity step at 1 mm/s, the shear stress then increases slowly to almost 1 MPa (Fig. 2b). The mechanical behavior is slightly different in experiment phv311 which was performed at lower normal stress of 3 MPa. During the first low-velocity step, the steady-state shear stress is c. 2 MPa (corresponding to a coefficient of friction that is slightly lower than that measured for the higher normal stress experiments). When the high-velocity step is induced, weakening initiates only after 35 cm of displacement. (See Chapter II, Fig. 4a of this thesis for plot of the strengthening phase vs. the normal stress.) The shear stress drops to c. 1.5 MPa and then gradually weakens further to 1.2 MPa until it slightly recovers to 1.4 MPa when the velocity is reduced to 0 mm/s at the end of the experiment (Fig. 2c).

Temperature

During the first low-velocity step, temperature increases slowly from room-temperature (22–23.5 °C) to 25 °C in the 3 MPa-experiment and to c. 34 °C in the 8.5-MPa experiments (Fig. 2d). The temperature increase during the high-velocity step appears to be relatively independent of the applied normal stress; maximum temperatures are c. 410–470 °C, with only slightly lower temperatures in the 3 MPa-experiment phv311. During the initial meters of displacement of the high-velocity step, the temperature increases continuously with increasing displacement, but then the rate with which the temperature changes decreases resulting in the temperature eventually staying constant at displacements of c. 3–5 m and even start to decrease at 6–8 m of displacement by 35–130 °C. When the velocity is reduced to 1 mm/s, the temperature decay follows a power law (Fig. 2e). E.g., after 5 cm displacement at low velocity, the temperature had decayed by 45–75%, with the faster decay in temperature occurring in the higher effective-stress experiments.

Axial Displacement

The axial displacement in the room-dry experiments (Fig. 2a) during the low-velocity step shows a compaction of the gouge layer of 50–160 µm which in experiment phv301 is followed by dilation of 60 µm. When the velocity is increased to 1 m/s, transient dilation of 5–30 µm is followed by compaction of 300–380 µm. Secondary dilation of c. 100 µm initiates after total displacements of c. 6.5 m in experiments phv299 and 301, respectively, which continues until the end of the high-velocity step. No dilation is observed in phv311, likely because the experiment was stopped at a much shorter displacement. In the 30 cm of displacement during third velocity step (1 mm/s) of experiments phv299 and 301, the gouge compacts again by c. 80 µm.

3.1.2. Fluid-saturated conditions

Of the twelve experiments conducted in fluid-pressure controlled experiments, ten were performed in pressurized conditions (pore-fluid factor $\lambda < 0.4$) and two in super-hydrostatic conditions (λ=0.6 and 0.7 in experiments phv305 and 290, respectively) (Table 1b). Two experiments (phv292 and 297) were performed under fluid-volume controlled conditions. In experiment phv292, Valve 2 (Fig. 1b), connecting upstream and downstream side of the sample, was closed. Equilibration of the fluid pressure upstream and downstream of the sample is thus controlled by the permeability of the sample, and the upstream and downstream fluid pressure may increase with different rates. Valve 2 was open in experiment phv297, causing upstream and downstream fluid pressure to equilibrate fast. The initial pore-fluid factor λ was 0.15 in both volume-controlled experiments. However, when the gouge layer is pressurized and the fluid-pressure increases, λ increases as well. The gouge samples were slid in three velocity steps (1 mm/s, 1 m/s, 1 mm/s), with the exception of phv300, 310, and 312 (only two velocity steps) and phv313 (only high velocity) (Table 1b). The mechanical behavior during each of the velocity steps is described separately in the following.

3.1.2.1. First velocity step (1 mm/s)

The first velocity step was conducted at an equivalent slip velocity of 1 mm/s. The gouge was slid to an equivalent displacements of c. 31 cm before the next velocity step was induced (Table 1b).

Shear-stress evolution

During the first low-velocity step, the pressurized gouges (λ of 0.15–0.33) exhibit a steady-state shear stress τ_{ss} ranging from 8.3 MPa at an effective normal stress of 12 MPa to τ_{ss}≈0.5 MPa at σ_{eff}=1 MPa (Fig. 3a). Steady state is reached after < 1 cm of displacement (strengthening to peak strength within 0.7–7 mm). In the experiments with a higher pore-fluid factor, the steady-state shear stress is drastically lower: it is reduced by 45% in phv305 (1 MPa effective stress, λ=0.6) and by 70% in phv290 (3 MPa, λ=0.7) compared to experiments performed at the same effective normal stress.

The frictional behavior of the fluid-volume controlled experiments (phv292 and phv297, Fig. 3a, grey curves) is similar to that observed in the fluid-pressure controlled experiments performed at the same normal stress (8.5 MPa) if Valve 2 (Fig 1b) was open as it was the case in experiment phv297. The steady-state shear stress is reached at displacements of c. 1.5 cm. In experiment phv292, where Valve 2 was closed during the experiment, the steady state is reached later and is decreased by c. 1 MPa, which corresponds to c. the same amount as the effective stress is decreased (Fig. 3a) due to a fluid-pressure increase of c. 1 MPa (Fig. 3e). The strengthening phase and peak strength are similar in fluid-volume and –pressure controlled conditions.

Temperature

During the first low-velocity step, temperature increases slowly from room-temperature (20.5–25 °C) to temperatures ranging from 22–31 °C (Fig. 3b). Larger temperature increases occur in the experiments performed at higher effective normal stresses > 3 MPa. The rate with which temperature increases is similar in the fluid-volume and –pressure controlled experiments (note the higher “starting” room temperature in experiments with apparently higher increase).

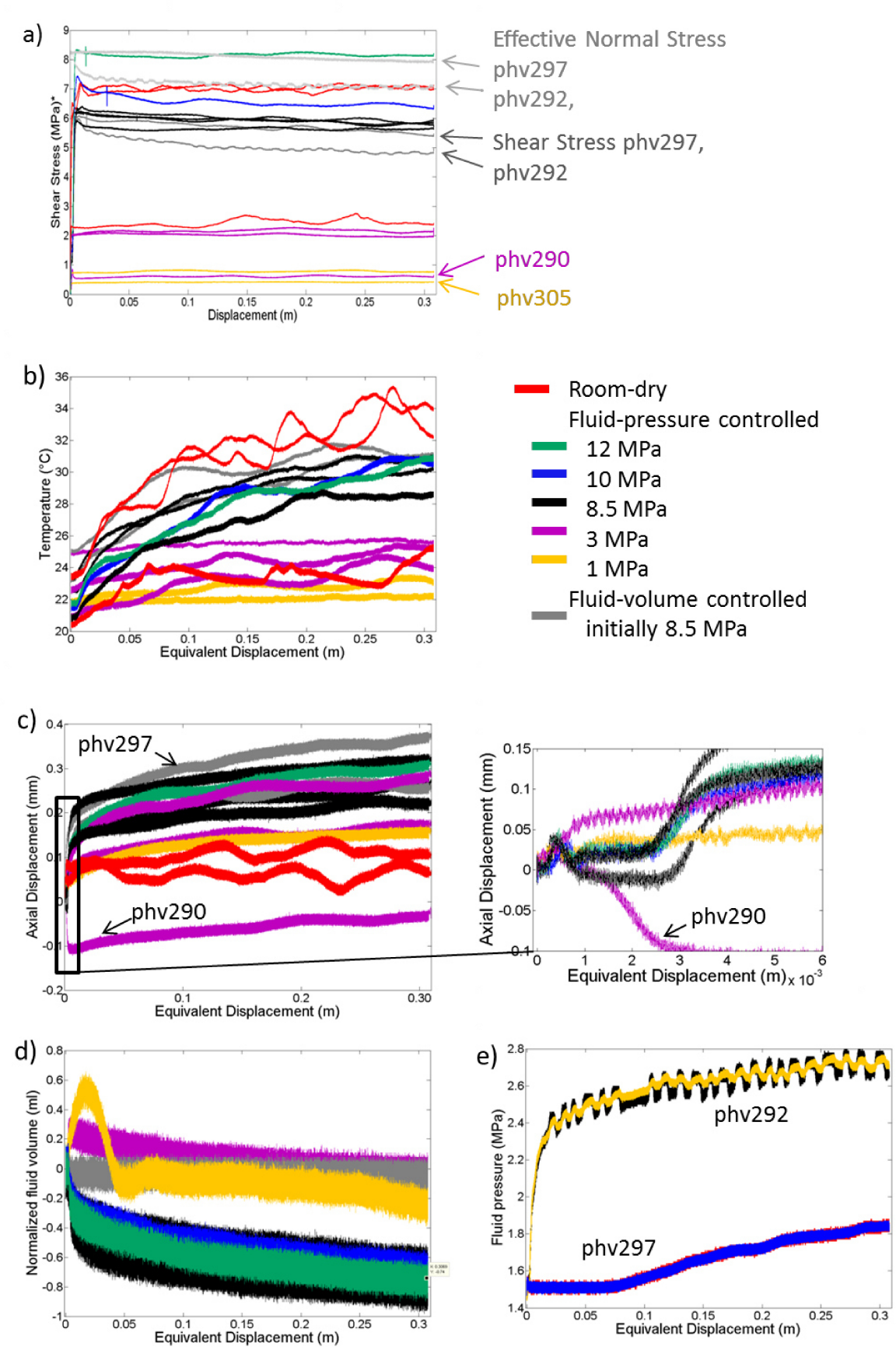

Figure 3. See next page for caption.

Figure 3. Mechanical data of the first velocity step (1 mm/s). Evolution with displacement of **a)** Shear stress (and effective normal stress only for volume-controlled experiments phv292 and 297, light grey curves), **b)** Temperature, **c)** Axial Displacement, **d)** Fluid Volume, and **e)** Fluid Pressure. Different colors correspond to different initial effective normal stresses as shown in the legend. Inset in **c)** shows zoom of the axial displacement during the first 6 mm of displacement. In **d)** only exemplary data are shown because of the large high-frequency oscillations. Note constant fluid volume in the volume-controlled experiment (grey curve). In **e)** the fluid pressure of phv292 is plotted in black and yellow (up- and downstream pressure, respectively) and of phv297 in blue and red. During the first low velocity step, upstream and downstream fluid pressures are equal for a given experiment.

Axial displacement

The axial displacement during the first low-velocity step of the fluid-pressure controlled experiments is generally characterized by initial compaction (20–60 µm) during the first 0.5 mm of displacement, which in the higher effective normal stress experiments is followed by transient dilation (5–35 µm) in the subsequent 0.5–2.5 mm displacement (zoom in Fig. 3c; black, blue and green curves). In all saturated experiments, the gouge then compacts (105–370 µm) until the end of the velocity step; the higher the effective pressure, the higher the degree of compaction (Fig 3c). In the super-hydrostatic experiment phv290, very large transient dilation (100 µm) is followed by only minor compaction (60 µm). In the fluid-volume controlled experiment phv292 (closed connecting valve) the axial displacement shows the same characteristics as in the pressure-controlled experiments. Phv297 (open connecting valve), however, compacts by 370 µm (higher net compaction than in any other experiment) and does not show any transient dilation, which is unique for the series of experiments we conducted.

Fluid-volume change

Because the fluid-pressure is held constant in the pressure-controlled experiments by adjusting the amount of fluid in the system, the change in fluid volume reflects the pressurization of the pore fluid during the experiment. Generally, the fluid-volume decrease is higher at normal stresses (Fig. 3d): In the first low-velocity step, the fluid volume decreases by 0.38 ml on average in the low (1–3 MPa) and 0.73 ml on average in the higher (8.5–12 MPa) effective-stress experiments. In some of the lower-σ_{eff} experiments (phv306, 310 and 290), a transient increase of 0.1 – 0.54 ml in the fluid volume occurs before the decrease.

Fluid pressure and pore-fluid factor

In the fluid-volume controlled experiments, upstream and downstream fluid pressures increase simultaneously throughout the low-velocity step (Fig. 3e). At the onset of sliding, the fluid pressure rises from its initial value of 1.47 MPa by c. 0.08 MPa during the first millimeter of slip. In phv292, fluid pressure stays constant for c. 1 mm displacement before it rises quite rapidly and reaches 2.3 MPa at a displacement of 1.5 cm. At larger displacements, the fluid pressure rises with a more moderate rate reaching 2.7 MPa at the end of the low-velocity step.

In phv297, after the initial rise by 0.08 MPa, the fluid pressure drops again to 1.52 MPa and only starts to increase at a displacement of 7.5 cm. Until the end of the low-velocity step, the fluid pressure rises quite linearly, reaching a maximum value of 1. 85 MPa. The pore-fluid factor, equal to 0.15 at the initiation of sliding, reaches a maximum of 0.32 and 0.22, respectively, in phv292 and 297.

3.1.2.2. High-velocity step

After 30 cm of sliding at a velocity of 1 mm/s, the velocity was increased by three orders of magnitude to 1 m/s. The torque was not lost in between the velocity steps and shearing continued uninterruptedly. As an exception, experiment phv313 was not sheared at low velocity prior to the high velocity step. The total displacement at high velocity ranged from 4.2 m (phv307) to 21.9 m (phv291) (Table 1b).

Shear-stress evolution

When the high velocity (1 m/s) is induced, the saturated gouges show a short initial strengthening (Fig. 4a, Fig. 5a, b) before they weaken dramatically. The length of the strengthening phase ranges between 1–15 mm and depends on the pore-fluid factor λ and the effective normal stress σ_{eff} (Fig. 5c, e). For a given effective normal stress, the strengthening phase is the longer, the higher the pore-fluid factor (Fig. 5c). For instance, in experiments performed at 3 MPa effective normal stress (purple symbols), the strengthening phase increases from 1.3 to 7.7 mm as λ increases from 0.17 to 0.7. The long strengthening phase of c. 1 cm at λ=0.17 occurs in experiment phv313 that did not have the first slow velocity step but was instead directly sheared at 1 m/s (Fig. 5c). [Note that these differences are small compared to the dry experiments, where the strengthening phase is c. 12 cm long (Fig. 5c, λ=0).] The length of the strengthening phase is similar in drained and undrained experiments performed at the same initial effective normal stress and pore-fluid factor (0.5–2 mm; Fig. 5c). Additionally, a higher pore-fluid factor appears to cause a decrease in the peak shear stress (Fig. 5e): in experiments performed at 1 and 3 MPa effective normal stress, for instance, the peak shear stress is reduced by c. 23 and 35% for a pore-fluid factor increase from 0.17 to 0.6 and 0.33 to 0.7, respectively. The strengthening phase and peak friction of phv290 (λ=0.7) could be affected by an overshoot of the slip rate that reached a value of 1.7 m/s before

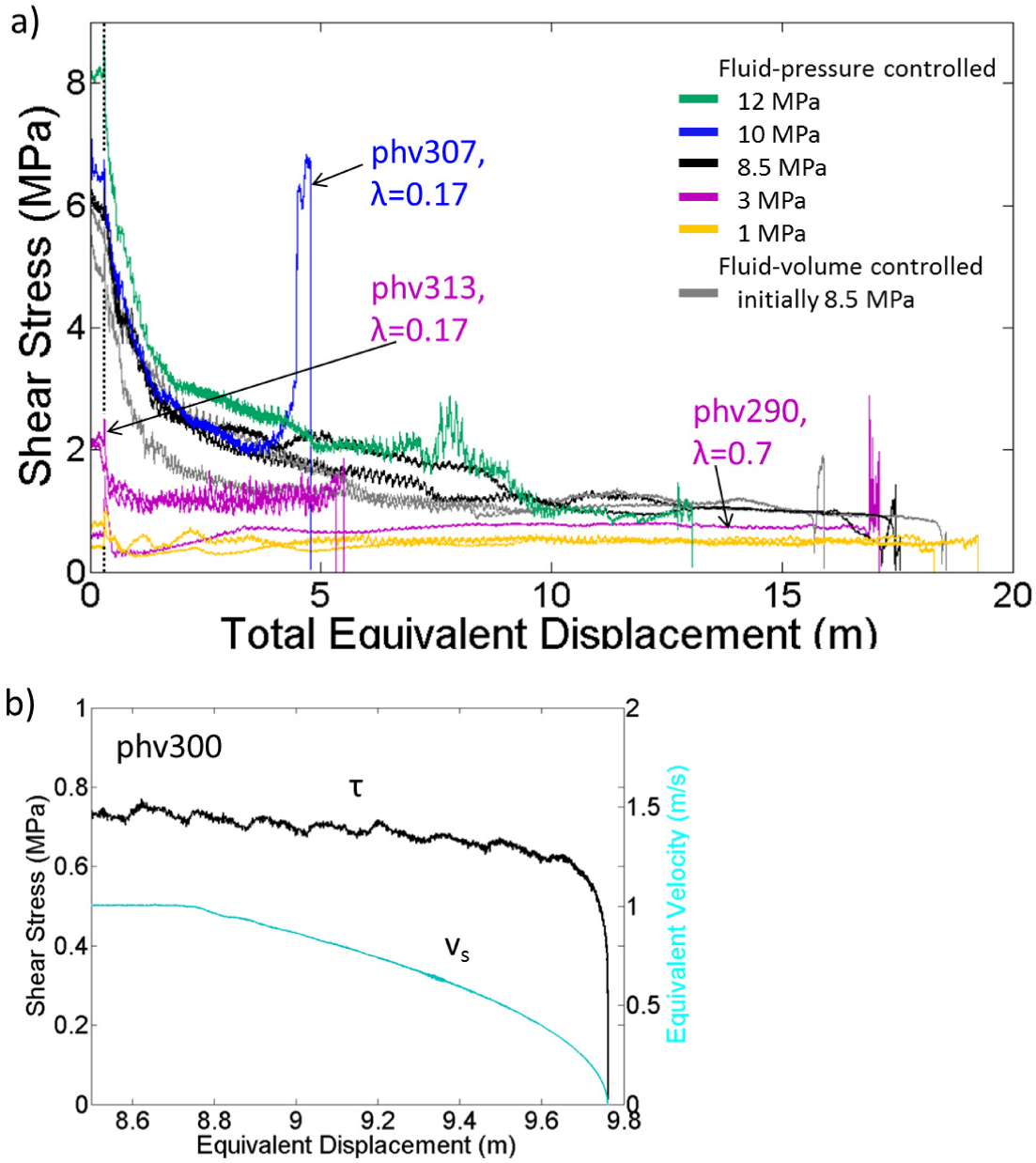

Figure 4. Shear-stress evolution of the saturated experiments. a) High velocity (1 m/s) is induced after 30 cm of displacement (denoted by dotted vertical line) and shear stress increases during a phase that lasts a few mm before peak strength is reached and dynamic weakening initiates. Renewed strengthening is due to the decrease in velocity at the end of the high-velocity step. Different colors correspond to different effective normal stresses as shown in legend: 12 MPa (green), 10 MPa (blue), 8.5 MPa (black and grey for pressure- and volume-control mode, respectively), 3 MPa (purple), and 1 MPa (yellow). Shown are exemplary data curves, the complete data set can be found in the Appendix C (***Fig. C1***). **b)** Zoom of the end of the high-velocity step of experiment phv300 (no third velocity step), showing that the shear stress (black curve) decreases when the equivalent velocity (cyan curve) is reduced from 1 m/s to 0 m/s.

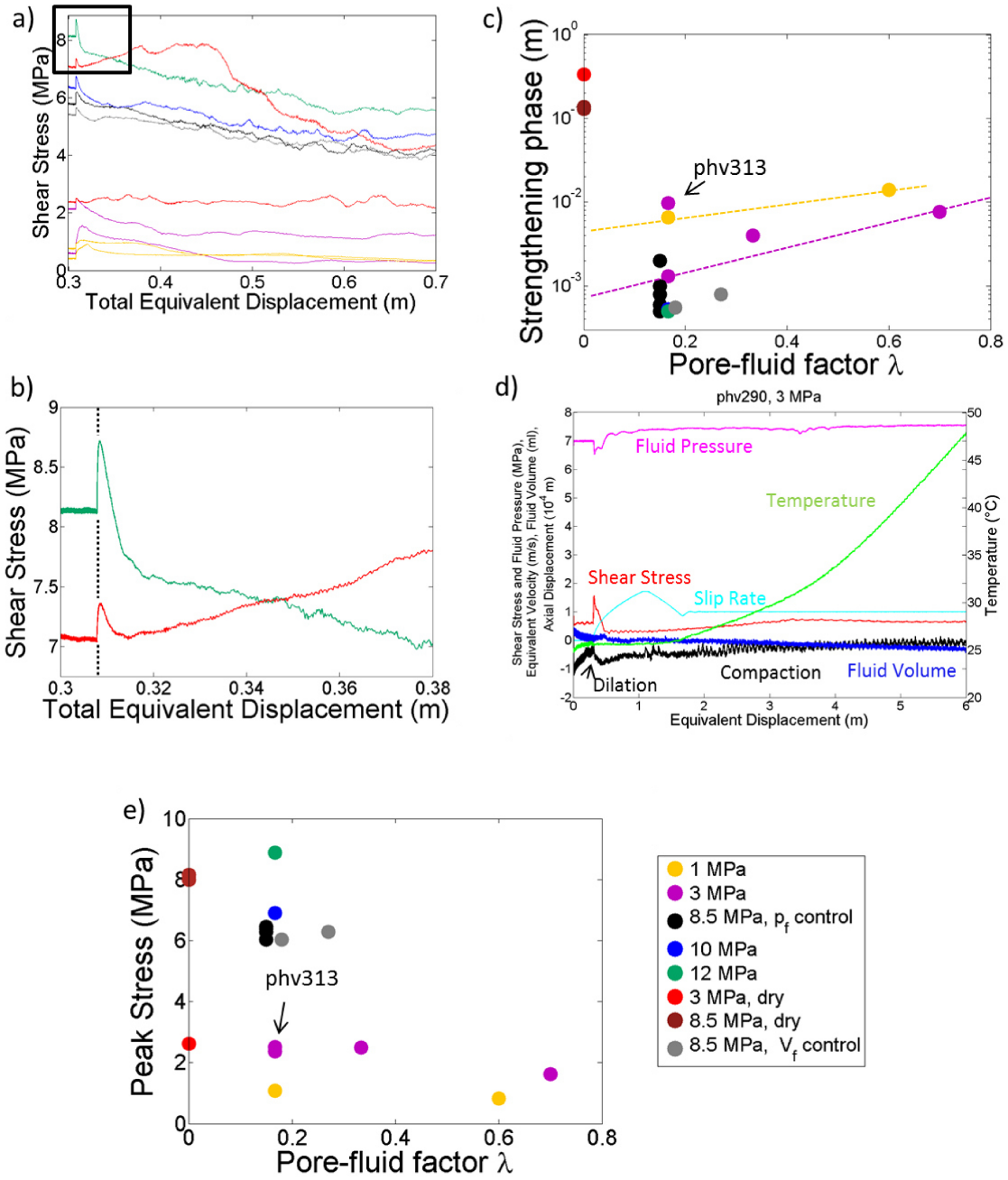

Figure 5. See next page for caption.

Figure 5 (previous page). Strengthening phase, peak friction and the effect of the pore-fluid factor. a) Zoom of the shear-stress evolution as shown in Fig. 4a showing the strengthening phase at the initiation of sliding at high velocity in water-saturated and room-dry gouges. For color-coding see legend in c). **b)** Larger zoom as marked by box in a). Vertical dotted lines mark onset of the high-velocity step. Both room-dry (red) and fluid-saturated (green) gouge shows an initial strengthening, but weakening in fluid-saturated gouges occurs almost instantaneously. **c)** Dependence of the length of the strengthening phase on the pore-fluid factor λ for effective normal stresses of 1 MPa (yellow symbols), 3 MPa (purple), 8.5 MPa (black), 10 MPa (blue), and 12 MPa (green) (see legend). The length of the strengthening phase increases with increasing pore-fluid factor. Phv313 was only sheared at 1 m/s, unlike the rest of the experiments that was pre-sheared at 1 mm/s for a displacement of c. 30 cm. Data for room-dry gouges are plotted in light red (σ_n=3 MPa) and dark red (8.5 MPa); the strengthening phase is c. two orders of magnitude longer than in water-saturated experiments deformed under the same conditions. **d)** Mechanical behavior in experiment phv290 (λ=0.7) for the low-velocity step (1 mm/s, < 0.31 m displacement) and the first c. 5.7 m of displacement at high velocity (1 m/s). Note the overshoot in the slip rate (cyan curve) in the high-velocity step. **e)** Dependence of peak stress on the pore-fluid factor. Color-coding as in c). Peak stress decreases with increasing pore-fluid factor and increasing effective normal stress. The peak stress in phv313 is as large as in phv310, that had experienced pre-shearing. The peak stress in room-dry gouges is slightly larger than in water-saturated gouges from experiments performed at the same effective normal stress.

Figure 6 (next page). Steady-state and residual shear stress. a) Shear vs. effective normal stress picked at 3.5 m of displacement at high velocity. Color-coding refers to different effective normal stresses as shown in legend. The shear stress shows a clear dependence on the effective normal stress. **b)** Residual shear stress picked just before end of the high-velocity step in each experiment vs. the total equivalent displacement of the respective experiment. Color-coding as in a). In the volume-controlled experiments the effective normal stress is c. 3 MPa at these displacements. The residual shear stress shows a dependence on the effective normal stress only up to a displacement of c. 5.5 m (marked by dotted vertical line). At larger displacements, the residual shear stress is c. 1 MPa independently of the applied effective normal stress, except for experiments performed at 1 MPa, where residual shear stress equals the steady-state shear stress (horizontal dotted line).

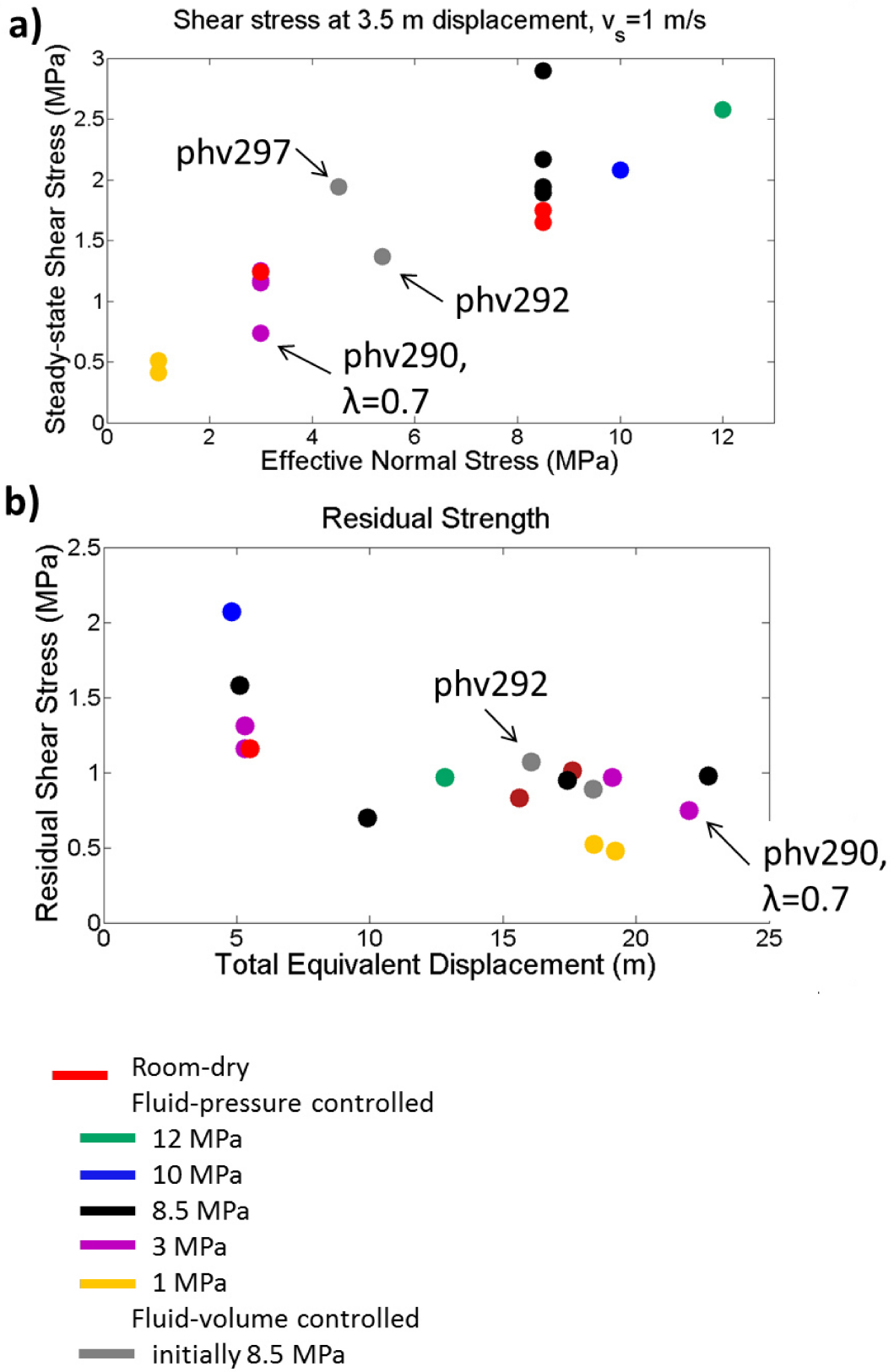

Figure 6. See previous page for description.

dropping down to the target velocity of 1 m/s (Fig. 5d). However, the dependence of the strengthening phase on the pore-fluid factor is obvious from the other experiments and the dependence of the peak stress is likely real, too, as suggested by the significantly lower steady-state shear stress at low velocity (Fig. 3a) and – as we will see –at high velocity. The effect of the normal stress on the peak shear stress, however, is much greater than that of the pore-fluid factor (Fig. 5e). The peak stress in phv313 that was only sheared at 1 m/s is not different from those in experiments that were pre-sheared at low velocity. In the room-dry gouges, the peak stress is slightly larger than in water-saturated gouges from experiments performed at the same effective normal stress (Fig. 5e).

Following strengthening and peak friction, weakening initiates. The steady-state shear stress depends on the effective normal stress, ranging from τ_{ss}≈0.5 MPa at 1 MPa effective normal stress to τ_{ss}≈2.5 MPa at σ_{eff}≈12 MPa (Fig. 6a). The steady-state shear stress in phv290, which had a high pore-fluid factor of 0.7, is decreased by c. 40% compared to the other experiments performed at 3 MPa effective normal stress.

Fig. 6a shows the average steady-state shear stress at displacements of 3–4 m at high velocity. At larger displacements, however, the gouge continues to weaken more gradually reaching a shear stress of 0.5–1.2 MPa that is almost independently of the normal stress (Fig. 6b). This “residual” shear stress – picked at the end of the high-velocity step – is equal to the “steady-state” shear stress only in the 1 MPa experiments (Fig. 6a, b, yellow symbols) and in the experiments with total equivalent displacements ≤5.5 m. Experiment phv290 is a peculiar case, as it weakens dramatically in the first cm of displacement, but then re-strengthens and shows a steady-state shear stress of c. 0.7 MPa throughout its long displacement of 22 m (Fig 5d, Fig. 6a, b). As in the long-displacement, room-dry experiments (Fig. 2b), shear stress in the saturated experiments with displacements > 9.9 m decreases further when the velocity is reduced at the end of the high-velocity step (Fig. 4b).

Temperature

The temperature increase during the high-velocity step in the saturated experiments is highly-dependent on the effective normal stress and the pore-fluid factor (Fig. 7a):

Temperatures in experiments performed at 1 MPa effective normal stress as well as at 3 MPa and high pore-fluid factor (phv290, λ=0.7) increase up to 140 °C during the c. 18 m of displacement. At 3 MPa and lower pore-fluid factor (λ=0.17–0.33), temperature increases up to c. 250 °C. In the higher effective normal stress experiments (8.5–12 MPa, λ=0.15–0.17) temperature increases more abruptly and reaches maximum temperatures of 480–650 °C. The temperature rise in fluid-volume compared to fluid-pressure controlled experiments is more moderate (maximum temperatures of 300 and 450°C for phv292 and 297, respectively), likely owing to a reduced effective normal stress due to an increased pore pressure. As in the dry experiments, the rate with which temperature changes starts to decrease at some point during the high-velocity step, resulting in the temperature eventually staying constant at displacements of c. 10 m in lower-σ_{eff} experiments and even decrease by c. 50–100 °C (starting at 6–12 m displacement) in the higher-σ_{eff} experiments.

Axial displacement

When the high velocity is induced, a transient dilation between 5 and 50 µm occurs in most experiments (phv313 and phv307 show only compaction) during the first 6 to 50 cm (Fig. 7b, c). The transient dilation is followed by compaction (30–465 µm) which is not dependent on the effective normal stress, but lower for higher pore-fluid factors (Fig. 7b). At total displacements of 2.1–7.7 m, secondary dilation (15–530 µm) initiates in some cases that generally continues until the end of the high-velocity step. Secondary dilation is generally higher in higher effective-stress experiments and increases with increasing total displacement. An exceptionally large secondary dilation occurs in experiment phv298 (Fig. 7b) initiating at c. 6 m of total displacement.

In the fluid volume-controlled experiments, transient dilation is in the same order of magnitude (20–40 µm), but the following compaction is significantly lower (same as previous transient dilation: 25–40 µm) as compared to fluid pressure-controlled experiments with similar total displacements. Secondary dilation of 90–150 µm initiates at c. 1.5–4 m total displacement, similarly as in fluid pressure-controlled experiments.

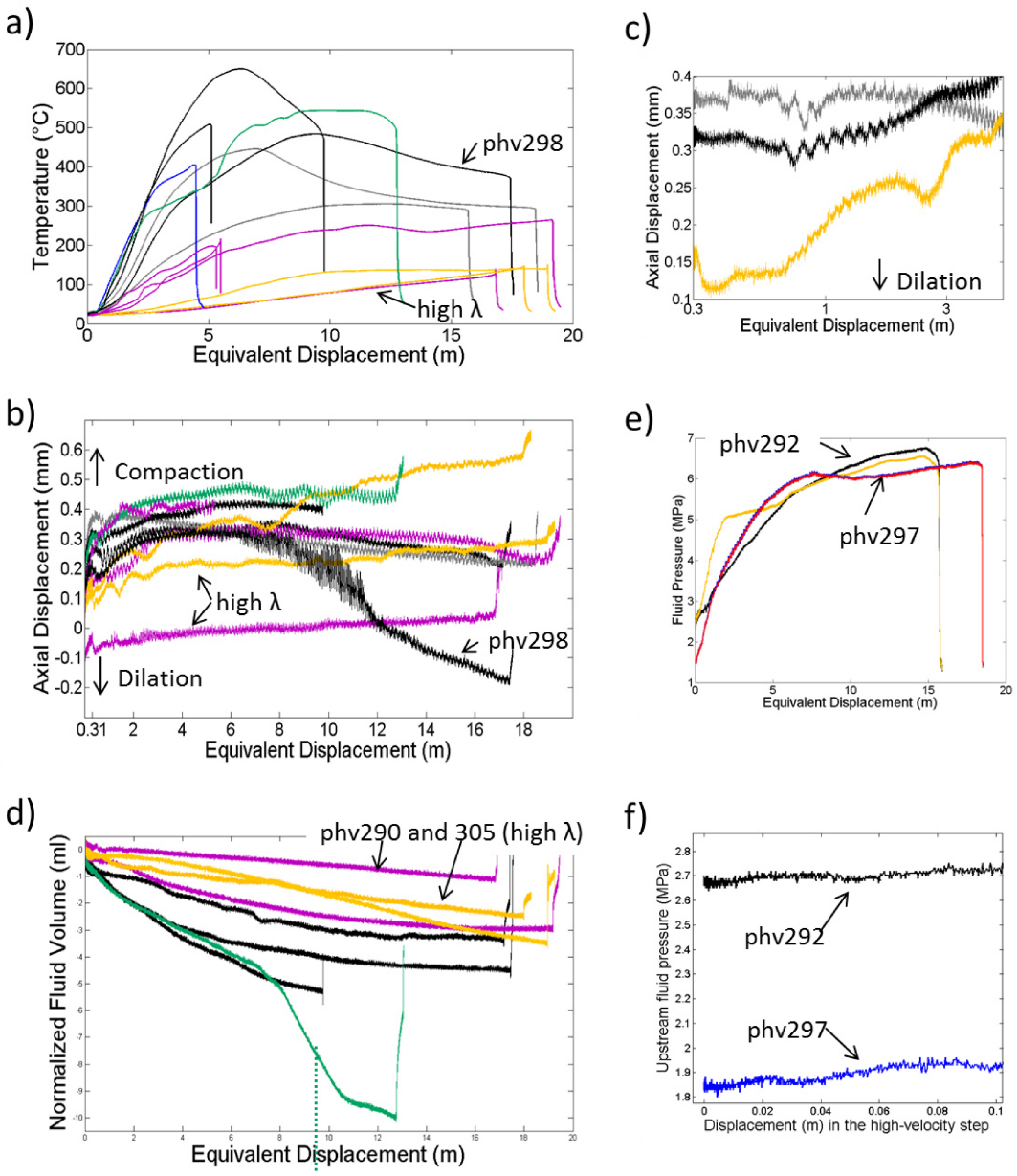

Figure 7. Mechanical data for all velocity steps. Evolution with displacement of **a)** Temperature for all experiments. **b)** Axial displacement for selected experiments (complete data set in Appendix C, Fig. C2). Positive trend denotes compaction, negative denotes dilation. The abrupt compaction at large displacement towards the end of an experiment is due to the decrease in velocity in the third (low-)velocity step and in some cases due to water leaks (see Fig. 8c for zoom of third velocity step). **c)** Axial displacement in the first meters of displacement at high velocity showing transient dilation followed by compaction for experiments phv297 (grey curve, volume control, $\sigma_{eff,initial}$=8.5 MPa), phv300 (black curve, pressure control, σ_{eff}=8.5 MPa, λ=0.15), phv305 (yellow curve, pressure control, σ_{eff}=1 MPa, λ=0.6), **d)** Normalized fluid volume, **e)** Fluid pressure in the volume-controlled experiments phv292 (open Valve 2 (Fig.1)) and phv297 (closed Valve 2), **f)** Constant fluid pressure in the first centimeter of sliding at high velocity.

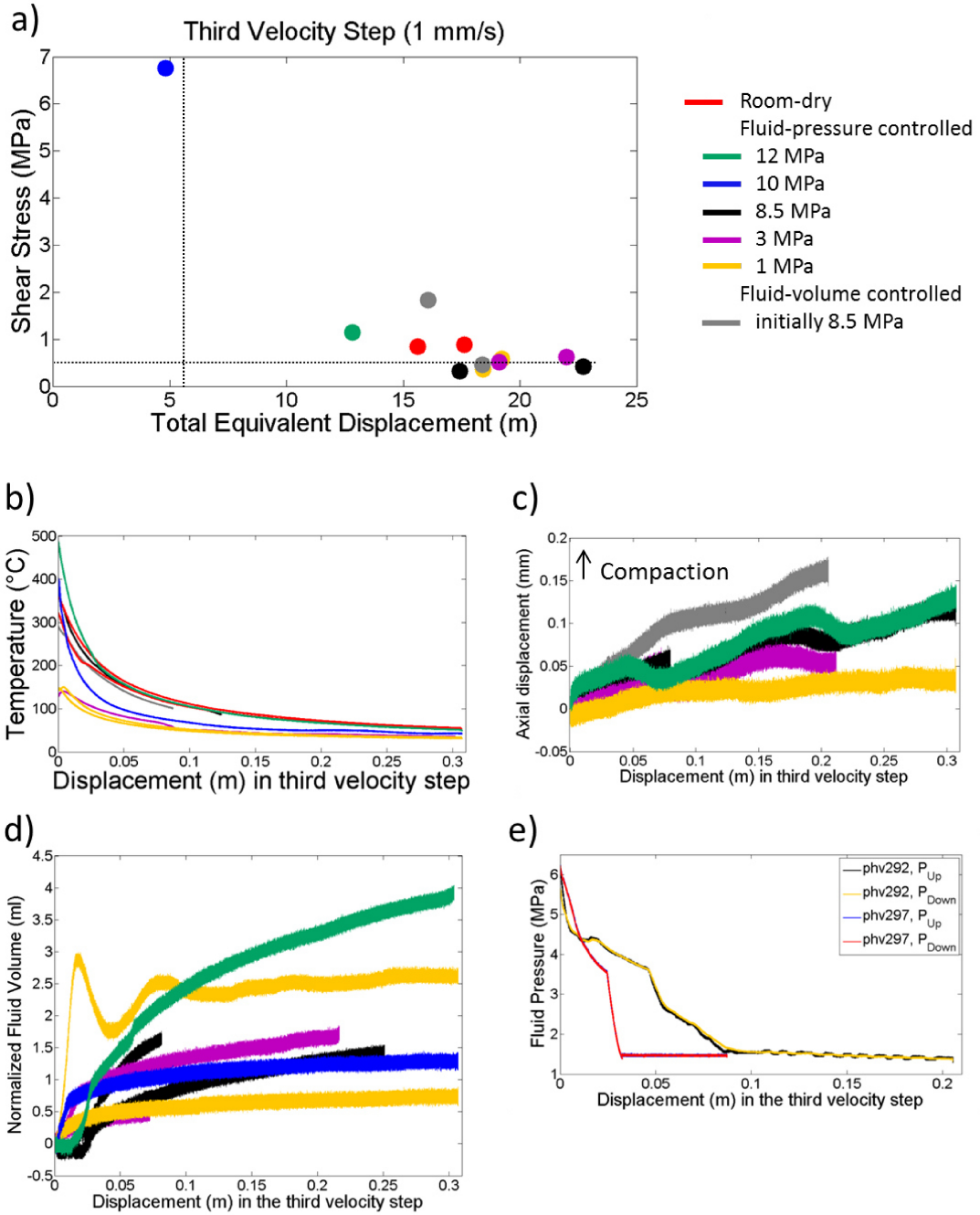

Figure 8. Third (low-)velocity step. **a)** Shear stress picked at the end of each experiment plotted against the total equivalent displacement of the respective experiment. Color-coding as shown in legend. **b)-e)** Evolution with displacement of **b)** Temperature decay with equivalent displacement for all experiments following a power law. Color-coding as in a). **c)** Axial displacement for selected experiments. **d)** Fluid volume for selected experiments**,** and **e)** Upstream- and downstream fluid pressures of phv292 and 297.

Fluid-volume change

In the high-velocity step, the average fluid-volume decrease in pressure-controlled conditions is 2.5 ml in the low (1–3 MPa) and 4.1 ml in the higher (8.5–12 MPa) effective-stress experiments (Fig. 7d). The rate of fluid-volume decrease is constant in experiments with high pore-fluid factor (phv290 and phv305; where also the temperature showed a linear increase throughout the high-velocity step), while in all other experiments, the fluid-volume decrease decays exponentially, the decrease leveling off at displacement of c. 7–10 m. An extreme fluid-volume decrease occurs in the highest σ_{eff}-experiment (phv309, 12 MPa, green curve in Fig. 7d) at a displacement of c. 8 m and a temperature of c. 500 °C, when a rate change to much higher fluid-volume decrease occurs while the temperature ceases to increase. This is accompanied by a fluid-pressure increase by 0.1 MPa and marked by the end of the compaction stage (Fig. 7a-d, dotted green line).

Fluid pressure and pore-fluid factor

In fluid-volume control mode, the fluid pressure increases by c. 5 MPa during a displacement of c. 7 m (Fig. 7e). In experiment phv292, Valve 2 (Fig. 1b), the “shortcut” between the upstream and downstream side of the sample was closed, and thus the pressure upstream and downstream of the sample increases with different rates (black and yellow curves in Fig. 7e), which is because equilibration was controlled by the permeability of the sample. Apparently, the pressure was “trapped” in the downstream side of the sample causing a higher pore-fluid pressure. In phv297, Valve 2 was open, so the pressure could equilibrate fast and up- and downstream pressure are equal (blue and red curves in Fig. 7e). Due to the fluid-pressure increase, super-hydrostatic pressure conditions ($\lambda > 0.4$) were reached in both experiments between displacement of c. 1 and 2.2 m. The pore-fluid factor λ increases to a maximum of about 0.65 and then drops again when the velocity is decreased for the third velocity step.

3.1.2.3. Third (low-)velocity step

Shear-stress evolution

During the last velocity step (1 mm/s), the shear stress recovers to c. the same value as in the first low-velocity step only in experiment phv307 stopped after short total displacement (c. 5 m; Fig. 8a, blue symbol) or in the two experiments performed at a low effective stress of 1 MPa (yellow symbols). In experiments with displacements > 5.5 m, instead of re-strengthening, the shear stress drops remains low (0.32–1.83 MPa) when the velocity is reduced to 1 mm/s.

Temperature

When the velocity is reduced to 1 mm/s, the temperature decay follows a power law (Fig. 8b). After a displacement of 5 cm at low velocity, the temperature had decayed by 45–75%, with the faster decay occurring in the higher effective-stress experiments (e.g., phv309 performed at 12 MPa effective normal stress, green curve).

Axial Displacement

As soon as the velocity is reduced, the gouge starts to compact (by 45–130 μm) (Fig. 8c). Compaction is slightly larger in the higher effective normal-stress experiments and in the fluid-volume controlled experiments in which secondary dilation was larger during the high-velocity step. The pore-fluid factor does not seem to have an effect on the axial displacement in the second low-velocity step.

Fluid-volume change

When the velocity is reduced to 1 mm/s, the pore-fluid volume increases (Fig. 8d). The largest increase occurs in the highest σ_{eff}-experiment (phv309, 12 MPa, green curve in Fig. 8d) where the most extreme fluid-volume decrease occurred during the high-velocity step.

Fluid pressure and pore-fluid factor

The fluid pressure in the volume-controlled experiments decreases to its initial value of 1.5 MPa in 3–10 cm of displacement during the third, low-velocity step (Fig. 8e). The decrease occurs faster in phv297, where Valve 2 connecting upstream and downstream lines was open. There are some abrupt changes in the pressure decrease rate that may be related to creation of new permeability pathways (no water leaks were detected).

3.2.Permeability Measurements

The permeability of deformed gouge layers was measured in two experiments sheared at a slip velocity of 1 m/s and an effective normal stress of 8 MPa, with a fluid pressure of 2 MPa, for total displacements of 5.2 m (phv295) and 1.6 m (phv296) (Table 1c). The steady-state flow achieved in the two experiments when a steady pressure difference of 0.2 MPa was established is shown in Fig. 9. For samples phv295 and 296 with a sample area of $7.1*10^{-4}$ m^2, post-shearing sample thicknesses of 2.8 and 2.57 mm, respectively, and a viscosity of 10^{-3} Pa*s, these flow rates yield permeabilities of $9.9*10^{-17}$ m^2 and $9.2*10^{-17}$, respectively, consistent with the order of magnitude determined in previous studies (e.g. Morrow et al., 1981). The gouge permeability after experiment phv296 which had the shorter total displacement (1.6 m) is slightly lower than in phv295. This is likely due to neglecting the temperature dependence of the viscosity of the water, which is lower at the higher temperatures reached in phv295. The permeability of the empty gouge holder that is controlled by the porous spacers proved to be too high to be measurable, because the upstream and downstream pressures equilibrated instantaneously and a steady flow-rate could not be determined. Based on the permeability measurements with gouge, it is assumed that the system permeability is >> 10^{-17} m^2.

3.3.Microanalysis

3.3.1. Scanning electron microscopy

Samples from seven room-dry and water-saturated experiments were investigated using the scanning electron microscope (SEM) as listed in Table 2. Images were obtained in backscattered and secondary electron mode. The microstructures of the two investigated room-dry samples are similar, even though the experiments were conducted at different normal stresses and for different total displacements [phv301 (8.5 MPa, 17.6 m of total displacement in three velocity steps) and phv311 (3 MPa, 5.5 m, two velocity steps)]. The post-experimental sample thickness of phv301 and 311 is c. 2.2 and 2.8 mm, respectively, and the bulk of the material consists of poorly-comminuted material with (sub-)angular particles up to c. 180 μm in size embedded in a more fine-grained matrix (Fig. 10a, Zone I). The transition from this textural Zone I to more comminuted material ("Zone II") is relatively abrupt, while the transition from Zone II to Zone III is gradual (Fig. 10a). The thickness of textural Zones II

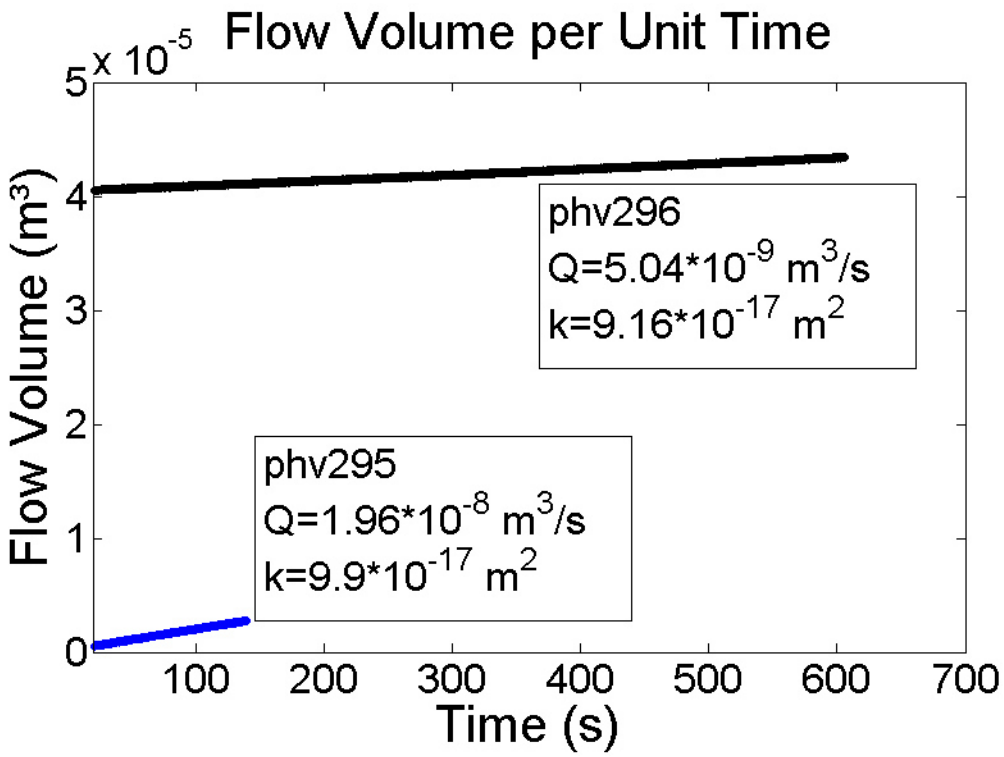

Figure 9. Permeability measurements. Flow volume (m3) per time (s), *Q*, for experiments phv295 and 296. *Q* was determined once a constant differential pressure was applied and used to calculate the permeability.

Figure 10 (next page). Microstructure of room-dry samples. Backscattered electron images showing the microstructure of **a)** sample phv301 showing three more or less distinct textural zones, labelled Zones I, II, and III. Zone III is located adjacent to the principal slip surface (PSS, red arrow points toward it). **b)** Zoom of box b) marked in a) showing recrystallized grains in Zone III. **c)** Zoom of box c) marked in a) showing area c. 300 µm from the PSS where grains are recrystallized and have an preferred orientation along a fracture as shown by red arrows. **d)** Zoom of box d) showing elongated and orientated grains directly adjacent to the PSS. **e)** Black porous material covering the PSS (red arrow points toward it). **f)** phv311 (σ_{eff}=3 MPa, d_{total}=5.5 m): a scrap (red arrow) of what is possibly resin or some of the black porous material.

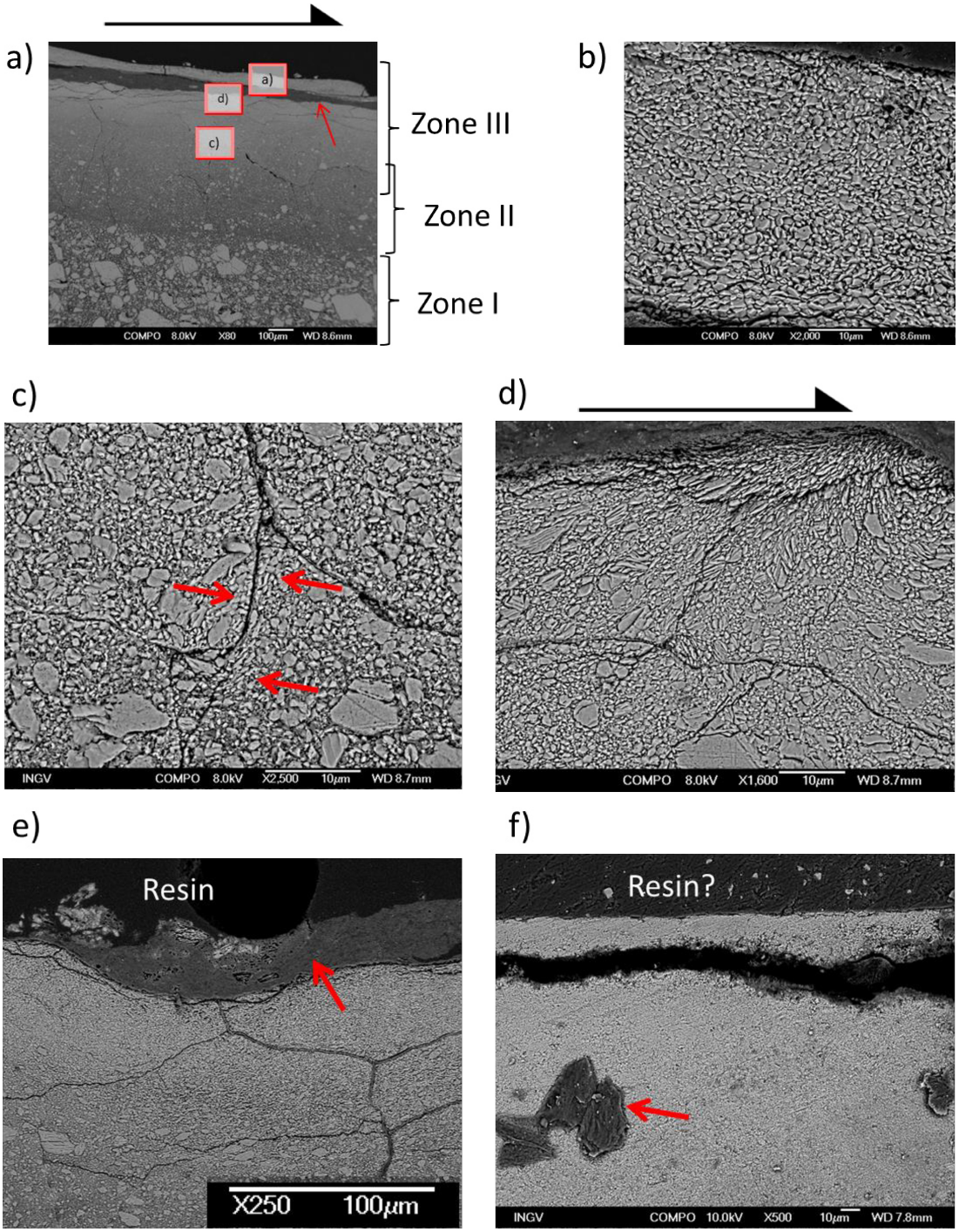

Figure 10. See previous page for description.

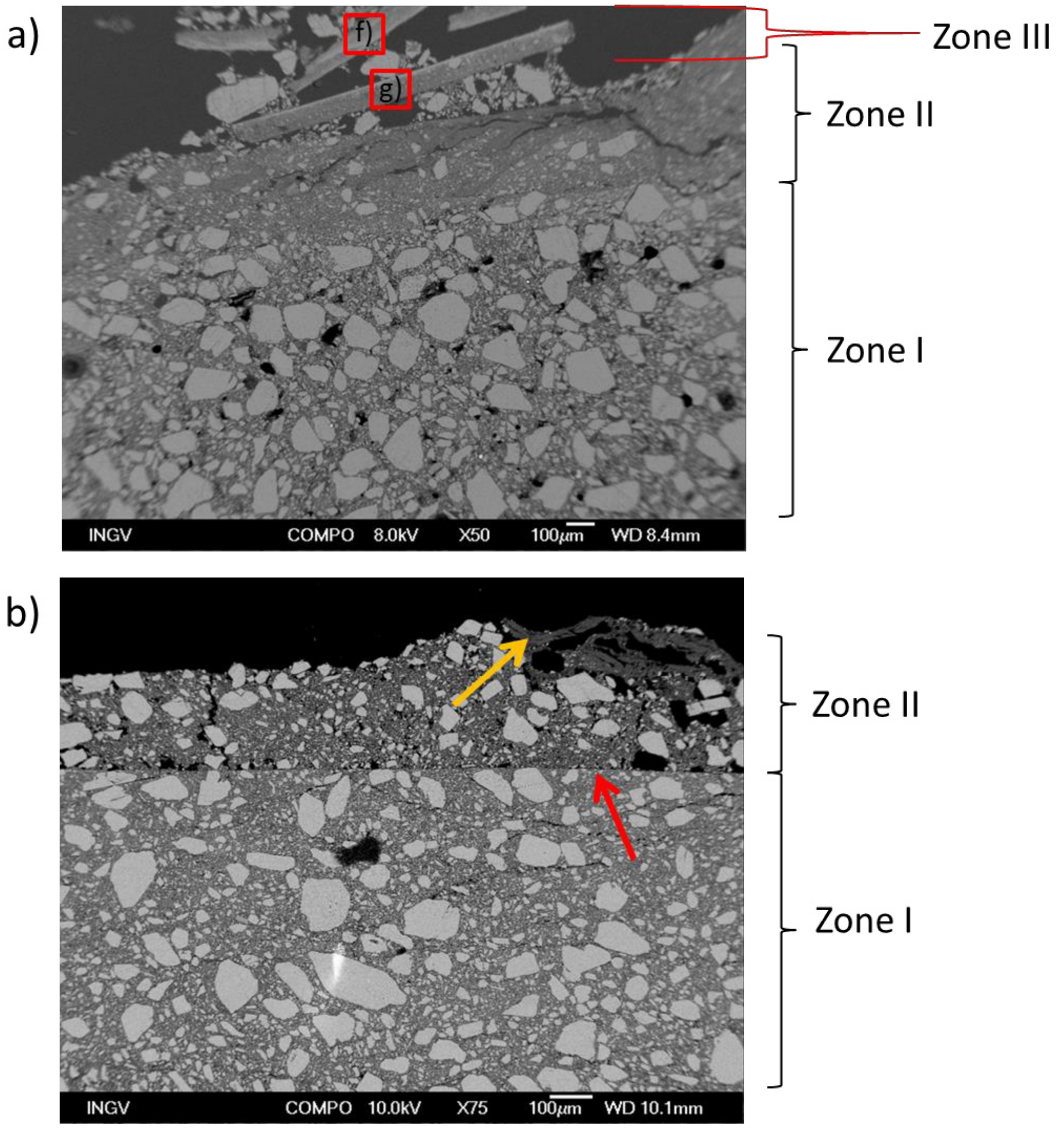

Figure 11. Microstructure of saturated samples. Backscattered electron images showing the microstructure of **a)** phv304 (σ_{eff}=3 MPa, λ=0.33, d_{total}=19.1 m), with textural Zones I, II, and III labeled. Red boxed show location of images in Fig. 12f and g. **b)** phv290 (σ_{eff}=3 MPa, λ=0.7, d_{total}=22 m). PSS marked by red arrow. Yellow arrow pointing at black porous material.

and III is c. 550 and 640 μm in samples phv301 and 311, respectively. In sample phv301 (high normal stress and total displacement), adjacent to what is assumed to be the principal slip surface (PSS) (Fig. 10a), a zone of recrystallized grains can be found. Recrystallized grains are subhedral in shape and c. 1–2 μm in size (Fig. 10b). The degree of recrystallization is highest closest to the PSS even though porosity is still relatively high (Fig. 10b), and decreases with distance from it (Fig. 10c). About 300 μm from the PSS, only the particles adjacent to fracture surfaces appear to be recrystallized, having subhedral shapes and being aligned parallel to the fracture (Fig. 10c). Shape-preferred orientation of elongated particles is also observed close to the PSS (Fig. 10d). In some regions of sample phv301, the PSS is covered with a porous, black material that has a melt-like structure (Fig. 10e). A scrap of apparently similar material is found in sample phv311. However, because it is located on top of the freshly polished surface, it is more likely a scrap of resin. No EDS analysis was performed on the black material in these samples.

The water-saturated samples that were investigated with the SEM were mostly performed at 3 MPa effective normal stress (phv290, 304, 310, 313) though with different pore-fluid factors and displacements (Table 2), with the exception of sample phv307 that was sheared at 10 MPa for only 4.8 m of total displacement, similar to phv310 and 313 (5.3 m). Like in room-dry conditions, three textural zones have developed in the water-saturated samples. However, the material in Zone I appears to be more rounded in water-saturated (Fig. 11a) than in room-dry samples that experienced a similar amount of displacement (Fig. 10a). In water-saturated samples, the rounded particles are up to 180 μm in size, and embedded in a fine-grained matrix with particle sizes < 1 μm. The thickness of Zones II and III in water-saturated conditions is c. 300–500 μm, with the higher values for larger total displacements, and thus slightly less than the thickness in the room-dry samples. An exception is sample phv290, from the experiment with the highest pore-fluid factor λ=0.7, that appears to consist only of relatively un-comminuted Zone I-material that is cut by a single through-going PSS (Fig. 11b).

Again with the exception of high λ-experiment phv290, zones of recrystallization also develop in water-saturated conditions, in the whole range of investigated displacements and normal stresses, and both in samples sheared in one, two or three velocity steps. In the short-

a)

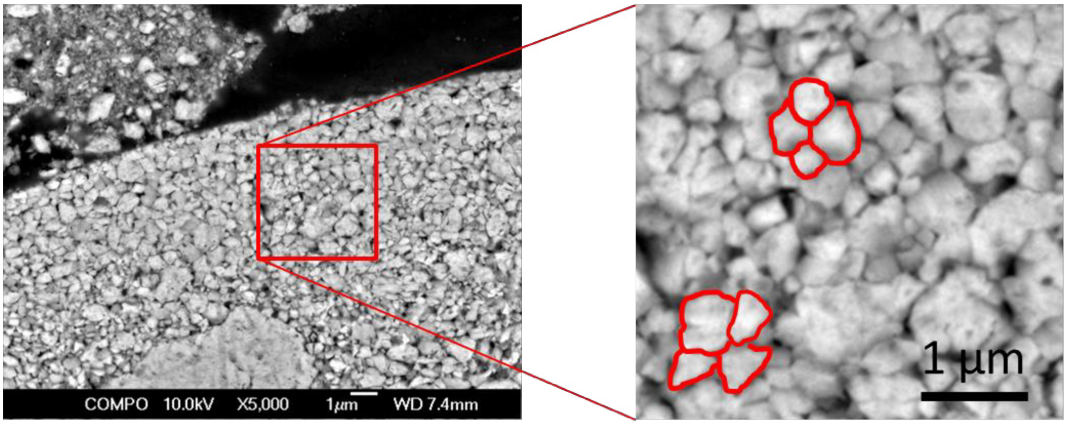
COMPO 10.0kV X5,000 1μm WD 7.4mm
1 μm

b)

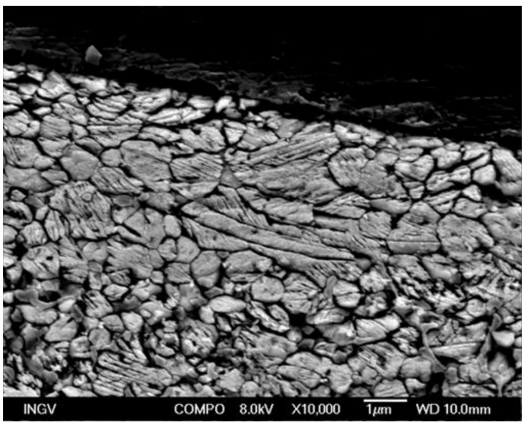
INGV COMPO 8.0kV X10,000 1μm WD 10.0mm

c)

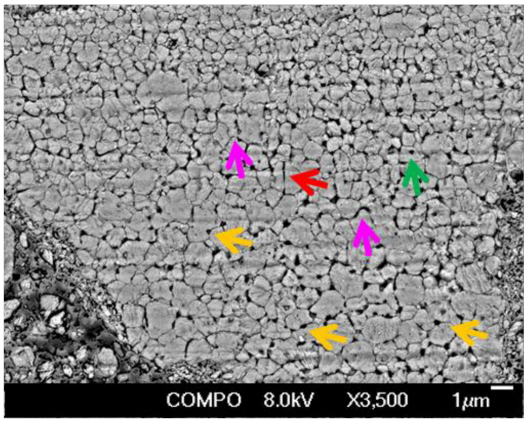
COMPO 8.0kV X3,500 1μm

d)

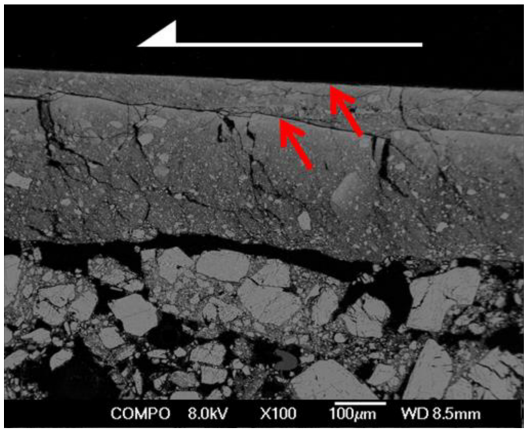
COMPO 8.0kV X100 100μm WD 8.5mm

e)

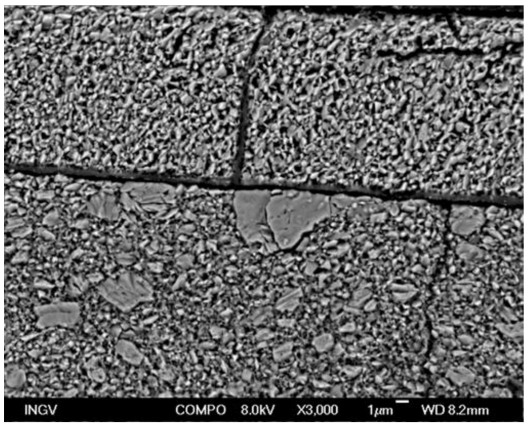
INGV COMPO 8.0kV X3,000 1μm WD 8.2mm

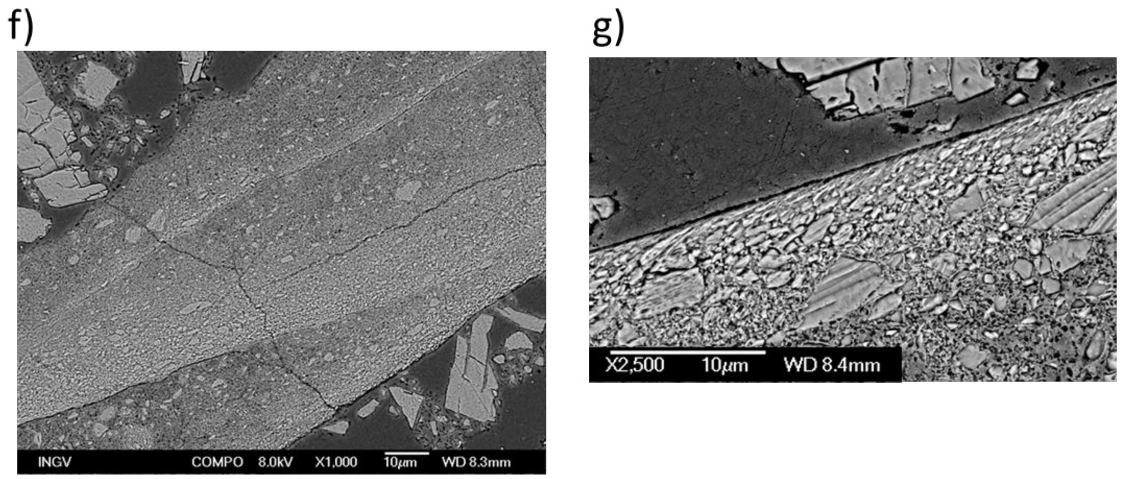

Figure 12 (see previous page for a-e). Crystal-plastic deformation in saturated samples. Backscattered electron images showing the microstructure of **a)** phv307 (σ_{eff}=10 MPa, λ=0.17, d_{total}=4.8 m), **b)-c)** phv310 (σ_{eff}=3 MPa, λ=0.17, d_{total}=5.3 m), cut perpendicular to slip direction. Red arrow in c) pointing at straight grain boundary, pink arrows at lobate grain boundaries, and yellow and green arrows at cavities that are located on grain boundaries (most common) or within grains, respectively. **d)** phv313 (σ_{eff}=3 MPa, λ=0.17, d_{total}=5.3 m), red arrows showing two slip surfaces. **e)** zoom of the upper slip surface in d) showing recrystallized grains, **f)** area of phv304 (σ_{eff}=3 MPa, λ=0.33, d_{total}=19.1 m) marked in Fig. 11a, showing recrystallized grains along several slip surfaces, **g)** Zoom of area marked in Fig. 11a with recrystallized grains orientated in the direction of shear.

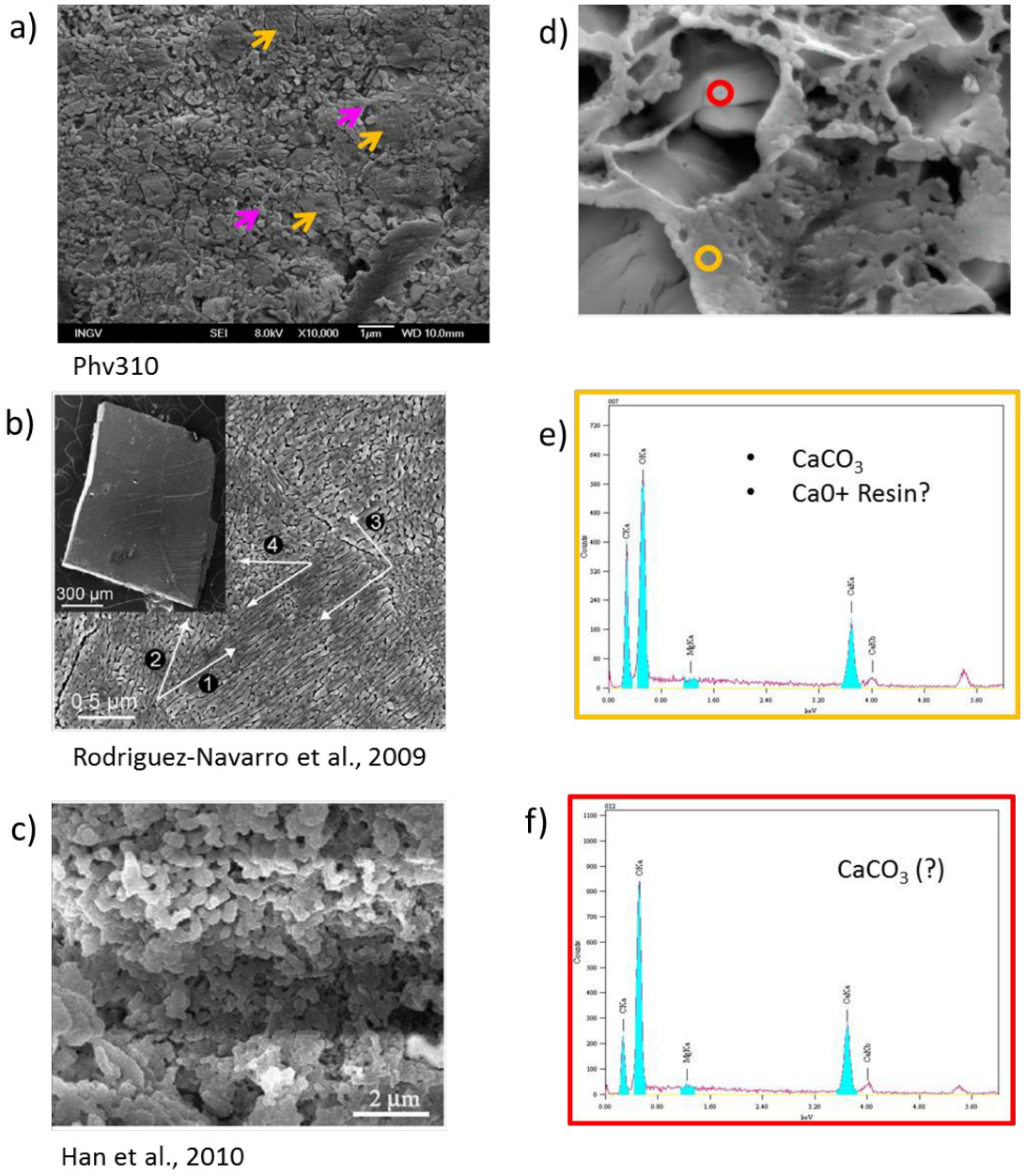

Figure 13. Possible evidence of decarbonation. a) Secondary electron image of sample phv310 (water-dampened, σ_{eff}=3 MPa, λ=0.17, d_{total}=5.3 m) showing calcite grains (yellow arrows) partly surrounded and/or covered by second phase (pink arrows). **b)** Image taken from Rodriguez-Navarro et al. (2009) showing "porous calcite pseudomorphs (inset) crisscrossed by cracks and showing four (1–4) sets (bundles) of oriented CaO rods (arrows)" that developed at 850 °C (Rodriguez-Navarro et al. 2009). **c)** Figure taken from Han et al. (2010) showing SEM photomicrograph of the decomposition zone in Carrara marble that was sheared at 12 MPa normal stress and a slip velocity of 1.2 m/s. The structure of the decomposition zone is "characterized by large pore volumes and nanograin aggregates" (Han et al., 2010). **d)** Secondary electron image of a calcite grain surrounded by the unknown phase. Red and yellow circles show regions where EDS analysis was performed. **e)** EDS spectrum for region marked by yellow circle in d), showing presence of C, O, and Ca. **f)** The EDS spectrum of the calcite grain marked by red circle in d) is equal to the spectrum shown in e).

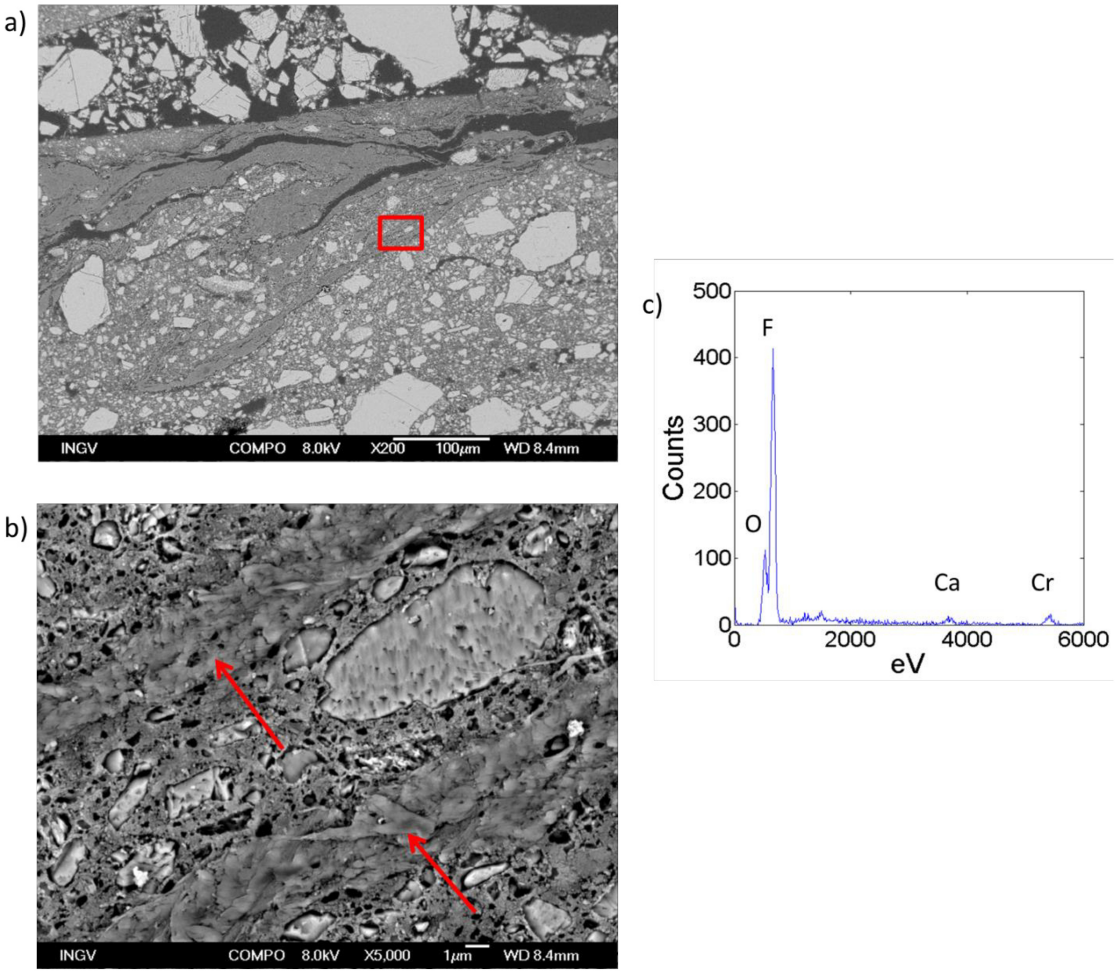

Figure 14. Contamination of saturated samples. Backscattered electron images showing the **a)** microstructure of phv304 (σ_{eff}=3 MPa, λ=0.33, d_{total}=19.1 m), **b)** zoom of area marked in a). **c)** EDS spectrum of the porous black material, revealing the presence of O, F, Ca, and Cr.

displacement, high-normal stress experiment phv307, the gouge is cut by one through-going slip surface that is partly lined with recrystallized grains < 1 µm in size (Fig. 12a). The geometrical arrangement of some grains (Fig. 12a, zoom) suggests that grain boundary sliding might have taken place. Also at lower normal stress (phv310, 3 MPa) grains adjacent to the PSS are plastically deformed, being elongated and possibly showing evidence of twinning (or just of dissolution along cleavage?) (Fig. 12b). In a piece of material that presumably broke from the principal slip zone and may have been rotated, on the other hand, no elongation of grains or twinning took place (Fig. 12c). Instead, porosity in between the < 1.5 µm in size, subhedral grains is highly reduced, with little porosity along grain boundaries or in the form of cavities (Fig. 12c, yellow arrows). Grain boundaries are mostly straight or only slightly curved (red arrow), but some evidence of bulging may be present (pink arrows). In phv313, that was only sheared at 1 m/s, two PSSs are present (Fig. 12d). Possibly, the lower one was abandoned after some displacement and was subsequently fractured when the upper PSS was established. Zones of crystal-plastic deformation are present adjacent to both slip surfaces. Recrystallized grains (Fig. 12e) have a similar subhedral shape with relatively high porosity as in the room-dry sample phv301. In samples with larger total displacements, e.g. in phv304, zones of recrystallization are existent along several slip surfaces (Fig. 12f, g) that thus appear to have developed at larger displacements. Recrystallized grains do not have such a preferred shape as in phv313 (Fig. 12e) or in the room-dry experiment phv301 (Fig. 10b), but in some cases they have a strong preferred orientation (Fig. 12g). In summary, evidence of recrystallization was found in each of the investigated water-saturated samples from experiments with pore-fluid factors < 0.7.

Evidence of decarbonation was possibly detected in sample phv310 (Fig. 13a). Here, the heavily twinning calcite grains are surrounded or covered by material that bears resemblance to the CaO “rods” observed by Rodriguez-Navarro et al. (2009) or the nanograins in the marble decomposition zone described by Han et al. (2010) (Fig. 13b, c). Unfortunately, this sample was covered with carbon to make it conductive for SEM analysis in addition to the C-content of the resin so qualitative EDS analysis of this material (Fig. 13d, e) remains speculative as to where it is made of CaO. The EDS results in Fig. 13e show the presence of Ca,

C and O, indicating that the material is $CaCO_3$ or CaO (possibly nanograined mixed with resin). However, comparison with EDS results of what appears to be a calcite grain (Fig. 13d) shows that the composition is identical (Fig. 13f). Better analysis should be conducted to determine whether calcite decomposition products are contained in our samples.

The black porous and melt-like material found in the room-dry sample phv301 (Fig. 10e) is also present in the water-saturated samples that experience displacements ≥ 19 m, namely phv290 and 304. In sample phv304, to the contrary of phv301 and 290, it seems to have penetrated into the sample (Fig. 14a, b). EDS analysis of the black material showed a strong fluorine peak (Fig. 14c) in addition to smaller peaks for oxygen, calcium and chromium, the latter of which was used to coat the sample for the SEM analysis. The presence of fluorine suggests that the black material is Teflon (C_2F_4) or a Teflon decomposition product that entered the sample. The lack of carbon likely reflects difficulties in the calibration of the EDS system (Andrea Cavallo, personal comment, 2014) and does not provide evidence that lime (CaO) was formed due to decarbonation. No evidence of contamination was found in the investigated water-saturated samples with displacements ≤5.3 m. Whether room-dry sample phv311 (3 MPa, 5.5 m) is contaminated remains unclear. EDS analysis will be performed in the future.

3.3.2. Raman spectroscopy

Analysis of the starting material using Raman spectroscopy revealed four distinct peaks characteristic for the Raman spectrum of calcite (Fig. 15a). Differentiation between different minerals of the carbonate group is possible by their different translational lattice modes in the 100–350 cm^{-1}-region (Frezzotti et al., 2012). Calcite was also detected in each of the investigated post-experimental samples. The macroscopic appearance of a sample containing only calcite (phv307) is shown in Fig. 15b. The sample is white with only small greyish patches.

A second phase that was detected in five of the eleven post-experimental samples was Polytetrafluoroethylene (PTFE), Teflon (Fig. 15c). Note that fitting of the Raman peaks yielded PTFE, not Teflon decomposition products. PTFE was detected in samples that experienced displacements ≥ 9.9 m (Table 2), but not in all of them. E.g., no PTFE was found in the high

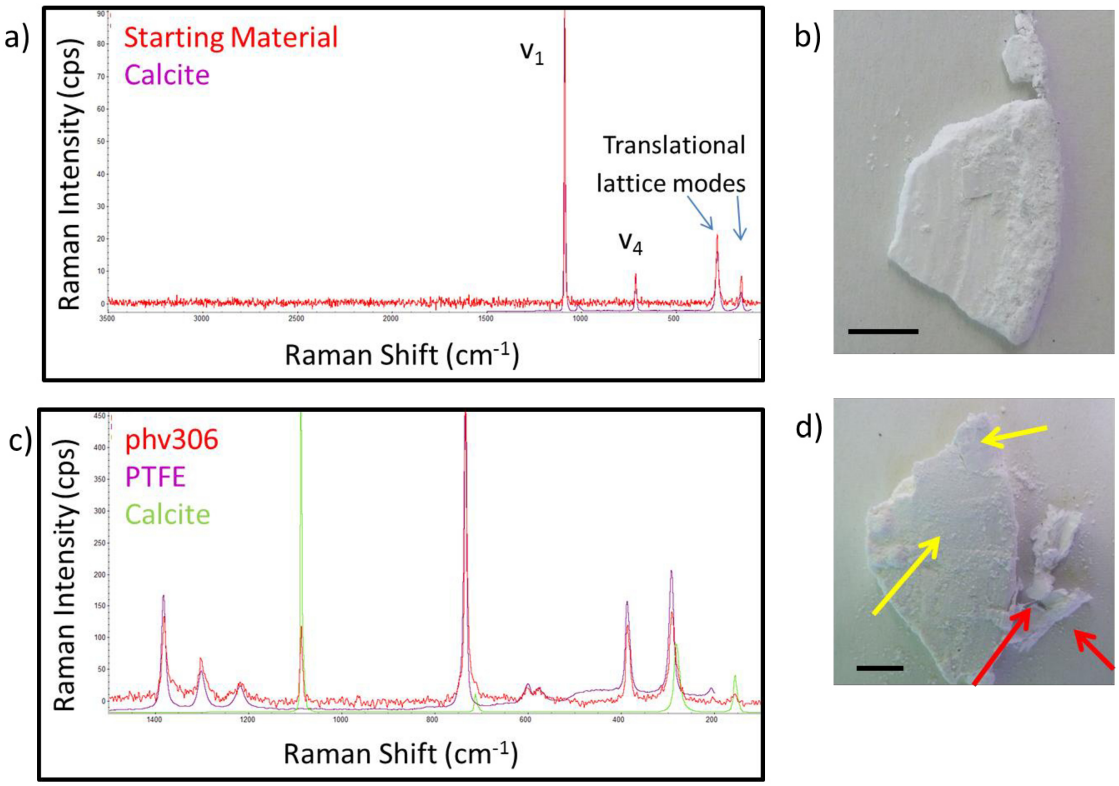

Figure 15. Raman spectroscopy. a) Raman spectrum (red curve) and **b)** photograph of the post-experimental sample phv307 (σeff=10 MPa, λ=0.17, dtotal=4.8 m), respectively, containing only calcite (purple curve in a). **c)** Raman spectrum and **d)** photograph of post-experimental sample phv306. Fitted to the sample's spectrum (red curve) are the standard curves for PTFE (purple) and calcite (green). In the photograph, red arrows point at "stringy" regions, where PTFE was detected. Powdery and shiny regions (yellow arrows) contained only calcite. Scale bars are 5 mm.

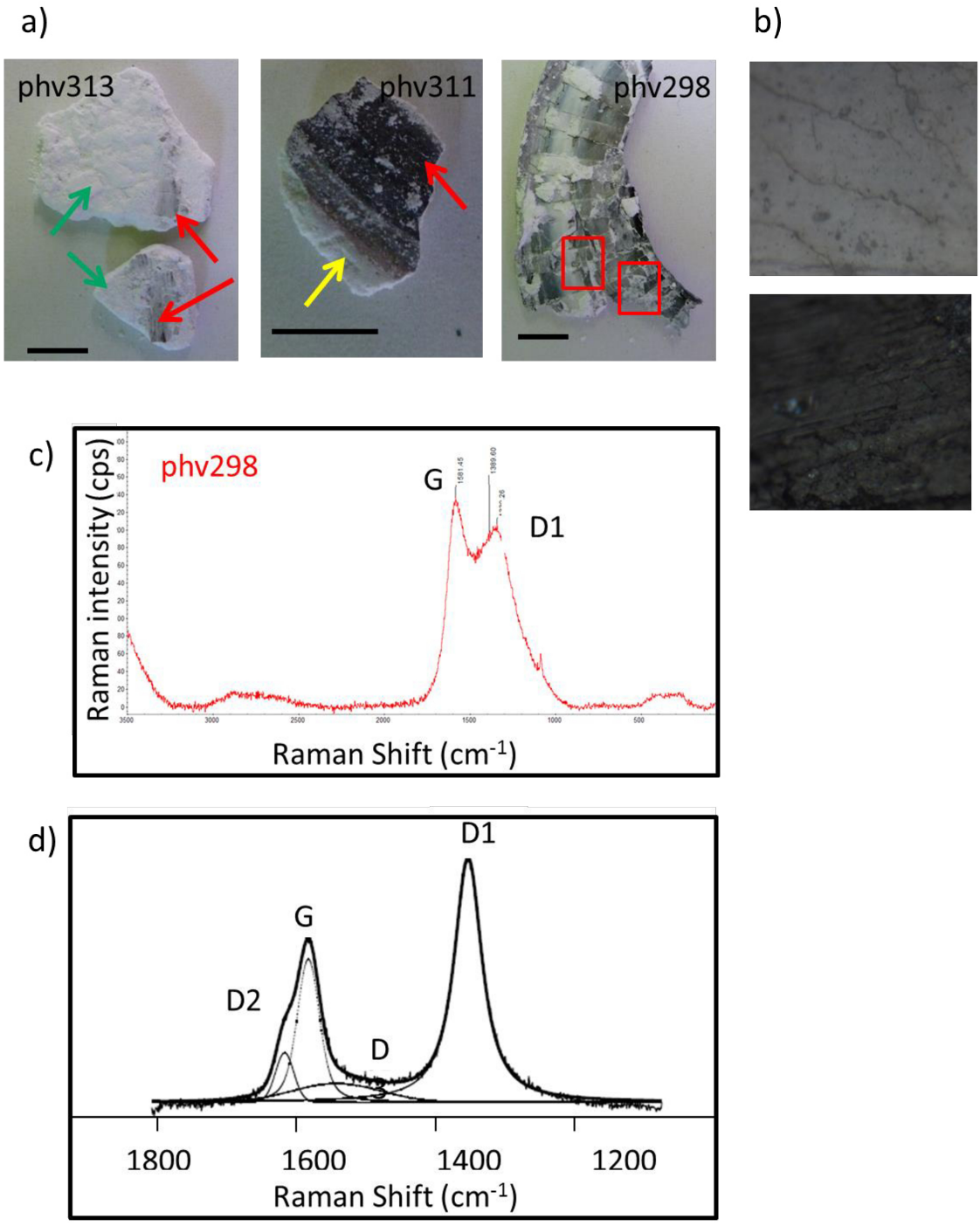

Figure 16. Raman spectroscopy of black samples. a) Photographs of samples phv313 (σ_{eff}=3 MPa, λ=0.17, d_{total}=5.3 m), 311 (room-dry, σ_{eff}=3 MPa, d_{total}=5.5 m), and 298 (σ_{eff}=8.5 MPa, λ=0.15, d_{total}=17.4 m) (from left to right). Phv313 contained only traces of carbon. Scale bars are 5 mm. **b)** Optical microphotographs showing greyish and black regions. **c)** Raman spectrum of sample phv298, and **d)** Example of decomposition of the Raman spectrum of carbonaceous material (modified after Beyssac et al., 2002).

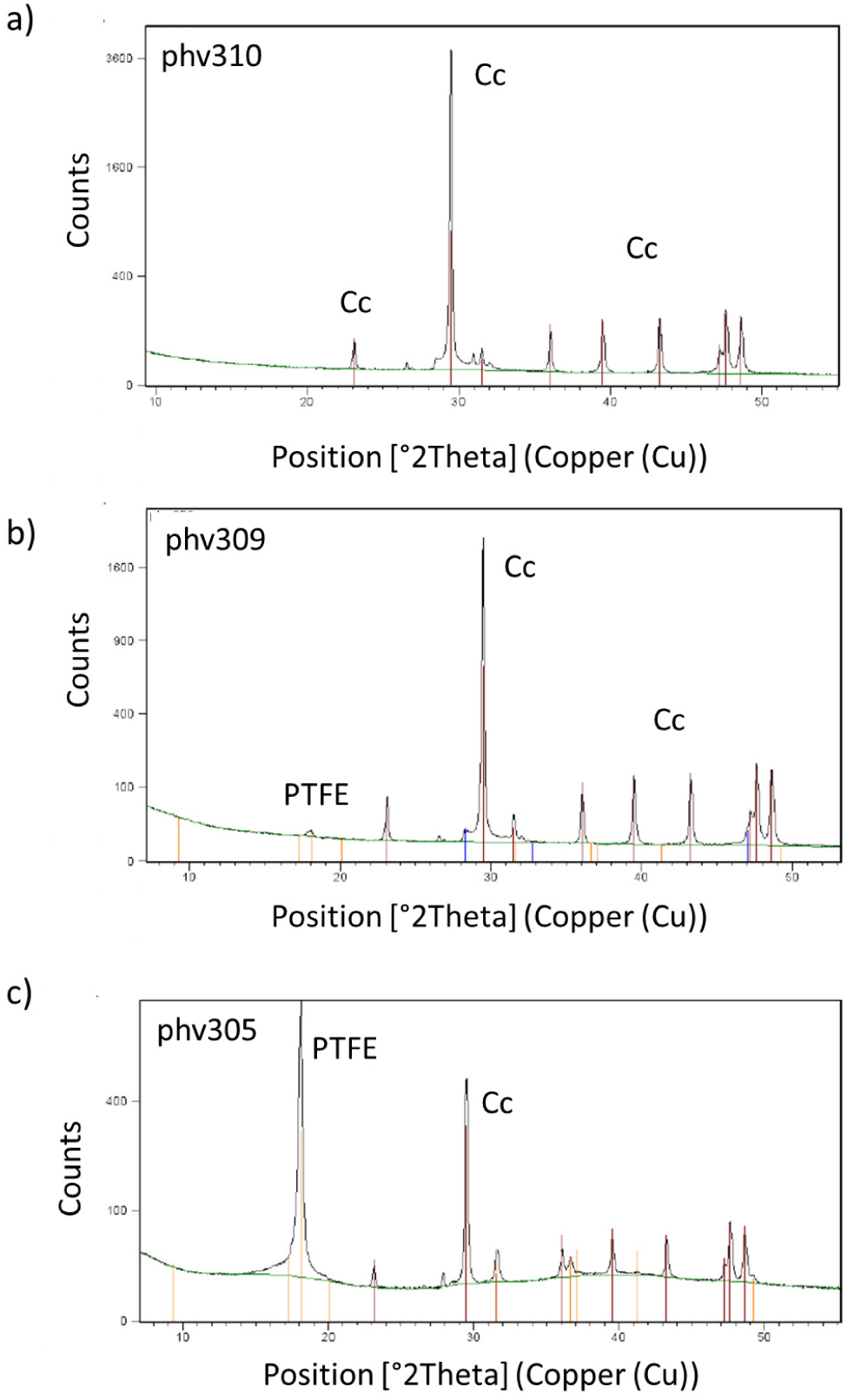

Figure 17. XRD spectra. a) phv310 (σ_{eff}=3 MPa, λ=0.17, d_{total}=5.3 m) containing only calcite , **b)** phv309 (σ_{eff}=12 MPa, λ=0.17, d_{total}=12.82 m) containing calcium and calcium fluorite, but no PTFE, **c)** phv305 σ_{eff}=1 MPa, λ=0.6, d_{total}=18.4 m) containing calcite and PTFE.

683 pore-fluid factor-experiment phv290, although SEM analysis suggests otherwise (Fig. 11b), nor
684 in experiments phv291 and 298, the former of which was performed with Valve 2 open and
685 thus possible at a lower effective normal stress. Sample phv306 was white in color (Fig. 15d),
686 but contained some “stringy” material. Powdery and shiny regions within the same sample did
687 not contain PTFE, only calcite.

688 Many samples were grey to dark black in color (Fig. 16a, b). Raman spectroscopy of
689 grey and black areas showed two broad peaks in the 1100–1800 cm^{-1}-region with an additional
690 broad band from 1500–3000 cm^{-1} (Fig. 16c). This phase was found in eight of the eleven post-
691 experimental samples and was attributed to be due to poorly-ordered carbon. According to
692 Beyssac et al. (2002) (Fig. 16d), the Raman spectrum of carbonaceous material exhibits a peak
693 at 1580 cm^{-1} (termed G (graphite)-band) that in poorly-ordered carbon also shows broad
694 peaks around 1350 cm^{-1} (D1-band) and 1620 cm^{-1} (D2-band), the latter of which is impossible
695 to distinguish from the G-band in highly-disordered carbon such that only one broad band
696 around 1600 cm^{-1} is observed. The area of the generally intense D1-band decreases with the
697 degree of graphitization (Beyssac et al., 2002). Additionally, the presence of a third D-band at
698 1500 cm^{-1} ”connects” the D1- and the G-peaks with a broad band in poorly-ordered carbon.
699 This description by Beyssac et al. (2002) precisely fits our data. We observe a G- and a D1-peak
700 that are not completely separated (Fig. 16c) and likely obscure the D2- and D3-bands. Thus we
701 can argue that the grey to black material covering the slip surface of our post-experimental
702 samples is made up of disordered carbonaceous material. In some cases (e.g., Fig. 16b), black
703 “dots” on the slip surface might be small holes that provide evidence of degassing.

704 ### 3.3.3. X-ray diffraction analysis

705 XRD analysis was performed on six post-experimental sample powders. Three of the
706 samples contained only calcite (phv300, 304 and 310, Fig. 17a), while in the other three also
707 contained fluorine (phv297, 305 and 309, Fig. 17b) or PTFE (Fig. 17c). In phv305, PTFE was only
708 detected in a white, stringy, strip. XRD analysis did not detect PTFE in samples phv300 and 304,
709 even though the analysis of their slip surfaces with Raman spectroscopy showed the presence
710 of PTFE. Also, no carbon was detected in any samples with XRD analysis, supporting the result
711 obtained from Raman spectroscopy that the carbonaceous material contained in some

samples is disordered. (Disordered carbon produces only diffuse scattering, not peaks, in an XRD pattern. Amorphous phases can be detected with XRD, however, they will only show as a wide band on the background if it is abundant within the sample (> 5–10% depending on the degree of disorder). Graphite, however, would be detectable in small amounts (< 1%) (Federico Zorzi, personal comment, 2015).)

3.4.Thermodynamic calculations

3.4.1. Thermal pressurization

The degree of thermal pressurization likely to occur in our experiments (or that *would* occur in the case of pressure control if the pressure was not kept constant) was estimated from the fluid-volume expansion assuming that only the volume of fluid in the pore space of the gouge layer $V_{f,gouge}$ is affected by the frictional heating, but that the volume expansion is accommodated by the total water volume in the fluid system $V_{f,total}$. The pore-fluid volume $V_{f,gouge}$ was estimated from the average measured starting thickness of gouge material (2.8 mm), the known area of the sample holder base plate, and a porosity of 6.8%. The porosity was again calculated from the difference between the measured volume of the gouge layer and a theoretical volume calculated from the weight of the starting material (15 g) and the calcite grain density of 2.71 g/cm^3, and likely provides a lower bound for the porosity. The resulting $V_{f,gouge}$ was 402.55 mm^3 and assumed to be constant throughout the experiment. The total water volume in the fluid system $V_{f,total}$ was different for each experiment, as it depends on the position of the piston controlling the fluid pressure. The pressure increase depending on the temperature rise was calculated for the minimum (27,160 mm^3) and maximum value (35,850 mm^3) of $V_{f,total}$ (Fig. 18). According to the calculation (Eq. 3), the pressure increase during the first velocity step, during which the temperature increases by < 10 °C, is c. 0.1 MPa. During the first 5.5 m of displacement of the high velocity step, the temperature increases by up to c. 200 °C in the experiments with low effective normal stress (≤3 MPa) yielding a fluid-pressure increase of up to 1.3 MPa. In experiments performed with higher effective normal stress, temperature increases of up to 600 °C cause a fluid-pressure increase of up to 3.8 MPa.

These values seem realistic when compared to the fluid pressure measured in the volume-controlled experiments. E.g., the pressure increase at a displacement of 5.5 m in experiments phv292 and 297 was 3.8 and 4.3 MPa for temperature increases of c. 220 and 410 °C (Fig. 7a, light grey curves), respectively. It can be seen in Fig. 18 that the calculated pressure increase at these temperatures are c. 1.4 and 2.65 MPa. The discrepancy between measured and calculated values may have several sources: the effectively heated fluid volume $V_{f,gouge}$ may be larger than assumed. Additionally, the actual local temperatures might be higher than the measured temperatures. Temperature rises larger by c. 80–380 °C than measured would account for the discrepancy. Also, pressurization is likely not caused by thermal expansion of the pore fluid alone. Compaction of the gouge layer would result in additional pressurization, as would the decarbonation of the calcite gouge (even though bulk temperatures are too low at these displacements to induce extensive CO_2 degassing; see section 3.4.2). Despite the discrepancy between measurements and calculations, it is obvious that in our experiments thermal pressurization of the pore fluid should arise from frictional heating.

3.4.2. Decarbonation temperatures

The thermodynamic calculations for the CaO-H_2O-CO_2-system conducted with the Perple_X software (Connolly, 1990) showed that at atmospheric pressure, the decarbonation of calcite occurs at c. 500°C for $X(CO_2)\rightarrow0$, i.e., pure water, and at c. 900 °C for $X(CO_2)\rightarrow1$, i.e. without water (Fig. 19a). For higher pressures, decarbonation temperatures increase, ranging in water-saturated conditions from c. 600 °C at 1 MPa to c. 700 °C at 8.5 MPa, and without the presence of water from c. 1100 °C at 1 MPa to 1300 °C at 8.5 MPa. Above 8.5 MPa, melting occurs for high CO_2 concentrations. Generally, decarbonation temperatures are c. 500 °C lower in water-saturated than in relatively H_2O-poor conditions. However, the first degassing of CO_2 in water-saturated conditions stabilizes the calcite phase because the decarbonation temperature increases for higher concentrations of CO_2 in the fluid phase. Decarbonation will reinitiate at higher temperatures as frictional heating continues. For the calculation of decarbonation temperatures it was assumed that our material consisted of pure calcite. If another phase, e.g. MgO (as it would be the case if dolomite was contained), was added to the system, CO_2 degassing would start earlier, at c. 400 °C (Fig. 19b). Similarly, in a dry experiment

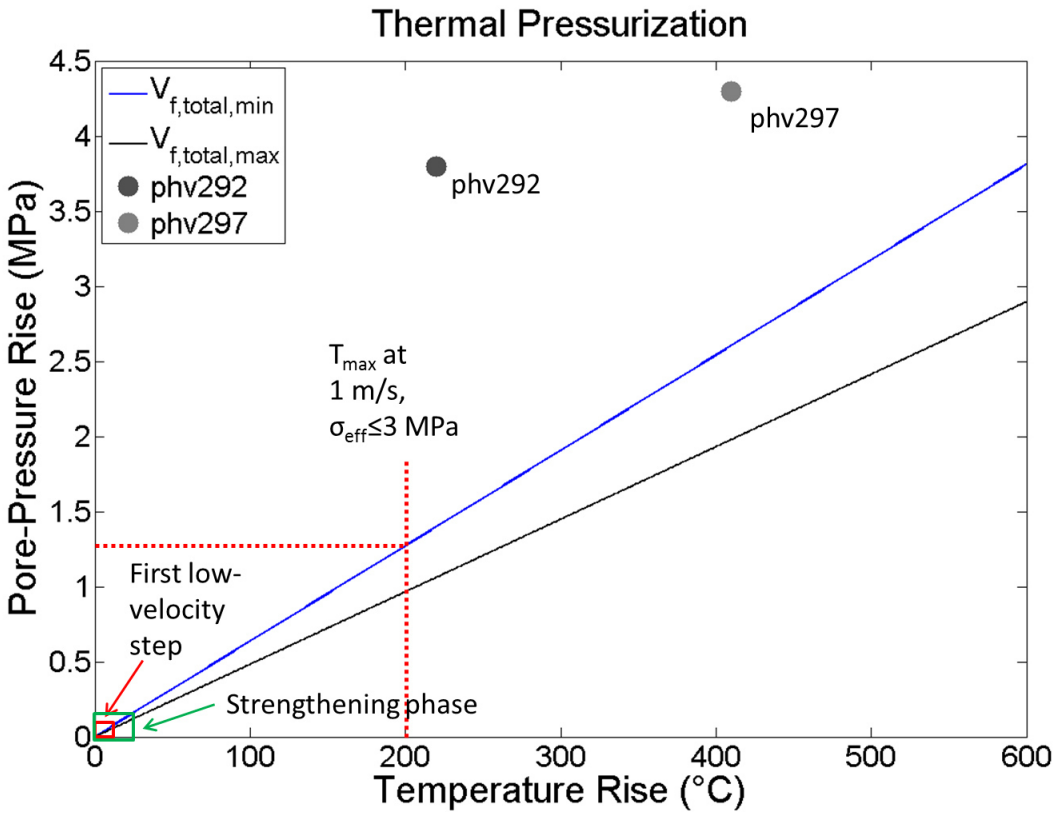

Figure 18. Expected thermal pressurization. Pore-pressure rise for a given temperature rise for minimum (blue curve) and maximum (black curve) total fluid volume as it differed between the experiments. Red box shows temperature and pressure change regions corresponding to values reached in the first velocity step. Red dotted line shows maximum temperature reached in the experiments performed at low effective normal stress (≤3 MPa) during the high-velocity step.

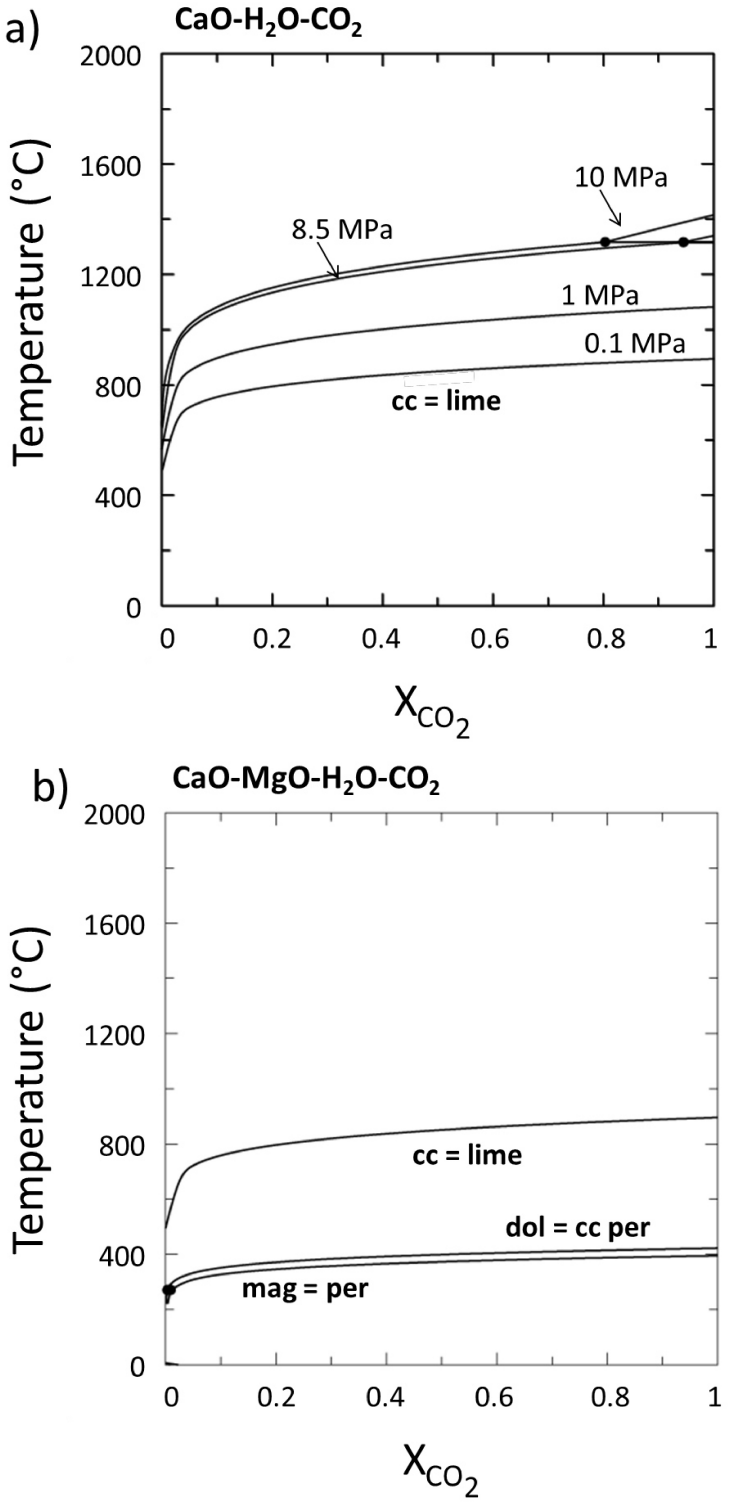

Figure 19. Thermodynamic calculations a) for the system CaO-CO_2-H_2O. Temperature vs. X_{CO2} ranging from 0 (pure water) to 1 (no water) for pressures ranging from 0.1 MPa (=1 bar, atmospheric pressure) to 10 MPa. Lines show equilibrium states of calcite (*cc*, $CaCO_3$), and lime (CaO, high-T phase). At 12 MPa, melting occurs. **b)** for the system MgO-CaO-CO_2-H_2O at 1 bar. **mag**: magnesite, $MgCO_3$; **per**: periclase, MgO; **dol**: Dolomite, CaMg(CO3)2. High-T assemblages are plotted to right of = sign.

768 that is not conducted in a CO_2-atmosphere, the decarbonation temperature should be lower
769 due to the surrounding air. This is consistent with the lower decarbonation temperature
770 usually reported for room-dry calcite experiments (720–900 °C, e.g. Han et al., 2007a).

771 # 4. Discussion

772 The aim of this study is to answer the question what controls the mechanical behavior
773 of the calcite gouge and specifically the weakening at high slip rates. What role is played by
774 thermal pressurization? Is the shear strain partly accommodated by crystal plastic processes?
775 The interplay of temperature, axial displacement and fluid pressure can provide evidence of
776 the pressurization process and its effect on the evolution of shear-stress. Answering these
777 questions requires careful consideration of the mechanical data and microstructures.

778 ## 4.1.Teflon contamination

779 The black or grey material covering the slip surface of some of our experimental
780 samples (Fig. 16a, b) as well as the ultralow shear stress observed in all of our experiments
781 with large displacements at the end of the high-velocity step (e.g., Fig 2b, Fig. 6b) and during
782 the third velocity step (Fig. 8a) raises the suspicion that our samples were contaminated by
783 Teflon or its decomposition products. Polytetrafluoroethylene (PTFE, chemical formula
784 $(C_2F_4)_n$), commonly known under its brand name *Teflon®* (DuPont company), is often used for
785 the jacket material which confines the gouge sample in rotary-shear gouge experiments due to
786 its very low coefficient of friction (c. 0.2, e.g. McLaren and Tabor, 1963; Kitajima et al., 2010).
787 In high-velocity experiments, this can provide problems when the Teflon decomposes due to
788 frictional heating and the sample is contaminated by the Teflon decomposition products. In
789 the gouge sample holder used in this study an additional problem is introduced by the o-rings
790 used to seal the fluids in the sample chamber as they also may decompose and release fluorine
791 (Sawai et al., 2012).

792 To evaluate the decomposition of PTFE, Blumm et al. (2010) measured the specific
793 heat of PTFE (for samples 5 mm in diameter and a thickness of 1 mm) for temperatures
794 between −130 °C and 370 °C. At temperatures between 240 and 360 °C, an endothermal peak
795 (peak temperature of 337.2 °C) in the specific heat indicated a phase change associated with

796 melting of the PTFE. This temperature range is roughly consistent with the PTFE decomposition
797 temperature of c. 315 °C reported by Jentgen (1971), although the reported "maximum
798 constant service temperature in air" is significantly lower (c. 260 °C; Jentgen, 1971).
799 Thermogravimetric analysis (where the sample is heated quickly and its weight is monitored
800 during the course of thermal decomposition) determined Teflon decomposition above a
801 temperature of c. 450 °C (Hondred et al., 2013) and 474 °C (Beyler & Hirschler, 2002),
802 respectively. The onset of degradation increases with increasing heating rate (Hondred et al.,
803 2013). The products of PTFE decomposition are CF_4 and small amounts of hydrogen fluoride
804 (HF) and hexafluoropropene (Beyler & Hirschler, 2002). It is also possible that CF_2 forms
805 directly in the gas phase (Beyler & Hirschler, 2002).

806 In our experiments, the measured temperature stayed below 315°C (the minimum
807 reported Teflon decomposition temperature) in several experiments (phv290–292, 304–6, 310
808 and 313). Assuming that the measured temperatures are indicative of the temperatures at the
809 Teflon sleeves, no thermal decomposition of Teflon should have taken place in those
810 experiments. However, fluorine was detected by EDS analysis in sample phv304. Raman
811 spectroscopy showed (traces of) PTFE on the slipping zones of phv304, 306 and 310. Phv304,
812 305 and 310 were examined using XRD and, out of these, PTFE traces were found in phv305. In
813 these cases, when the sample was contaminated even though the temperature was low, parts
814 of the Teflon sleeve or the o-rings may have been scraped off and been mixed in with the
815 calcite gouge. To evaluate the effect of contamination by this process, we performed rotary-
816 shear experiments on Teflon gouge. The Teflon gouge was produced by grinding pieces of a
817 Teflon ring in a coffee grinder (*Cloer*, 200 W). After grinding for some minutes, the Teflon
818 powder had an approximate particle size of < 500 µm. A layer of 2 mm was sheared using the
819 rotary-shear apparatus ROSA, installed at the Department for Geosciences of the University
820 Padua (for a detailed description of the apparatus see Rempe et al., 2014). The experiments
821 were conducted at a normal stress of 3 MPa; with velocity steps ranging from 1 m/s to 100
822 µm/s (Table 3) with varying displacements. Two experiments (r234, r235) were conducted
823 using a mixture of calcite and Teflon gouge (Table 3). After sliding, the Teflon powder had
824 compacted or sintered to a cohesive slice of Teflon. The roughness of the pistons was

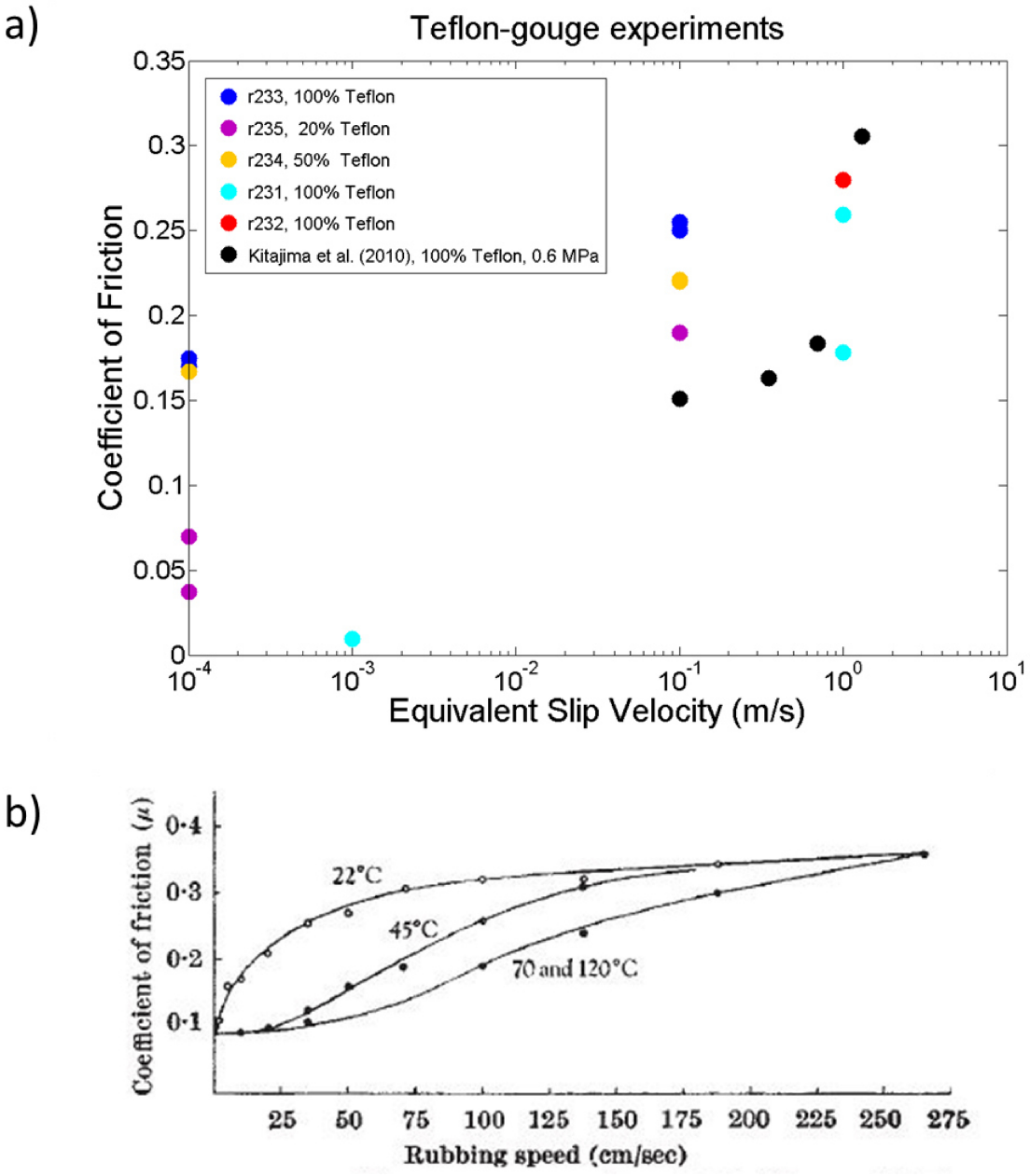

Figure 20. Frictional behavior of Teflon gouge. a) Rotary-shear experiments with Teflon gouges at 3 MPa normal stress. r233 (100% Teflon, blue symbols), r235 (20% Teflon, purple symbols), r234 (50% Teflon, yellow symbols) and r231 (100% Teflon, cyan symbols) where sheared with several velocity steps as summarized in Table 3. Experiments r234 and r235 were performed with a mixture of calcite and Teflon gouge (mixtures of 50/50 and 80/20, respectively). Data from Kitajima et al. (2010) were obtained with 100% Teflon gouge slid in single velocity experiments at 0.6 MPa normal stress. **b)** Variation of the coefficient of friction with rubbing speed of PTFE sliding on PTFE (49% crystalline), from McLaren and Tabor, 1963. "At room temperature the friction rises from about μ=0.07 to μ=0.3 when the sliding speed is increased to about 100 cm/s. As the ambient temperature is increased the rise in friction is shifted into the higher speed range."

imprinted on both sides of the layer, which shows that the slip had actually occurred within the gouge layer. The data from the velocity-step experiments show that the frictional behavior of Teflon is strongly velocity-strengthening. Adding of calcite gouge to the Teflon powder decreases the coefficient of friction (Fig. 20a). In two velocity-step experiments, the velocity was decreased from a) 1 m/s to 1 mm/s which decreased the steady-state friction coefficient μ_{ss} by 0.18 to a value as low as μ_{ss} = 0.01 at 1 mm/s (Fig. 20a, cyan symbols) and b) from 0.1 m/s to 100 µm/s which decreased μ_{ss} by only 0.1 to μ_{ss} > 0.17 at 100 µm/s (Fig. 20a, blue symbols). The velocity-strengthening effect is evident in both cases, however, the lowest absolute friction value was measured at v_s=1 mm/s, not at v_s=100 µm/s. This discrepancy might be due a temperature-weakening effect, that was described by McLaren and Tabor (1963) for Teflon gouges. They showed that at higher temperatures, Teflon weakens at higher slip velocities (Fig. 20b). In our Teflon experiments, the stronger weakening in case a) (when the velocity was reduced from 1 m/s to 1 mm/s; cyan symbols), might thus be due to higher temperatures caused by sliding at higher velocities and for longer total displacements.

This is also applicable to our contaminated calcite gouge experiments: in the experiments phv292 and 297 (the fluid-volume controlled experiments) and phv304 (low effective normal stress of 3 MPa), the coefficient of friction drops down from c. 0.3–0.4 at a slip velocity of 1 m/s to values < 0.1 at slip velocities of c. 1 mm/s. In the experiments at higher normal stress, where the temperatures were higher (Fig. 7a), the coefficient of friction is already low (ranging from 0.09–0.13) before the velocity is reduced and a further friction drop to values as low as 0.02 in induced. This friction value, however, is still much lower than that measured in our Teflon gouge experiments or in comparable experiments performed by Kitajima et al. (2010). However, the tests performed with mixtures of 50% calcite and 50% Teflon gouge, and 80% calcite and 20% Teflon gouge, respectively, showed that the presence of calcite further decreases the friction. For instance, at 0.1 m/s, the coefficient of friction without calcite is c. 0.25, with 50% calcite it is 0.22 and with 80% calcite it is only 0.19. This is to the contrary of the effect observed by Kitajima et al. (2010), who added natural clay-bearing gouge to the Teflon gouge, which yielded an increase in the coefficient of friction with increasing natural gouge content. This opposite effect of a second phase on the friction of

Teflon is likely due to the different chemistry, but might also be due to the experimental set-up, the grain size, etc..

Additionally, in our experiments, the contamination did not necessarily have to occur by bits of Teflon being scraped off and mixed in with the calcite gouge, as it was simulated in the Teflon gouge experiments. If the Teflon decomposes and then covers the slip surface, the effect on the frictional behavior of our sample could be different, which might also explain, why we measure a lower coefficient of friction in the contaminated calcite gouges as compared to the Teflon gouge experiments. It is also possible that a different mechanism, e.g. related to locally high pore-fluid pressures, acts in addition to the effect of the contamination and further reduces the friction.

Still, evidence of Teflon contamination in our experiments should most likely be provided by the decrease in friction when the velocity is reduced at the end of our experiments. This is in fact the case for phv291, 292, 297–301, 304 and 309: the experiments performed at high normal stress (3–12 MPa) and/or with large displacement (> 9.9 m). The coefficient of friction in our experiments shows a recovering in experiments phv290, 305–307 and 310–313, which are the experiments performed either with low effective normal stress (phv305 and 306, 1 MPa), high pore-fluid factor (phv290, λ=0.7), or short displacements (phv307, 310–313, < 5.5 m). Samples from these experiments are thus likely NOT contaminated. This conclusion is supported by the microanalysis we performed, with the exception of phv305 and 306, where traces of PTFE were detected by XRD and Raman analysis, respectively. However, the contamination in these samples seems to be minor, so that the frictional behavior of the material is not influenced. This is consistent with the conclusions of Sawai et al. (2012), who investigated the distribution of fluorine in their post-experimental gouges with electron microprobe analysis. They found that the fluorine content is lower in the high-strain slip zone than in the adjacent less comminuted, lower-strain zone, which might be due to the higher porosity in the low-strain zone. Except for the difference in grain size, no differences in textures between fluorine-rich and fluorine-poor zones was observed and fluorine did not seem to cement the particles. Based on these conclusions, and taking into account the macroscopic appearance of our post-experimental samples and evidence from

frictional data, Raman spectroscopy and XRD and EDS analysis, the mechanical data in all our experiments are most likely not influenced by Teflon decomposition up to a displacement of at least 5 m. In the following, when interpreting the frictional behavior and the pressurization of the gouges, only the data for displacements < 5 m are thus taken into account.

4.2.Temperature evolution

The temperatures are measured with thermocouples located on the stationary side of the gouge layer, i.e. close to the principal slip layer, as in this apparatus slip localizes on the stationary side of the gouge holder (see Discussion section in Chapter II of this thesis). Thus we can assume that the temperatures are representative of the temperatures in the gouge layer. The comparison between the fluid pressure rise measured in the volume-controlled experiments with that calculated support this conclusion. However, temperatures on the localized principal slip surface may be much higher as shown by e.g. Smith et al. (2012) and Violay et al. (2013) following Carslaw and Jaeger (1959) and Nielsen et al. (2008). This is shown by some evidence of decarbonation adjacent to or on the principal slip surface. This decarbonation is thought to result from flash heating (e.g., Rice, 2006; Han et al., 2007b). However, the temperatures necessary to induce extensive decarbonation (> 600 °C at σ_{eff}=3 MPa; Fig. 19a) in the bulk of the material where not reached in our experiments. (Note, that the calculated decarbonation temperatures (Fig. 19) are higher – especially in dry conditions – than those usually reported (720–900 °C for dry calcite, e.g. Han et al., 2007a). However, the maximum temperatures reached in our experiments are also lower than those values and thus no extensive decarbonation should occur even if our values overestimate the decarbonation temperature.)

It is possible, that the thermocouple moves away from the PSL when the gouge layer dilates. However, dilation should mainly occur in the bulk of the material on the rotary side of the PSL, such that the effect of dilation on the temperature measurement should be minor. If a fluid layer should form between the principal slip layer and the base plate of the stationary side of the holder, on the other hand, the measured temperatures might be lower than that in the PSL. This might be the cause for the low temperatures in phv290 (Fig. 7a).

The decrease in the rate with which temperature increases (mostly occurring at displacements of 3–8 m; Fig. 7a) might be due to the higher thermal conductivity of the metal of the sample holder (Ma et al., 2014) causing a faster heat conduction away from the slipping zone (and the thermocouple) once the "heat front reaches" the metal part of the sample holder. Another possible explanation for the ceasing temperature increase are endothermic reactions, e.g. decarbonation or Teflon decomposition. However, the onset of the temperature decrease does not systematically occur at a specific temperature. For example, in experiments conducted at 8.5 MPa effective normal stress, the temperatures range from c. 300–650 °C. Similarly, secondary dilation occurs at apparently random temperatures ranging from 300 °C in phv292 to 480 °C in phv298 and c. 600 °C in phv300 (all conducted at the same effective normal stress of 8.5 MPa), but not necessarily coinciding with the temperature decrease. Thus, the cause for the secondary dilation remains unclear.

4.3. Evidence of pressurization? Interplay of friction, temperature and axial displacement in the fluid-pressurized experiments

The pore-pressure measurements in the volume-controlled experiments (Fig. 3e and 7e) as well as our thermodynamic calculations showed that for the temperature rises measured in our experiments, thermal expansion of the pore fluid leads to pressurization (Fig. 18). In this section, we will look for evidence of pressurization in the mechanical data of our water-saturated experiments and aim to answer the question when pressurization is thermally-driven and when due to compaction and, if the data show evidence of *thermal* pressurization, if it is due to decarbonation (CO_2) or thermal expansion/evaporation of the pore fluid (H_2O).

Pressurization of the pore fluid is directly determined in the volume-controlled experiments by the measurement of upstream- and downstream pore-fluid pressure (Fig. 7e). In the pressure-controlled experiments, a fluid-volume decrease (Fig. 7d) shows that a pressurizing mechanism is active, although the pressurization itself is immediately compensated by the decrease in the fluid volume. The pressurization here is thus only indirectly measured by the fluid-volume decrease.

4.3.1. First low-velocity step: mechanical pressurization

During the first low-velocity step the fluid pressure measured in the volume-controlled experiments rises by up to 1.2 MPa (Fig. 3e). This pressure rise is accompanied by a temperature increase of only 6–8 °C (Fig. 3b), consistent with the low sliding velocity which causes less frictional heat. The gouge compacts by 250–350 µm (Fig. 3c). The low temperature and the high degree of compaction suggest, that the pressurization was mechanical (caused by the compaction) rather than thermal (caused by fluid temperature increase).

During the first low-velocity step, the steady-state shear stress is drastically lower in the experiments with a higher pore-fluid factor (Fig. 3a). The lower shear stress causes less frictional heating: temperature increases only by 0.5 °C in experiments phv305 (λ=0.6) (Fig. 3b, yellow curve). Here, the axial displacement and the fluid-volume change exhibit the same characteristics as in the experiments with smaller λ, showing that, at a low velocity of 1 mm/s, the frictional heating does not influence the degree of pressurization.

The fluid-volume controlled experiment phv297 showed a much smaller pore-pressure increase and a higher degree of compaction than phv292 (Fig. 3c, e). Additionally, the axial displacement in experiment phv297 does not show any transient dilation. Possibly, the system wasn't completely saturated before the start of the experiment limiting the amount of pressurization and resulting in the large compaction.. The higher fluid pressure in experiment phv292 is thus most likely more representative (and more compatible with the calculated pressure increase (Fig. 18)**.**

In the fluid-pressure controlled experiments, frictional heating causes temperature to increase by 1–8 °C depending on σ_{eff} (Fig.3b). The gouge compacts strongly during the first 5 mm of sliding and then continues to compact almost throughout the low-velocity step with the higher degree of compaction in the higher-σ_{eff} experiments (Fig. 3c). Consistent with the degree of compaction, the fluid volume, as an "inverse proxy" for fluid pressure, shows a fast decrease in the first 5 mm of displacement followed by a more moderate decrease throughout the low-velocity step, with the decrease being stronger at higher σ_{eff} (Fig. 3d). The fluid-volume *de*crease shows that the gouge is pressurized. Even though the average degree of compaction

968 is slightly lower than in the fluid-volume controlled experiments, the low temperatures suggest
969 that pressurization is rather caused by the compaction instead by thermal pressurization in
970 pressure-controlled conditions as well. Consistent with this, in cases where fast compaction in
971 the first millimeters of sliding is delayed (due to the phase of transient dilation in the higher-
972 σ_{eff} experiments), the onset of fluid-volume decrease is delayed as well.

973 In experiments phv310 and 306 a transient *increase* in the fluid volume at the start of
974 the experiment was observed. In the case of phv310 this can be attributed to a small
975 oscillation in the fluid pressure. Phv306 neither shows oscillations in fluid pressure or normal
976 stress nor any transient dilation that would cause a fluid-volume increase. Possibly, like in the
977 case of phv297, the system wasn't completely saturated before the start of the experiment;
978 with the start of shearing, fluid pathways may have been created causing the initial fluid-
979 volume increase of 0.54 ml.

980 At constant effective normal stress (i.e., in the pressure-controlled experiments), the
981 shear stress is nearly constant during the low-velocity step. However, when the fluid-pressure
982 is allowed to increase, this influences the effective normal stress, which, results in a decrease
983 in the shear stress; consistent with the Terzaghi law, $\tau = \mu(\sigma_n - p_f)$. This is the case for both
984 phv292 and 297, although the effect is greater in phv292, where the decrease in σ_{eff} of 1.2
985 MPa results in a decrease of the steady-state shear stress τ_{ss} in the same order of magnitude
986 compared to the average τ_{ss} of the pressure-controlled experiments. The short initial
987 strengthening phase at initiation of sliding followed by slight weakening is also observed in the
988 pressure-controlled experiments, and thus not due to a pressure-related mechanism.

989 #### 4.3.2. High-velocity step

990 All experiments that were stopped after short displacements of c. 5.5 m typically show
991 a re-strengthening as the velocity is decreased (e.g., phv307 in Fig. 4a and 8a). This suggests
992 that a velocity-dependent weakening mechanism is active at least in the first 5.5 m of
993 displacement. Additionally, Teflon or Teflon decomposition products were only found in the
994 longer-displacement (≥ 9.9 m) samples. In the following, we thus discuss the interplay of

friction, axial displacement, temperature and pressurization for the first < 5.5 m of displacement.

4.3.2.1. The first millimeters: strengthening phase and initiation of weakening

During the strengthening phase in the first 0.7–4 mm of slip at high velocity, the gouge strengthens to a peak strength, while axial displacement, fluid-volume and fluid-pressure (Fig. 7f) are relatively constant**.** Since the heat wave produced by frictional heating may not have reached the thermocouple after a displacement of only 4 mm, the temperatures along the principal slip surface may be higher than the measured temperatures, and weakening may be thermally activated. To test this, the bulk temperature rise along the principal slip surface can be estimated using the 1D heat diffusion equation of Carslaw and Jaeger (1959):

$$\Delta T = \frac{\tau\, v \sqrt{t}}{\rho\, c_p \sqrt{\pi\, \kappa}}. \qquad (4)$$

For an equivalent velocity v accelerating at 0.5 m/s^2 from a starting velocity of 1 mm/s (thus yielding v≈0.05 m/s after a slip distance of 4 mm), a density ρ=2700 kg/m^3, a specific heat capacity c_p=800 J/kg*K, and a thermal diffusivity κ=1.48*10^{-6} m^2/s, the bulk temperature rise ΔT after 4 mm of slip on the principal slip surface ranges from 5.7 °C to c. 25 °C assuming a constant shear stress τ ranging from 2 MPa to 8.5 MPa (corresponding to the peak shear stresses reached in experiments with σ_{eff} ranging from 3 MPa to 12 MPa). According to our previous calculations (Fig. 18), a temperature increase of 5.7–25 °C yields a pressure increase of 0.036–0.16 MPa, significantly smaller than the pressure rice during the low-velocity step (1.2 MPa). Additionally, since the calculation assumes an extreme localization of slip, a constant high shear stress, and neglect any latent heat, these values will overestimate the real bulk temperature increase along the principal slip surface. Thus, no significant pressurization occurs in the low σ_{eff}-experiments. However, it is possible that the faster dynamic weakening in experiments with higher effective normal stress (as shown by the shorter strengthening phase, Fig. 5c; see also Fig. 4 in Chapter II of this thesis) is due to higher temperature and – in undrained conditions – pore-pressure increase along the principal slip surface in the high σ_{eff}-experiments.

In the water-saturated experiments, transient dilation initiates at a similar range of displacements (c. 0.7–7.6 mm) as the onset of weakening (0.7–4 mm). But even though the order of magnitude of displacements agrees, weakening and transient dilation do not systematically occur simultaneously and it is thus doubtful that one is the cause of the other. The transient dilation does not seem to be associated with a transient pressurization, either. In fluid-pressure controlled experiments, the fluid-pressure is generally constant and the dilation does not occur simultaneously with the start of the fluid-volume decrease. The minor amount of dilation (< 50 µm) might be too small to induce a measureable fluid-volume or –pressure change. The transient dilation may be caused by shear dilatancy due to comminution of the gouge material, and the end of the transient dilation might mark the point in the experiment when localization is achieved and all slip is hosted on one single slip surface.

4.3.2.2. Post-weakening

Following transient dilation, the main compaction stage initiates. In the volume-controlled experiments the gouge compacts by only 25–40 µm, the same amount as the previous transient dilation and significantly less than in the fluid-pressure controlled experiments with similar total displacements (Fig. 7b). The lower amount of compaction in the volume-controlled experiments is due to the increase in pore pressure prohibiting compaction. Overall, the saturated gouges compact by a smaller amount than the room-dry gouges possibly because the wet gouges already compacted by c. 5 – 15% during the low-velocity step. Further compaction may be impeded by the water in the pore-space of the saturated gouge material.

Secondary dilation of 150 µm initiates at c. 1.5 m of displacement in phv297 (Fig. 21a), similarly as in some fluid-pressure controlled experiments, while phv292 does not show secondary dilation. In both experiments, the pressure is increasing throughout the high-velocity step (that is, during the first 5 m that are being evaluated here), even during the transient and secondary dilation (in the case of phv297, Fig. 21a) and while the axial displacement is constant (phv292). This suggests that the pressurization is not compaction-induced and thus likely due to thermal pressurization.

Continuous fluid-volume decrease in the pressure-controlled experiments shows that the gouge is continuously pressurized (Fig. 7d, 21b). At the start of the high-velocity step, the main compaction takes place which is likely responsible for the pressurization. However, at larger displacements the fluid volume continues to decrease while the axial displacement is steady (e.g., Fig. 21b, 3–5.5 m of displacement). This suggests that the fluid-volume decrease, and thus the pressurization, is at least partly compaction-induced during the first < 3 m of displacement, while at higher displacements, thermal pressurization is dominant. In fact, the temperature at these displacements is relatively high, increasing from c. 100 to 200 °C which – as our calculations showed – should result in a pressurization of c. 1–3.5 MPa. The maximum temperature (measured in experiment phv300, σ_{eff}=8.5 MPa) was c. 650 °C. This is smaller than the calcite decarbonation temperature at this pressure (c. 700°C, Fig. 19a) indicating that thermal pressurization was caused by the thermal expansion and evaporation of water and not by CO_2 degassing.

4.3.2.3. Pore-pressure measurements: problems related to gouge permeability

A problem that is always encountered when performing experiments with fluid pressure is the impracticality of measuring the pressure within the pores of the sample. Also in our study, the fluid pressure was measured outside of the gouge holder (Fig. 1b). Low permeability of the gouge or clogging of the fluid tubes by fine material particles could lead to the pressure in the gouge layer being different from the pressure we measure. This could lead to a misinterpretation of the pressurization mechanism: With continued shearing, the gouge becomes less permeable. Then, when pressurized e.g. due to compaction of the gouge, the movement of the fluid (leaving the gouge/sample chamber) could be delayed by the low permeability. This delay could be responsible for the continued fluid-volume decrease after the compaction has already stopped and an in fact compaction-induced pressurization could be interpreted as being thermally-induced.

Evidence for the pressure being trapped is provided in experiment phv291, where Valve 2 (the shortcut between upstream and downstream line) was closed (Fig. 21c). The fluid volume is controlled by a piston upstream of the sample. Thus, in phv291, the upstream fluid

pressure stays constant at the initial 1.5 MPa while the downstream pressure shows an increase of 2.5 MPa during the first 5 m of displacement (Fig. 21c). The high pressure seems to be trapped on the downstream side of the impermeable principal slip surface that forms at the stationary, "upstream" side of the sample. However, when Valve 2 is open, as it is in the majority of our experiments, upstream- and downstream pressures are equal and a high pressure cannot build up, at least not to this degree. SEM analysis shows that no localization of slip occurred on the rotary side ("downstream") of the sample. The gouge material here is relatively un-comminuted and porous and, as it can be assumed, relatively permeable. It is thus unlikely that a high fluid pressure would build up within the gouge layer.

Permeability measurements of sheared samples yielded permeabilities in the order of 10^{-17} m^2 (Fig. 9). This is relatively permeable supporting the conclusion that it is unlikely that the high pore-fluid pressure gets trapped within the sample chamber and could cause the delayed fluid-volume increase at least at these short displacements (≤5.2 m) and when sheared only at high velocity. The additional low-velocity step in the majority of our experiments might have further decreased the permeability. Experiment phv313 was performed at similar conditions as the permeability experiment phv295, only the effective normal stress and pore-fluid factor were smaller (3 MPa, 0.17). Phv313 was also run with a single velocity step of 1 m/s. The permeability of the gouge in experiment phv313 should thus be in the order of 10^{-17} m^2. The mechanical data of phv313 show the same characteristics as the pre-sheared, experiments (Fig.4), again supporting the conclusion that fluid pressure did not get trapped in the sample chamber also in those experiments.

4.3.3. Larger displacements/Second low-velocity step

At larger displacements (> 5.5 m of slip) in the high-velocity step, as well as during the second low-velocity (1 mm/s) step of most of our experiments, the samples are likely contaminated by Teflon or

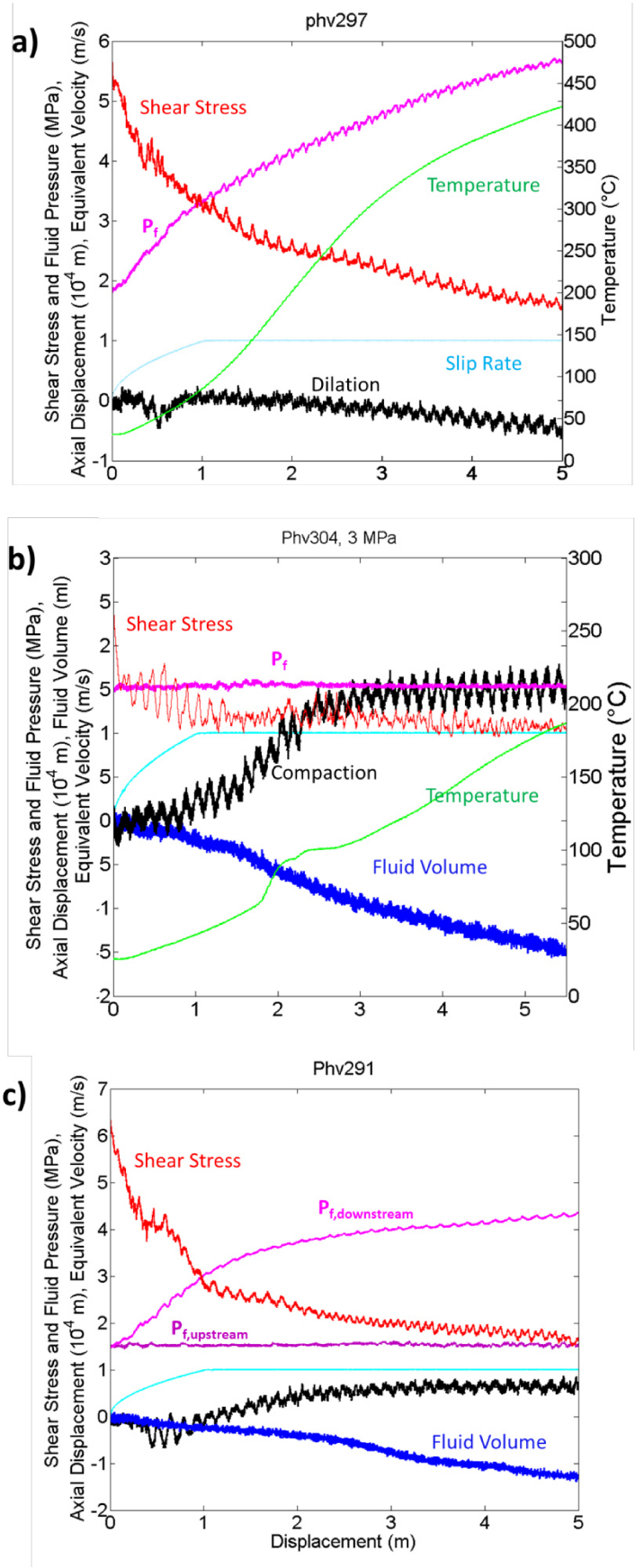

Figure 21. See next page for description.

Figure 21 (previous page). Summary plots of the mechanical data of two experiments. a) phv297 (volume-controlled, initial experimental parameters: σ_{eff}=8.5 MPa, λ=0.15; d_{total}=18.4 m), **b)** phv304 (pressure-controlled, 3 MPa, λ=0.33; d_{total}=19.1 m) , and c) phv291 (pressure-controlled, 8.5 MPa, λ=0.15; d_{total}=22.7 m) where Valve 2 was closed. Plotted on the primary y-axes again the equivalent displacement are the shear stress (MPa, red curves), the fluid pressure (MPa, pink curves), the axial displacement (10^{-4} m, black curve), the equivalent velocity (m/s, cyan curves) and in the case of phv304 the fluid-volume (ml, blue curve). The secondary y-axes show the temperature (°C, green curves).

Figure 22 (below). Comparison of room-dry and water-saturated experiments. a) Evolution of shear stress for the first c. 5.5 m of displacement (low- and high-velocity step) of experiments performed at an (initial) effective normal stress of 8.5 MPa. Black dotted line shows onset of high velocity. Red curves: room-dry experiments, black curves: pressure-controlled experiments, grey curves: volume-controlled experiments. **b)** Evolution of axial displacement with displacement shown separately for the low- and high-velocity steps. Color-coding as in a). Positive change denotes compaction, negative change dilation.

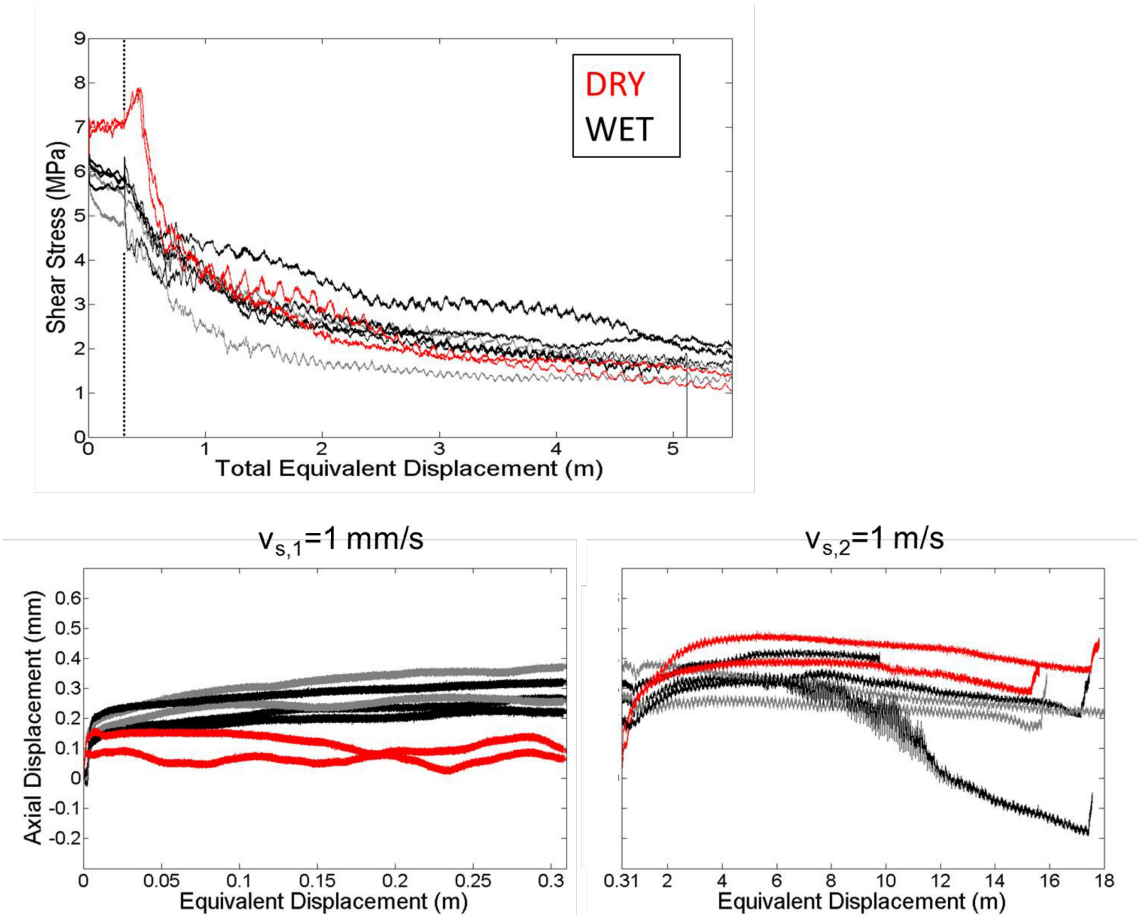

its decomposition products (Table 2). In the high-velocity step, continued fluid-volume decrease (Fig. 7d), fluid-pressure increase (Fig. 7e), as well as secondary dilation (Fig. 7b) may be caused by pressurization due to the Teflon decomposition. At low velocity, de-pressurization occurs in all experiments, as shown by (1) the fluid-volume increase for pressure-controlled experiments (Fig. 8d), (2) the fluid-pressure decrease for volume-controlled experiments (Fig. 8e) and (3) the gouge layer compaction (Fig. 8c). That the former pressurization was thermally induced is now supported by the de-pressurization being accompanied by a fast temperature drop (Fig. 8b).

4.4.Dynamic weakening mechanisms

4.4.1. Role of thermal pressurization and alternative weakening mechanisms

In the previous section it was shown that in our water-saturated experiments pressurization is induced by compaction at low velocities (1 mm/s, section 4.3.1.). At high velocity, pressurization is due to frictional heating and (prior to secondary dilation) enhanced by compaction (1 m/s, section 4.3.2.). In the room-dry experiments, pressurization could only occur by calcite decarbonation due to high temperatures along the principal slip surface. However, if decarbonation increases the pore pressure, it should equilibrate with the atmospheric pressure, because the sample chamber is open to the atmosphere (through the disconnected tubes of the fluid system). Thus, no pressurization should occur in the room-dry experiments and the effect of pressurization on the frictional behavior of the calcite gouge can be deduced by comparing the shear-stress evolution of room-dry and volume-controlled saturated gouges. Additionally, the effect of the presence of water on the mechanical behavior of calcite gouges is discussed.

In our study, the dry gouges sheared at low velocity (1 mm/s) generally have a higher steady-state shear stress than the saturated gouges sheared at the same effective normal stress (Fig. 3a, Fig. 22a). At the same time, the room-dry gouges compact only slightly during the low-velocity step compared to the saturated gouges (Fig. 3c, Fig. 22b). At high velocity (1 m/s), however, dry gouges compact abruptly before secondary dilation takes place, and the

water-saturated gouges compact much less (Fig. 22). The difference to the room-dry gouges is even larger in fluid-volume controlled conditions both at low and high velocity (Fig. 22b). The shear stress at high velocity shows a much longer strengthening phase of the dry gouge followed by abrupt weakening to steady-state values which are lower than for the fluid-pressure controlled experiments that, instead, showed instantaneous weakening at the initiation of sliding at high velocity (Fig. 22a). The lower steady-state shear stress of the fluid-volume controlled experiments than in pressure-control mode and in dry conditions is due to the fluid-pressurization reducing the effective normal stress as discussed above.

4.4.1.1. First low-velocity step

The lower steady-state friction of the water-dampened gouge is consistent with the results obtained by Verberne et al. (2013), who conducted calcite gouge experiments at much lower slip rate of 0.1–10 µm and a higher effective normal stress of 40 MPa (but with a similar pore-fluid factor of 0.2) and obtained coefficients of friction of 0.6 in wet and 0.7–0.8 in dry gouges. They attributed the lower strength of wet gouges to enhanced pressure solution, subcritical crack growth and intergranular lubrication in the presence of water. Even though the relatively high compaction in our water-saturated experiments is consistent with pressure solution, due to the compared to natural conditions relatively high strain rates (c. 10^{-1} s^{-1}) it will likely play a minor role in our high-velocity experiments. But the 2–3 times higher fracture surface energy of calcite in the presence of fluids (Røyne et al., 2011) will result in accelerated subcritical crack growth also in our experimental conditions (e.g. Rice et al., 1978, Atkinson, 1984). Faster comminution due to enhanced subcritical cracking and subsequent closing of pore space might also be responsible for the relatively high compaction. Thirdly, intergranular lubrication may be enhanced as well in our experiments. Microstructural analysis showed that large grains are more rounded in water-saturated (Fig. 11a) than in room-dry conditions (Fig. 10a). In the presence of water, particles might slide past each other more easily causing mere abrasion of edges, while in dry conditions collision and shattering of particles may prevail. Another explanation for the different texture might be that in room-dry conditions less deformation is hosted in Zone I as compared to water-saturated conditions. However, results from experiments with strain markers suggest that it is the other way around (Chapter II of this

thesis, Fig. 11c). Additionally, if deformation was more localized in room-dry conditions, this should result in less dilation (Rathbun and Marone (2010), who use dilation as a proxy for localization), or with other words, larger compaction rates, than in water-saturated conditions, which is the opposite of what we observe.

4.4.1.2. High-velocity step: weakening

In addition to the different characteristics of the axial displacement (saturated gouges compact mainly during the low-velocity step, room-dry gouges during the high-velocity step), room-dry and water-saturated gouges exhibit significantly different weakening behavior. Weakening in room-dry calcite gouges sheared at high velocity was previously attributed to flash heating (Smith et al., 2015). This is supported by evidence of almost instantaneous CO_2 degassing at the beginning of sliding at velocities < 0.2 m/s) when bulk temperatures are much too low to induce decarbonation (Smith et al., 2015). For decarbonation to occur, temperatures in the slip zone must be higher (> 1000 °C according to our thermodynamic calculation, Fig. 19a). Evidence of locally high temperatures is found in the microstructures of our samples, where zones of recrystallized grains or possibly decarbonated material are found adjacent to the principal slip surface. Additionally, the disordered carbon found on the slipping surfaces of several samples investigated with Raman spectroscopy might provide further evidence of decarbonation (Green et al., 2010; Spagnuolo et al., 2014). Weakening by flash heating could be accelerated in the presence of water due to the lower fracture surface energy of calcite causing the almost instantaneous weakening in the water-saturated experiments at the initiation of the high-velocity step. The presence of water should not have a large cooling effect on the flash temperatures, as modeled by Violay et al. (2014) for asperities of solid Carrara marble sheared at seismic velocities, and thus should not result in delayed onset of flash weakening in water-saturated conditions.

Additionally, amorphous carbon forming on the slip surface of carbonate-bearing faults might result in lubrication and subsequent weakening (Arai et al., 2002; Oohashi et al., 2014). Amorphous carbon that was found in the slipping zones of solid Carrara marble samples deformed at high velocity in ambient conditions was inferred to derive from the decomposition of the calcite (Spagnuolo et al., 2014). The precise carbon formation process,

however, is only understood for anoxic conditions (Oohashi et al., 2014; Kuo et al., 2014). If carbon derives from the CO_2 of decomposed calcite, its formation could be accelerated in the presence of water due to lower decarbonation temperatures which could explain the accelerated weakening in water-saturated conditions. Further analysis by transmission electron microscopy will help to determine if the disordered carbon detected on the slipping zones of several of our post-experimental sample is amorphous and could cause such a lubrication.

4.4.1.3. High-velocity step: steady state

In addition to this physico-chemical weakening mechanism, weakening in the volume-controlled experiments is stress related. As described by the Terzaghi law, the increase in the pore-fluid pressure causes a decrease of the effective normal stress and thus of the shear stress. This effect was observed in both the low- and the high-velocity step (Fig. 3a, 5a). However, at displacements > 4 m during the high-velocity step, the shear stress of room-dry, pressure-controlled, and volume-controlled experiments assimilates (Fig. 22). The weakening effect of the physico-chemical mechanisms observed at low velocity and in the beginning of the high-velocity step as well as of the thermal pressurization observed in the volume-controlled experiments appears to become negligible. This might suggest that at larger displacement it is not a frictional, brittle process controlling the shear stress but possibly a crystal-plastic process. Unfortunately we do not have images of the slip surface of our samples. However, evidence of recrystallization found in room-dry as well as in water-saturated samples (Fig. 10b-d, Fig. 12) cut perpendicular to the slip surface supports the hypothesis. The shape-preferred orientation of recrystallized grains in many samples (Fig. 10d, 12b, e and g) indicated that recrystallization occurred at least partly dynamically. Geometry of grains adjacent to the principal slip surface suggests that grain boundary sliding possibly aided by diffusion creep took place (Fig. 12a) (e.g., Twiss and Moores, 1992), as does the presence of cavities in a slab of material containing recrystallized grains that might be a piece of the slip surface that was reworked into the bulk material (Fig. 12c). However, some cavities are also located within the grains, which might be due to decarbonation.

Evidence of strain accommodation by crystal-plastic processes active at sub-seismic strain rates was previously reported by Verberne et al. (2014), who proposed diffusion-accommodated grain boundary sliding to occur in nominally dry calcite gouge sheared at 1 µm/s. The activation of this process was attributed to enhanced diffusion rates in nanofibers (Würschum et al., 2003; Tjong and Chen, 2004) that developed in the slip zone. Nano-particles were also observed in the slip zones of samples from high-velocity experiments (Green et al., 2010; Holdsworth et al., 2013; Schubnel et al., 2013). It was suggested by Green et al., 2010, that a "pavement" of nanometric (100–300 nm) crystalline dolomite that formed on the slip surface of solid rocks sheared at high-velocity might be due to superplastic flow. In experiments with calcite gouge, Holdsworth et al. (2013) observed similar nanograins composing the slip zone and proposed that dynamic weakening of their calcite gouge was caused by diffusion-dominated grain boundary sliding that was activated due to cataclastic grain size reduction and frictional heating. The shear stress measured in the high-strain experiments of Holdsworth et al. (2013) could be predicted by the Coble creep flow law. In accordance with our microstructural results that suggest grain boundary sliding possibly aided by diffusion creep to occur in our experiments, we estimate the steady-state shear stress in the high-velocity step of our experiments using the law for superplastic flow given by Schmid et al. (1977) for grain sizes < 10.5 µm:

$$\tau_{SS} = \sqrt[n]{\frac{\dot{\varepsilon}}{A\, d^3\, e^{\frac{-H}{RT}}}} \qquad (5)$$

where τ_{ss} is the steady-state shear stress; $\dot{\varepsilon}$, the strain rate; A, a constant expressing strain-rate effecting structural factors; d, the grain size; H, the activation energy for diffusion creep; R, the gas constant; T, the temperature; and n, a parameter describing the stress-dependence of strain rate. For diffusion creep in calcite, Schmid et al. (1977) empirically determined average values for n=1.66, A=4.98*10^{-18} m^3/Pa*s, and H=213 kJ/mol. In our experiments, the strain rate $\dot{\varepsilon}$≈10^3 s^{-1}. The minimum grain size observed in our SEM images is d_{min}≈100 nm (e.g., Fig. 12a). However, most grains observed in the SEM images are at least one order of magnitude larger (d≈1 µm). As suggested by zones of decarbonation in our samples, we assume that the temperature at the slip surface was high enough to induce a decarbonation reaction: T≈1000 K. Thus, assuming steady-state conditions and constant

temperature, τ_{ss}≈1.5 MPa and 17 MPa, for d_{min} and d, respectively. The steady-state shear stress in our experiments ranges from c. 1–2 MPa (at displacements of c. 5 m; Fig. 16) and is thus similar to the calculated shear stress for grain sizes d_{min}≈100 nm, while the calculated τ_{ss} for grain sizes d≈1 µm is significantly larger. Using the smaller grain size for the calculations might be appropriate as some grain growth associated with sintering is expected to happen after the experiment, when the gouge is still under load and the temperature in the slipping zone is still relatively high (Kang, 2005; Mitchell et al., 2015). Further microstructural investigations, e.g. using transmission electron microscopy, could provide information on the size of the particles that make up the slip surface.

Consistent with superplastic deformation, the shear stress in our experiments continues to decrease while the temperature increases with increasing displacement. Shear stress is only truly constant at displacements ≥ 10 m, when the temperature has ceased to increase as well and is constant in most experiments. However, at these large displacements samples have most likely already become contaminated with Teflon.

Schmid et al. (1977) do not give information whether the parameters A, H, or n are different for wet calcite and could thus explain the slightly higher steady-state shear stress in our water-saturated as compared to the room-dry samples. The size of grains adjacent to the PSS does not seem to be significantly different in different ambient conditions. Possibly, it's a bit smaller in water-saturated conditions, but this would lead to a lower τ_{ss} in saturated conditions. Studies of diffusion rates in calcite showed that oxygen diffusion rates are enhanced in the presence of water (Farver, 1994; Farver and Yund, 1996), but carbon diffusion rates are not (Kronenberg et al., 1984; Farver and Yund, 1996). In calcite, calcium is the slowest diffusing species (Farver and Yund, 1996), however, no experimental results of the effect of water have yet been published to our knowledge. It thus remains unclear whether the slightly higher steady-state shear stress in water-saturated conditions is consisted with grain boundary sliding aided by diffusion creep.

4.4.2. Effect of the pore-fluid factor

In experiments performed at a given effective normal stress, a difference in the pore-fluid factor resulted in (1) a longer strengthening phase (Fig. 5c), (2) a lower peak stress (Fig. 5e) and, (3) a lower steady-state stress (Fig. 6a), for higher pore-fluid factors. Additionally, the microstructure is characterized by a relatively low degree of comminution and a sharp principal slip surface, which indicates a high degree of localization. However, the principal slip surface is not lined by sintered or recrystallized grains (Fig. 11b), consistent with the relatively low temperatures (Fig. 7a). The effect of λ, that is most extreme in experiment phv290 (λ=0.7, σ_{eff}=3 MPa), could partly be attributed to the formation of a fluid layer on the slip surface once high-velocity sliding initiates. The formation of a fluid layer would be consistent with the low degree of frictional heating compared to other experiments at σ_{eff}=3 MPa (Fig. 7a), which again explains the very low degree of pressurization (the total decrease in the fluid volume is only 0.02 ml, which is 1 to almost 2 orders of magnitudes lower than the decrease in the lower-λ experiments). It remains unclear, however, why the gouge shows a large transient dilation at the initiation of sliding which appears to cause a transient fluid pressure decrease (Fig. 5d).

4.5.Comparison to cohesive Carrara marble

The effect of pore fluids on the frictional behavior of cohesive carbonate rocks was studied by Violay et al. (2013, 2014) by conducting high-velocity rotary-shear experiments on Carrara marble. As in our gouge experiments the cohesive rocks weakened more abruptly when they were saturated with pressurized pore fluids than in dry conditions. Consistent with our conclusion, Violay et al. (2013, 2014) suggested that weakening in carbonate rocks was triggered by flash heating that was accelerated in the presence of fluids due to subcritical crack grow leading to brittle failure of the asperities. The difference in the weakening behavior is stronger in the gouges, due to the prolonged strengthening phase in room-dry gouges compared to room-dry cohesive rocks (Fig. 22a). The prolonged strengthening phase was previously attributed to the need to localize slip in room-dry gouges prior to weakening by flash heating (Proctor et al., 2014; Smith et al., 2015). The strengthening phase in the water-dampened cohesive rocks appears to be c. < 1 mm at σ_{eff}=20 MPa which is roughly in agreement with the data from the gouge experiments (see Chapter II, Fig. 4a of this thesis).

In addition, the steady-state shear stress of the cohesive rocks is slightly lower (τ_{ss}≈1 MPa at σ_{eff}=10 MPa; Violay et al., 2013) than in the gouges (τ_{ss}≈1–2 MPa for σ_{eff}=8.5–12 MPa; Fig. 4a, 22). This might be due to the higher pore-fluid factor used in the experiments with Carrara marble rocks (λ=0.33 as opposed to λ=0.17 in most of our experiments). In the cohesive rocks, evidence of decarbonation was found that was thought to occur post-weakening, but no carbon was detected on the slipping surfaces of the cohesive samples (Violay et al., 2013). Since the steady-state stress of cohesive rocks are slightly higher than that of the gouges, this raises the doubt whether the disordered carbon found on the slipping surface of our samples lubricated the sample.

4.6.Implications for natural faults

The experimental results indicate that carbonate-bearing fault zones are more prone to slip in the presence of pore fluids. Additionally, it was shown that the higher the pore-fluid factor λ, the weaker the fault. These implications are relevant for understanding the behavior of natural fault zones cutting through carbonates, e.g. the long-lasting earthquake sequences of Umbria-Marche (1997-1998; Cocco et al., 2000; Chiaraluce, 2004; Collettini et al., 2009) and L'Aquila (2008-1009; Chiaraluce et al., 2011; Chiaraluce, 2012). In addition to physico-chemical fluid effects that would facilitate earthquake nucleation on the fault zones that hosted these earthquake sequences, borehole drilling (Chiodini and Cioni, 1989; Collettini and Barchi, 2002) and seismological modeling (Miller et al., 2004; Di Luccio et al., 2010; Terakawa et al., 2010) provided evidence of high-pressure fluids at depth. The high-pressure fluids are likely controlling earthquake nucleation and occurrence of aftershocks due to the stress-related effects of pore fluids.

5. Conclusion

Intermediate- to high-velocity rotary-shear experiments on calcite gouges revealed significant differences in the mechanical behavior in room-dry and water-saturated and –pressurized conditions. At intermediate velocity (1 mm/s), the shear stress of water-saturated gouges was significantly lower than in room-dry conditions, which was attributed to intergranular lubrication and to the lower calcite fracture surface energy accelerating

subcritical cracking. This is consistent with the higher degree of compaction. At this velocity, temperatures were inferred to be too low to induce thermal pressurization. To the contrary, at high velocity (1 m/s) frictional heating leads to thermal pressurization and subsequent decrease of the shear stress in the experiments performed in undrained conditions. Thermal pressurization is most likely caused by thermal expansion of the pore fluid (water), as the temperatures should be too low to induce extensive decarbonation.

Weakening in saturated gouges occurs abruptly at the initiation of sliding at high velocity, while the room-dry gouges show a pronounced strengthening phase before the onset of weakening. Additionally, for a given effective normal stress, the peak stress was lower for higher pore-fluid factors $\lambda = \frac{p_f}{\sigma_n}$. This suggests that carbonate-bearing faults are more prone to slip in the presence of pore fluids and even more so if those are pressurized, which might explain the long-lasting earthquake sequences of Umbria-Marche and L'Aquila hosted on carbonate-bearing faults. Pressurization by frictional heating does not influence the initiation of weakening (the strengthening phase and peak stress of gouges in undrained and drained experiments are the same) probably because the weakening occurs too abruptly. Thus the acting weakening mechanism is likely due to a physico-chemical effect. We suggest that weakening in room-dry and water-saturated gouges occurs by flash heating, which is accelerated in the presence of fluids by subcritical crack growth. The detection of carbon on the slipping surface of our calcite samples indicated that decarbonation has occurred which is consistent with flash heating. Lubrication by amorphous carbon resulting from the decarbonation of calcite, however, is yet to be confirmed.

Zones of recrystallized grains adjacent to the principal slip surfaces possibly featuring microstructures characteristic for grain boundary sliding aided by diffusion creep suggest that strain was not only accommodated by frictional processes, but possibly by superplasticity. At larger displacements, the similarly low steady-state shear stress of room-dry and water-saturated gouges is roughly consistent with values calculated using the law for superplastic flow given by Schmid et al. (1977).

6. Acknowledgements

MR thanks Takehiro Hirose, Kentaro Hatakeda and Manami Kitamura for comprehensive support during and following her time in Kochi. Osamu Tadai and Federico Zorzi are acknowledged for XRD analysis. Andrea Cavallo and Leonardo Tauro are thanked for support with SEM analyses and Francesca Prando for assistance with Raman spectroscopy. Thanks to Thomas Mueller (University of Leeds) for help with the thermo-dynamical calculations using Perple_X. Silvio Ferrero (Potsdam University) and John Wheeler (University of Liverpool) are thanked for helpful discussions. MR acknowledges funding by Ca.Ri.Pa.Ro.; MR, GDT, TMM, and SAFS acknowledge the European Research Council Grants USEMS (no. 205175) and NOFEAR (no. 614705).

7. Figure Captions

Figure 1. **Experimental Set-up. a)** Schematic diagram of the rotary-shear apparatus installed at the Kochi Institute for Core Sample Research (from Tanikawa et al., 2012). **b)** Schematic diagram of the pore-fluid pressure system. Red: main fluid path, yellow: fluid path used to build up initial pressure or to control downstream pressure individually. ***S***: Main fluid-pressure control using moving piston to control fluid volume and pressure; P_{up}/P_{down}: upstream/downstream pressure gauge; *P*: Pneumatic pump to apply initial pressure; *G*: Gas-pressure control of down-stream pressure. **c) Gouge holder assembly.** Yellow: stationary parts; blue, green and grey: rotary parts. Grey: Teflon. "*IN*" and "*OUT*": fluid inlet and outlet, respectively. "*TC*": thermocouples. With the set-up used during the experiments, the upper part of the holder is almost fully extracted and the size of the sample chamber is adjusted by using porous spacers.

Figure 2. Mechanical data of room-dry experiments. a) Evolution of shear stress (primary y-axis) and axial displacement (secondary y-axis) with displacement (on logarithmic x-axis) of experiments performed in room-dry conditions, at a normal stress of 8.5 MPa (phv299, yellow curves; phv301, blue curves) and 3 MPa (phv311, magenta curves), respectively, and with slip velocities of 1 mm/s, 1 m/s, and – in the case of phv299 and 301 – 1 mm/s. The switch from velocity step 1 to step 2 is marked by the vertical dotted line. Positive changes in the axial displacement denote compaction, negative changes dilation of the gouge layer. **b-c)** Evolution with displacement (linear scale) of shear stress, axial displacement and equivalent velocity when the velocity is reduced at the end of the high-velocity step of **b)** experiment phv301 (blue curves, upper plot) and **c)** phv311 (magenta curves, lower plot). **d)** Evolution of temperature of the experiments shown in a). **e)** Temperature evolution with displacement (linear scale) during the third (low-) velocity step of experiment phv301.

Figure 3. Mechanical data of the first velocity step (1 mm/s). Evolution with displacement of **a)** Shear stress (and effective normal stress only for volume-controlled experiments phv292 and 297, light grey curves), **b)** Temperature, **c)** Axial Displacement, **d)** Fluid Volume, and **e)** Fluid Pressure. Different colors correspond to different initial effective normal stresses as shown in the legend. Inset in **c)** shows zoom of the axial displacement during the first 6 mm of

displacement. In **d)** only exemplary data are shown because of the large high-frequency oscillations. Note constant fluid volume in the volume-controlled experiment (grey curve). In **e)** the fluid pressure of phv292 is plotted in black and yellow (up- and downstream pressure, respectively) and of phv297 in blue and red. During the first low velocity step, upstream and downstream fluid pressures are equal for a given experiment.

Figure 4. Shear-stress evolution of the saturated experiments. a) High velocity (1 m/s) is induced after 30 cm of displacement (denoted by dotted vertical line) and shear stress increases during a phase that lasts a few mm before peak strength is reached and dynamic weakening initiates. Renewed strengthening is due to the decrease in velocity at the end of the high-velocity step. Different colors correspond to different effective normal stresses as shown in legend: 12 MPa (green), 10 MPa (blue), 8.5 MPa (black and grey for pressure- and volume-control mode, respectively), 3 MPa (purple), and 1 MPa (yellow). Shown are exemplary data curves, the complete data set can be found in the Appendix C (***Fig. C1***). **b)** Zoom of the end of the high-velocity step of experiment phv300 (no third velocity step), showing that the shear stress (black curve) decreases when the equivalent velocity (cyan curve) is reduced from 1 m/s to 0 m/s.

Figure 5. Strengthening phase, peak friction and the effect of the pore-fluid factor. a) Zoom of the shear-stress evolution as shown in Fig. 4a showing the strengthening phase at the initiation of sliding at high velocity in water-saturated and room-dry gouges. For color-coding see legend in c). **b)** Larger zoom as marked by box in a). Vertical dotted lines mark onset of the high-velocity step. Both room-dry (red) and fluid-saturated (green) gouge shows an initial strengthening, but weakening in fluid-saturated gouges occurs almost instantaneously. **c)** Dependence of the length of the strengthening phase on the pore-fluid factor λ for effective normal stresses of 1 MPa (yellow symbols), 3 MPa (purple), 8.5 MPa (black), 10 MPa (blue), and 12 MPa (green) (see legend). The length of the strengthening phase increases with increasing pore-fluid factor. Phv313 was only sheared at 1 m/s, unlike the rest of the experiments that was pre-sheared at 1 mm/s for a displacement of c. 30 cm. Data for room-dry gouges are plotted in light red (σ_n=3 MPa) and dark red (8.5 MPa); the strengthening phase is c. two orders of magnitude longer than in water-saturated experiments deformed under the

same conditions. **d)** Mechanical behavior in experiment phv290 (λ=0.7) for the low-velocity step (1 mm/s, < 0.31 m displacement) and the first c. 5.7 m of displacement at high velocity (1 m/s). Note the overshoot in the slip rate (cyan curve) in the high-velocity step. **e)** Dependence of peak stress on the pore-fluid factor. Color-coding as in c). Peak stress decreases with increasing pore-fluid factor and increasing effective normal stress. The peak stress in phv313 is as large as in phv310, that had experienced pre-shearing. The peak stress in room-dry gouges is slightly larger than in water-saturated gouges from experiments performed at the same effective normal stress.

Figure 6. Steady-state and residual shear stress. a) Shear vs. effective normal stress picked at 3.5 m of displacement at high velocity. Color-coding refers to different effective normal stresses as shown in legend. The shear stress shows a clear dependence on the effective normal stress. **b)** Residual shear stress picked just before end of the high-velocity step in each experiment vs. the total equivalent displacement of the respective experiment. Color-coding as in a). In the volume-controlled experiments the effective normal stress is c. 3 MPa at these displacements. The residual shear stress shows a dependence on the effective normal stress only up to a displacement of c. 5.5 m (marked by dotted vertical line). At larger displacements, the residual shear stress is c. 1 MPa independently of the applied effective normal stress, except for experiments performed at 1 MPa, where residual shear stress equals the steady-state shear stress (horizontal dotted line).

Figure 7. Mechanical data for all velocity steps. Evolution with displacement of **a)** Temperature for all experiments. Color-coding as shown in legend to the right. **b)** Axial displacement for selected experiments (complete data set in Appendix C, Fig. C2). Positive trend denotes compaction, negative denotes dilation. The abrupt compaction at large displacement towards the end of an experiment is due to the decrease in velocity in the third (low-)velocity step and in some cases due to water leaks (see Fig. 8c for zoom of third velocity step). **c)** Axial displacement in the first meters of displacement at high velocity showing transient dilation followed by compaction for experiments phv297 (grey curve, volume control, $\sigma_{eff,initial}$=8.5 MPa), phv300 (black curve, pressure control, σ_{eff}=8.5 MPa, λ=0.15), phv305 (yellow curve, pressure control, σ_{eff}=1 MPa, λ=0.6), **d)** Normalized fluid volume, **e)** Fluid pressure in the

volume-controlled experiments phv292 (open Valve 2 (Fig.1)) and phv297 (closed Valve 2), **f)** Constant fluid pressure in the first centimeter of sliding at high velocity.

Figure 8. Third (low-)velocity step. **a)** Shear stress picked at the end of each experiment plotted against the total equivalent displacement of the respective experiment. Color-coding as shown in legend. **b)-e)** Evolution with displacement of **b)** Temperature decay with equivalent displacement for all experiments following a power law. Color-coding as in a). **c)** Axial displacement for selected experiments. **d)** Fluid volume for selected experiments**,** and **e)** Upstream- and downstream fluid pressures of phv292 and 297.

Figure 9. Permeability measurements. Flow volume (m3) per time (s), *Q*, for experiments phv295 and 296. *Q* was determined once a constant differential pressure was applied and used to calculate the permeability.

Figure 10. Microstructure of room-dry samples. Backscattered electron images showing the microstructure of **a)** sample phv301 showing three more or less distinct textural zones, labelled Zones I, II, and III. Zone III is located adjacent to the principal slip surface (PSS, red arrow points toward it). **b)** Zoom of box b) marked in a) showing recrystallized grains in Zone III. **c)** Zoom of box c) marked in a) showing area c. 300 µm from the PSS where grains are recrystallized and have an preferred orientation along a fracture as shown by red arrows. **d)** Zoom of box d) showing elongated and orientated grains directly adjacent to the PSS. **e)** Black porous material covering the PSS (red arrow points toward it). **f)** phv311 (σ_{eff}=3 MPa, d_{total}=5.5 m): a scrap (red arrow) of what is possibly resin or some of the black porous material.

Figure 11. Microstructure of saturated samples. Backscattered electron images showing the microstructure of **a)** phv304 (σ_{eff}=3 MPa, λ=0.33, d_{total}=19.1 m), with textural Zones I, II, and III labeled. Red boxed show location of images in Fig. 12f and g. **b)** phv290 (σ_{eff}=3 MPa, λ=0.7, d_{total}=22 m). PSS marked by red arrow. Yellow arrow pointing at black porous material.

Figure 12. Crystal-plastic deformation in saturated samples. Backscattered electron images showing the microstructure of **a)** phv307 (σ_{eff}=10 MPa, λ=0.17, d_{total}=4.8 m), **b)-c)** phv310 (σ_{eff}=3 MPa, λ=0.17, d_{total}=5.3 m), cut perpendicular to slip direction. Red arrow in c) pointing at straight grain boundary, pink arrows at lobate grain boundaries, and yellow and green arrows

at cavities that are located on grain boundaries (most common) or within grains, respectively. **d)** phv313 (σ_{eff}=3 MPa, λ=0.17, d_{total}=5.3 m), red arrows showing two slip surfaces. **e)** zoom of the upper slip surface in d) showing recrystallized grains, **f)** area of phv304 (σ_{eff}=3 MPa, λ=0.33, d_{total}=19.1 m) marked in Fig. 11a, showing recrystallized grains along several slip surfaces, **g)** Zoom of area marked in Fig. 11a with recrystallized grains orientated in the direction of shear**.**

Figure 13. Possible evidence of decarbonation. **a)** Secondary electron image of sample phv310 (water-dampened, σ_{eff}=3 MPa, λ=0.17, d_{total}=5.3 m) showing calcite grains (yellow arrows) partly surrounded and/or covered by second phase (pink arrows). **b)** Image taken from Rodriguez-Navarro et al. (2009) showing "porous calcite pseudomorphs (inset) crisscrossed by cracks and showing four (1–4) sets (bundles) of oriented CaO rods (arrows)" that developed at 850 °C (Rodriguez-Navarro et al. 2009). **c)** Figure taken from Han et al. (2010) showing SEM photomicrograph of the decomposition zone in Carrara marble that was sheared at 12 MPa normal stress and a slip velocity of 1.2 m/s. The structure of the decomposition zone is "characterized by large pore volumes and nanograin aggregates" (Han et al., 2010). **d)** Secondary electron image of a calcite grain surrounded by the unknown phase. Red and yellow circles show regions where EDS analysis was performed. **e)** EDS spectrum for region marked by yellow circle in d), showing presence of C, O, and Ca. **f)** The EDS spectrum of the calcite grain marked by red circle in d) is equal to the spectrum shown in e).

Figure 14. Contamination of saturated samples. Backscattered electron images showing the **a)** microstructure of phv304 (σ_{eff}=3 MPa, λ=0.33, d_{total}=19.1 m), **b)** zoom of area marked in a). **c)** EDS spectrum of the porous black material, revealing the presence of O, F, Ca, and Cr.

Figure 15. Raman spectroscopy. a) Raman spectrum (red curve) and **b)** photograph of the post-experimental sample phv307 (σ_{eff}=10 MPa, λ=0.17, d_{total}=4.8 m), respectively, containing only calcite (purple curve in a). **c)** Raman spectrum and **d)** photograph of post-experimental sample phv306. Fitted to the sample's spectrum (red curve) are the standard curves for PTFE (purple) and calcite (green). In the photograph, red arrows point at "stringy" regions, where PTFE was detected. Powdery and shiny regions (yellow arrows) contained only calcite. Scale bars are 5 mm.

Figure 16. Raman spectroscopy of back samples. a) Photographs of samples phv313 (σ_{eff}=3 MPa, λ=0.17, d_{total}=5.3 m), 311 (room-dry, σ_{eff}=3 MPa, d_{total}=5.5 m), and 298 (σ_{eff}=8.5 MPa, λ=0.15, d_{total}=17.4 m) (from left to right). Phv313 contained only traces of carbon. Scale bars are 5 mm. **b)** Optical microphotographs showing greyish and black regions. **c)** Raman spectrum of sample phv298, and **d)** Example of decomposition of the Raman spectrum of carbonaceous material (modified after Beyssac et al., 2002).

Figure 17. XRD spectra of **a)** phv310 (σ_{eff}=3 MPa, λ=0.17, d_{total}=5.3 m) containing only calcite , **b)** phv309 (σ_{eff}=12 MPa, λ=0.17, d_{total}=12.82 m) containing calcium and calcium fluorite, but no PTFE, **c)** phv305 σ_{eff}=1 MPa, λ=0.6, d_{total}=18.4 m) containing calcite and PTFE.

Figure 18. Expected thermal pressurization. Pore-pressure rise for a given temperature rise for minimum (blue curve) and maximum (black curve) total fluid volume as it differed between the experiments. Red box shows temperature and pressure change regions corresponding to values reached in the first velocity step. Red dotted line shows maximum temperature reached in the experiments performed at low effective normal stress (≤3 MPa) during the high-velocity step.

Figure 19. Thermodynamic calculations a) for the system CaO-CO_2-H_2O. Temperature vs. X_{CO2} ranging from 0 (pure water) to 1 (no water) for pressures ranging from 0.1 MPa (=1 bar, atmospheric pressure) to 10 MPa. Lines show equilibrium states of calcite (*cc*, $CaCO_3$), and lime (CaO, high-T phase). At 12 MPa, melting occurs. **b)** for the system MgO-CaO-CO_2-H_2O at 1 bar. **mag**: magnesite, $MgCO_3$; **per**: periclase, MgO; **dol**: Dolomite, CaMg(CO3)2. High-T assemblages are plotted to right of = sign.

Figure 20. Frictional behavior of Teflon gouge. **a)** Rotary-shear experiments with Teflon gouges at 3 MPa normal stress. r233 (100% Teflon, blue symbols), r235 (20% Teflon, purple symbols), r234 (50% Teflon, yellow symbols) and r231 (100% Teflon, cyan symbols) where sheared with several velocity steps as summarized in Table 3. Experiments r234 and r235 were performed with a mixture of calcite and Teflon gouge (mixtures of 50/50 and 80/20, respectively). Data from Kitajima et al. (2010) were obtained with 100% Teflon gouge slid in single velocity experiments at 0.6 MPa normal stress. **b)** Variation of the coefficient of friction with rubbing

speed of PTFE sliding on PTFE (49% crystalline), from McLaren and Tabor, 1963. “At room temperature the friction rises from about μ=0.07 to μ=0.3 when the sliding speed is increased to about 100 cm/s. As the ambient temperature is increased the rise in friction is shifted into the higher speed range.”

Figure 21. Summary plots of the mechanical data of two experiments. a) phv297 (volume-controlled, initial experimental parameters: σ_{eff}=8.5 MPa, λ=0.15; d_{total}=18.4 m), **b)** phv304 (pressure-controlled, 3 MPa, λ=0.33; d_{total}=19.1 m) , and c) phv291 (pressure-controlled, 8.5 MPa, λ=0.15; d_{total}=22.7 m) where Valve 2 was closed. Plotted on the primary y-axes again the equivalent displacement are the shear stress (MPa, red curves), the fluid pressure (MPa, pink curves), the axial displacement (10^{-4} m, black curve), the equivalent velocity (m/s, cyan curves) and in the case of phv304 the fluid-volume (ml, blue curve). The secondary y-axes show the temperature (°C, green curves).

Figure 22. Comparison of room-dry and water-saturated experiments. a) Evolution of shear stress for the first c. 5.5 m of displacement (low- and high-velocity step) of experiments performed at an (initial) effective normal stress of 8.5 MPa. Black dotted line shows onset of high velocity. Red curves: room-dry experiments, black curves: pressure-controlled experiments, grey curves: volume-controlled experiments. **b)** Evolution of axial displacement with displacement shown separately for the low- and high-velocity steps. Color-coding as in a). Positive change denotes compaction, negative change dilation.

8. Tables

Table 1. Experimental Conditions and Set-up. a) Velocity-step experiments conducted in room-dry and **b)** in water-saturated (drained and undrained) conditions. **c)** Experimental parameters used in permeability measurements. Phv293 was performed without gouge material to determine the system permeability.

Table 2. Microanalytical Techniques and Results.

Table 3. Teflon gouge experiments. Experimental parameters.

		Experiment	σ_n	σ_{eff}*	p_f*	$\lambda=p_f/\sigma_n$*	Initial gouge layer thickness	Velocity steps (m/s)			Displacement (cm)				Fluid system control mode	Valve 2 (Shortcut)
			(MPa)	(MPa)	(MPa)		(mm)	v_1	v_2	v_3	d_1	d_2	d_3	total		
a)	Room-dry	phv299	8.5	8.5	room-dry		3.24	0.001	1	0.001	0.31	15	0.31	15.62		
		phv301	8.5	8.5	oven-dry		3.51	0.001	1	0.001	0.31	17	0.31	17.62	dry	
		phv311	3	3	room-dry		3.2	0.001	1	-	0.31	5.19	-	5.5		
b)	Water-saturated	phv306	1.2	1	0.2	0.17	2.67	0.001	1	0.001	0.31	18.6	0.31	19.22	pressure	open
		phv305	2.5	1	1.5	0.60	1.79	0.001	1	0.001	0.31	17.8	0.31	18.42	pressure	open
		phv310	3.6	3	0.6	0.17	2.74	0.001	1	-	0.31	5	-	5.31	pressure	open
		phv313	3.6	3	0.6	0.17	3.02	1	-	-	5.32	-	-	5.32	pressure	open
		phv304	4.5	3	1.5	0.33	2.82	0.001	1	0.001	0.31	18.5	0.31	19.12	pressure	open
		phv290	10	3	7	0.70	2.56	0.001	1	0.001	0.4	21.2	0.4	22	pressure	open
		phv291	10	8.5	1.5	0.15	3	0.001	1	0.001	0.4	21.9	0.4	22.7	pressure	closed
		phv292	10	8.5	1.5	0.15	2.8	0.001	1	0.001	0.31	15.5	0.25	16.06	volume	closed
		phv297	10	8.5	1.5	0.15	3.12	0.001	1	0.001	0.31	18	0.086	18.396	volume	open
		phv298	10	8.5	1.5	0.15	2.93	0.001	1	0.001	0.31	17	0.12	17.43	pressure	open
		phv300	10	8.5	1.5	0.15	3.11	0.001	1	-	0.31	9.6	-	9.91	pressure	open
		phv312	10	8.5	1.5	0.15	2.6	0.001	1	-	0.31	4.81	-	5.12	pressure	open
		phv307	12	10	2	0.17	2.87	0.001	1	0.001	0.31	4.2	0.31	4.82	pressure	open
		phv309	14.4	12	2.4	0.17	2.95	0.001	1	0.001	0.31	12.2	0.31	12.82	pressure	open

* for experiments in volume-control mode initial values at the start of the experiment are given

		Experiment	σ_{eff}	$p_{f,initial}$	$\lambda=p_f/\sigma_n$	Initial gouge layer thickness	Velocity	Total Displacement	Δp_f	Permeability
			(MPa)	(MPa)		(mm)	(m/s)	(m)	(MPa)	m^2
c)	Saturated	phv293	3	2	0.67	0	0	0	0.5	No steady flow rate
		phv295	8	2	0.25	3	1	5.19	0.2	9.90E-17
		phv296	8	2	0.25	2.57	1	1.63	0.2	9.20E-17

Table 1. Experimental Conditions and Set-up. a) Velocity-step experiments conducted in room-dry and **b)** in water-saturated (drained and undrained) conditions. **c)** Experimental parameters used in permeability measurements. Phv293 was performed without gouge material to determine the system permeability.

Sample name	Total Displacement	σ_{eff}	λ	T_{max}	Scanning electron microscopy		Raman spectroscopy		EBS	XRD
	(m)	(MPa)		(°C)	Recrystallization/ Crystal-plasticity	PTFE	Carbon	PTFE	Fluorine	PTFE
phv307	4.82	10	0.17	405	Y	N		N	N	N
phv312	5.12	8.5	0.15	510	-	-	-	-	-	-
phv310	5.31	3	0.17	215	Y	N	-	-	N	N
phv313	5.32	3	0.17	200	Y	N	Y*	N	N	-
phv311[d]	5.5	3	dry	400	Y?	N?	Y	N	N	-
phv300	9.91	8.5	0.15	650	-	-	Y	Y	-	N
phv309	12.82	12	0.17	550	-	-	-	-	-	Y
phv299[d]	15.62	8.5	dry	465	-	-	Y	Y	-	-
phv292	16.06	8.5	0.15	305	-	-	-	-	-	-
phv298	17.43	8.5	0.15	535	-	-	Y	N	-	-
phv301[d]	17.62	8.5	dry	410	Y	Y	-	-	N	-
phv297	18.396	8.5	0.15	445	-	-	Y	Y*	-	Y
phv305	18.42	1	0.60	150	-	-	-	-	-	Y
phv304	19.12	3	0.33	265	Y	Y	Y	Y	Y	N
phv306	19.22	1	0.17	150	-	-	N	Y	-	-
phv290	22	3	0.70	130	N	Y	N	N	-	-
phv291	22.7	8.5	0.15	-	-	-	Y	N	-	-

[d] room-dry, * sample contains traces

Table 2. Microanalytical Techniques and Results.

Experiment	% Teflon	σ_{eff}	Velocity steps (m/s)				
		(MPa)	v_1	v_2	v_3	v_4	v_5
r231	100	3	1	0.001	0.000001	0.001	1
r232	100	3	1	-	-	-	-
r233	100	3	0.1	0.0001	0.1	0.0001	-
r234	50	3	0.1	0.0001	0.1	-	-
r235	20	3	0.1	0.0001	0.1	0.0001	-

Table 3. Teflon gouge experiments. Experimental parameters.

Concluding Remarks

The main results of the studies described in this thesis are

1) Clast-cortex aggregates in calcite-bearing slip zones cannot be used as indicators of seismic slip as they formed in experiments performed at slip rates of 100 µm/s. They likely form in the shallow portions of faults during shearing in relatively dry conditions.
2) There is no unambiguous evidence of faster strain localization in water-dampened calcite gouges as compared to room-dry gouges.
3) Carbonate-bearing faults are more prone to slip in the presence of fluids, even if the degree of saturation is relatively low (as shown by the similar dynamic weakening behavior of water-dampened and water-saturated gouges). Weakening is more efficient if the ratio of pore-fluid pressure and normal stress (i.e., the pore-fluid factor) is high.

Regarding the first point, it was recently suggested (Rowe and Griffith, 2014) that CCAs could nevertheless be taken as a seismic indicator, because the "sub-seismic" slip velocities of 100 µm/s applied in our experiments are still relatively high compared to the slip rates expected in an aseismic fault. Further low-velocity experiments (e.g. at slip rates of 1 µm/s) could provide assurance.

As demonstrated in Chapters II and III of this thesis, dynamic weakening in calcite gouge is likely due to flash heating that is accelerated in the presence of fluids due to enhanced subcritical crack growth. However, the nature of the flash weakening mechanism remains unclear. Further microstructural analysis using transmission electron microscopy (TEM) might provide further information. For instance, if the carbon that was detected on the slip surface by Raman microspectroscopy is amorphous, this might suggest that flash weakening acts by calcite decarbonation and formation of a lubricating film of amorphous carbon (Spagnuolo et al., 2014). TEM could also identify if the slip surface consists of calcite nanoparticles, as in the

27 case of Green et al. (2010) and Holdsworth et al. (2013), which would further explain the
28 activation of diffusion creep at seismic strain rates.

References

Anders, M. H., Aharonov, E., and Walsh, J. J., 2000. Stratified granular media beneath large slide blocks: Implications for mode of emplacement. Geology, 28(11), 971-974.

Anders, M.H., Fouke, B.W., et al., 2010. The role of Calcining and basal fluidization in the Long Runout of carbonate slides: an example from the heart mountain slide block, Wyoming and Montana, U.S.A. J. Geol. 118, 577e599.

Atkinson, B. K., 1984. Subcritical crack growth in geological materials. Journal of Geophysical Research: Solid Earth (1978–2012), 89(B6), 4077-4114.

Atkinson, B.K., and Meredith, P.G., 1987, The theory of subcritical crack growth with applications to minerals and rocks, in Atkinson, B.K., ed., Fracture mechanics of rock: London, Academic Press, p. 111–166.

Arai, T., Tanaka, H., Ikeda, R., Omura, K., and Matsuda, T., 2002, Concentration of carbon at the central plane in the Nojima fault zone: In Japan Geoscience Union Meeting 2002, abstract: G061-P011.

Bastesen, E., Braathen, A., Nøttveit, H., Gabrielsen, R. H., and Skar, T., 2009. Extensional fault cores in micritic carbonate–Case studies from the Gulf of Corinth, Greece. Journal of Structural Geology, 31(4), 403-420.

Beeler, N. M., Tullis, T. E., Blanpied, M. L., and Weeks, J. D., 1996. Frictional behavior of large displacement experimental faults. Journal of Geophysical Research: Solid Earth (1978–2012), 101(B4), 8697-8715.

Ben-Zion, Y., and Sammis, C. G., 2003. Characterization of fault zones. Pure and Applied Geophysics, 160(3-4), 677-715.

Bernabe, Y., 1987. A wide range permeameter for use in rock physics. In International Journal of Rock Mechanics and Mining Sciences and Geomechanics Abstracts (Vol. 24, No. 5, pp. 309-315). Pergamon.

Bestmann, M., Pennacchioni, G., et al., 2012. Deformation and ultrafine dynamic recrystallization of quartz in pseudotachylyte-bearing brittle faults: a matter of a few seconds. J. Struct. Geol. 38, 21e38.

Beutner, E. C., and Craven, A. E., 1996. Volcanic fluidization and the Heart Mountain detachment, Wyoming. Geology, 24(7), 595-598.

Beutner, E.C., Gerbi, G.P., 2005. Catastrophic emplacement of the heart mountain block slide, Wyoming and Montana, USA. Geol. Soc. Am. Bull. 117 (5e6), 724e735.

Beyler, C. L., and Hirschler, M. M., 2002. Thermal decomposition of polymers. SFPE handbook of fire protection engineering, 2.

Beyssac, O., Goffé, B., Chopin, C., and Rouzaud, J. N., 2002. Raman spectra of carbonaceous material in metasediments: a new geothermometer. Journal of metamorphic Geology, 20(9), 859-871.

Billi, A., 2005. Grain size distribution and thickness of breccia and gouge zones from thin (< 1m) strike-slip fault cores in limestone. Journal of Structural Geology, 27(10), 1823-1837.

Blumm, J., Lindemann, A., Meyer, M., and Strasser, C., 2010. Characterization of PTFE using advanced thermal analysis techniques. International Journal of Thermophysics, 31(10), 1919-1927.

Boneh, Y., Sagy, A., et al., 2013. Frictional strength and wear-rate of carbonate faults during high-velocity, steady-state sliding. Earth Planet. Sci. Lett. 381 (0), 127e137.

Boullier, A. M., and Gueguen, Y., 1975. SP-mylonites: origin of some mylonites by superplastic flow. Contributions to Mineralogy and Petrology, 50(2), 93-104.

Boullier, A.M., Yeh, E.C., et al., 2009. Microscale anatomy of the 1999 Chi-Chi earthquake fault zone. Geochem. Geophys. Geosyst. 10.

Boutareaud, S., Calugaru, D. G., Han, R., Fabbri, O., Mizoguchi, K., Tsutsumi, A., and Shimamoto, T., 2008. Clay-clast aggregates: A new textural evidence for seismic fault sliding?. *Geophysical Research Letters*, *35*(5).

Boutareaud, S., Boullier, A. M., Andreani, M., Calugaru, D. G., Beck, P., Song, S. R., and Shimamoto, T., 2010. Clay clast aggregates in gouges: New textural evidence for seismic faulting. Journal of Geophysical Research: Solid Earth (1978–2012), 115(B2).

Boyer, S. E., and Hossack, J. R., 1992. Structural features and emplacement of surficial gravity-slide sheets, northern Idaho-Wyoming thrust belt. Geological Society of America Memoirs, 179, 197-214.

Brace, W. F., and Byerlee, J. D., 1966. Stick-slip as a mechanism for earthquakes. Science, 153(3739), 990-992.

Brantut, N., Schubnel, A., Rouzaud, J. N., Brunet, F., and Shimamoto, T., 2008. High-velocity frictional properties of a clay-bearing fault gouge and implications for earthquake mechanics. Journal of Geophysical Research: Solid Earth (1978–2012), 113(B10).

Brantut, N., Schubnel, A., Corvisier, J., and Sarout, J., 2010. Thermochemical pressurization of faults during coseismic slip. Journal of Geophysical Research: Solid Earth (1978–2012), 115(B5).

Brantut, N., Han, R., et al., 2011. Fast slip with inhibited temperature rise due to mineral dehydration: evidence from experiments on gypsum. Geology 39 (1), 59e62.

Brune, J. N., Henyey, T. L., and Roy, R. F., 1969. Heat flow, stress, and rate of slip along the San Andreas fault, California. Journal of Geophysical Research, 74(15), 3821-3827.

Brune, J., 2001. Fault normal dynamic loading and unloading: an explanation for ‘‘non-gouge’’ rock powder and lack of fault-parallel shear bands along the San Andreas fault. EOS Trans. Am. Geophys. Union 82, 47.

Byerlee, J., 1990. Friction, overpressure and fault normal compression. Geophysical Research Letters, 17(12), 2109-2112.

Carslaw, H. S., and Jaeger, J. C., 1959. Heat in solids (Vol. 19591). Clarendon Press, Oxford.

Chen, X., Madden, A.S., et al., 2013. Dynamic weakening by nanoscale smoothing during high-velocity fault slip. Geology 41 (7), 739e742.

Chester, F. M., Evans, J. P., and Biegel, R. L., 1993. Internal structure and weakening mechanisms of the San Andreas fault. Journal of Geophysical Research: Solid Earth (1978–2012), 98(B1), 771-786.

Chester, F. M., and Logan, J. M., 1986. Implications for mechanical properties of brittle faults from observations of the Punchbowl fault zone, California. Pure and Applied Geophysics, 124(1-2), 79-106.

Chester, F. M., and Logan, J. M., 1987. Composite planar fabric of gouge from the Punchbowl fault, California. Journal of Structural Geology, 9(5), 621-IN6.

Chester, F. M., J. S. Chester, D. L. Kirschner, S. E. Schulz, and J. P. Evans, 2004, Structure of large-displacement, strike-slip fault zones in the brittle continental crust, in Rheology and Deformation in the Lithosphere at Continental Margins, edited by G. D. Karner, B. Taylor, N. W. Driscoll and D. L. Kohlstedt, chap. 8, pp. 223–260, Columbia Univ. Press, New York.

Chiaraluce, L., Amato, A., Cocco, M., Chiarabba, C., Selvaggi, G., Di Bona, M., Piccinini, D., Deschamps, A., Margheriti, L., Courboulex, F., Ripepe, M., 2004. Complex normal faulting in the Apennines thrust-and-fold belt: the 1997–98 seismic sequence in central Italy. BSSA 94 (1), 99–116.

Chiaraluce, L., Valoroso, L., Piccinini, D., Di Stefano, R., De Gori, P., 2011. The anatomy of the 2009 L'Aquila normal fault system (central Italy) imaged by high resolution foreshock and aftershock locations. J. Geophys. Res. 116, B12311.

Chiaraluce, L., 2012. Unraveling the complexity of Apenninic extensional fault systems: a review of the 2009 L'Aquila earthquake (Central Apennines, Italy). J. Struct. Geol. 42, 2–18, http://dx.doi.org/10.1016/j.jsg.2012.06.007.

Chiodini, R. and Cioni, G. Gas, 1989. Geobarometry for hydrothermal systems and its application to various Italian geothermal areas. Appl. Geochem. 4, 564–572.

Chistyakov, A.D., 2007. The permittivity of water and water vapor in saturation states. Russ. J. Phys. Chem. A 81 (1), 5e8.

Cirella, A., Piatanesi, A., Cocco, M., Tinti, E., Scognamiglio, L., Michelini, A., ... and Boschi, E., 2009. Rupture history of the 2009 L'Aquila (Italy) earthquake from non-linear joint inversion of strong motion and GPS data. Geophysical Research Letters, 36(19).

Cocco, M., Nostro, C., Ekstrom, G., 2000. Static stress changes and fault interaction during the 1997 Umbria–Marche earthquake sequence. J. Seismol. 4, 501–516.

Cocco, M., Tinti, E., Marone, C., and Piatanesi, A., 2009. Scaling of slip weakening distance with final slip during dynamic earthquake rupture. International Geophysics, 94, 163-186.

Collettini, C., and Barchi, M. R., 2002. A low-angle normal fault in the Umbria region (Central Italy): a mechanical model for the related microseismicity. Tectonophysics, 359(1), 97-115.

Collettini, C., and Holdsworth, R. E., 2004. Fault zone weakening and character of slip along low-angle normal faults: insights from the Zuccale fault, Elba, Italy. Journal of the Geological Society, 161(6), 1039-1051.

Collettini, C., De Paola, N., and Faulkner, D. R., 2009. Insights on the geometry and mechanics of the Umbria–Marche earthquakes (Central Italy) from the integration of field and laboratory data. Tectonophysics, 476, 99-109.

Colthup, N. B., Daly, L. H., and Wiberley, S. E., 1990. Introduction to infrared and Raman spectroscopy. Elsevier.

Connolly, J. A. D., 1990. Multivariable phase diagrams; an algorithm based on generalized thermodynamics. American Journal of Science, 290(6), 666-718.

Cowan, D.S., 1999. Do faults preserve a record of seismic slip? A field geologist's opinion. J. Struct. Geol. 21 (8), 995e1001.

De Paola, N., Collettini, C., Faulkner, D. R., and Trippetta, F., 2008. Fault zone architecture and deformation processes within evaporitic rocks in the upper crust. Tectonics, 27(4).

De Paola N., Holdsworth R., Viti C., Collettini C., Bullock R., Faoro I., 2014. Can grain size sensitive creep lubricate faults during earthquake propagation? AGU Fall Meeting, abstract MR42-03.

Dieterich, J. H., 1981. Constitutive properties of faults with simulated gouge. Mechanical behavior of crustal rocks: the Handin volume, 103-120.

Di Luccio, D., Ventura, G., Di Giovambattista, R., Piscini, A., Cinti, F.R., 2010. Normal faults and thrusts reactivated by deep fluids: the 6 April 2009 Mw 6.3 L'Aquila earthquake, central Italy. J. Geophys. Res. 115, B06315

Di Toro, G., Goldsby, D. L., and Tullis, T. E., 2004. Friction falls towards zero in quartz rock as slip velocity approaches seismic rates. Nature, 427(6973), 436-439.

Di Toro, G., and Pennacchioni, G., 2005. Fault plane processes and mesoscopic structure of a strong-type seismogenic fault in tonalites (Adamello batholith, Southern Alps). Tectonophysics, 402(1), 55-80.

Di Toro, G., Pennacchioni, G., and Teza, G., 2005. Can pseudotachylytes be used to infer earthquake source parameters? An example of limitations in the study of exhumed faults. Tectonophysics, 402(1), 3-20.

Di Toro, G., Pennacchioni, G., et al., 2009. Pseudotachylytes and earthquake source mechanics. Int. Geophys. 94, 87e133.

Di Toro, G., Niemeijer, A., Tripoli, A., Nielsen, S., Di Felice, F., Scarlato, P., ... and Mariano, S., 2010. From field geology to earthquake simulation: a new state-of-the-art tool to investigate rock friction during the seismic cycle (SHIVA). Rendiconti Lincei, 21(1), 95-114.

Di Toro, G., Han, R., Hirose, T., De Paola, N., Nielsen, S., Mizoguchi, K., ... and Shimamoto, T., 2011. Fault lubrication during earthquakes. Nature, 471(7339), 494-498.

Di Toro, G., Rempe, M., et al., 2013. Strain localization in experimentally sheared gouge layers. In: Abstract MR13A-2258 presented at 2013 Fall Meeting, AGU, San Francisco, Calif., 9e13 Dec.

Di Stefano, R., Chiarabba, C., Chiaraluce, L., Cocco, M., De Gori, P., Piccinini, D., and Valoroso, L., 2011. Fault zone properties affecting the rupture evolution of the 2009 (Mw 6.1) L'Aquila earthquake (central Italy): Insights from seismic tomography. Geophysical Research Letters, 38(10).

Dor, O., Ben-Zion, Y., et al., 2006. Pulverized rocks in the Mojave section of the San Andreas Fault Zone. Earth Planet. Sci. Lett. 245 (3e4), 642e654.

Dor, O., Rockwell, T. K., and Ben-Zion, Y., 2006. Geological observations of damage asymmetry in the structure of the San Jacinto, San Andreas and Punchbowl faults in Southern California: a possible indicator for preferred rupture propagation direction. Pure and Applied Geophysics, 163(2-3), 301-349.

Evans, J. P., 1990. Thickness-displacement relationships for fault zones. Journal of Structural Geology, 12(8), 1061-1065.

Famin, V., Nakashima, S., Boullier, A. M., Fujimoto, K., and Hirono, T., 2008. Earthquakes produce carbon dioxide in crustal faults. Earth and Planetary Science Letters, 265(3), 487-497.

Farver, J. R., 1994. Oxygen self-diffusion in calcite: dependence on temperature and water fugacity. Earth and Planetary Science Letters, 121(3), 575-587.

Farver, J. R., and Yund, R. A., 1996. Volume and grain boundary diffusion of calcium in natural and hot-pressed calcite aggregates. Contributions to Mineralogy and Petrology, 123(1), 77-91.

Faulkner, D. R., Jackson, C. A. L., Lunn, R. J., Schlische, R. W., Shipton, Z. K., Wibberley, C. A. J., and Withjack, M. O., 2010. A review of recent developments concerning the structure, mechanics and fluid flow properties of fault zones. Journal of Structural Geology, 32(11), 1557-1575.

Faulkner, D.R., Lewis, A.C., Rutter, E.H., 2003. On the internal structure and mechanics of large strike-slip fault zones: field observations of the Carboneras fault in southeastern Spain. Tectonophysics 367 (3e4), 235e251.

Faulkner, D. R., Mitchell, T. M., Jensen, E., and Cembrano, J., 2011. Scaling of fault damage zones with displacement and the implications for fault growth processes. Journal of Geophysical Research: Solid Earth (1978–2012), 116(B5).

Faulkner, D. R., and E. H. Rutter, 2001, Can the maintenance of overpressured fluids in large strike-slip fault zones explain their apparent weakness? Geology, 29(6), 503–506

Feda, J., 1982. Mechanics of Particulate Materials (Elsevier, New York).

Flinn, D., 1977. Transcurrent faults and associated cataclasis in Shetland. Journal of the Geological Society, 133(3), 231-247.

Fondriest, M., Smith, S.A.F., et al., 2013. Mirror-like faults and power dissipation during earthquakes. Geology 41 (11), 1175e1178.

Fondriest, M., Smith, S. A., Di Toro, G., Zampieri, D., and Mittempergher, S., 2012. Fault zone structure and seismic slip localization in dolostones, an example from the Southern Alps, Italy. Journal of Structural Geology, 45, 52-67.

Frezzotti, M. L., Tecce, F., and Casagli, A., 2012. Raman spectroscopy for fluid inclusion analysis. Journal of Geochemical Exploration, 112, 1-20.

Goldsby, D. L., and Tullis, T. E., 2011. Flash heating leads to low frictional strength of crustal rocks at earthquake slip rates. Science, 334(6053), 216-218.

Gratier, J. P., & Gueydan, F., 2007. Effect of Fracturing and Fluid–Rock Interaction on Seismic Cycles. Tectonic Faults: Agents of Change on a Dynamic Earth, 95, 319e356.

Greason, W.D., 2000. Investigation of a test methodology for triboelectrification. J. Electrostat. 49 (3e4), 245e256.

Green, H., D. Lockner, K. Bozhilov, A. Maddon, N. Beeler, and Z. Reches, 2010, Nanometric gouge in high-speed shearing experiments: Superplasticity?, AGU, Fall Meet. Suppl., Abstract T31D-08.

Han, R., Hirose, T., and Shimamoto, T., 2010. Strong velocity weakening and powder lubrication of simulated carbonate faults at seismic slip rates. Journal of Geophysical Research: Solid Earth (1978–2012), 115(B3).

Han, R., Hirose, T., Shimamoto, T., Lee, Y., and Ando, J. I., 2011. Granular nanoparticles lubricate faults during seismic slip. Geology, 39(6), 599-602.

Han, R., and Hirose, T., 2012. Clay–clast aggregates in fault gouge: An unequivocal indicator of seismic faulting at shallow depths?. Journal of Structural Geology, 43, 92-99.

Han, R., Shimamoto, T., Hirose, T., Ree, J. H., and Ando, J. I., 2007a. Ultralow friction of carbonate faults caused by thermal decomposition. Science, 316(5826), 878-881.

Han, R., Shimamoto, T., Ando, J. I., and Ree, J. H., 2007b. Seismic slip record in carbonate-bearing fault zones: An insight from high-velocity friction experiments on siderite gouge. Geology, 35(12), 1131-1134.

Handy, M. R., Hirth, G., and Hovius, N. (Eds.)., 2007. Tectonic faults: agents of change on a dynamic Earth (Vol. 95). MIT Press.

Hatano, T., 2009. Scaling of the critical slip distance in granular layers. Geophysical Research Letters, 36(18).

Hector, L.G., Schultz, H.L., 1936. The dielectric constant of air at radiofrequencies. J. Appl. Phys. 7 (4), 133e136.

Heermance, R., Shipton, Z. K., and Evans, J. P., 2003. Fault structure control on fault slip and ground motion during the 1999 rupture of the Chelungpu fault, Taiwan. Bulletin of the seismological society of America, 93(3), 1034-1050.

Heilbronner, R., Barrett, S., 2013. Image Analysis in Earth Sciences: Microstructures and Textures of Earth Materials. Springer.

Hickman, S. H., 1991. Stress in the lithosphere and the strength of active faults. Reviews of Geophysics, 29, 759-775.

Hickman, S., Sibson, R., and Bruhn, R., 1995. Introduction to special section: Mechanical involvement of fluids in faulting. Journal of Geophysical Research: Solid Earth (1978–2012), 100(B7), 12831-12840.

Hirose, T., Shimamoto, T., 2005. Growth of molten zone as a mechanism of slip weakening of simulated faults in gabbro during frictional melting. J. Geophys. Res. Solid Earth 110 (B5).

Holdsworth, R., N. De Paola, I. Faoro, R. Bullock, C. Viti, and C. Collettini, 2013. Nano-scale diffusion-accommodated weakening triggered by frictional sliding during earthquakes in carbonate rocks, Geol. Soc. Am. Abstr. Programs, 45, 679.

Holland, T. J. B., and Powell, R., 1998. An internally consistent thermodynamic data set for phases of petrological interest. Journal of Metamorphic Geology **16**:309-343.

Hondred, P. R., Yoon, S., Bowler, N., and Kessler, M. R., 2013. Degradation kinetics of polytetrafluoroethylene and poly(ethylene-alt-tetrafluoroethylene) *High Performance Polymers August 2013 25: 535-542, doi:10.1177/0954008312473491*

Hubbert, M. K., and Rubey, W. W., 1959. Role of fluid pressure in mechanics of overthrust faulting I. Mechanics of fluid-filled porous solids and its application to overthrust faulting. *Geological Society of America Bulletin*, *70*(2), 115-166.

Italiano, F., Martinelli, G., Bonfanti, P., and Caracausi, A., 2009. Long-term (1997-2007) geochemical monitoring of gases from the Umbria-Marche region. Tectonophysics, 476(1), 282-296.

Jentgen, R., 1971. Solid lubricants: how they work and where to use them. Parts, Hybrids, and Packaging, IEEE Transactions on, 7(2), 86-93.

Kim, J.W., Ree, J.-H., Han, R., and Shimamoto, T., 2010, Experimental evidence for the simultaneous formation of pseudotachylyte and mylonite in the brittle regime: Geology, v. 38, p. 1143–1146, doi:10.1130/G31593.1.

Kirkpatrick, J. D., Rowe, C. D., White, J. C., and Brodsky, E. E., 2013. Silica gel formation during fault slip: Evidence from the rock record. Geology, 41(9), 1015-1018.

Kitajima, H., Chester, J. S., Chester, F. M., and Shimamoto, T., 2010. High-speed friction of disaggregated ultracataclasite in rotary shear: Characterization of frictional heating, mechanical behavior, and microstructure evolution. Journal of Geophysical Research: Solid Earth (1978–2012), 115(B8).

Kitajima, H., F. M. Chester, and J. S. Chester, 2011, Dynamic weakening of gouge layers in high-speed shear experiments: Assessment of temperature-dependent friction, thermal pressurization, and flash heating, J. Geophys. Res., 116, B08309, doi:10.1029/2010JB007879.

Kohli, A. H., Goldsby, D. L., Hirth, G., and Tullis, T., 2011. Flash weakening of serpentinite at near-seismic slip rates. Journal of Geophysical Research: Solid Earth (1978–2012), 116(B3).

Kuo, L. W., Li, H., Smith, S. A., Di Toro, G., Suppe, J., Song, S. R., ... and Si, J., 2014. Gouge graphitization and dynamic fault weakening during the 2008 Mw 7.9 Wenchuan earthquake. Geology, 42(1), 47-50.

Lachenbruch, A.H., 1980. Frictional heating, fluid pressure, and the resistance to fault motion. J. Geophys. Res. Solid Earth 85 (B11), 6097e6112.

Lachenbruch, A. H., and Sass, J. H., 1980. Heat flow and energetics of the San Andreas fault zone. Journal of Geophysical Research: Solid Earth (1978–2012), 85(B11), 6185-6222.

Lee, J. C., Chen, Y. G., Sieh, K., Mueller, K., Chen, W. S., Chu, H. T., ... and Yeats, R., 2001. A vertical exposure of the 1999 surface rupture of the Chelungpu fault at Wufeng, western Taiwan: structural and paleoseismic implications for an active thrust fault. Bulletin of the Seismological Society of America, 91(5), 914-929.

Li, Y. G., Aki, K., Vidale, J. E., and Alvarez, M. G., 1998. A delineation of the Nojima fault ruptured in the M7. 2 Kobe, Japan, earthquake of 1995 using fault zone trapped waves. Journal of Geophysical Research: Solid Earth (1978–2012), 103(B4), 7247-7263.

Lin, A.M., 1996. Injection veins of crushing-originated pseudotachylyte and fault gouge formed during seismic faulting. Eng. Geol. 43 (2e3), 213e224.

Logan, J., Friedman, M., et al., 1979. Experimental studies of simulated gouge and their application to studies of natural fault zones. U.S. Geol. Surv. Open File Rep. 1978, 305e343.

Long, D. A., and Long, D. A., 1977. Raman spectroscopy (Vol. 206). New York: McGraw-Hill.

Ma, S., Shimamoto, T., Yao, L., Togo, T., and Kitajima, H., 2014. A rotary-shear low to high-velocity friction apparatus in Beijing to study rock friction at plate to seismic slip rates. Earthquake Science, 27(5), 469-497.

Mair, K., and Abe, S., 2008. 3D numerical simulations of fault gouge evolution during shear: Grain size reduction and strain localization. Earth and Planetary Science Letters, 274(1), 72-81.

Mandl, G., De Jong, L. N. J., and Maltha, A., 1977. Shear zones in granular material. Rock Mechanics, 9(2-3), 95-144.

Marone, C., Scholz, C.H., 1988. The Depth of Seismic Faulting and the Upper Transition from Stable to Unstable Slip Regimes. Geophysical Research Letters 15, 621-624.

Marone, C., Raleigh, C. B., and Scholz, C. H., 1990. Frictional behavior and constitutive modeling of simulated fault gouge. Journal of Geophysical Research: Solid Earth (1978–2012), 95(B5), 7007-7025.

Marone, C., Hobbs, B. E., and Ord, A., 1992. Coulomb constitutive laws for friction: Contrasts in frictional behavior for distributed and localized shear. Pure and Applied Geophysics, 139(2), 195-214.

Marone, C., and Kilgore, B., 1993. Scaling of the critical slip distance for seismic faulting with shear strain in fault zones.

Marone, C., 1998. Laboratory-derived friction laws and their application to seismic faulting. Annual Review of Earth and Planetary Sciences, 26(1), 643-696.

Marone, C., Cocco, M., Richardson, E., and Tinti, E., 2009. The critical slip distance for seismic and aseismic fault zones of finite width. International Geophysics, 94, 135-162.

Matsusaka, S., Maruyama, H., et al., 2010. Triboelectric charging of powders: a review. Chem. Eng. Sci. 65 (22), 5781e5807.

McLaren, K. G., and Tabor, D., 1963. Visco-elastic properties and the friction of solids: friction of polymers: influence of speed and temperature. Nature, 197, 856-858.

Miller, S. A., Collettini, C., Chiaraluce, L., Cocco, M., Barchi, M., and Kaus, B. J., 2004. Aftershocks driven by a high-pressure CO2 source at depth. Nature, 427(6976), 724-727.

Miller, S. A., 2013. The role of fluids in tectonic and earthquake processes. Advances in Geophysics, 54, 1-46.

Mitchell, T. M., and Faulkner, D. R., 2008. Experimental measurements of permeability evolution during triaxial compression of initially intact crystalline rocks and implications for fluid flow in fault zones. Journal of Geophysical Research: Solid Earth (1978–2012), 113(B11).

Mitchell, T. M., and Faulkner, D. R., 2009. The nature and origin of off-fault damage surrounding strike-slip fault zones with a wide range of displacements: a field study from the Atacama fault system, northern Chile. Journal of Structural Geology, 31(8), 802-816.

Mitchell, T. M., Ben-Zion, Y., and Shimamoto, T., 2011. Pulverized fault rocks and damage asymmetry along the Arima-Takatsuki Tectonic Line, Japan. Earth and Planetary Science Letters, 308(3), 284-297.

Mitchell, T. M., Smith, S. A., Anders, M. H., Di Toro, G., Nielsen, S., Cavallo, A., and Beard, A. D., 2015. Catastrophic emplacement of giant landslides aided by thermal decomposition: Heart Mountain, Wyoming. Earth and Planetary Science Letters, 411, 199-207.

Moretti, I., Sakellariou, D., Lykousis, V., and Micarelli, L., 2003. The Gulf of Corinth: an active half graben?. Journal of Geodynamics, 36(1), 323-340.

Morrow, C. A., Moore, D. E., and Lockner, D. A., 2000. The effect of mineral bond strength and adsorbed water on fault gouge frictional strength. Geophysical Research Letters, 27(6), 815-818.

Morrow, C., Shi, L. Q., and Byerlee, J., 1981. Permeability and strength of San Andreas fault gouge under high pressure. Geophysical Research Letters, 8(4), 325-328.

Nielsen, S., Di Toro, G., Hirose, T., and Shimamoto, T., 2008. Frictional melt and seismic slip. Journal of Geophysical Research: Solid Earth (1978–2012), 113(B1).

Nomura, T., Satoh, T., et al., 2003. The environment humidity effect on the tribocharge of powder. Powder Technol. 135, 43e49.

Nur, A., and Byerlee, J., 1971. An exact effective stress law for elastic deformation of rock with fluids. Journal of Geophysical Research, 76(26), 6414-6419.

Oohashi, K., Hirose, T., Kobayashi, K., and Shimamoto, T., 2012. The occurrence of graphite-bearing fault rocks in the Atotsugawa fault system, Japan: origins and implications for fault creep. Journal of Structural Geology, 38, 39-50.

Oohashi, K., Hirose, T., et al., 2013. Graphite as a lubricating agent in fault zones: an insight from low- to high-velocity friction experiments on a mixed graphite-quartz gouge. J. Geophys. Res. Solid Earth 118 (5), 2067e2084.

Oohashi, K., Han, R., Hirose, T., Shimamoto, T., Omura, K., and Matsuda, T., 2014. Carbon-forming reactions under a reducing atmosphere during seismic fault slip. *Geology*, *42*(9), 787-790.

Passchier, C. W., and Trouw, R. A., 1996. Microtectonics (Vol. 256). Berlin: Springer.

Pavlis, T. L., Serpa, L. F., and Keener, C., 1993. Role of seismogenic processes in fault-rock development: An example from Death Valley, California. Geology, 21(3), 267-270.

Pino, N. A., and Di Luccio, F., 2009. Source complexity of the 6 April 2009 L'Aquila (central Italy) earthquake and its strongest aftershock revealed by elementary seismological analysis. Geophysical Research Letters, 36(23).

Platt, J.D., Rudnicki, J.W., et al., 2014. Stability and localization of rapid shear in fluid e saturated fault gouge: 2. Localized zone width and strength evolution. J. Geophys. Res. Solid Earth 119 (5), 4334e4359.

Poirier, J. P., 1985. Creep of Crystals, 260 pp. Cambridge Univer-sity Press, New York.

Polissar, P.J., Savage, H.M., et al., 2011. Extractable organic material in fault zones as a tool to investigate frictional stress. Earth Planet. Sci. Lett. 311 (3), 439e447.

Power, W. L., Tullis, T. E., and Weeks, J. D., 1988. Roughness and wear during brittle faulting. Journal of Geophysical Research: Solid Earth (1978–2012), 93(B12), 15268-15278.

Proctor, B. P., Mitchell, T. M., Hirth, G., Goldsby, D., Zorzi, F., Platt, J. D., and Di Toro, G., 2014. Dynamic weakening of serpentinite gouges and bare surfaces at seismic slip rates. Journal of Geophysical Research: Solid Earth, 119(11), 8107-8131.

Rabinowitz, H.S., Savage, H.M., et al., 2013. Detecting the frictional temperature rise during the 2011 Tohoku earthquake using the thermal maturity of biomarkers. In: Abstract T41F-07 presented at 2013 Fall Meeting, AGU, San Francisco, Calif., 9e13 Dec.

Rathbun, A. P., and Marone, C., 2010. Effect of strain localization on frictional behavior of sheared granular materials. Journal of Geophysical Research: Solid Earth (1978–2012), 115(B1).

Reches, Z. E., & Dewers, T. A., 2005. Gouge formation by dynamic pulverization during earthquake rupture. Earth and Planetary Science Letters, 235(1), 361-374.

Reches, Z. E., and Lockner, D. A., 2010. Fault weakening and earthquake instability by powder lubrication. Nature, 467(7314), 452-455.

Rempe, M., Mitchell, T., et al., 2013. Damage and seismic velocity structure of pulverized rocks near the San Andreas Fault. J. Geophys. Res. Solid Earth 118 (6), 2813e2831.

Rempe, M., Smith, S. A., Ferri, F., Mitchell, T. M., and Di Toro, G., 2014. Clast-cortex aggregates in experimental and natural calcite-bearing fault zones. Journal of Structural Geology, 68, 142-157.

Rempel, A.W., Rice, J.R., 2006. Thermal pressurization and onset of melting in fault zones. J. Geophys. Res. Solid Earth 111 (B9) (1978e2012).

Rice, J. R., 1992. Fault stress states, pore pressure distributions, and the weakness of the San Andreas fault. International Geophysics, 51, 475-503.

Rice, J. R., 2006. Heating and weakening of faults during earthquake slip. Journal of Geophysical Research: Solid Earth (1978–2012), 111(B5).

Rice, J. R., 1978. Thermodynamics of the quasi-static growth of Griffith cracks. Journal of the Mechanics and Physics of Solids, 26(2), 61-78.

Rice J. R., J. W. Rudnicki, and J. D. Platt, 2014, Stability and localization of rapid shear in fluid-saturated fault gouge: 1. Linearized stability analysis, J. Geophys. Res. Solid Earth, 119, doi:10.1002/2013JB010710.

Rice, J. R., and Cocco, M., 2007. Seismic fault rheology and earthquake dynamics. Tectonic Faults: Agents of Change on a Dynamic Earth, 99-137.

Rietveld, H.M., 1967. Line profiles of neutron powder-diffraction peaks for structure refinement. Acta Crystallogr. 22 (1), 151e152.

Roberts, G.P., Michetti, A.M., 2004. Spatial and temporal variations in growth rates along active normal fault systems: an example from the Lazio Abruzzo Apennines, central Italy. J. Struct. Geol. 26 (2), 339e376.

Robertson, E. C., 1983. Relationship of fault displacement to gouge and breccia thickness. Min. Eng., 35, 1426-1432

Robin P.Y., 1978 Pressure solution at grain-to-grain contacts. Geochim Cosmochim Acta, 42:1383–1389

Rockwell, T. K., and Ben-Zion, Y., 2007. High localization of primary slip zones in large earthquakes from paleoseismic trenches: Observations and implications for earthquake physics. Journal of Geophysical Research: Solid Earth (1978–2012), 112(B10).

Rodriguez-Navarro, C., Ruiz-Agudo, E., Luque, A., Rodriguez-Navarro, A. B., and Ortega-Huertas, M., 2009. Thermal decomposition of calcite: Mechanisms of formation and textural evolution of CaO nanocrystals. American Mineralogist, 94(4), 578-593.

Rowe, C.D., Kirkpatrick, J.D., et al., 2012. Fault rock injections record paleo-earthquakes. Earth Planet. Sci. Lett. 335, 154e166.

Rowe C. and Griffith A.W., 2014. Earthquake signatures from fast slip and dynamic fracture propagation: state of the art. Abstract T14A-01, AGU Fall Meeting

405 Røyne, A., Bisschop, J., and Dysthe, D. K., 2011. Experimental investigation of surface energy
406 and subcritical crack growth in calcite. Journal of Geophysical Research: Solid Earth (1978–
407 2012), 116(B4).

408 Rudnicki, J. W., and Rice, J. R., 2006. Effective normal stress alteration due to pore pressure
409 changes induced by dynamic slip propagation on a plane between dissimilar materials. Journal
410 of Geophysical Research: Solid Earth (1978–2012), 111(B10).

411 Ruina, A., 1983. Slip instability and state variable friction laws. Journal of Geophysical
412 Research: Solid Earth (1978–2012), 88(B12), 10359-10370.

413 Rutter E.H., 1976. The kinetics of rock deformation by pressure solution. Phil Trans R Soc Lond
414 A283:203–219

415 Rutter, E. H., Maddock, R. H., Hall, S. H., and White, S. H., 1986. Comparative microstructures
416 of natural and experimentally produced clay-bearing fault gouges. Pure and Applied
417 Geophysics, 124(1-2), 3-30.

418 Sagy, A., and Brodsky, E. E., 2009. Geometric and rheological asperities in an exposed fault
419 zone. Journal of Geophysical Research: Solid Earth (1978–2012), 114(B2).

420 Sammis, C. G., and Biegel, R. L., 1989. Fractals, fault-gouge, and friction. In Fractals in
421 geophysics (pp. 255-271). Birkhäuser Basel.

422 Savage, H. M., and Brodsky, E. E., 2011. Collateral damage: Evolution with displacement of
423 fracture distribution and secondary fault strands in fault damage zones. Journal of Geophysical
424 Research: Solid Earth (1978–2012), 116(B3).

425 Savage, H.M., Polissar, P.J., et al., 2014. Biomarkers heat up during earthquakes: new evidence
426 of seismic slip in the rock record. Geology 42 (2), 99e102.

427 Sawai, M., Shimamoto, T., et al., 2012. Reduction in BET surface area of Nojima fault gouge
428 with seismic slip and its implication for the fracture energy of earthquakes. J. Struct. Geol. 38,
429 117e138.

430 Schaff, D. P., G. H. R. Bokelmann, G. C. Beroza, F. Waldhauser, and W. L. Ellsworth, 2002. High-
431 resolution image of Calaveras Fault seismicity, J. Geophys. Res., 107(B9), 2186,
432 doi:10.1029/2001JB000633.

433 Schmid, S. M., Boland, J. N., and Paterson, M. S., 1977. Superplastic flow in finegrained
434 limestone. Tectonophysics, 43(3), 257-291.

435 Scholz, C.H., 1987. Wear and Gouge formation in brittle faulting. Geology 15 (6), 493e495.

436 Scholz, C. H., Wyss, M., and Smith, S. W., 1969. Seismic and aseismic slip on the San Andreas
437 fault. Journal of geophysical research, 74(8), 2049-2069.

438 Scholz, C. H., 2002. The mechanics of earthquakes and faulting. Cambridge university press.

439 Schindelin, J., Arganda-Carreras, I., et al., 2012. Fiji: an open-source platform for biological-
440 image analysis. Nat. Meth. 9 (7), 676e682.

441 Schubnel, A., Brunet, F., Hilairet, N., Gasc, J., Wang, Y., and Green, H. W., 2013. Deep-focus
442 earthquake analogs recorded at high pressure and temperature in the laboratory. Science,
443 341(6152), 1377-1380.

444 Scruggs, V.J., Tullis, T.E., 1998. Correlation between velocity dependence of friction and strain
445 localization in large displacement experiments on feldspar, muscovite and biotite gouge.
446 Tectonophysics 295 (1), 15e40.

447 Segall, P., and J. R. Rice, 2006, Does shear heating of pore fluid contribute to earthquake
448 nucleation?, J. Geophys. Res., 111, B09316, doi:10.1029/2005JB004129.

449 Shelly, D. R., 2010. Migrating tremors illuminate complex deformation beneath the
450 seismogenic San Andreas fault. Nature, 463(7281), 648-652.

451 Shimamoto, T., and Logan, J. M., 1981. Effects of simulated fault gouge on the sliding behavior
452 of Tennessee sandstone: nonclay gouges. Journal of Geophysical Research: Solid Earth (1978–
453 2012), 86(B4), 2902-2914.

454 Shimamoto, T., Togo, T., 2012. Earthquakes in the lab. Science 338 (6103), 54e55. Sibson, R.H.,
455 1975. Generation of pseudotachylyte by ancient seismic faulting. Geophys. J. Int. 43 (3),
456 775e794.

457 Shimamoto, T., and Tsutsumi, A., 1994. A new rotary-shear high-speed frictional testing
458 machine: its basic design and scope of research. J. Tecton. Res. Group Jpn, 39, 65-78.

459 Shimamoto, T., Togo, T., 2012. Earthquakes in the lab. Science 338 (6103), 54e55.

460 Sibson, R. H., 1986. Brecciation processes in fault zones: inferences from earthquake rupturing.
461 Pure and Applied Geophysics, 124(1-2), 159-175.

462 Sibson, R. H., 1973. Interactions between temperature and pore-fluid pressure during
463 earthquake faulting and a mechanism for partial or total stress relief. Nature, 243(126), 66-68.

464 Sibson, R. H., 1975. Generation of pseudotachylyte by ancient seismic faulting. Geophysical
465 Journal International, 43(3), 775-794.

466 Sibson, R. H., 1977. Fault rocks and fault mechanisms. Journal of the Geological Society, 133(3),
467 191-213.

468 Sibson, R. H., 1981. Fluid flow accompanying faulting: field evidence and models. Earthquake
469 prediction, 593-603.

470 Sibson, R. H., 1990. Conditions for fault-valve behaviour. Geological Society, London, Special
471 Publications, 54(1), 15-28.

472 Sibson, R. H., 1990. Rupture nucleation on unfavorably oriented faults. Bulletin of the
473 Seismological Society of America, 80(6A), 1580-1604.

474 Sibson, R. H., 1992. Implications of fault-valve behaviour for rupture nucleation and
475 recurrence. Tectonophysics, 211(1), 283-293.

476 Sibson, R.H., 2003. Thickness of the seismic slip zone. Bull. Seismol. Soc. Am. 93 (3),
477 1169e1178.

478 Siman-Tov, S., Aharonov, E., et al., 2013. Nanograins form carbonate fault mirrors. Geology 41
479 (6), 703e706.

480 Skempton, A. W., 1960. Terzaghi's discovery of effective stress. From Theory to Practice in Soil
481 Mechanics: Selections from the Writings of Karl Terzaghi, 42-53.

482 Smith, S.A.F., Collettini, C., et al., 2008. Recognizing the seismic cycle along ancient faults: CO2-
483 induced fluidization of breccias in the footwall of a sealing low-angle normal fault. J. Struct.
484 Geol. 30 (8), 1034e1046.

485 Smith, S. A., Billi, A., Di Toro, G., and Spiess, R., 2011. Principal slip zones in limestone:
486 microstructural characterization and implications for the seismic cycle (Tre Monti Fault, Central
487 Apennines, Italy). Pure and Applied Geophysics, 168(12), 2365-2393.

488 Smith, S.A.F., Di Toro, G., et al., 2013. Coseismic recrystallization during shallow earthquake
489 slip. Geology 41 (1), 63e66.

490 Smith, S.A.F., Di Toro, G., et al., 2012. Field and experimental constraints on seismic
491 localization in granular fault gouge. In: Abstract S11A-06 presented at 2012 Fall Meeting, AGU,
492 San Francisco, Calif., 3e7 Dec.

493 Smith, S.A.F., Nielsen, S., Di Toro, G., 2015. Strain localization and the onset of dynamic
494 weakening in fault gouge. Earth and Planetary Science Letters, in press.

495 Snoke, A.W., Tullis, J., et al., 1998. Fault-related Rocks: a Photographic Atlas. Princeton
496 University Press.

497 Spagnuolo E., Plumper O., Violay M., Cavallo A., Di Toro G., 2014. Shock Waves Trigger Fault
498 Weakening in Calcite-bearing Rocks During Earthquakes, American Geophysical Union Annual
499 Meeting Abstracts S11C-4359, December 2014.

500 Speranza, F., and Minelli, L., 2014. Ultra-thick Triassic dolomites control the rupture behavior
501 of the central Apennine seismicity: Evidence from magnetic modeling of the L'Aquila fault
502 zone. Journal of Geophysical Research: Solid Earth, 119(9), 6756-6770.

503 Sulem, J., and Famin, V., 2009. Thermal decomposition of carbonates in fault zones: Slip-
504 weakening and temperature-limiting effects. Journal of Geophysical Research: Solid Earth
505 (1978–2012), 114(B3).

506 Thurber, C., Zhang, H., Waldhauser, F., Hardebeck, J., Michael, A., and Eberhart-Phillips, D.,
507 2006. Three-dimensional compressional wavespeed model, earthquake relocations, and focal
508 mechanisms for the Parkfield, California, region. Bulletin of the Seismological Society of
509 America, 96(4B), S38-S49.

510 Tadai, O., W. Tanikawa, T. Hirose, M. Sakaguchi, and W. Lin 2009, Design of new frictional
511 testing machine for shallow fault materials, Eos Trans. AGU, 90(52), Fall Meet. Suppl., Abstract
512 T41A-2003.

513 Tanikawa, W., Mukoyoshi, H., and Tadai, O., 2012. Experimental investigation of the influence
514 of slip velocity and temperature on permeability during and after high-velocity fault slip.
515 Journal of StructuralGeology, 38, 90-101.

516 Tenthorey, E., & Cox, S. F., 2006. Cohesive strengthening of fault zones during the interseismic
517 period: An experimental study. Journal of Geophysical Research: Solid Earth (1978–2012),
518 111(B9).

519 Terakawa, T., Zoporowski, A., Galvan, B., Miller, S.A., 2010. High-pressure fluid at hypocentral
520 depths in the L'Aquila region inferred from earthquake focal mechanisms. Geology 38, 995–
521 998

522 Terzaghi, K., 1923. Die Berechnung des Durchlassigkeitsziffer des Tones aus dem Verlauf der
523 hydrodynamischen Spannungserscheinungen. Sitz. Akad. Wiss. Wien, abt IIa, 132, 125–138.

524 Tjong, S. C., and Chen, H., 2004. Nanocrystalline materials and coatings. Materials Science and
525 Engineering: R: Reports, 45(1), 1-88.

526 Twiss, R. J., and Moores, E. M., 1992. Structural Geology.

527 Ujiie, K., and A. Tsutsumi, 2010, High-velocity frictional properties of clay-rich fault gouge in a
528 megasplay fault zone, Nankai subduction zone, Geophys. Res. Lett., 37, L24310,
529 doi:10.1029/2010GL046002.

530 Valoroso, L., Chiaraluce, L., and Collettini, C., 2014. Earthquakes and fault zone structure.
531 Geology, 42(4), 343-346.

532 Verberne, B. A., Spiers, C. J., Niemeijer, A. R., De Bresser, J. H. P., De Winter, D. A. M., and
533 Plümper, O., 2013. Frictional Properties and Microstructure of Calcite-Rich Fault Gouges
534 Sheared at Sub-Seismic Sliding Velocities. Pure and Applied Geophysics, 1-24.

535 Verberne, B. A., Plümper, O., de Winter, D. M., and Spiers, C. J., 2014. Superplastic nanofibrous
536 slip zones control seismogenic fault friction. Science, 346(6215), 1342-1344.

537 Vermilye, J. M., and Scholz, C. H., 1998. The process zone: A microstructural view of fault
538 growth. Journal of Geophysical Research: Solid Earth (1978–2012), 103(B6), 12223-12237.

539 Veveakis, E., Vardoulakis, I., & Di Toro, G., 2007. Thermoporomechanics of creeping landslides:
540 The 1963 Vaiont slide, northern Italy. Journal of Geophysical Research: Earth Surface (2003–
541 2012), 112(F3).

542 Violay, M., Nielsen, S., Spagnuolo, E., Cinti, D., Di Toro, G., and Di Stefano, G., 2013. Pore fluid
543 in experimental calcite-bearing faults: Abrupt weakening and geochemical signature of co-
544 seismic processes. Earth and Planetary Science Letters, 361, 74-84.

545 Violay, M., Nielsen, S., Gibert, B., Spagnuolo, E., Cavallo, A., Azais, P., ... and Di Toro, G., 2014.
546 Effect of water on the frictional behavior of cohesive rocks during earthquakes. Geology, 42(1),
547 27-30.

548 Violay, M., Di Toro, G., Nielsen, S., Spagnuolo, E., and Burg, J.P., in preparation. Experimental
549 evidence of thermo-mechanical pressurization of faults during earthquakes.

550 Voight, B., and Faust, C., 1982. Frictional heat and strength loss in some rapid landslides.
551 Geotechnique, 32(1), 43-54.

552 Warr, L.N., Cox, S., 2001. Clay mineral Transformations and Weakening Mechanisms along the
553 Alpine Fault, New Zealand. In: Geological Society, London, Special Publications, vol. 186, pp.
554 85e101 (1).

555 Wheeler J, 1992. Importance of pressure solution and Coble creep in the deformation of
556 polymineralic rocks. J Geophys Res 97: 4579–4586

557 Wibberley, C. A., 2005. J. Initiation of basement thrust detachments by fault-zone reaction
558 weakening. SPECIAL PUBLICATION-GEOLOGICAL SOCIETY OF LONDON, 245, 347.

559 Wibberley, C. A., and Shimamoto, T., 2003. Internal structure and permeability of major strike-
560 slip fault zones: the Median Tectonic Line in Mie Prefecture, Southwest Japan. Journal of
561 Structural Geology, 25(1), 59-78.

562 Wintsch, R. P., Christoffersen, R., and Kronenberg, A. K., 1995. Fluid-rock reaction weakening
563 of fault zones. Journal of Geophysical Research: Solid Earth (1978–2012), 100(B7), 13021-
564 13032.

565 Würschum, R., Herth, S., and Brossmann, U., 2003. Diffusion in nanocrystalline metals and
566 alloys—a status report. Advanced Engineering Materials, 5(5), 365-372.

567 Yao, L., Shimamoto, T., et al., 2013. Rapid postseismic strength recovery of Pingxi fault gouge
568 from the Longmenshan fault system: experiments and implications for the mechanisms of
569 high-velocity weakening of faults. J. Geophys. Res. Solid Earth 118 (8), 4547e4563.

570 Zhang, L., and He, C., 2013. Frictional properties of natural gouges from Longmenshan fault
571 zone ruptured during the Wenchuan Mw7. 9 earthquake. Tectonophysics, 594, 149-164.

Appendix A

Rempe, M., Smith, S. A., Ferri, F., Mitchell, T. M., and Di Toro, G., 2014. Clast-cortex aggregates in experimental and natural calcite-bearing fault zones. Journal of Structural Geology, 68, 142-157.

Appendix B

1. Additional figures

a. Coefficient of friction in selected experiments

b. Strain data for the low- and intermediate-strain zones

2. SEM images

a. Room-dry experiments, 8.5 MPa, 1 m/s

b. Water-dampened experiments, 8.5 MPa, 1 m/s

c. Room-dry experiments, 3, 15, and 20 MPa, 1 m/s

d. Room-dry experiments, 8.5 MPa, 1 mm/s

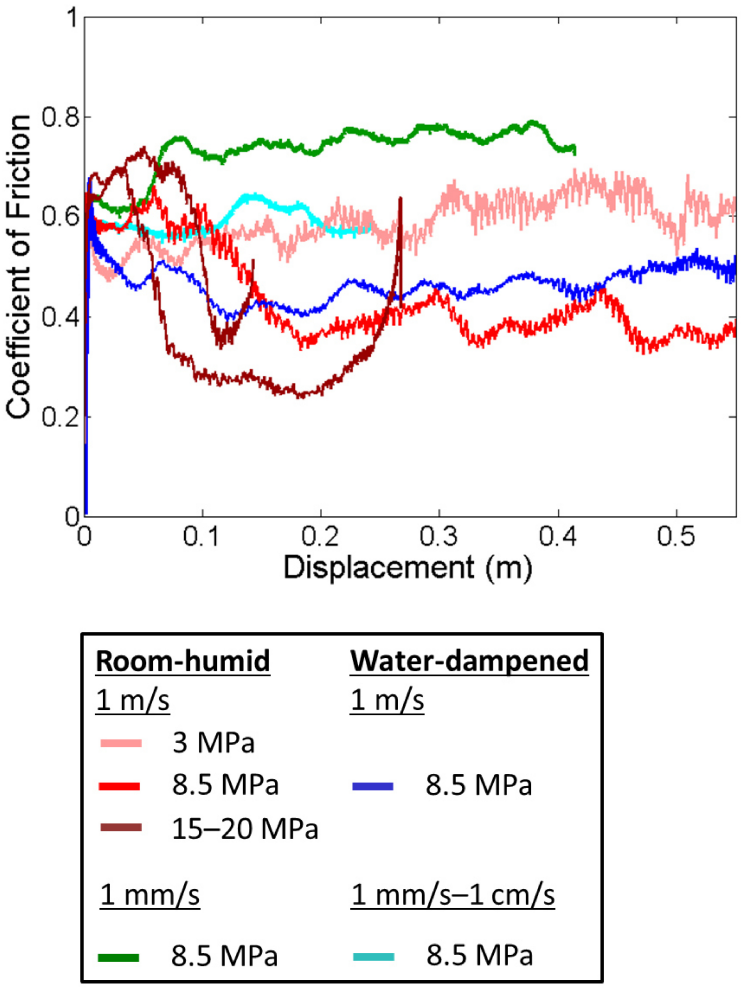

Figure B1a. Evolution of the coefficient of friction. The coefficient of friction $\mu = \frac{\tau}{\sigma}$ versus the displacement of exemplary experiments performed with different slip velocities (1 mm/s–1 m/s), normal stresses (3–20 MPa) and in room-dry and water-dampened conditions. See legend for color-coding of the curves. Note that the peak coefficient of friction is similar in all conditions (c. 0.6–0.75) with only slightly higher values in those room-dry experiments that were performed at high normal stress or low velocity. However, the steady-state coefficient of friction is c. 0.6 at 3 MPa, 0.4 at 8.5 MPa, 0.35 at 15 MPa, and 0.25 at 20 MPa, showing that weakening is much stronger at higher normal stress. In water-dampened conditions, the steady-state shear strength is c. 0.5 in the experiments performed at 8.5 MPa and 1 m/s, and c. 0.6 at 8.5 MPa and 1 mm/s. The strength recovers as the velocity is reduced at the end of the experiment; this effect is very pronounced in the high-normal stress experiments.

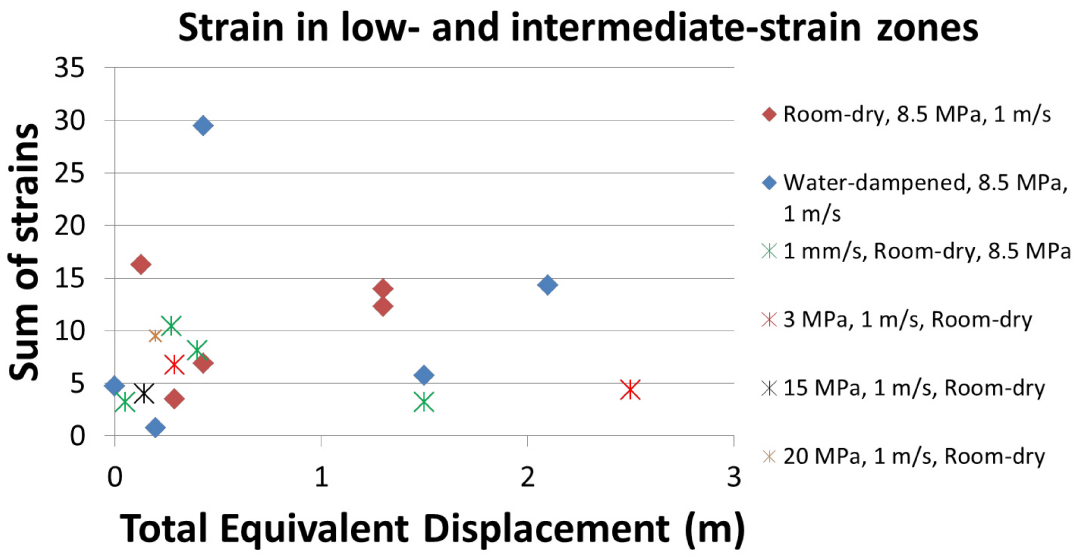

Figure B1b. Strain in the low- and intermediate-strain zones. All data; experiments performed at a range of velocities, normal stresses and ambient conditions. Red diamonds: Room-dry conditions, 8.5 MPa, 1 m/s; blue diamonds: Water-dampened, 8.5 MPa, 1 m/s; Green stars: Room-dry conditions, 8.5 MPa, 1 mm/s; Red stars: Room-dry conditions, 3 MPa, 1 m/s; Black stars: Room-dry conditions, 15 MPa, 1 m/s; Orange stars: Room-dry conditions, 20 MPa, 1 m/s. When taking into account the experiments at normal stresses different from 8.5 MPa and at low velocity, as it was not done in Fig. 9c, the wide spread in the data becomes more apparent.

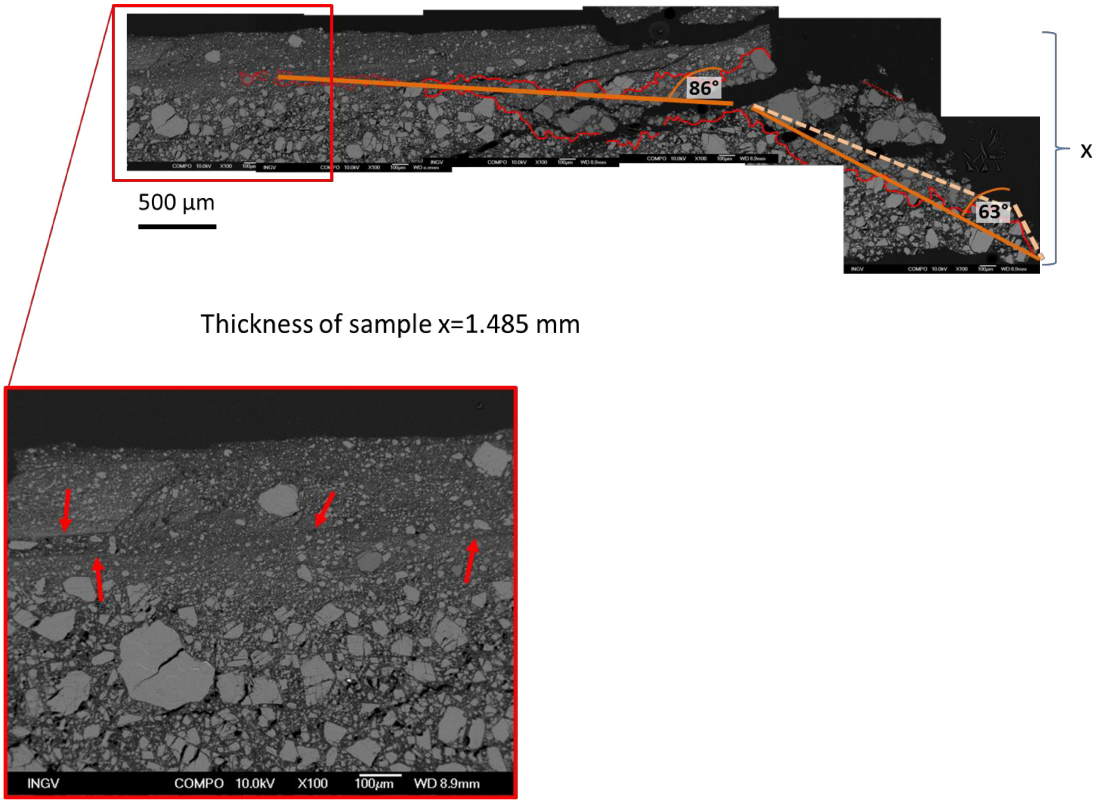

2a. Room-dry experiments, 8.5 MPa, 1 m/s, **s953, 0.13 m**

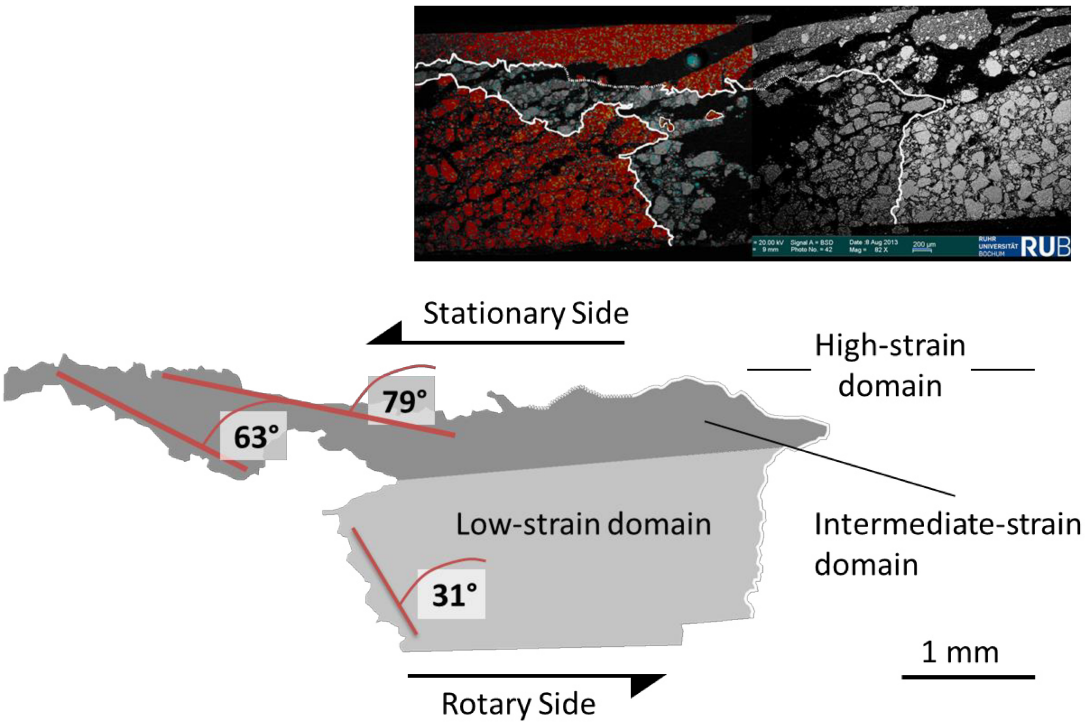

2a. Room-dry experiments, 8.5 MPa, 1 m/s, **s887, 0.29 m**

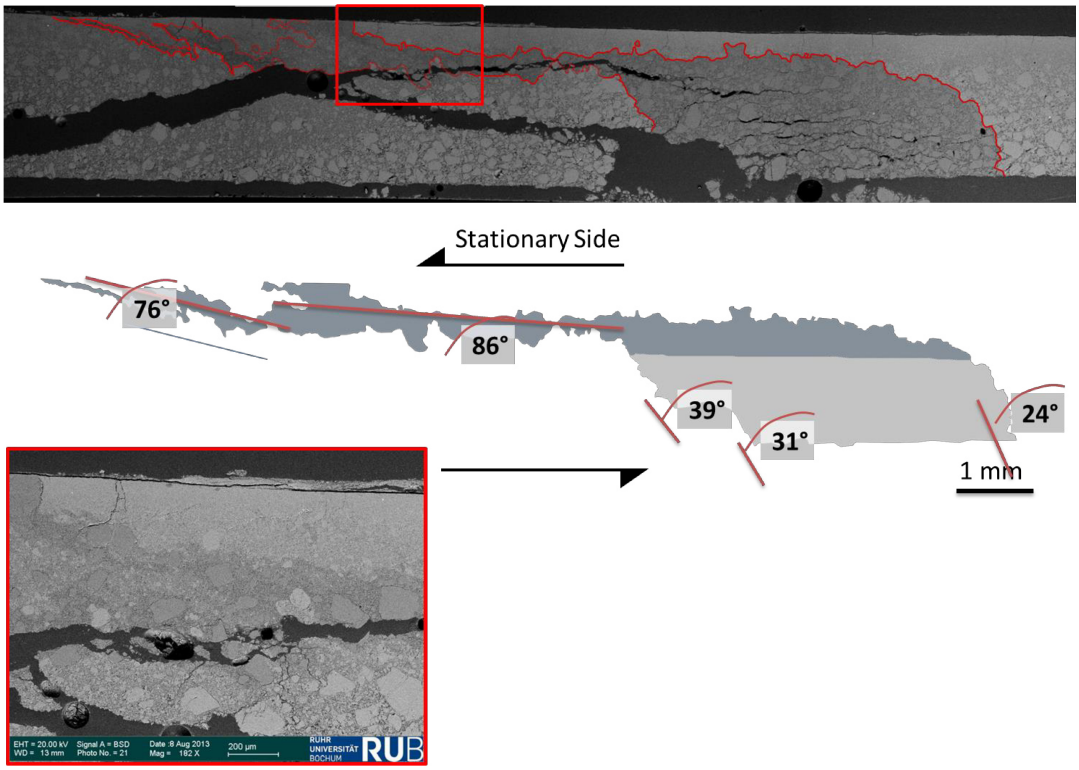

2a. Room-dry experiments, 8.5 MPa, 1 m/s; **s881, 0.43 m**

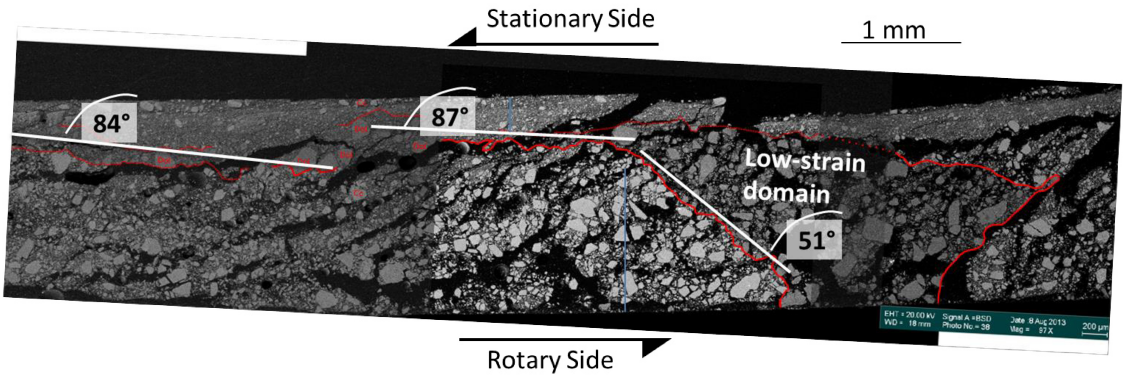

2a. Room-dry experiments, 8.5 MPa, 1 m/s; **s896, 1.3 m**

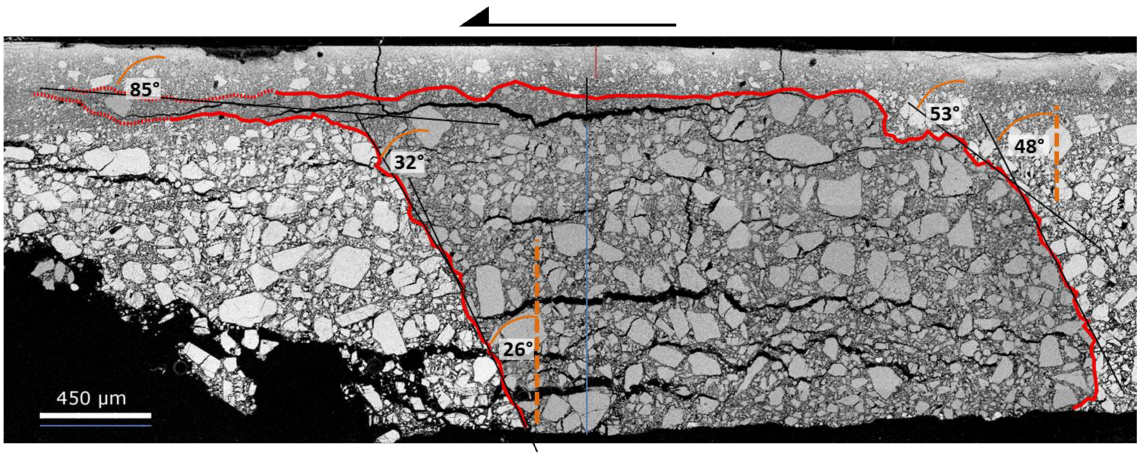

tan26=0.49
tan32=0.63

tan48=1.11
tan53=1.33

2a. Room-dry experiments, 8.5 MPa, 1 m/s; **s943, 1.3 m**

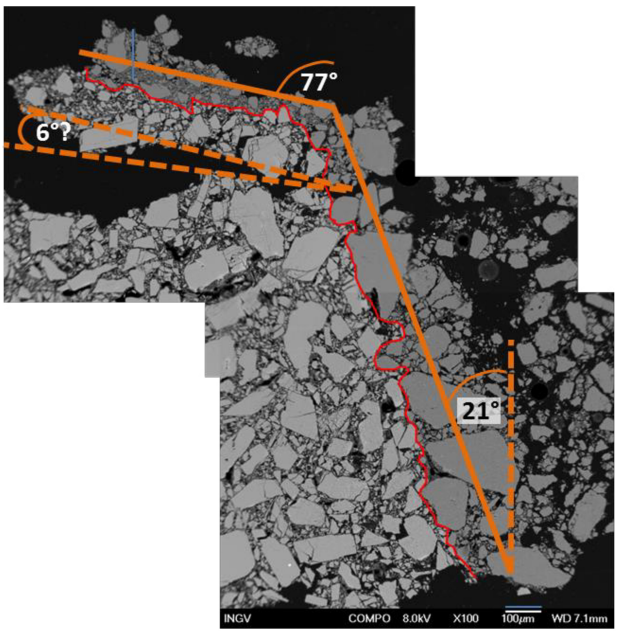

Thickness: 1.4 mm
Bulk strain: 0.011/0.0014= 7.9

2b. Water-dampened experiments, 8.5 MPa, 1 m/s; **s959, 1.1 cm**

s959 second marker
Localization has at least started

Smooth surface is due to preserving
(sample lay on this side)

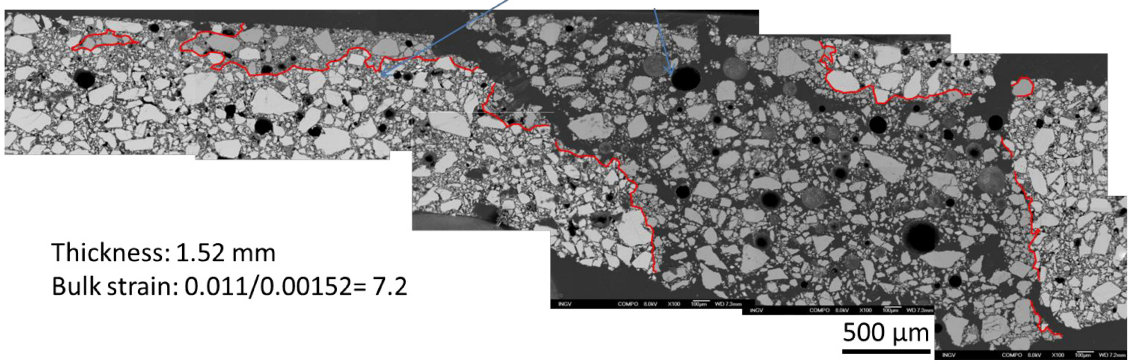

Thickness: 1.52 mm
Bulk strain: 0.011/0.00152= 7.2

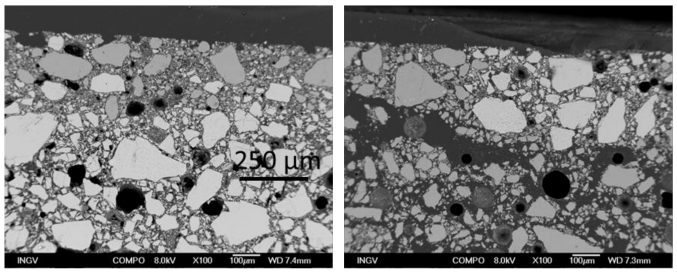

2b. Water-dampened experiments, 8.5 MPa, 1 m/s; **s959, 1.1 cm**

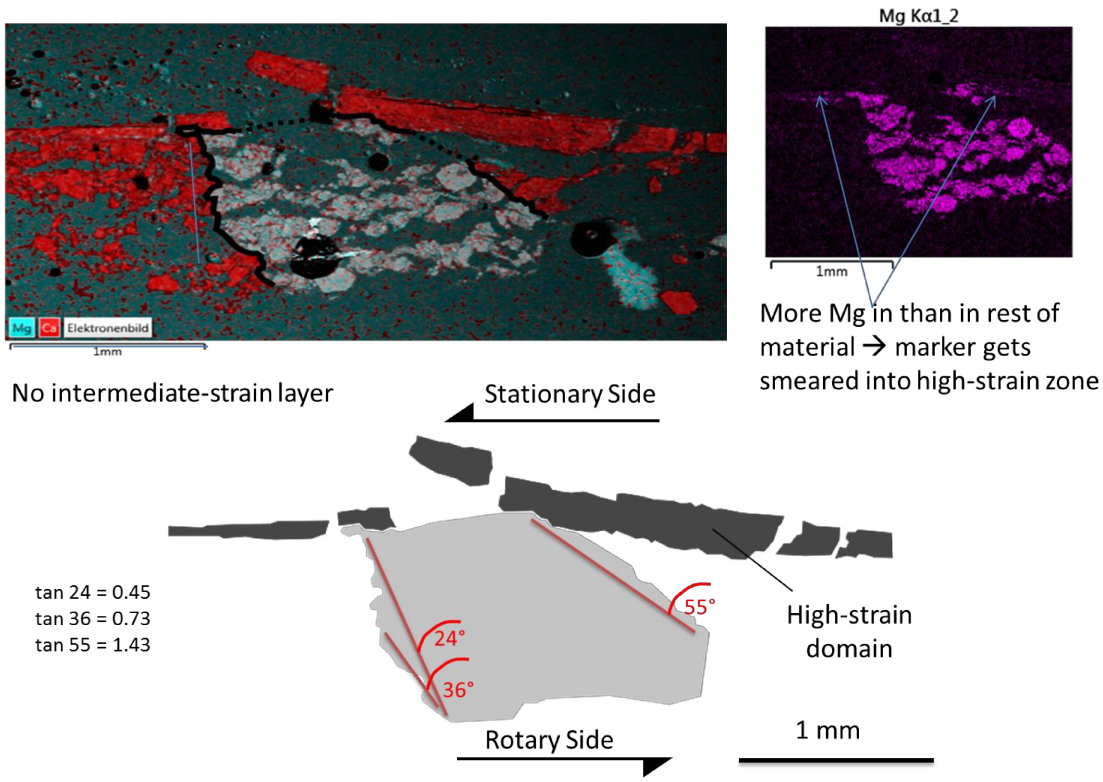

2b. Water-dampened experiments, 8.5 MPa, 1 m/s; **s895, 20 cm**

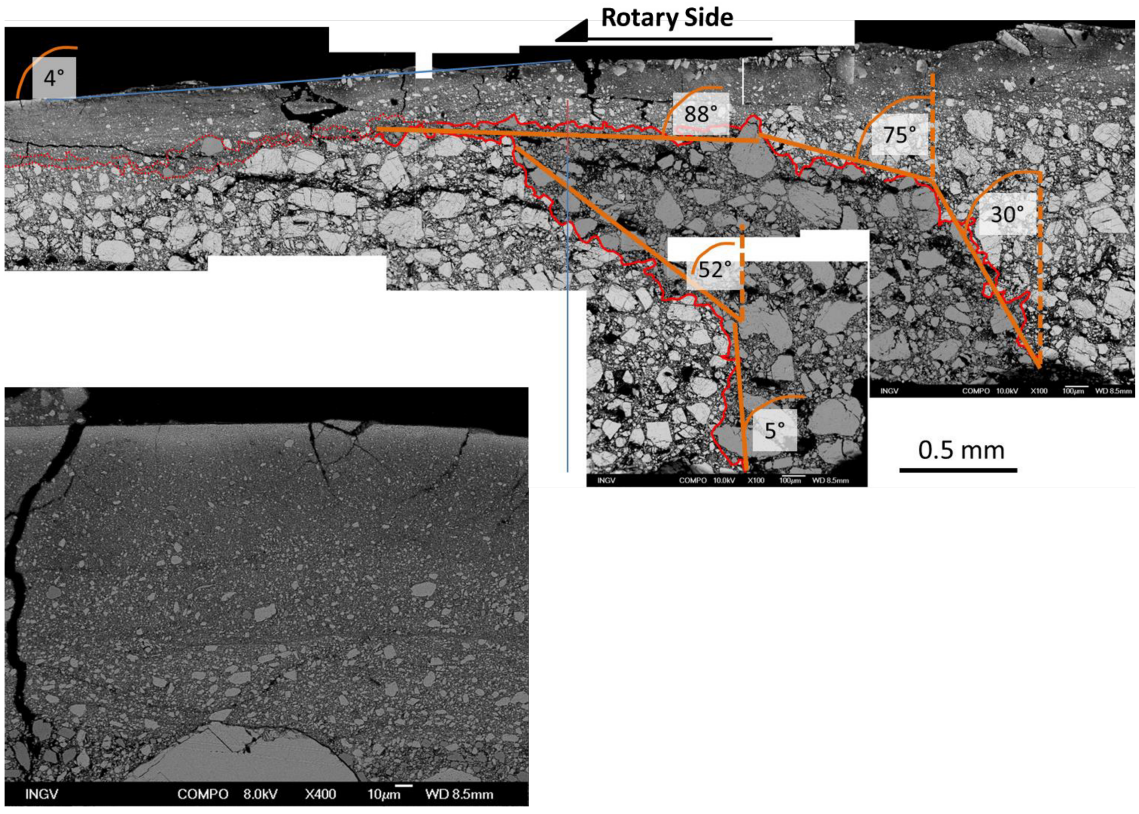

2b. Water-dampened experiments, 8.5 MPa, 1 m/s; **s961, 43 cm**

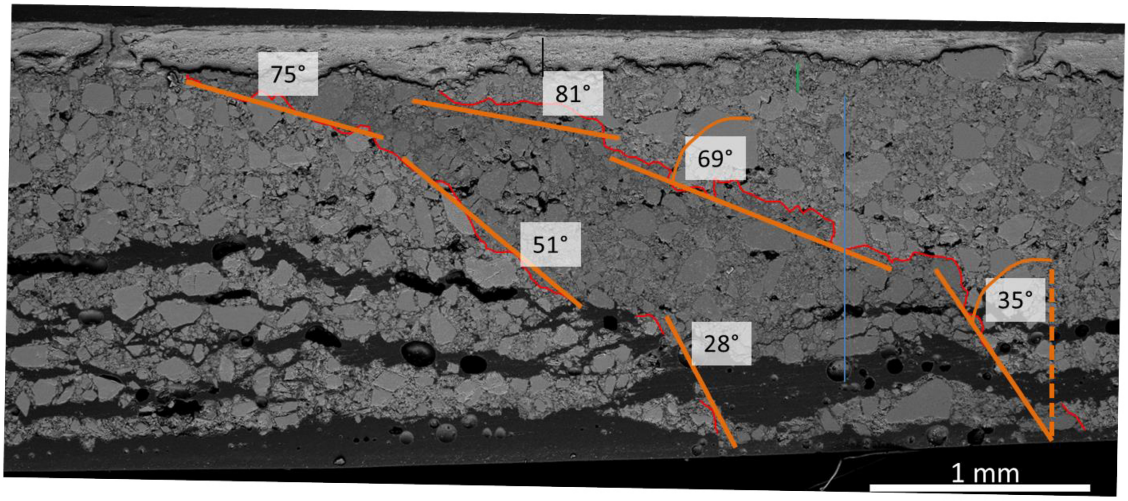

2b. Water-dampened experiments, 8.5 MPa, 1 m/s; **s898, 1.5 m**

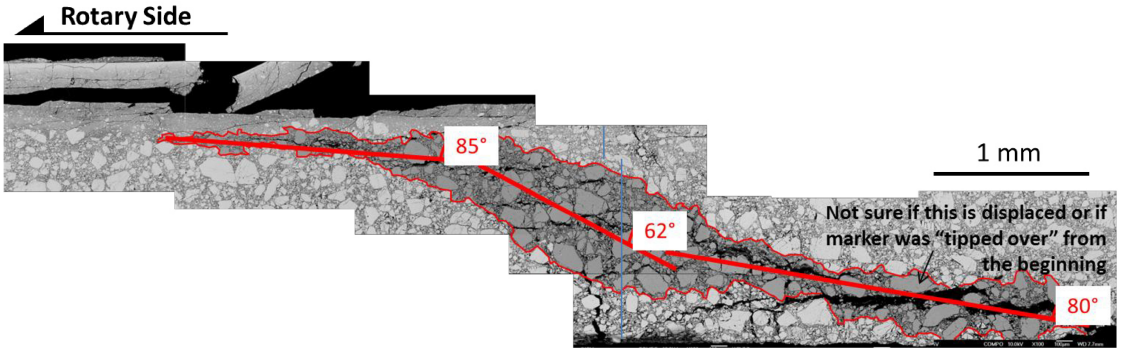

2b. Water-dampened experiments, 8.5 MPa, 1 m/s; **s962, 2.1 m**

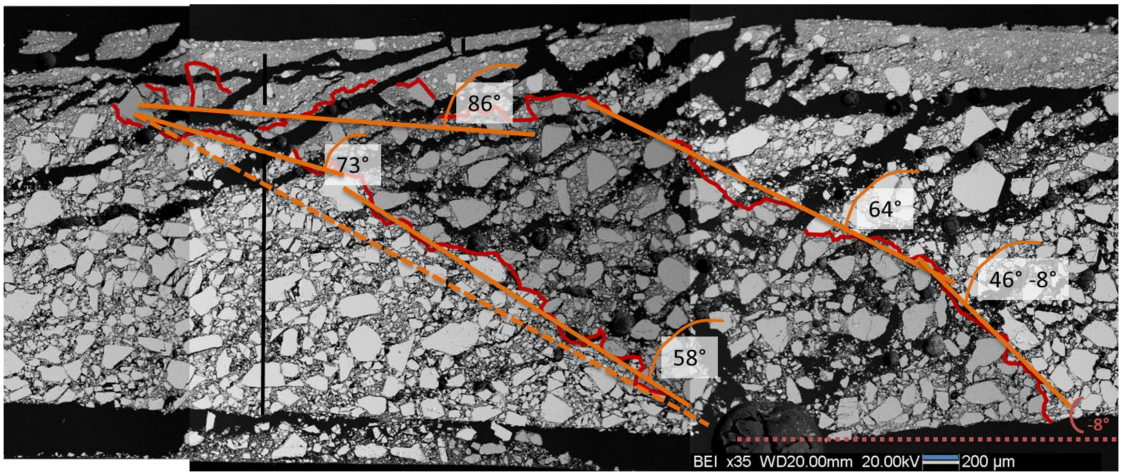

2c. Room-dry experiments, 3 MPa, 1 m/s, **s897, 0.29 m**

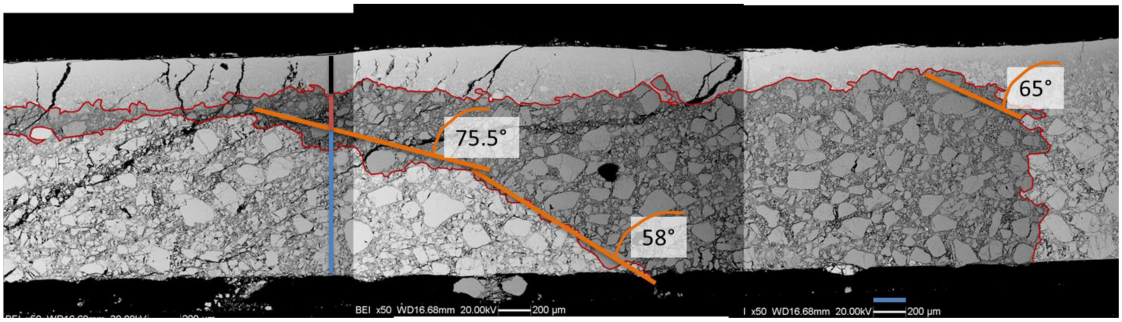

2c. Room-dry experiments, 3 MPa, 1 m/s, **s886, 2.5 m**

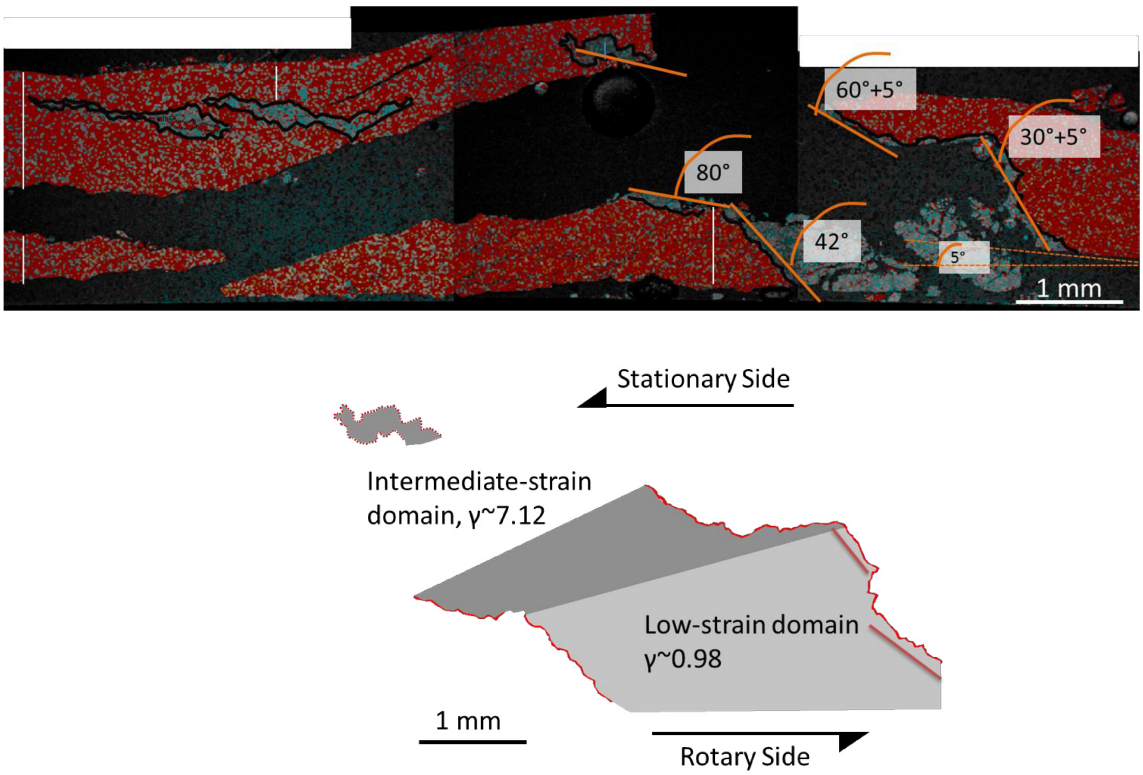

2c. Room-dry experiments, 15 MPa, 1 m/s, **s875, 0.143 m**

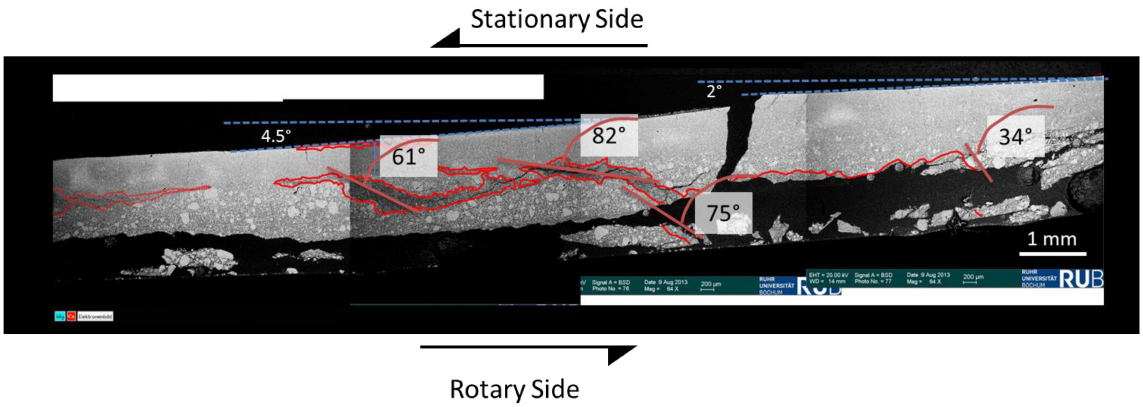

2c. Room-dry experiments, 20 MPa, 1 m/s, **s889, 0.20 m**

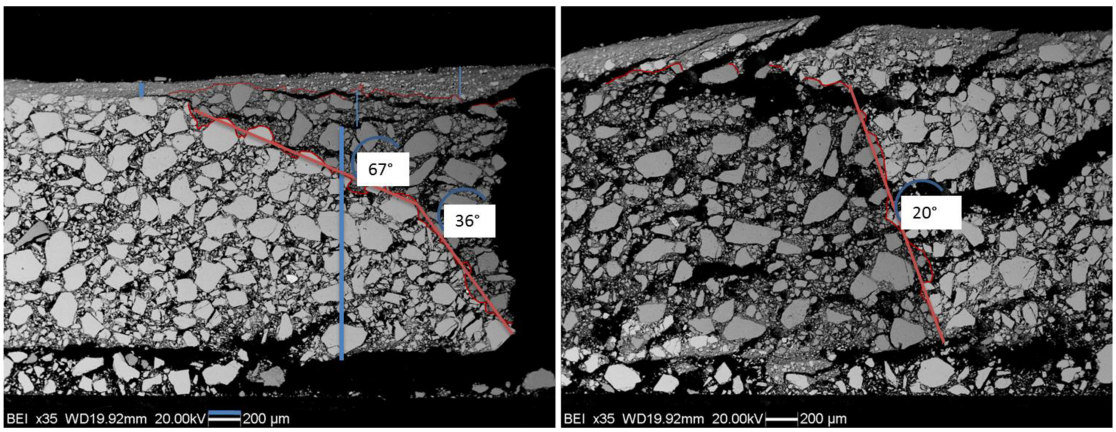

2d. Room-dry experiments, 8.5 MPa, 1 mm/s, **s883, 0.052 m**

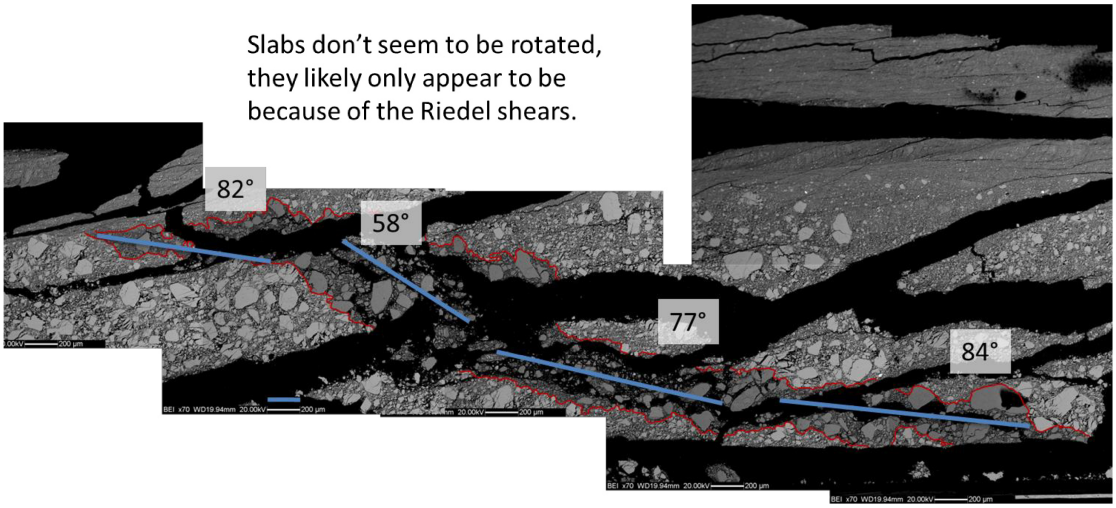

2d. Room-dry experiments, 8.5 MPa, 1 mm/s, **s974, 0.275 m**

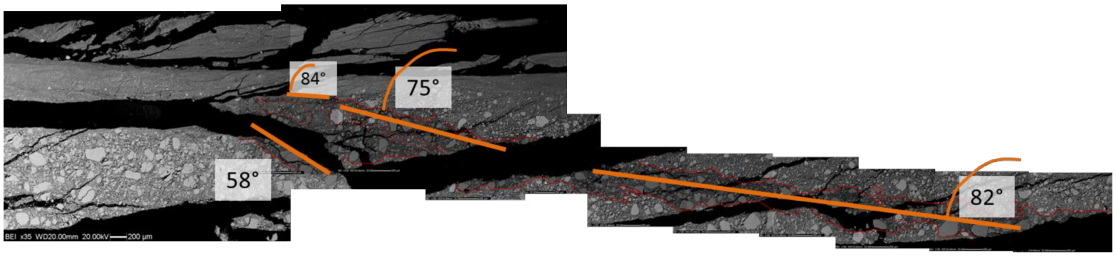

2d. Room-dry experiments, 8.5 MPa, 1 mm/s, **s882, 0.4 m**

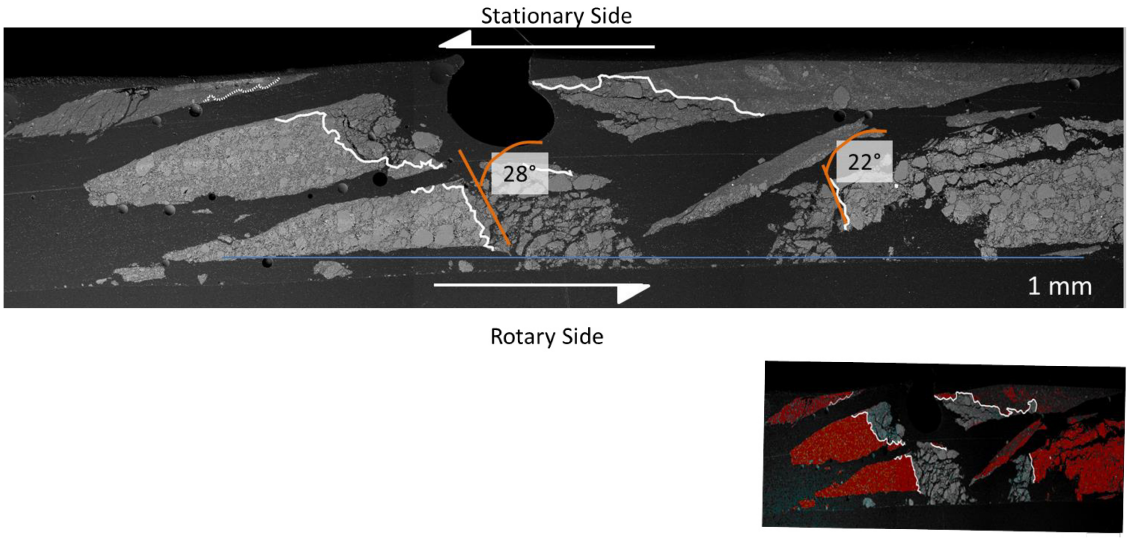

2d. Room-dry experiments, 8.5 MPa, 1 mm/s, **s885, 1.5 m**

Appendix C

Additional figures for Chapter III

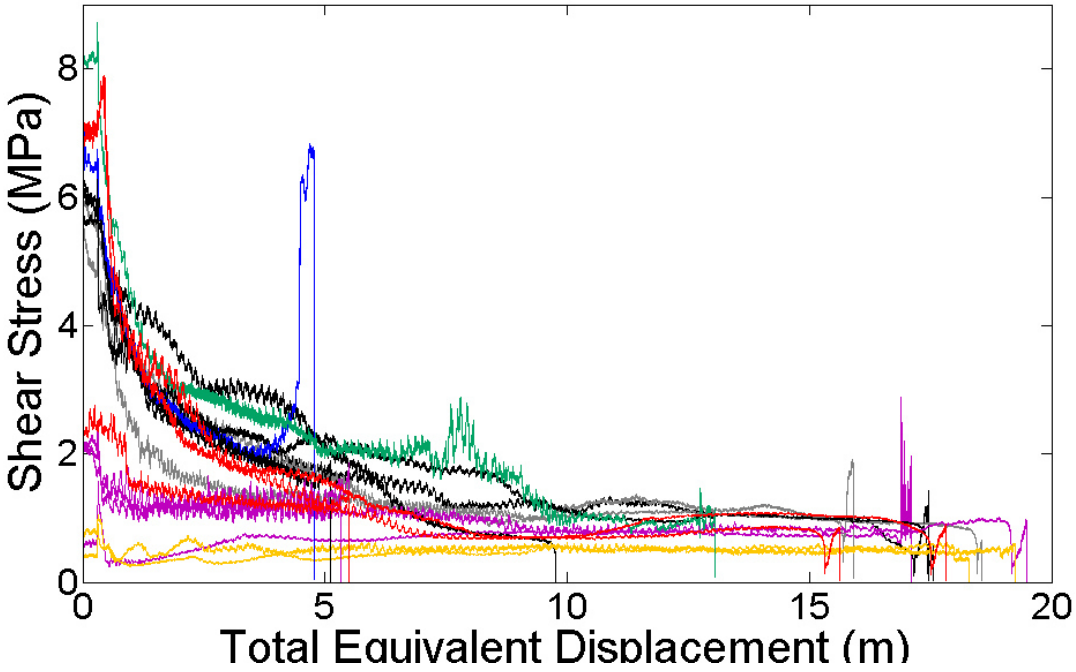

Figure C1. Shear-stress evolution of all saturated experiments. High velocity (1 m/s) is induced after 30 cm of displacement (denoted by dotted vertical line) and shear stress increases during a phase that lasts a few mm before peak strength is reached and dynamic weakening initiates. Renewed strengthening is due to the decrease in velocity at the end of the high-velocity step. Different colors correspond to different effective normal stresses: 12 MPa (green), 10 MPa (blue), 8.5 MPa (black and grey for pressure- and volume-control mode, respectively), 3 MPa (purple), and 1 MPa (yellow). Exemplary data curves are shown in Fig. 4, Chapter III.

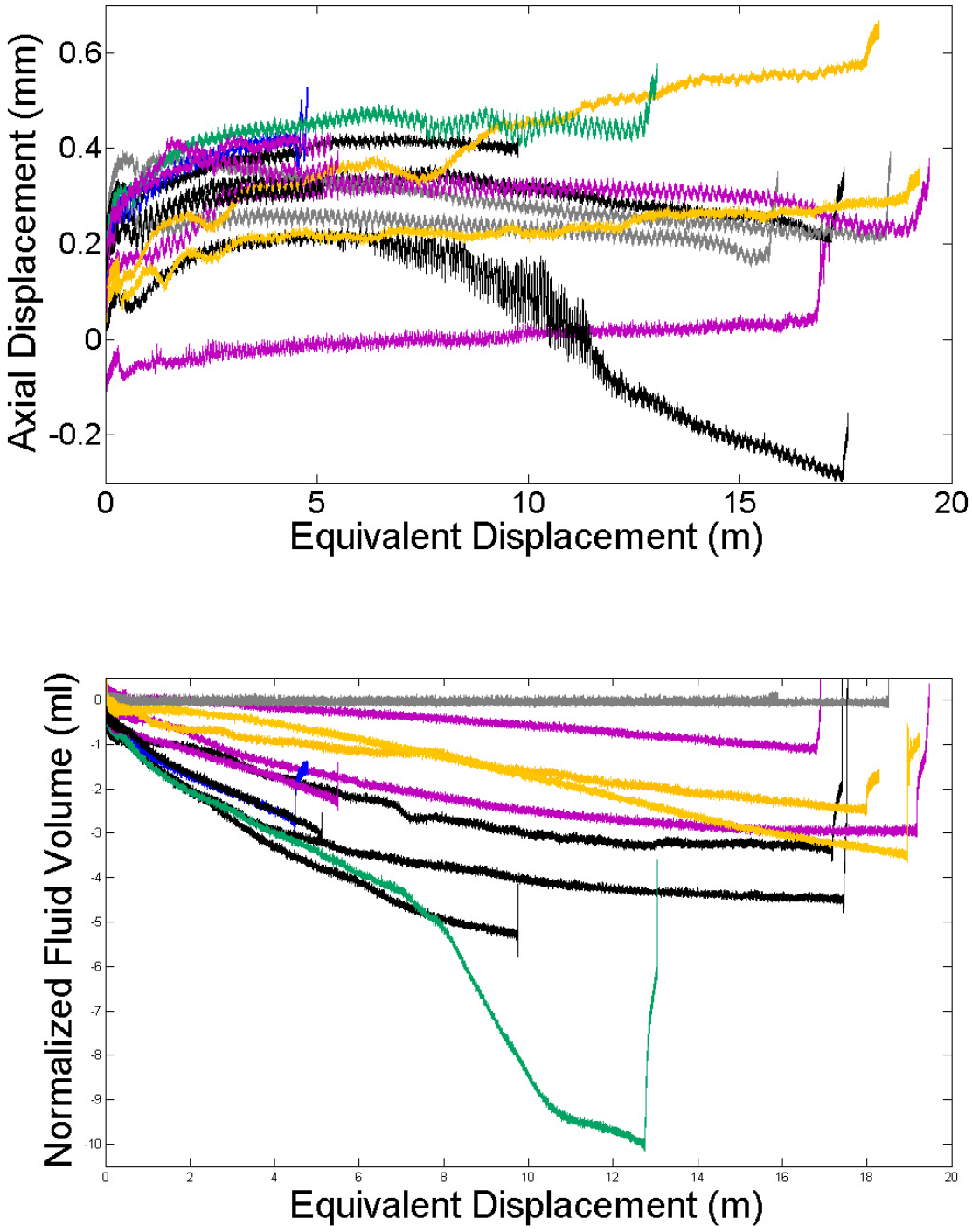

Figure C2. Mechanical data for all velocity steps. a) Axial displacement (selected experiments and description in Fig. 7b, Chapter III). Positive trend denotes compaction, negative denotes dilation (see Fig. 8c, Chapter III, for zoom of third velocity step). **b)** Normalized fluid volume (selected experiments and description in Fig. 7b, Chapter III).